Composition and morphology of C-A-S-H in pastes of alite and cement blended with supplementary cementitious materials

THÈSE N^{O} 6294 (2014)

PRÉSENTÉE LE 24 JUILLET 2014
À LA FACULTÉ DES SCIENCES ET TECHNIQUES DE L'INGÉNIEUR
LABORATOIRE DES MATÉRIAUX DE CONSTRUCTION
PROGRAMME DOCTORAL EN SCIENCE ET GÉNIE DES MATÉRIAUX

ÉCOLE POLYTECHNIQUE FÉDÉRALE DE LAUSANNE

POUR L'OBTENTION DU GRADE DE DOCTEUR ÈS SCIENCES

PAR

John Espen ROSSEN

acceptée sur proposition du jury:

Prof. H. Hofmann, président du jury
Prof. K. Scrivener, Dr B. Lothenbach, directrices de thèse
Dr J. Chen, rapporteur
Prof. A. P. Nonat, rapporteur
Prof. P. Stadelmann, rapporteur

ÉCOLE POLYTECHNIQUE
FÉDÉRALE DE LAUSANNE
Suisse
2014

Acknowledgements

Funding for this thesis was provided by the Swiss National Science Foundation under grant n°130419 and by Nagra (National Cooperative for the Disposal of Radioactive Waste) from the Long-Term Cement Studies (LCS).

I thank the members of the jury for reviewing this work and their feedback.

I must begin by thanking Karen for her undivided support again, especially during very difficult times.

I was particularly fortunate to spend my days in the best office one could hope for, MXG239!!! With Olga, Mathieu and Arnaud. You are the best! Fun and patient with me, you've contributed enormously to the success of this work and the good atmosphere. I'll miss you... guys!

Mathieu, you have a special place for being so enthusiastic and good to others. I was honored to share work and non-work times with you. Arnaud, how lucky I was to have you join my office when that's all I was hoping for! You truly were a great part of the Ph.D. life. I'll never forget those moments during trips, particularly in Québec. Thanks man! Olga, thank you for always being there for me! You were so patient with me. It means so much!

When I was not hearing the meetings going on in the room in front of me, I enjoyed the wonderful company of Lionel. Hilarious, yet serious in his work. I will miss those interruptions of work and the laughs (I won't quote any joke... most are NSFW!).

I've always appreciated how everyone found time to invest in organising activities and helping each other. It also contributed to a great atmosphere and as Karen said, a great generation of Ph.D. students, post-docs and collaborators!

I particularly appreciated finishing the studies with Julien "Bizzo" with who I could often talk (thank you!), Berta's joy of living, Mo's great organising skills for doing fun (and sometimes dangerous?) things, Marie-Alix's computer problems and trips to our office, Maude and Anne-Sandra's great help over the years (and Sandra's too!), Ashley's fun character, the good times with the post-docs (Cédric at the SEM, Ruben and Hadi for outdoor activities, the newcomer Aurélie for her fun spirits, and Christophe's humour), Elise's kindness, Pawel's hilarious play on words, Theo and Alexandra's relaxed way of being, the two "Yoshi's", the times I spent solving computer problems with Alain, talking technology with Joao and the thesis corrections "ça va pas" from Cyrille!

Amélie, you have no idea how lucky I was to finish my studies with you! You are a friend I'm truly blessed to have. You've really helped me on every level. And look at that! I finished my Ph.D.! Who'd thought!

I would therefore like to thank everyone who contributed to the success of this work.

I thank Helmut Kolb from Holcim for calcining the alite.

I thank Jean-Philippe Sacchetto from FEI and Daniel Galy from Synergie4 for helping me manage the SEM.

I thank Vanessa Kocaba and Emmanuel Gallucci who helped me with several questions during my thesis.

I thank all those from our Sinergia project: Barbara Lothenbach (and your funny jokes!), André Nonat, Isabele Pochard, Christophe Labbez, Sergey Churakov and Dmitrii Kulik, Luis Pegado, Gilles Plusquellec and Emilie L'Hôpital for this shared C–A–S–H experience!

I thank many from the LTP: Paul Bowen, Jacques Lemaître, Carlos Morais, Heinrich Hofmann, Abhishek Kumar and Lionel Maurizi for their help.

I thank the CIME staff: Fabienne Bobard, Gregoire Baroz, Duncan Alexander, Guillaume Pasche, Guillaume Lucas, Davide Demurtas, Quentin Jeangros, Colette Vallotton, Brian Ebersold and especially Emad Oveisi, Marco Cantoni, Danièle Laub and Amélie for their help.

I thank Karen Scrivener, Barbara Lothenbach and the LMC for having given me the opportunity to carry out this thesis. Thank you Marie-Alix, Maude, Anne-Sandra and Sandra. Thank you to the two "Phillipe" and Amor. Thank you Cédric, Christophe and Emmanuelle for your help on the SEM. Thank you Théo, Alexandra, Julien (Ston), Hui, Cheng, Quang Huy, Alain, Ruben (also for the Rietveld analysis of the cement), Hadi, Aurélie, Cyrille (for spending time improving my writing), François, Lilian, Huang, Keren, Shigeyoshi, Aslam, Mohamad, Julien (Bizzo), Berta, Elise, Pawel and finally Lionel, Arnaud, Mathieu and Olga.

I thank my fellow musicians for helping me loose myself outside the thesis Benny, David, Rachid, Loïc, Frank, Marc, Alexis (Heraief), Florian, Halima, Adrien (Fauconnet) and Manohar.

I thank my fellow ski partners for the fun moments in the mountains: Delphine, Alexis (Leibbrandt), Niels, Laurent, Patrick, Sébastien, Julien (Dimitriou), Laure, Valérie, Nicolas and Marion.

I thank those in Geneva and Lausanne: Stephan, Olivier, Morgan, Mélanie, Fabrice and Cécile. Also, I thank the Péclard, Jaques Henry and Béatrice Steiner.

I dedicate this thesis to those who parted with this world during the past years. Niccolo, Uncle Petey, Mutti, Oncle Joël, Tante Randi, Unkel Stein, and my only Farfar and Farmor.

I thank my family in Switzerland, Norway and Puerto-Rico for always being there for me. My dear cousins Adrien and Andrea, aunt Mernie and uncle Eddo. My parents, Stig and Maria, and my only "superman-guitarist-drummer-bodybuilder" brother, and future "Doctor" (but not before I have anything to say about that!), Michael.

Lausanne, 09 July 2014 J. E. Rossen

Abstract

C–A–S–H is short for $CaO-Al_2O_3-SiO_2-H_2O$ and is the main phase which forms in blends of ordinary Portland cement (OPC) with supplementary cementitious materials (SCMs). C–A–S–H forms at least half the volume of a fully hydrated cement paste and contributes to the cohesion of the material. SCMs are added to reduce the amount of clinker in a given mix − clinker being cement before it is ground into a fine powder and mixed with gypsum and fine limestone − and is an efficient way to reduce CO_2 emissions associated with the decarbonation of limestone used to fabricate the clinker.

C–A–S–H has a variable composition, indicated by hyphens, which depends on the formulation of the mix. In pure cement the composition of the C–A–S–H is Ca:Si ≈ 1.75 but is lower in presence of SCMs. C–A–S–H exists with two main morphologies: fibrils and foils. Both were observed in different mixes but no study has focused on linking them to the observed composition of C–A–S–H in realistic systems. Also, Portlandite ($Ca(OH)_2$) forms in pure cements but can be consumed by the reaction of SCMs. The link between the composition of C–A–S–H, its morphology and the consumption of Portlandite is of particular interest when using predictive tools such as thermodynamic modelling which allow simulation of the reaction of different mixes without the need for numerous experiments to predict the performance.

The aim of the thesis was the study of the composition and morphology of C–A–S–H in blended cement pastes. In order to study the effect of the presence of Portlandite, two sets of samples with a low water:binder ratio (similar to what is done in practice) were considered. Matured systems hydrated five years still contained Portlandite were characterised by SEM-EDS and STEM-EDS. New samples of cement or alite (used as a model cement) blended with reactive materials (either silica fume or metakaolin) were prepared in different conditions and also characterised using the same techniques.

The main outcomes from the thesis are that in realistic systems there is a strong link between the change in amount of Portlandite and the Ca/Si ratio of C–A–S–H and the idea that even in pastes it is mostly the pore solution which appears to dictate the formation of solid phases. When Portlandite is no longer present, the composition and morphology compare well to what is observed in the different conditions of synthetic preparations. Overall, the composition of C–A–S–H in blended cement pastes ranges Ca/Si ≈ 0.80-1.90 and Al/Si ≈ 0.00-0.30.

Keywords: C–S–H, C–A–S–H, blended cements, microstructure, composition, morphology

Résumé

Le C–A–S–H est une notation condensée de $CaO-Al_2O_3-SiO_2-H_2O$ et constitue la phase hydratée principale qui se forme dans les mélanges de ciment Portland ordinaire (OPC) avec des additions minérales reactives (SCMs en anglais). Dans une pâte de ciment complètement réagie, le C–A–S–H remplit plus de la moitié du volume et contribue à la cohésion du matériau. Les SCMs sont ajoutées pour remplacer une fraction du clinker dans un mélange donné – le clinker étant le ciment brut avant broyage et mélange avec du gypse et du calcaire finement broyé – et est une solution efficace pour diminuer la quantité d'émissions de CO_2 associées à la décarbonatation de la roche calcaire utilisée pour fabriquer le clinker.

Le C–A–S–H a une composition variable, indiquée par l'utilisation de traits d'union, qui dépend de la formulation du mélange. Dans le ciment pur la composition du C–A–S–H est $Ca/Si \approx 1.75$ mais est abaissé en présence de SCMs. Le C–A–S–H existe principalement avec deux morphologies : les fibrilles et les rubans. Les deux sont observés dans différents mélanges mais aucune étude précise n'a eu comme but de les lier à la composition du C–A–S–H mesurée dans des systèmes réalistes. Aussi, la Portlandite ($Ca(OH)_2$) précipite dans les ciments purs mais peut être consommée par réaction avec les SCMs. Le lien entre la composition du C–A–S–H, sa morphologie et la consommation de la Portlandite est d'un grand intérêt pour une meilleure utilisation d'outils dit “prédictifs” tels que la modélisation thermodynamique qui permet de simuler la réaction de différents mélanges sans avoir à recourir à de nombreuses expériences pour en prédire les performances.

Le but de cette thèse de doctorat a été l'étude de la composition et la morphologie du C–A–S–H dans des pâtes de ciment mélangé. Afin d'étudier l'effet de la présence de la Portlandite sur ces caractéristiques, deux séries d'échantillons ont été étudiées. Il y a eu une série d'échantillons dits “matures” qui ont réagi pendant plusieurs années et qui contenaient toujours de la Portlandite. Ils ont été charactérisés par microscopie électronique à balayage et à transmission. De nouveaux échantillons de ciment ou d'alite (utilisée comme “ciment modèle”) mélangés avec des matériaux réactifs (fumée de silice ou métakaolin) ont été préparés dans des conditions différentes et charactérisées avec les mêmes outils.

Les résultats principaux de cette thèse sont que dans les systèmes réalistes il y a un lien étroit entre le changement de quantité de Portlandite et le rapport Ca/Si du C–A–S–H et l'idée que la solution de pores semble avoir le rôle dominant dans la formation des phases solides. Quand la Portlandite n'est plus présente, la composition et la morphologie du C–A–S–H sont comparables à ce qui est observé dans les conditions très différentes des préparations dites synthétiques. Globalement, la composition du C–A–S–H dans les pâtes de ciment mélangé couvre un domaine de Ca/Si ≈ 0.80-1.90 et de Al/Si ≈ 0.00-0.30.

Mots clés : C–S–H, C–A–S–H, ciments mélangés, microstructure, composition, morphologie

Contents

List of Figures

List of Tables

Glossary

The chemistry of cement is discussed using the following notation for oxides (Table 1).

Table 1: Cement notation for oxides

Cement notation	C	S	A	$\$$	$\underline{C}$	H
Oxide	CaO	SiO_2	Al_2O_3	SO_3	CO_3	H_2O

Table 2: Acronyms

Acronyms	**Description**
OPC	Ordinary Portland cement
SCM	Supplementary cementitious material
SF	Silica fume
MK	Metakaolin
FA	Fly ash
Q	Quartz
Ip	Inner product C–S–H or C–A–S–H
Op	Outer product C–S–H or C–A–S–H
MCL	Mean chain length (C–S–H or C–A–S–H)
SEM	Scanning electron microscopy
SE	Secondary electron
BSE	Backscattered electron
BF	Bright field
HAADF	High angle annular dark field
TEM	Transmission electron microscopy
STEM	Scanning TEM
EDS or EDX	Energy-dispersive X-ray spectrometry
XRD	X-ray diffraction
TGA	Thermogravimetric analysis
XRF	X-ray fluorescence
^{27}Al or ^{29}Si MAS NMR	Magic angle spinning nuclear magnetic resonance

Table 3: Phases

Compound	Chemical formula	Name
Phases in unreacted cement		
$\mathrm{C_3S}$	$\mathrm{3\,CaO \cdot SiO_2}$	Tricalcium silicate
Impure $\mathrm{C_3S}$	$\mathrm{3\,CaO \cdot SiO_2}$	Alite
$\mathrm{C_2S}$	$\mathrm{2\,CaO \cdot SiO_2}$	Dicalcium silicate (belite)
$\mathrm{C_3A}$	$\mathrm{3\,CaO \cdot Al_2O_3}$	Tricalcium aluminate (aluminate)
$\mathrm{C_4AF}$	$\mathrm{4\,CaO \cdot Al_2O_3 \cdot Fe_2O_3}$	Ferrite or Brownmillerite
$\mathrm{C\$H_2}$	$\mathrm{CaSO_4 \cdot 2\,H_2O}$	Gypsum
$\mathrm{C}\underline{C}$	$\mathrm{CaCO_3}$	Calcium carbonate (calcite)
Hydrates		
C–S–H	$\mathrm{CaO{-}SiO_2{-}H_2O}$	Calcium silicate hydrate
C–A–S–H	$\mathrm{CaO{-}Al_2O_3{-}SiO_2{-}H_2O}$	Calcium silicate hydrate with alumina
CH	$\mathrm{Ca(OH)_2}$	Portlandite (calcium hydroxide)
$\mathrm{C_6A\$_3H_{32}}$	$\mathrm{3\,CaO \cdot Al_2O_3 \cdot 3\,CaSO_4 \cdot 32\,H_2O}$	Ettringite (AFt)
$\mathrm{C_4A\$H_{12}}$	$\mathrm{3\,CaO \cdot Al_2O_3 \cdot CaSO_4 \cdot 12\,H_2O}$	Monosulfoaluminate (Ms)
$\mathrm{C_4A}\underline{C}\mathrm{H_{11}}$	$\mathrm{3\,CaO \cdot Al_2O_3 \cdot CaCO_3 \cdot 11\,H_2O}$	Monocarboaluminate (Mc)
$\mathrm{C_3A(CH)_{0.5}(C}\underline{C}\mathrm{)_{0.5}H_{11.5}}$	$\mathrm{3\,CaO \cdot Al_2O_3 \cdot 0.5Ca(OH)_2 \cdot 0.5CaCO_3 \cdot 11.5H_2O}$	Hemicarboaluminate (Hc)
$\mathrm{C_2ASH_8}$	$\mathrm{2\,CaO \cdot Al_2O_3 \cdot SiO_2 \cdot 8\,H_2O}$	Strätlingite

1 Introduction

Concrete is the most important building material. It is composed of cement and aggregates which are mixed together with water to form a highly durable material. It has many advantages over most other materials available. The raw materials (limestone, clays and aggregates) are widely available and contribute to its low price. The process of firing limestone and clays to create cement clinker is relatively straightforward and optimised in modern plants, which makes the process energy-efficient and also contributes to the low price of cement and concrete. Clinker is the raw material before it is ground and mixed with gypsum and fine limestone to form the raw cement. Cement also has the advantage that there are well documented norms to control the quality of any given mix. However, there is the inevitable decarbonation of limestone which causes CO_2 to be released. Because of the high volumes of concrete produced each year, worldwide production already accounts for five percent of global CO_2 emissions [1], sixty percent of which are caused by the decarbonation of the limestone [2].

Ordinary Portland cements (OPC) hydrate to form a phase assemblage which is always composed mainly of calcium silicate hydrates (C–S–H or $CaO-SiO_2-H_2O$) and Portlandite ($Ca(OH)_2$). The hyphens indicate that a range of stoichiometries for C–S–H are possible. Other sulfo-aluminate and carbo-aluminate phases contribute to the properties of concrete but constitute a minority of the volume of products in a completely reacted OPC.

One way to reduce the CO_2 emissions, costs and make better use of often locally available materials is to replace part of the cement with supplementary cementitious materials (SCMs). Cements blended with SCMs therefore offer many advantages but are richer in silica and alumina compared to OPC. SCMs change the final composition and morphology of the C–S–H phase which can include more silica and alumina to form C–A–S–H (calcium silicate hydrate with alumina). It is not known to what extent C–A–S–H in realistic cement pastes can vary in composition. These changes are important because they change the final amount of CH and other sulfo-aluminate and carbo-aluminate phases. These changes can impact the properties on a macroscopic scale and change the long-term durability. With many possible combinations of cement and SCMs, it becomes interesting to be able to predict these changes for any given mix.

A successful approach to predicting the phase assemblage in cementitious systems is through the use of thermodynamic modelling. Thermodynamic modelling relies on the existence of a database of the chemical reactions and their solubility data (e.g. "cemdata07" [3]), models for the solid solutions – especially for the C–S–H phase – and assumes all species have reacted to reach equilibrium. This often implies dilute conditions for reaction. Once these conditions are met, simulated reactions of cement and SCM(s) are compared to experiments. This works quite well for simple systems such as OPC at different temperatures [3], modelling the hydration of pure cement [4] and simple blends [5]. However the model for C–S–H did not previously include the possible incorporation of alumina to form C–A–S–H (calcium silicate hydrate containing alumina) and considered a simple solid-solution of two varieties of C–S–H. Creating a sound model for C–A–S–H for thermodynamic modelling is an essential step towards a "thermo-poro-mechanical" model for cement and concrete [6] which could link the microstructure to the performance of any given material.

Considering the Al_2O_3 incorporation in C–A–S–H has become important because up to half of the alumina from blended cements can be incorporated in C–A–S–H and can theoretically replace up to 25% (atomic) of SiO_2 in its structure, instead of ≈ 5% in OPC (Al:Si ≈ 0.05-0.10 in most hydrated OPC pastes). As a consequence, other hydrated phases containing alumina can form or not depending on how much alumina is taken by C–A–S–H.

Results on the composition of C–A–S–H in realistic systems are necessary. There is therefore a need to understand the effect of SCMs on the long-term (metastable) equilibrium of C–A–S–H in pastes (i.e. not dilute systems) and how the presence of SCMs and the external variables such as temperature change its overall composition and morphology. The main parameters studied are the level of substitution, alkali, temperature and choice of materials.

This thesis is part of a collaborative research project between several groups. In addition to this EPFL project at the Laboratory of construction materials (Lausanne, Switzerland), there are two Ph.D. students working respectively in Empa (Dübendorf, Switzerland) and in Institut Carnot de Bourgogne (Dijon, France). There is also a post-doctoral fellow at PSI (Willigen, Switzerland). The four projects were defined to complement each other in developing a sound geochemical model for C–A–S–H in blends of cement with SCMs.

This multidisciplinary project therefore focused on obtaining:

- Structural information and surface properties of C–A–S–H derived from atomistic simulations (L. Pegado)
- Synthesised C–A–S–H and its solubility in presence of alkali ions (E. L'Hôpital)
- Synthesised C–A–S–H and its solubility in presence of chloride ions (G. Plusquellec)
- Characterisation of the morphology of synthesised C–A–S–H and comparison with the composition and morphology of C–A–S–H in real cementitious systems (this thesis)

This approach allows comparison between the real systems with synthetic C–A–S–H from the partners. Such a comparison is beneficial to improve our general understanding of the thermodynamic stability of the phase and because the model is ultimately useful for realistic systems. Additionally, the current work will also study blends of alite (the main component of cement) and SCMs in order to also provide an intermediate model system which represents cement to a certain extent.

The remainder of the thesis is divided into the following chapters.

Chapter 2 gives the state of the art on the knowledge of C–A–S–H phase with an emphasis on the findings from experiments on cement pastes samples and the main models used to describe the variable composition of C–A–S–H. The relation between the variable composition and morphology in pastes is discussed and compared to diluted preparations to identify gaps in our current state of knowledge.

Chapter 3 gives an overview of the different materials and methods used throughout the thesis.

Chapter 4 summarises work done on the optimisation of the SEM-EDS (scanning electron microscopy with energy-dispersive spectrometry) setup used to locally measure the composition of C–A–S–H in polished sections. The data treatment is also discussed.

Chapter 5 focuses on systems still containing Portlandite and is divided into two parts. Part i) deals with the comparison between systems of pure Portland cement and alite and part ii) focuses on systems blended with SCMs and still containing Portlandite. The composition and morphology of the C–A–S–H are discussed.

Chapter 6 presents results from systems with high additions of silica fume. The composition and morphology of the C–A–S–H are discussed in the case where little or no Portlandite is present. The reaction of silica fume with $Ca(OH)_2$ was studied in more detail than previously.

Chapter 7 discusses the main results on the C–A–S–H phase and relates them to the current models for C–A–S–H.

Chapter 8 provides a summary of the thesis and its main conclusions and perspectives.

At the time of writing there still were doubts pertaining to aluminium quantification by STEM which could come from the setup or the samples themselves. Results on metakaolin blends are therefore presented in the Appendix.

2 C–A–S–H in cementitious binders

2.1 Cement clinker and SCMs composition

Cement clinker is composed of four main phases. They are alite (impure C_3S), belite (C_2S), aluminate (C_3A) and ferrite solid solution (C_4AF). Gypsum ($C\$H_2$) is added to control setting of cement because of the presence of aluminate phases. In CEM I class OPC ("pure" cement), up to 5% of fine limestone is added because it reduces the clinker factor without reducing the strength [7].

SCMs exist in many varieties (Figure 2.1). In the Ca-Si-Al ternary diagram, the Portland cement is located on the Ca-rich side. SCMs contain more silica and alumina. Those which are relatively rich in CaO (slag and calcareous fly ash) are more hydraulic while those richer in silica and alumina are more pozzolanic (silica fume, natural pozzolan, siliceous fly ash and metakaolin). The pozzolanic reaction is discussed further. The impact of SCMs on the final phase assemblage will therefore depend in large part on the composition of the raw material. Generally SCMs contribute to form additional C–S–H or C–A–S–H unlike "filler" materials which are by definition chemically inert but can enhance the formation of other phases.

In the same diagram the C–S–H and C–A–S–H are represented in respective domains which are still not well defined. The extent to which the C–A–S–H domain exists is a question which this study aims to answer.

2.2 C–A–S–H in cement pastes

C–S–H and CH are the main hydrates in Portland cement. They are the main products from the reaction of alite and belite with water. The Ca:Si atomic ratio of C–S–H in cement pastes is in the range ≈ 1.75 but varies between 1.2 and 2.3 (e.g. [8]). Variations of the Ca:Si ratio can be observed even in small scales (e.g. [9]). Because cement contains alumina in alite and aluminate phases (C_3A and C_4AF), alumina released in solution can incorporate C–S–H in place of silica, even in absence of SCMs. Typical values for Al:Si in C–A–S–H from pure cement

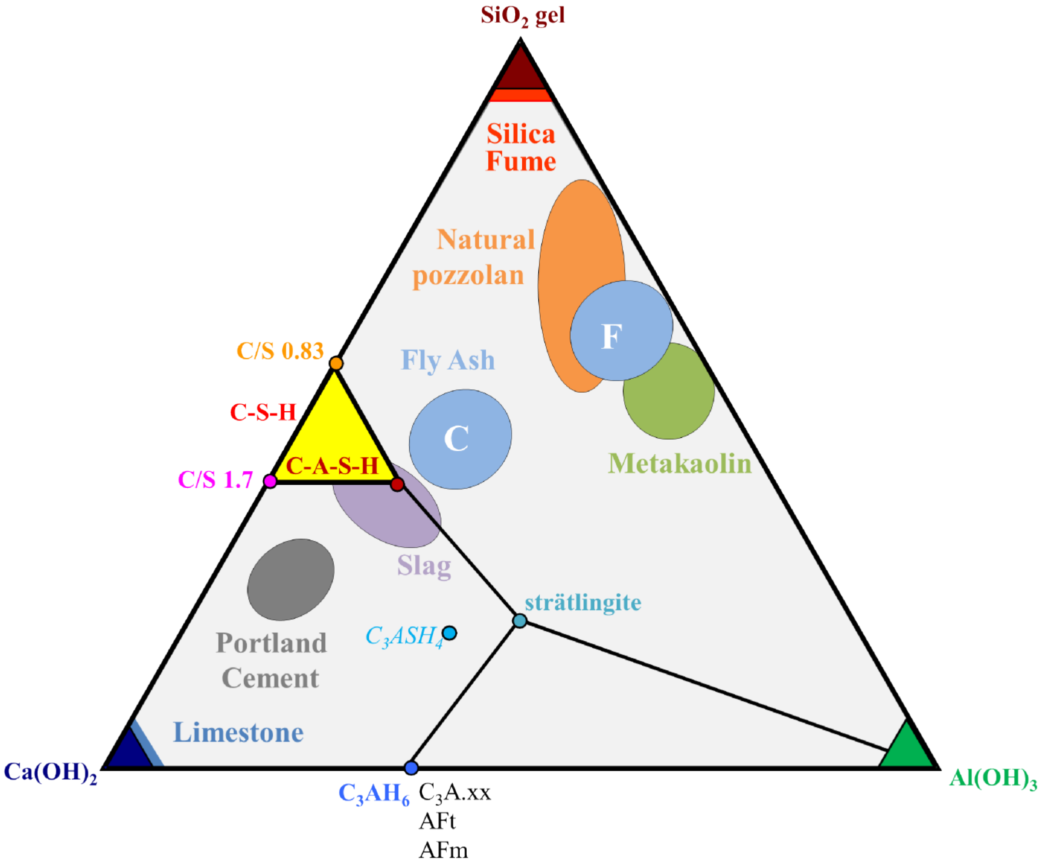

Figure 2.1: Ca-Si-Al ternary diagram showing the different average compositions of Portland cement, limestone and SCMs. Adapted from B. Lothenbach.

are ≈ 0.05-0.10.

In presence of SCM(s), the main hydrate in a blended cement paste is still C–S–H or C–A–S–H, but with an expected range of values for Ca:Si ≈ 0.8-2.3. The Ca:Si is generally lower than in OPC, and the Al:Si is expected to increase as well if the SCM is rich in alumina. CH can be consumed by pozzolanic reaction to form C–A–S–H. If we do a simplistic mass balance, silica and alumina from SCMs may have reacted with CH to form C–A–S–H according to Eq. 2.1, assuming no other phases precipitated.

$$x \cdot CH + S + z \cdot A + (y - x)H \rightarrow C_x A_z S H_y \tag{2.1}$$

Note that Al_2O_3 (“A” above) itself is not soluble but is provided SCMs such as metakaolin (which is rich in silica).

The formation of C–S–H and other phases are classically described by separate reactions but all occur simultaneously at rates which depend on temperature, pH and the activities of all the species present in solution. It is well known that alite and C_3A react at early age, while belite reacts at later age. C_4AF reacts but slower than C_3A. When SCMs are present, their contribution to the reaction is sensitive to the temperature and to the pH. The pH is increased by the initial reaction of OPC and release of alkali from the OPC into solution. Only once the conditions are favorable [5] will the SCMs begin to dissolve, impact the reactions of C–A–S–H formation and that of other phases.

2.3 Models for the nanostructure of C–A–S–H

Main features of all models

The characterisation of a crystalline (nano)structure occurring in C–A–S–H has always proven to be a difficult task because in cement pastes X-ray diffraction (XRD) on hydrated samples shows that C–A–S–H does not give very distinct reflections, but rather a broad background signal which is commonly referred to as an amorphous background [10]. C–A–S–H is therefore usually considered as being X-ray amorphous and often called a “gel”. C–A–S–H is not an amorphous phase but rather has short range order or regions of “microcrystalline” material.

Data emanating from studies using NMR and other techniques on hydrated C_3S [11, 12], pure cement paste [13, 14] and in OPC blended with slag [14, 15] support the view that C–A–S–H has a nanostructure related to a group of natural minerals which have a silicate “dreikerketten” structure. Minerals from that group contain calcium-oxygen layers on both sides of which there are infinite linear chains of silicate tetrahedra. The tetrahedra coordinate to the central hexagonal layer of octahedrally coordinated Ca^{2+} ions in such a way that every third tetrahedron bridges (B) both adjacent "paired" tetrahedra (P) as shown in Figure 2.2. Each layer of Ca^{2+} ions is flanked on both sides by a silicate chain, and the distance between two such Ca^{2+} layers is defined as the interlayer spacing. The spacing of the interlayer depends on the exact mineral and may be filled with variable amounts of both Ca and water. Silicate chain lengths in pastes and synthetic C–A–S–H are not infinite but have values which obey the 3n – 1 rule, n being an integer.

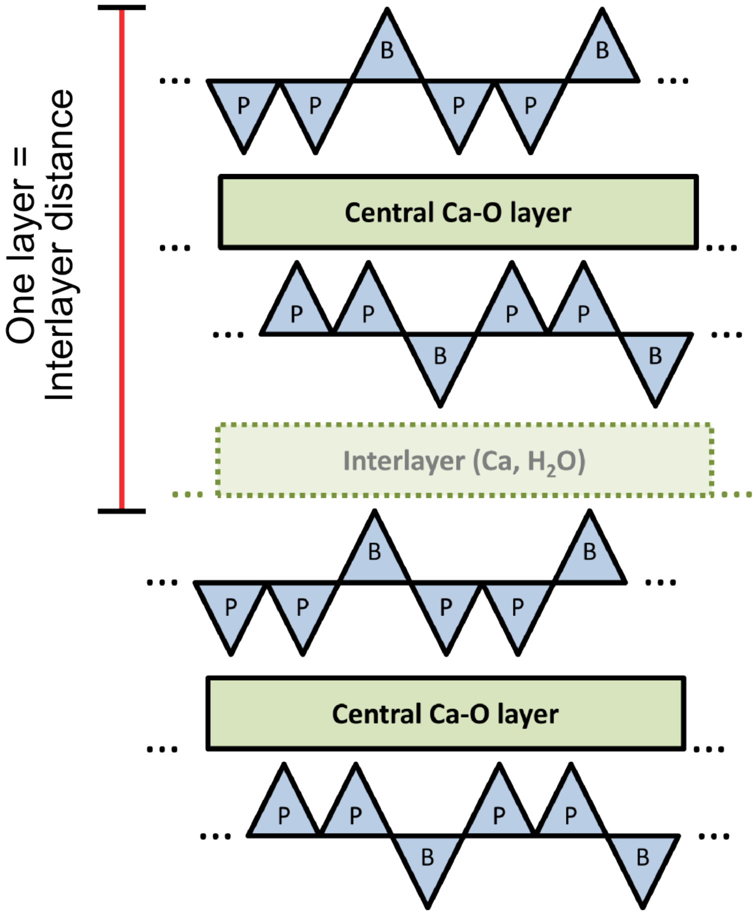

Figure 2.2: Schematic of a dreierketten structure showing the central octahedral Ca–O layer flanked on both sides by chains of tetrahedral silicates which are kinked in such a way that every third tetrahedra bridges (B) both adjacent pairing ones (P). The interlayer region which separates such dreierketten structures contains calcium and water. The distance between two interlayer regions defines the interlayer distance and is characteristic of a specific mineral.

Tobermorite and jennite minerals

Most studies have led us to relate the nanostructure of C–A–S–H to two natural but rare minerals: 14 Å tobermorite (also known as Plombierite, Figure 2.3) and jennite (Figure 2.4) [16, 17], the structures of which were only recently completely resolved [18, 19].

14 Å tobermorite has the chemical formula $Ca_5Si_6O_{16}(OH)_2 \cdot 7\,H_2O$. In this mineral, two oxygens from paired tetrahedra are coordinated to the central calcium ions. The Ca:Si is 0.83. The interlayer spacing is 14 Å in the example of Figure 2.3 and corresponds to the most hydrated mineral of the tobermorite group. No Ca−OH bonds exist in the natural structure.

Jennite has the chemical formula $Ca_9Si_6O_{18}(OH)_6 \cdot 8\,H_2O$. The resulting Ca:Si is 1.50. In jennite, only one oxygen coordinates from the pairing silicate to a central calcium, a hydroxide ion providing the second oxygen to the calcium. This results in a more corrugated structure in which every other dreierkette is replaced by a row of OH groups, indicated by “H” in Figure 2.4. No Si−OH bond exist in the natural structure.

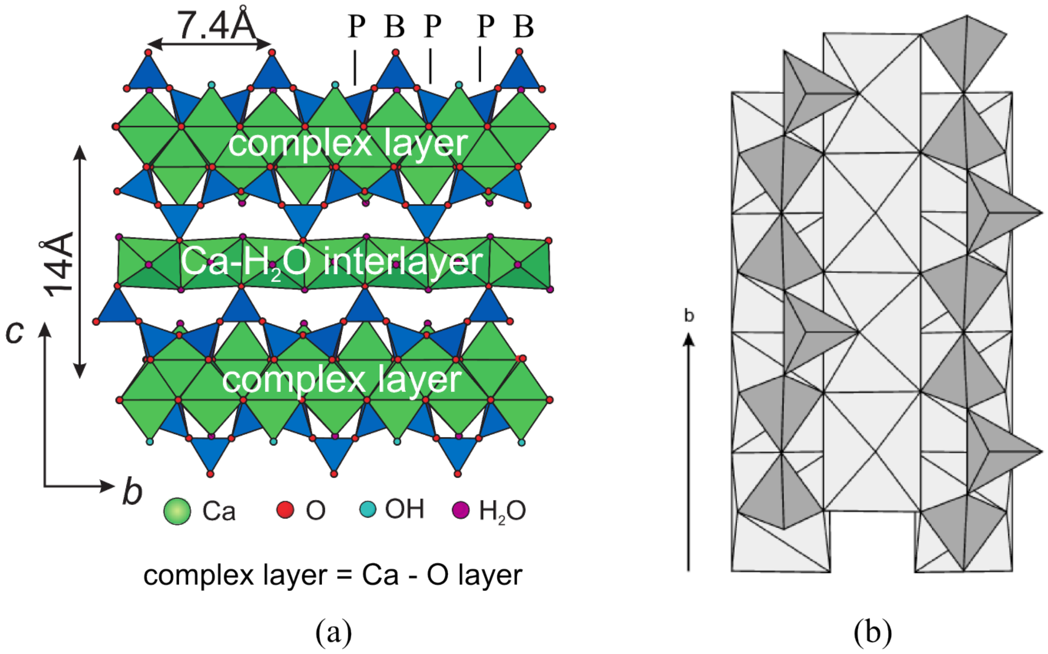

Figure 2.3: Structure of 14 Å tobermorite. (a) The structure as seen along [100], with two “complex layers” (Ca-O layers) separated 14 Å apart [20]. (b) Connection of silicate chains (dark gray) to the layer of calcium polyhedra (light gray), as seen down [001] [18].

Both structures in theory have chains of infinite length. If chains of finite length are considered (Table 2.1) by removal of bridging tetrahedra, the Ca:Si ratio increases for decreasing mean chain length (MCL). If all bridging tetrahedra are removed (MCL = 2), the Ca:Si for 14 Å tobermorite and jennite increases from 0.83 to 1.25 and from 1.50 to 2.25 respectively. In 14 Å tobermorite, the maximum Ca:Si can be increased to 1.50 by replacing two protons by a

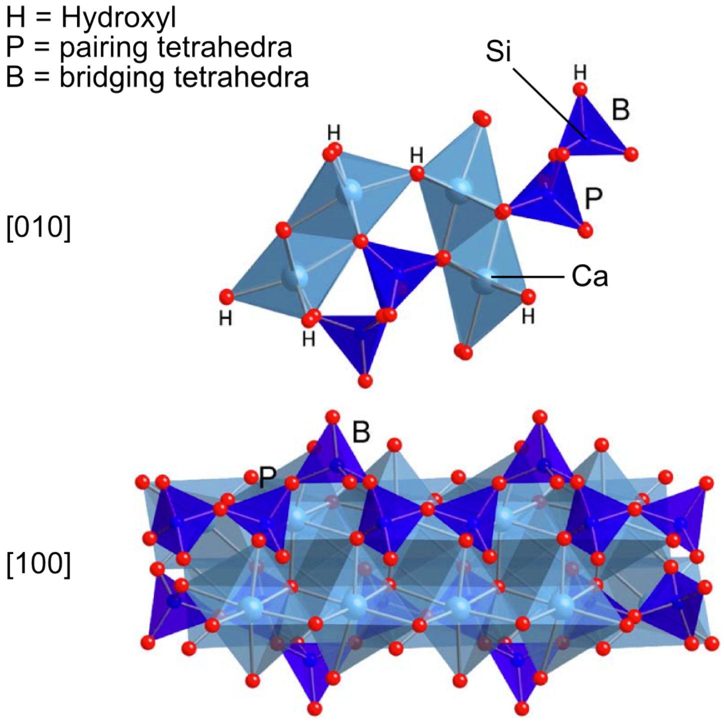

Figure 2.4: Structure of jennite as seen along [010] (top) and [100] (bottom). "H" indicate hydroxyl groups. Reproduced from Richardson [21] who used data from [19].

calcium ion.

Table 2.1: Formulae and Ca:Si ratio for 14 Å tobermorite [18] and jennite [19]

Mineral	**14 Å tobermorite**	**jennite**
Formula	$Ca_5Si_6O_{16}(OH)_2 \cdot 7\,H_2O$	$Ca_9Si_6O_{18}(OH)_6 \cdot 8\,H_2O$
Ca:Si	0.83	1.50
Ca:Si (MCL = 2)	1.25	2.25
Ca:Si (MCL = 2, each H^+ replaced by 0.5 Ca^{2+})	1.50	-
Comments	Known as plombierite. It is the most hydrated of the tobermorite group which has other possible basal spacings (9 and 11 Å). They correspond to different degrees of hydration, i.e. water molecules in the interlayer region. It does not contain Ca−OH bonds.	All hydroxyl groups are bound to three calcium cations. No Si−OH groups are present in the natural structure. [19].

Varying Ca:Si in C–S–H

Solubility data shows the link between the molar concentrations in solution compared to the composition of the equilibrated solids. Many experiments conducted around room temperature [3] show in Figure 2.5 that increasing Ca concentrations between 2 mmol/L and 20 mmol/L affects the Ca:Si at equilibrium in pure solid C–S–H (in absence of aluminium) which varies from 1.0 to 1.5. The Ca:Si can be increased from 1.50 to 2.00 but causes the precipitation of CH. This in turn causes a plateau at 20 mmol/L as the solution is saturated in $Ca(OH)_2$. The solid line in the graph indicates the modelled data used in thermodynamic modelling software (cemdata2007 database). From such data it is concluded that the C–S–H at thermodynamic equilibrium with saturated lime solution has a Ca:Si = 1.50. Some points reach higher Ca:Si and are discussed further.

There is a good level of agreement on the structural changes explaining the Ca:Si in C–A–S–H up to 1.50. A “defect-tobermorite” structure [22, 23] has been proposed in which defects are introduced by removing the bridging tetrahedra [24] to reach Ca:Si = 1.25. Then if two protons are also substituted by a Ca^{2+} cation [25], the Ca:Si can reach 1.50.

In order to include additional Ca−OH groups in the structure above Ca:Si = 1.50, they can be included in the main Ca−O layer as part of a different arrangement of silicate chains, which is equivalent to forming jennite-like structures (tobermorite/jennite viewpoint) or including them in the tobermorite interlayer or main layer − not as part of the structure −, thus maintaining a tobermorite structure but with “solid-solution” CH. There is still debate regarding the most suitable model.

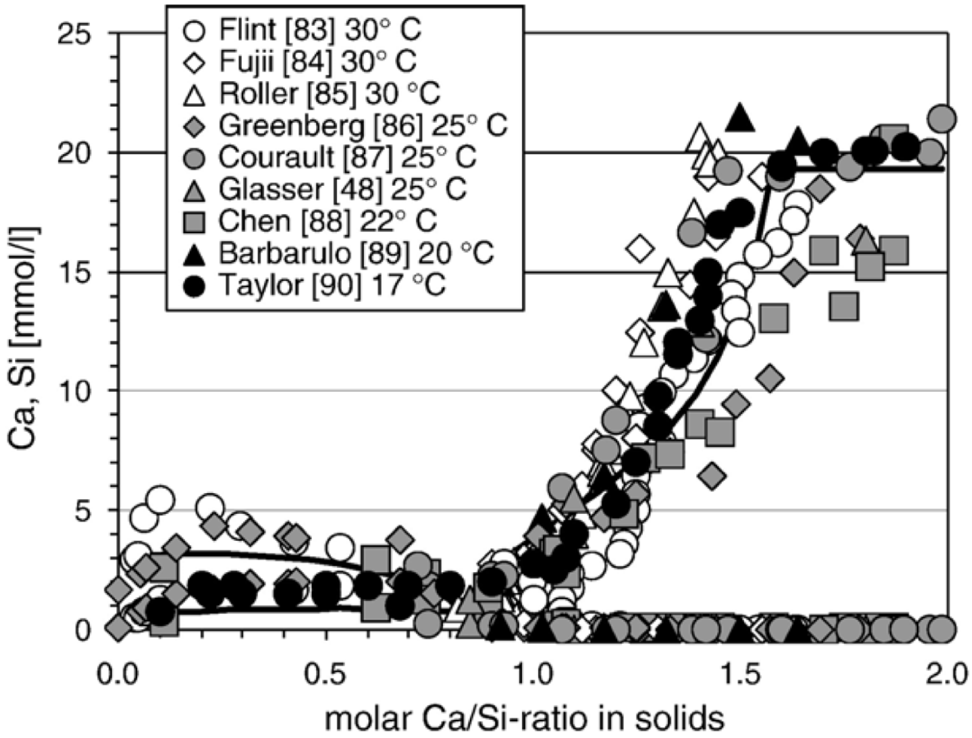

Figure 2.5: Solubility of C–S–H given as the concentrations of Ca and Si in solution versus the Ca:Si ratio in the equilibrated solid. The graphs are compiled from various data. From [3]

Richardson [21] made a review, which is summarised in [26], on the two main viewpoints and showed that most models can be seen as particular cases of Richardson and Groves' "General model". Richardson and Groves' model [12, 14] does not imply any specific structure – and should be regarded as a compositional model – but considers a disordered dreierketten structure of finite length and which is able to accommodate other ions (such as aluminium), in "solid-solution" with a variable amount of $Ca(OH)_2$ and with variable amounts of bound water (i.e. hydroxyl groups) which need not to be in a specific part of the structure. The model also charge balances silicate chains with Ca^{2+}. The flexibility of the model is due to the absence of structural considerations aside from the finite dreierketten structure.

The tobermorite/jennite viewpoint was first suggested by Taylor [16, 17] who explained the observed Ca:Si by the existence of a majority of jennite-like regions and minority of tobermorite-like regions.

Other authors suggest that C–S–H has a tobermorite-like structure up to Ca:Si = 2 and should considered from the tobermorite/"solid-solution CH" viewpoint. Strictly speaking the term "solid-solution" was used to describe Richardson and Groves' way of building their disordered structure with $Ca(OH)_2$ units but is not appropriate when considering atomic structures. The discussion here pertains to Ca−OH groups, not a microcrystalline form of Portlandite. Cong and Kirkpatrick [22] suggested that Ca−OH could go in the main layer of tobermorite from results on C–S–H prepared from dilute reaction of β-C_2S with silica fume or synthesis from CaO and silica fume. Nonat and Lecoq [23, 28] argued from data on C_3S hydrated at high water:binder ratio that the tobermorite structure could be maintained from Ca:Si from Ca:Si 0.66 to 2.0 by the replacement of a silanol proton by the addition of a $Ca-OH^+$ group in the interlayer to maintain a neutral charge.

The data from Chen and co-workers [27] suggested the occurrence of a transition at Ca:Si = 1.2-1.3 and supported the tobermorite/jennite viewpoint. They showed that while the synthetic samples followed solubility curves closer to that of pure tobermorite (Figure 2.6), the curves of C_3S hydrated with water:binder = 0.5 approached that of C–S–H (II) linked to pure jennite. Their data from both synthetic preparations and hydrated C_3S strongly suggested the existence of several metastable phases of C–S–H which each have a specific behaviour in solubility experiments (Figure 2.6). Curves C, C' and C" represent data both from the authors and other investigators on synthetic preparations and hydrated C_3S pastes. It is discussed [27] that dilute hydration of C_3S and synthetic phases tend to form tobermorite-like structures along curve A while other systems with equilibrated C–S–H from solution or hydrated C_3S begin by first following curve A from low calcium concentrations but only up to a Ca:Si of ≈ 1.2-1.3. They then depart at ratios of 1.2-1.3, follow the three intermediate curves to reach ratios of 1.7-1.9 when the solution is saturated with respect to CH at about 20 mmol/l. Curves C, C' and C" tend towards the curves for jennite and are considered to be related to jennite. This was supported for two main reasons. First, the mean chain length does not evolve much over Ca:Si = 1.3. Secondly, they argued that the occurrence of Ca−OH bonds occurs only once all Si−OH bonds have been removed at Ca:Si 1.2-1.3, which is a agreement with the upper limit for Ca:Si of

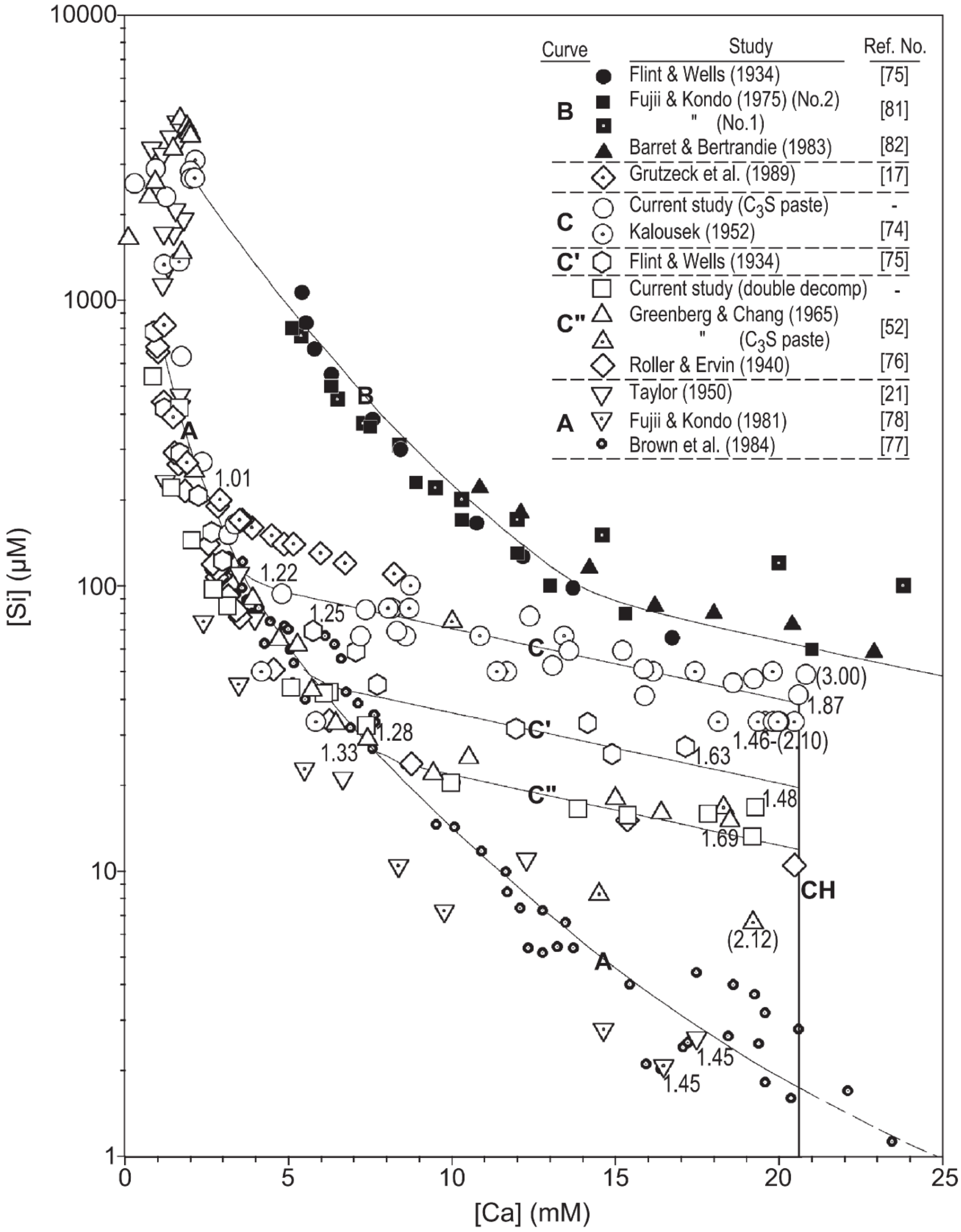

Figure 2.6: Solubility compiled from different sources and represented as [Si] versus [Ca], with the Ca:Si ratios indicated at each relevant point. From [27].

tobermorite and lower limit for Ca:Si of jennite.

However there is other evidence, related to the mobility of calcium, for the validity of a tobermorite model over the whole range of Ca:Si. Stade and Wieker [29] showed that $Ca(OH)_2$ could be leached from C–S–H with high Ca:Si to obtain C–S–H with Ca:Si$\approx$ 1.25. They could not leach $Ca(OH)_2$ from C–S–H with Ca:Si less than $\approx$ 1.25. Also, gentle carbonation experiments on C_3S [30, 31] and OPC pastes [32] lowers the Ca:Si of C–S–H to $\approx$ 1.00-1.20 and causes the formation of $CaCO_3$ crystals and silica gel. It seems unlikely in both experiments that Ca−OH groups part of a jennite-like structure would so readily be removed. Finally, X-ray diffraction data does not strongly support the existence of a jennite-like C–S–H occurring in OPC [33, 34]. Note that most XRD data is from synthetic C–S–H rather than cement.

2.4 Microstructural characterisation of C–A–S–H in pastes

Inner product (Ip) and outer product (Op) C–A–S–H

The microstructural development of hydrated cement shows that we observe two C–A–S–H phase morphologies by scanning electron microscopy (SEM) in backscattered electron (BSE) images of polished sections and which do not significantly differ in mean composition, but in morphology [9]. We define [35] the "inner" and "outer" products (abbreviated "Ip" and "Op" respectively). Such inner and outer products are shown in Figure 2.7. The C–A–S–H which forms during the first 24 hours is mostly outer product C–A–S–H (Op) which forms in originally water-filled space (Figure 2.7 (a)). Upon setting, the Op in the cement is quite porous and is intimately mixed with ettringite (AFt) and monosulfoaluminate (Ms). It can continue to form if space and water are still available. The unreacted phases later also react with the pore solution to form inner product C–A–S–H (Ip) within the approximate boundaries of original grain (Figure 2.7 (b)). This occurs at a very slow rate and begins after about one day. As with the Op, other phases are also sometimes intermixed within the Ip at a fine scale [9]. The C–A–S–H observed in polished paste samples tends to show little variation in grey levels between regions of reacted paste, even between the Ip and Op. Any variation within a same sample would normally be attributed to the presence of other highly intermixed phases such as hydrotalcite phases in slag blends [36], but this does not reflect a true difference in the composition of the C–A–S–H.

A particular feature of OPC is the presence of Hadley grains, which appear as hollow shells in the SEM at early age (example in Figure 2.7 (a)) but which in fact contain low density C–S–H products [37]. These are not so visible in C_3S and alite pastes and their presence is attributed to the simultaneous presence of aluminate and sulphate [38].

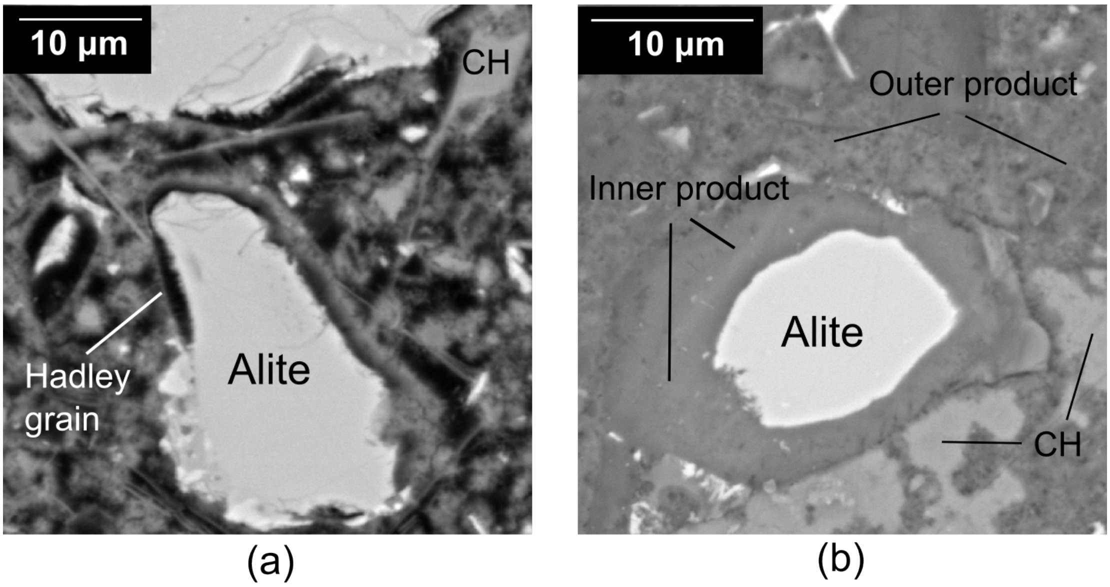

Figure 2.7: Backscattered electron (BSE) image of a CEM I cement hydrated under distilled water for (a) 24 hours and (b) 90 days. It was prepared at 20°C and with w:c = 0.4. The typical features are indicated.

Morphologies of C–A–S–H by TEM and chain length by NMR

C–A–S–H observed by transmission electron microscopy (TEM) also shows that the phase can have different morphologies. The Ip generally exhibits globular morphologies and the Op is fibrillar (Figure 2.8 (a)) and directional [9] but as it has recently been shown [39] the maximum length of fibrils not limited by space. The fibrils are usually several nanometers wide [21]. When 5 M of KOH is used to activate a cement paste, Portlandite can become intimately intermixed even at the nanometer level [15]. Such activation by 5 M of KOH can yield a foil-like morphology instead of fibrils without changing the Ca:Si ratio [21]. Note that the amount of alkali in this example is particularly high compared to ordinary cement.

When cement is blended with SCM(s) (Table 2.2), the Ca:Si is generally lowered and causes a change to foil-like morphology compared to the fibrillar C–A–S–H observed in OPC. The parameters determining whether fibrillar or foil-like morphology occurs are not well understood but appears mainly linked to the composition. When the Ca:Si is lowered below 1.50, the morphology of C–A–S–H is affected and appears mostly foil-like (Figure 2.8 (b)). Fibrils are present in cases where low amounts of slags are introduced [40] and in the Op of fly ash blends [41]. When the Al:Ca increases we seem to see more foil-like [21] and the aluminium enters the bridging site of chains of C–A–S–H as shown by ^{27}Si MAS NMR [42]. The addition of alkali hydroxide (NaOH, KOH) can strongly increase the reactivity of SCMs in blended cements, which in turn affects the activities of calcium, silicon and aluminium in the pore solution. Alkalis can change the final composition and the morphology of C–A–S–H in blended systems

[8], and may charge balance the presence of aluminium [43]. Generally speaking, very few TEM studies on the phase composition have been done on blended paste samples in realistic conditions, see Table 2.2.

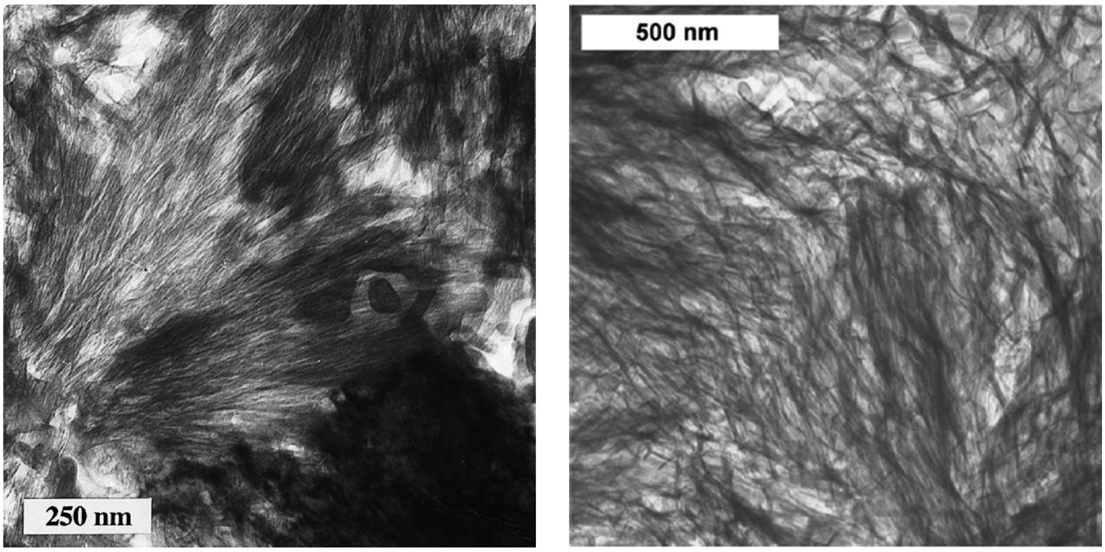

(a) (b)

Figure 2.8: (a) Bright-field (BF) electron image of a pure OPC, from [44]. Fibrillar morphology is apparent in the outer product shown. (b) BF image of a OPC - 75% Slag blend, from [21]. Here the increase in initial Al:Ca and lowering of Ca:Si in C–A–S–H causes the morphology of the outer product to be foil-like.

The Q_n resonances in ^{29}Si MAS NMR (magic angle spinning solid state nuclear magnetic resonance) can be used to calculate the mean chain length of the silicates in C–A–S–H. In cements structural units are typically of mean chain length (MCL) ≈ 3, with dimeric chains dominating at early age and pentameric dominating after several years as seen e.g. in C_3S model systems [24]. In presence of SCM(s) the value for mean chain length can increase to high numbers, particularly at higher temperatures.

Table 2.2: Examples of data for OPC and the four main blended systems. Data from *[44], $^{\#}$[41], $^{\#\#}$[45], **[46]

Blend	SCM [%]	Ca:Si	Al:Si	MCL	W:S	T [°C]	Time	Ip Morphology	Op Morphology
OPC	0	1.7-1.8	0.05	3.3-5	0.4	20	1y, 26y	Fine	Fibrillar
OPC-Slag##	10 90	1.6 1.18	0.12 0.18	6.7 14.3	0.4	20	20y	Fine (Ip and Slag rim)	Fibrils to foil
OPC-FA#	30	1.57	0.2	15.6	-	55	1 mth	Low density foil Fibrillar in FA	Foil and fibrils
OPC-MK**	20	1.43	0.25	11	0.55	25	1 mth	Fine	Foil-like
OPC-SF*	50	0.7-0.8	-	8.5	0.7	40	3 mths	20% SF: Fine >50% SF: foil	Foil-like

Role of alumina in C–A–S–H

Aluminium is known to incorporate C–A–S–H [47, 48] from data on both synthetic and hydrated C_3S preparations and can enter bridging sites of silicate chains. Tetrahedrally coordinated Al^{3+} (Al^{IV}) substitutes mainly for Si^{4+} in bridging sites of C–A–S–H from cements [43, 49]. This was first confirmed in ^{27}Si MAS NMR data from hydrated synthetic slags [50, 15].

However the bridging site of Si is not the only site for substitution. Octrahedral Al^{3+} (Al^{VI}) was suggested to substitute Ca^{2+} in the interlayer [47, 48], but may be attributed to the presence of AFm or a third aluminium hydrate which is a separate phase [49]. It is also suggested that Al in a pentacoordination (Al^{V}) may substitute with Ca^{2+} in the interlayer as seen in a white Portland cement [43] or adsorb on C–A–S–H in diluted synthesized samples [51]. There are instances where Al^{IV} may substitute non-bridging (pairing) positions [52, 51] in synthetic samples at lower pH than that in cement. Aluminium is known to allow crosslinking between silicate chains [53] and generally increases the final degree of polymerisation of silicate chains at high pH [43, 54]. Despite these different sites for alumina incorporation, it is generally assumed that the bridging site is the most favorable for alumina substitution at low Ca:Si ratios. This is supported by recent work by L. Pegado.

Values from Table 2.2 indicate that the alumina in C–A–S–H can be highly variable, depending on the availability of aluminium and possibly on the Ca:Si ratio. The data from Table 2.2 also suggests that both a decrease in Ca:Si and increase in Al:Si can influence the morphology of C–A–S–H. It is not clear to which extent alumina can impact the final morphology.

2.5 Synthetic preparations versus paste samples to study C–A–S–H

It is apparent that the biggest challenge in converging towards a better knowledge of the C–A–S–H phase will depend on our ability to bridge the gap between synthetic preparations and pastes of low water:binder ratio typically around 0.3 to 0.5 [10]. Table 2.3 summarises the information in the literature. Points in bold indicate the outstanding uncertainties and questions.

Table 2.3: Characteristics of the C–S–H and CH in different types of systems. DOH = degree of hydration. Sol.:bind. = solution to binder ratio. *Synthetic preparations often have a maximum Ca:Si = 1.50 but can be prepared with Ca:Si up to ≈ 1.90 [27, 55, 56]. **C_3S can be hydrated in dilute conditions to synthesise C–S–H.

Type.	**Mixing**	**Grains**	**Sizes [μm]**	**Sol.:bind.**	**Ca:Si**	**Morphology**	**CH distribution**	**Reactivity**
Synthetic	Various	—	—	50	**0.67-1.50+***	**Foil-like**	—	Variable
C_3S	Hand	Small	0-4	0.3-0.7**	1.50-2.00	Fibrillar	Clusters	Very high (70% DOH at 1 day)
Alite	Hand***	Larger	0-100	0.3-0.7	**1.50-2.00**?	Fibrillar	Clusters	**Lower DOH than OPC**
White PC	Mixer	Larger	0-100	0.3-0.7	1.3-2.3	Fibrilar	Clusters and platelets	80% DOH at 28 days
OPC	Mixer	Larger	0-100	0.3-0.7	1.3-2.3	Fibrillar	Clusters and platelets	80% DOH at 28 days
OPC with SCMs	Mixer	Variable	0-100	0.3-0.7	**0.8-2.3**	**Fibrillar/Foil-like**	Clusters and platelets, absent	**Highly variable**

The biggest question still pertains to synthetic preparations and how they compare to the C–S–H in pastes. Chen suggested that the C–S–H formed in dilute conditions is different from those formed in low:water binder pastes [27] but that both are able to reach equilibrium which is at the very least metastable. The stability of C–S–H is not entirely understood and is central to thermodynamic modelling.

Synthetic phases are foil-like and precipitating with maximum Ca:Si = 1.50 in absence of CH, although it was reported in [27] and in other recent studies [55, 56] that it can be formed with Ca:Si ≈ 1.70-1.90. Preparation times are often long (several months) but some occasions are within a few hours. It has been possible to observe fibrillar morphologies, with Ca:Si ≈ 1.75 in dilute solution from controlled dissolution of C_3S [55] when the solution is above lime saturation but has not yet precipitated CH.

C–S–H forms in pastes within hours. The C–S–H, pure C_3S, alite and OPC has fibrillar morphology in the Op and Ca:Si ≈ 1.75 in presence of CH. Fibrillar morphologies persist after as long as 20 years [57] and after gentle carbonation [32]. The presence of these fibrils in blended pastes is investigated in a selection of samples.

In blends with SCMs where there are several morphologies and very different C–A–S–H compositions which are affected in large part by the reactivity of the SCMs. The link between the composition and morphology of C–A–S–H in realistic pastes needs to be further explored. The role of CH on the C–A–S–H composition and morphology in blended pastes will be highlighted in Chapter 5 and a comparison with synthetic preparations of low Ca:Si is made in the Chapter 7.

The thesis focuses on less reacted systems from the project of V. Kocaba [36] which still contain CH, and then pastes with reactive SCMs (silica fume and metakaolin) to change the composition and morphology of the C–A–S–H in absence of CH. This will allow discussion of the stability of the C–A–S–H in pastes and attempt to relate the observed compositions and morphologies to the conditions in which C–A–S–H may have formed and may have evolved over time.

Most results on metakaolin blends are grouped in the Appendix, p. 131.

3 Materials and methods

3.1 Raw materials

Samples with reactive SCMs were prepared with three "cements", i.e. two "model cements" based on alite, and an OPC. One series was prepared with a model cement containing only alite, and SCMs. A second contained a model cement composed of alite, C_3A and gypsum, which was blended with SCMs. The third series was with OPC and SCMs.

Alite, aluminate and gypsum

Synthesis of the pure phases was done using analysis-grade materials from MERCK Chemicals according to protocols in [58, 59] for alite and according to [59] for C_3A. The amounts of reactants given in Table 3.1 were mixed in a 5 liter jar and homogenised during 24 hours by ball milling. The mix was then dried for 24 hours in an oven set at 105°C, ground by hand using a mortar to obtain a homogeneous powder. The resulting powder was pressed into pellets about 5 cm in diameter and 0.6 cm thick. The firing cycle were specific to alite and to C_3A.

Table 3.1: Mix design for synthesising the pure phases.

[g]	$CaCO_3$	SiO_2	Al_2O_3	MgO	Water
Alite	635.8	130.0	5.1	10.3	1200.0
C_3A	400.0	-	153.0	-	750

Alite was burned at Holcim in three steps to ensure that the free lime (CaO) content was reduced to the minimum. For each step the pellets were placed in the furnace which was then heated from ambient temperature to 1450°C in 2 hours. The pellets were quenched in air after the full step at constant temperature. The first step was at 1450°C for 60 hours. The second and third steps were 14 and 16 hours at 1450°C respectively.

C_3A was synthesised in the laboratory. Pellets were placed in the furnace which had the following heating cycle: 200°C/hour up to 1000°C, 1000°C for 8 hours, 200°C/hour up to 1400°C, 1400°C for 8 hours, quenched in air, ground for 60 seconds in a ring crusher and pressed into pellets again and then fired up to 1400°C at 200°C/hour followed by a last calcination at 1400°C for 5 hours.

The pellets of both materials were ground in a ring crusher for 30 seconds. They were then both sieved with a 100 μm sieve to remove large grains.

Gypsum, calcium dihydrate ($CaSO_4 \cdot 2\,H_2O$), was from Merck and was ground 1 minute in the ring crusher.

The reactivity of alite and C_3A were checked by isothermal calorimetry (Figure 3.1) and their purity by X-ray fluorescence (XRF) (Table 3.2). Calorimetry of the alite in Figure 3.1 (a) was slightly less reactive than in [59] and the heat release of the C_3A-20% gypsum mix in Figure 3.1 (b) was quite similar to results given in [59]. X-ray diffraction (XRD) of the powders showed no traces of other products. The XRF results showed no traces of impurities.

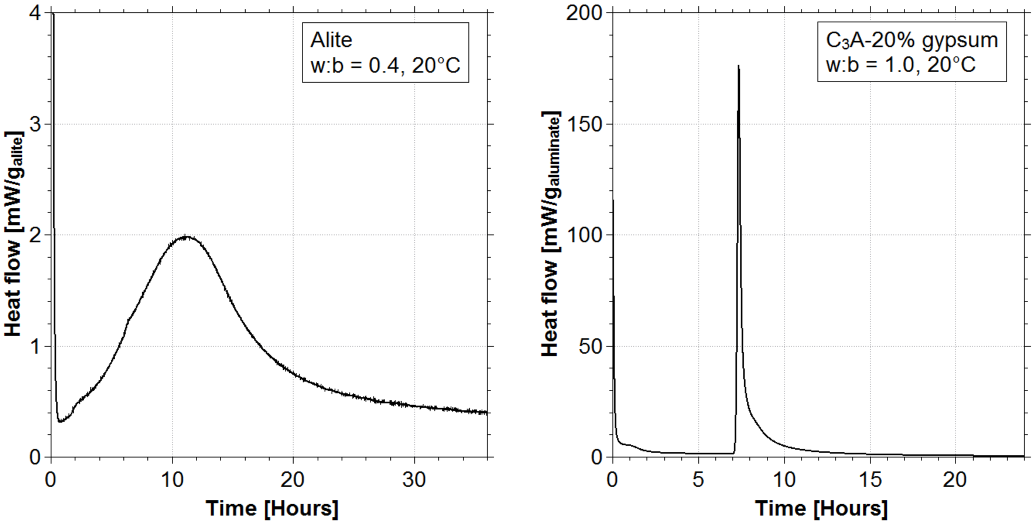

(a)

(b)

Figure 3.1: Isothermal calorimetry of the pure phases synthesised for the project. Samples were hydrated at 20°C. (a) Alite prepared with water:binder = 0.4. (b) C_3A-20% gypsum mix prepared with water:binder = 1.0.

Table 3.2: XRF data of the pure phases, in %wt. LOI = loss on ignition.

	SiO_2	Al_2O_3	CaO	MgO	SO_3	LOI
Alite	25.43	1.10	71.24	2.03	-	0.11
C_3A	-	36.67	62.27	-	-	0.66
Gypsum	-	0.14	40.35	-	52.17	7.17

OPC and SCMs

The raw materials used here are a CEM I 32.5 ordinary Portland cement (PC), quartz (Q), silica fume (SF) and metakaolin (MK). XRF data is given in Table 3.3. The anhydrous phases of the PC are given in Table 3.4.

Table 3.3: XRF data of the raw materials, in %wt. LOI = loss on ignition.

	SiO_2	Al_2O_3	Fe_2O_3	CaO	MgO	SO_3	Na_2O_3	K_2O	TiO_2	P_2O_5	Mn_2O_3	LOI
PC	21.1	5.6	2.6	64.9	1.6	2.8	0.2	0.9	0.3	0.1	0.1	1.9
Q	98.1	1.1	0.0	-	-	-	0.1	0.6	0.1	0.0	0.0	0.2
SF	98.7	0.3	0.0	0.2	0.0	-	0.1	0.3	0.4	0.0	0.0	0.5
MK	51.4	44.9	0.4	0.2	0.0	0.0	0.2	0.1	1.4	0.1	-	1.4

Table 3.4: XRD data for the PC quantified by Rietveld analysis, in wt%. LOI = loss on ignition.

	Alite	Belite	C_3A	C_4AF	CaO	MgO	$CaCO_3$	SiO_2	$CaSO_4$	K_2SO_4
PC	55.2	14.0	10.8	6.2	0.3	1.1	3.3	0.6	5.8	2.6

Raw materials of matured systems

Samples prepared in a previous Ph.D. study were made with three cements: Cement A, B, and C with compositions by XRF given in Table 3.5 and by XRD given in Table 3.6 (see [36, 60] for additional details). Cement A is a white cement with high amounts of alite, little C_3A and low amounts of alkali. Cement B contains low amounts of alite, high amounts of alumina and alkali. Cement C has high amounts of alite and alkali, some alumina and calcite.

Table 3.5: Composition of cements A, B and C by XRF in %wt (From V. Kocaba). LOI = loss on ignition.

Name	SiO_2	Al_2O_3	Fe_2O_3	CaO	MgO	SO_3	Na_2O	K_2O	TiO_2	P_2O_5	Mn_2O_3	LOI
A	24.5	2.1	0.3	69.2	0.6	2.2	0.1	0.2	-	-	-	0.19
B	20.6	5.2	3.1	62.0	2.6	2.9	0.3	1.4	-	-	-	1.14
C	21.6	5.0	2.8	65.9	1.7	0.8	0.1	0.9	0.3	0.4	0.1	0.72

They were blended with five SCMs. Two slags ("S1" and "S8"), two fly ashes ("FA1" and "FA2") and a silica fume ("SF"). The compositions by XRF are given in Table 3.7. The S1 and S8 (see [36, 60] for additional details) both have calcium, silica and alumina in high amounts. S1 is completely amorphous according to XRD and has more silica and calcium compared to S8 which has more alumina but has less amorphous content. Both fly ashes have the same alumina content and are siliceous. FA1 contains more magnesium oxide, iron oxide and alkali oxide. FA2 contains traces of iron oxide and titanium oxide. Silica fume is pure SiO_2, and is the same batch of material used in experiments of the Chapter 6.

Table 3.6: Composition of cements A, B and C by XRD, amounts in %wt (From V. Kocaba).

Name	**C_3S**	**C_2S**	**C_4AF**	**C_3A**	**Lime**	**Periclase**	**$CaSO_4$**	**$CaCO_3$**	**$Ca(OH)_2$**
A	67.3	23.3	0.4	3.6	0.6	0.0	4.3	0.0	0.5
B	51.1	22.2	9.2	8.1	1.8	2.3	3.8	1.0	0.6
C	66.9	10.3	8.8	4.5	0.0	0.5	4.2	4.9	0.0

Table 3.7: Composition of the SCMs from matured systems by XRF (wt%) (From V. Kocaba).

Name (%amorphous)	**SiO_2**	**Al_2O_3**	**Fe_2O_3**	**CaO**	**MgO**	**SO_3**	**Na_2O_{equ}**	**K_2O**	**TiO_2**
Slag 01 (99%)	36.5	11.6	1.4	40.8	7.5	2.1	0.5	-	-
Slag 08 (85%)	30.5	16.5	0.2	32.0	10.0	1.7	0.0	-	-
Fly ash 01	49.9	23.9	8.8	4.8	2.6	0.3	1.0	3.8	0.9
Fly ash 02	70.0	23.9	2.2	0.2	0.2	0.0	0.0	0.6	1.4
Silica fume	98.6	0.3	0.0	0.2	0.1	0.1	0.2	-	-

3.2 List of samples

Samples from previous studies

The list of matured systems with three different cements are given in Tables 3.8, 3.9 and 3.10 for cements A, B and C respectively. S1 and S8 are slags. FA1 and FA2 are fly ashes. SF is silica fume. Here the pure cement and slag blends hydrated for 5 years. Those with fly ash and silica fume hydrated for 3 years. All samples had a water:binder ratio of ≈ 0.40.

Table 3.8: Series A

Sample	**Comp.**
A	100% OPC
A-S1	60% - 40%
A-S8	60% - 40%
A-FA1	70% - 30%
A-FA2	70% - 30%
A-SF	90% - 10%

Table 3.9: Series B

Sample	**Comp.**
B	100% OPC
B-S1	60% - 40%
B-S8	60% - 40%
B-FA1	70% - 30%
B-FA2	70% - 30%
B-SF	90% - 10%

Table 3.10: Series C

Sample	**Comp.**
C	100% OPC
C-S1	60% - 40%
C-S8	60% - 40%
C-FA1	70% - 30%
C-FA2	70% - 30%
C-SF	90% - 10%

New samples

The mix designs are summarised here for both the alite ("model cements", i.e. MC) series (Table 3.11) and the grey cement (Portland cement, i.e. PC) series of blends (Table 3.12). Alite blends were prepared with different amounts of alkali (0, 0.1 and 0.5 M of KOH) and at different temperatures (10, 20 and 38°C). Not all combinations were made (see right side of Table 3.11). When C_3A and gypsum were added, the samples were labelled MC* (with a star symbol). The PC series were made at the same three temperatures. Both MC and PC series were hydrated for 90 days and had a combination of silica fume and quartz.

Superplasticiser was used in PC-18.8MK (0.5%wt of the total binder) and PC-41.2MK (1.5%wt).

Additional drops were added if needed, but no more than 2%wt.

A second series with the same cement and silica fume was cast for studying at earlier ages. The PC2 series is summarised in Table 3.13.

Table 3.11: List of alite blends hydrated for 90 days. E.g. T10 = 10°C, 0.1K = 0.1 M KOH. See p. 1 for the definition of the acronyms.

Series	Alite wt%	C_3A wt%	$C\$H_2$ wt%	SF wt%	MK %wt	Q %wt	0K	0.1K	0.5K
Alite (MC)	100.0	-	-	-	-	-	T20	T20	T10-20-38
MC(Q)-SF	60.0	-	-	20.0	-	20.0	T20	T20	T10-20-38
MC-MK	58.8	-	-	-	41.2	-	T20	T20	T10-20-38
MC*(Q)-SF	50.0	5.0	5.0	20.0	-	20.0	T20	T20	T10-20-38
MC*-MK	48.8	5.0	5.0	-	41.2	-	T20	T20	T10-20-38

Table 3.12: List of PC blends hydrated for 90 days. E.g. T10 = 10°C.

Name / %wt	PC	SCM	Q	Temperatures
PC	100.0	0.0	0.0	T10-20-38
PC(Q)-10SF	81.8	9.1	9.1	T10-20-38
PC(Q)-25SF	60.0	20.0	20.0	T10-20-38
PC-45SF	55.0	45.0	0.0	T10-20-38
PC-18.8MK	81.2	18.8	0.0	T10-20-38
PC-41.2MK	58.5	41.5	0.0	T10-20-38

Table 3.13: List of PC2 blends. E.g. T10 = 10°C. This series was studied at difference ages and did not contain quartz as did the PC series.

Name / wt%	OPC	SCM	Temperatures
PC2	100	0	T10-20-38
PC2-10SF	90	10	T10-20-38
PC2-25SF	75	25	T10-20-38
PC2-45SF	55	45	T10-20-38

3.3 Sample preparation and experimental methods

Casting

Plastic containers of 250 ml in volume first contained the anhydrous material which was homogenised by shaking the container by hand for about a minute. The vertical mixer (IKA LABORTECHNIK RW20.n) set to a rotation speed of about 1,600 rpm was switched on prior to adding liquid. The water, slurry or solution (initially at room temperature) was poured into it while the mixer was on. The paste was then mixed for two minutes at the same speed. If superplasticiser was required, it was added with the water and additional drops were added if needed during the two-minute mixing. Additional mixing (not more than 2 minutes) was done if needed to ensure the whole paste was homogenised. Samples were cast into cylindrical tubes and stored first during 24 hours at the designated temperature. They were then removed from the mould and stored in a second container of slightly larger size. A small amount of additional distilled water (initially at room temperature) was added to maintain the sample under water. The amount of additional water was limited to minimize leaching of the pore solution.

For the silica fume containing blends, the silica fume was prepared with the whole amount of distilled water as a slurry using a kitchen blender set at approximately 12,000 rpm. The slurry was first homogenised for about 2-4 minutes without superplasticiser. The slurry was then homogenised a second time for two minutes before each casting to limit the aggregation of silica fume particles.

Solutions of KOH were prepared with distilled water (initially at room temperature) and MERCK Titrisol® KOH 1.0 M for 1 l prior to mixing.

All samples were then left to hydrate 90 days in sealed containers at 10, 20 and 38°C with distilled water (which was initially at room temperature). Samples for hydration at 10°C were placed in a fridge, those for hydration at 20°C were placed in an air-conditioned room, and a hot chamber in our laboratory was used for samples hydrating at 38°C.

Stopping hydration

At different hydration times slices approximately 2 mm thick were cut out of the samples using a diamond saw and distilled water as lubricant. The slices were stored five days in isopropanol to remove the water by solvent exchange, with the solution being completely changed at least once within the first day of isopropanol storage to enhance the removal of water. After five days, the samples were stored in a desiccator for several days to evaporate the isopropanol. Care was taken to not observe the surface which was exposed to water in order to avoid leached areas. In most cases a second slice was taken for characterisation and the first one kept as backup.

For XRD and thermogravimetric analysis (TGA) techniques, powders were ground by hand in a mortar.

Electron microscopy

Basic principles The irradiation of a sample by an incident electron beam of energy E_0 causes different types of interaction to occur.

In a bulk material, there are secondary electrons (SE) which are incident electrons which have lost most of their energy through inelastic interactions with the sample. They are of low energy (5-50 eV) and yield a mostly topographic contrast. There are also backscattered electrons (BSE), i.e. incident electrons which have diffused from within the sample and ejected. BSE have an energy close to E_0. The number of such electrons per unit of time is proportional to the atomic number Z and the density ρ. This contrast is of great interest to study cementitious samples. Auger electrons are electrons which were ejected from atoms whose cloud of electron interacted with the incident electrons. They are of an energy characteristic of the target atom.

When electrons undergo inelastic diffusion, there is a transfer of energy, and the target atom can be ionised. The change in energy causes the emission of X-ray radiations. They are of two main kinds. One mechanism involves an electron from an inner energy level of an atom to be ejected by the incident electron, causing an electron from a higher energy level of the atom to replace it and release the excess energy as characteristic X-rays. These characteristic X-rays are detected and counted to form X-ray spectra which can be processed for qualitative or quantitative analysis, such as it is done in energy-dispersive spectrometry (EDS). Another type is a continuum of X-rays caused by the deceleration of incident electrons which change in energy is released as X-rays. These contribute to the Bremstrahlung background (the "slow-down radiation").

Backscattered electrons and X-rays originate from a finite volume within bulk materials, i.e. the interaction volume. The interaction volume increases with the incident energy E_0. The incident energy could be minimised to obtain the best lateral resolution. However, the generation of X-rays of an energy E_X requires that the incident energy E_0 is about twice that of E_X to sufficiently ionise it. This often results in a compromise between a sufficient lateral resolution and optimal X-ray generation. This limitation is overcome by TEM.

In electron transparent samples for the TEM, there is in principle no absorption of electrons. Incident electrons can either go through the sample and form the bright field image (BF) or be elastically scattered at low or high angles. This gives rise to the dark field contrast (DF). Electrons can interact with the core of the atoms and be scattered at high angles. An annular detector can collect information from these electrons to form the high angle annular dark field image (HAADF). Because of the interaction with the core of atoms, this contrast is strongly dependent on the atomic number Z. The formation of X-rays is the same as in bulk samples.

Sample preparation For scanning electron microscopy (SEM), each piece of dried sample was impregnated using epoxy-based EPO-TEK® 301 resin, polished at 150 rpm with a STRUERS Rotopol machine down to 1 μm using STRUERS DP-Spray M diamond sprays and with petrol as a lubricant. All polished SEM samples were bulk samples at least 2 mm thick. The sample was then coated with a $\approx$ 30 nm carbon film using a BAL-TEC CED 030 Carbon Evaporator. Samples were stored in desiccators.

For the transmission electron microscopy (TEM), a smaller piece was impregnated using EMS Embed 812 resin, cut to a thin slice (of dimensions 1.7 mm × 1.7 mm × 0.7 mm) using a WELL diamond saw, thinned down mechanically to a bevel by mean of the Tripod method (supplied by ALLIED Tech) to yield a thickness of about 20-30 μm on the thick side. It was then glued to a copper ring (for which a third was cut off to limit redeposition of Cu during ion thinning), ion-thinned with an Argon PIPS (GATAN Precision Ion Polishing System Model 691) operated at maximum 1.5 keV to achieve electron transparency and carbon coated with a thin 5 nm layer using a CRESSINGTON 208 high vacuum carbon coater. Samples were coated only prior to observation in the TEM. Samples were stored in a high vacuum desiccator at the CIME (Interdisciplinary Centre for Electron Microscopy).

Microscope parameters Observation in the SEM was done in high vacuum conditions ($\approx 5\times10^{-5}$ Pa) using backscattered electron imaging (BSE) at 15 kV. The SEM was a FEI Quanta 200 equipped with a tungsten filament. The spot size was adjusted to yield a ≈ 0.7-0.8 nA current. A map was acquired over two hours at a moderate beam current of ≈ 1.4 nA (spot size 6) and caused minimal damage as seen in Figure 6.9 (c), in Chapter 6, p. 106.

TEM observations were done in scanning mode using the nanoprobe mode of the FEI Tecnai Osiris equipped with a high brightness XFEG source. Bright field (BF) and high angle annular dark field (HAADF) imaging modes were used. The spot size was either 8 or 9 to yield a current of 0.160 nA or less using a high “gun lens” setting.

Details on the experimental protocols are found in Chapter 4 and particularly in Section 4.2, p. 35.

X-ray diffraction (XRD)

X-Ray Diffraction (XRD) provided a method to observe the formation of crystalline hydrates and non-reacted raw materials in hydrated pastes. A Panalytical X’Pert Pro MPD diffractometer was used in a $\Theta-\Theta$ configuration using CuK_α source (λ = 1.54 Å) with a fixed divergence slit size of 0.5°. Samples were scanned on a rotating stage between 7 and 70 [°2Θ] using a X’Celerator detector with a step size of 0.0167°2Θ and a time per step of 30 s.

Thermogravimetric analysis (TGA)

Thermogravimetric analysis (TGA) was used to measure the mass loss upon heating a sample. About 50 mg of powder was taken for TGA using a Mettler-Toledo TGA/SDTA 851 balance with a 10°C/min ramp from 30°C to 900°C under a constant 30 ml/min flux of nitrogen. The amount of CH was determined using the tangent method on the normalised curve. The loss of water around 650°C was assumed to be dehydroxilation of $Ca(OH)_2$ to form CaO and H_2O.

Isothermal calorimetry

Isothermal calorimetry was conducted on samples in order to measure the heat flow released during hydration of the paste samples. A Thermometric TAM AIR calorimeter was used. It measures up to 8 channels simultaneously with a range of -600 to 600 mV. An amount of water (4.14 g) of approximately equivalent specific heat to 10 g of cement paste was used as a reference (assuming water:binder = 0.4), even for blended systems. Experiments were conducted at 20°C in a room cooled at ≈ 20°C.

XRF

X-Ray Fluorescence (XRF) is a method to obtain a basic chemical analysis of the oxides in a sample by analysing characteristic X-Rays that are reemitted after being hit by an incident X-Ray beam. Measurements were provided by APC Solutions SA in Denges, Switzerland.

3.4 Definition of C–A–S–H morphologies

The present work provides numerous observations of the morphology of the C–A–S–H phases in blended pastes and in synthetic samples. The following terminology (Figure 3.2) was used to describe it. Ip designates the inner product C–A–S–H and the Op designates the outer product C–A–S–H. The fine or coarse “foil-like” terminology is due to Richardson, e.g. [21].

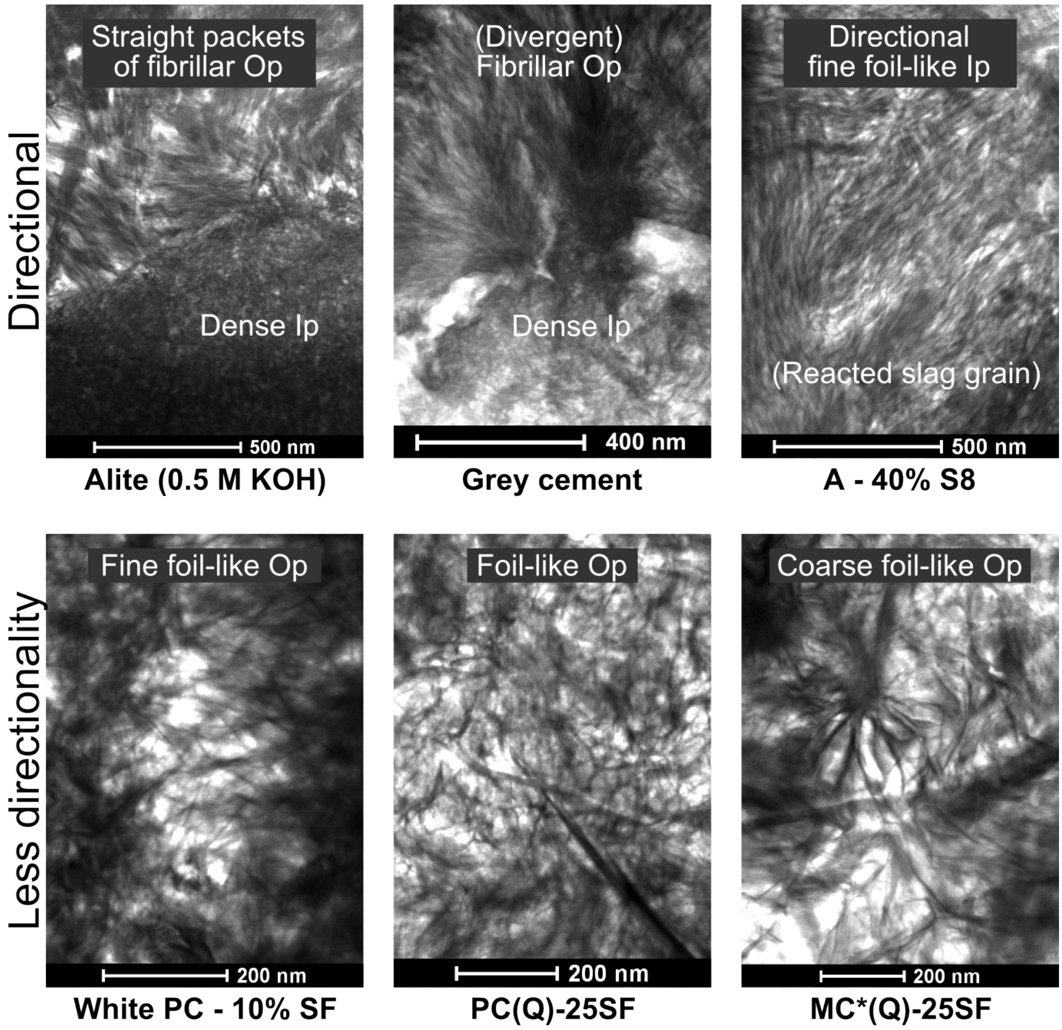

Figure 3.2: C–A–S–H morphologies observed in pastes and defined in the thesis.

4 Assessing the C–S–H composition in matured paste samples

4.1 Introduction

A study was done to determine the optimal conditions for assessing C–S–H composition in SEM. New modern silicon-drifted detectors (SDD) for EDS allow the use of lower beam currents and which are critical for cements as they are very sensitive to electron beam irradiation. It was important to get the best estimation of the C–S–H or C–A–S–H composition in pastes by SEM, because TEM requires different efforts for sample preparation and analysis, and have different representativeness for samples. The problem of intermixing of C–A–S–H with other phases in the interaction volume of the SEM can in fact be dealt with in many systems by a suitable consideration of the data.

Wavelength-dispersive spectrometry (WDS) is usually considered superior in energy resolution for quantitative analysis but it requires high electron doses which damages cementitious samples. EDS analyses can be made at low electron doses and are preferred for hydrated samples.

Most of this study was made on a 5 year old cement paste prepared by V. Kocaba [36], a white cement (cement A) hydrated for five years at room temperature with water:cement ratio of 0.4.

The effect of various acquisition parameters and data treatments for assessing the C–S–H composition was examined. The composition obtained in the SEM and TEM were compared for the white cement paste, and for two other samples which were a grey cement (PC) paste hydrated for 90 days and a sample of white cement blended with 40% slag hydrated for five years (A-S8).

Sources of variability of results using energy dispersive spectrometry (EDS) in an electron microscope

The C–S–H composition may be estimated from direct EDS analyses in bulk samples in the scanning electron microscope (SEM) and for thinned specimens in the transmission electron microscope (TEM).

Because of the interaction volume in the SEM, each measurement is likely to contain information from both C–S–H and other phases and bias results with increasing high voltage [61]. Quantitative analysis is only possible for flat specimens [62, 63] because matrix corrections cannot account for the surface roughness of fractured surfaces where the Ca:Si ratios obtained are wrong [64, 65]. The fact that hydrates are susceptible to electron beam damage means that the results may also be sensitive to the counting time [66] and the beam current.

The analysis of C–S–H in electron transparent samples provides a method to measure "pure" C–S–H, but this advantage is outweighed by the difficulty, time consuming nature and expense of sample preparation and the much lower availability of TEM instruments compared to SEM. In TEM beam damage is also critical [9, 67], but can be limited by the use of low currents and rastering of the beam (typically by using the scanning "STEM" mode).

Finally, there are several instrumental errors and statistical variations which cumulate and may limit precision and accuracy [68, 69]. These sources of errors are reduced by appropriate use of a standards database acquired in the same conditions as for the sample.

Disagreement between SEM and TEM analyses have been reported which may be attributed to the problem of intermixing [70]. However discrepancies may also arise from the way in which the average C–S–H composition is determined. Technical improvements in SEM-EDS and TEM-EDS which allow usage of lower electron doses have the potential to improve the agreement between both methods. In particular, Silicon Drift Detectors (SDD) have become available, which have greatly improved EDS analysis in the SEM. Their increased active surface and thermal stability enable the use of low beam currents and low exposure times while recording sufficient X-ray counts in each spectrum. The same applies to modern TEM instruments which have begun to integrate such detectors.

Samples and specimen preparation

The white cement and white cement blended with 40% slag are the same samples discussed more in detail in Chapter 5. They are matured samples hydrated for five years under distilled water at room temperature and with water:binder = 0.4. The grey cement is the same as in the PC series discussed in Chapter 6. It was hydrated for 90 days at room temperature and with the same water:binder of 0.4.

All samples were prepared according to the methods described in Chapter 3. A particular precaution for the TEM samples were is that the ion thinning was done with low energy Argon beams (no more than 1.5 keV).

4.2 Microscopes and analysis methods

Details on the experimental parameters for the electron microscopes

A scanning electron microscope and a transmission electron microscope with an integrated STEM mode were used in the study of this chapter. Both are equipped with one or several modern SDD EDS detectors.

All SEM results were obtained on a FEI Quanta 200 SEM equipped with a tungsten thermionic filament. It was operated at 15 kV with a spot size small enough to have a sufficient backscattered electron (BSE) image resolution (to allow the user to reasonably position the EDS points) and a relatively low beam current (0.7-0.8 nA as measured with a Faraday cage), but high enough to achieve 12-15,000 counts per second in hydrate phases. 15 kV was also chosen to have a sufficient overvoltage with respect to Fe – the element with the highest transition energy in cementitious samples. With an incident energy of 15 keV, and the Fe-K_α of 6.39 keV, the overvoltage $U/U_0 = 2.35$ is sufficient to well ionise iron. The detector was a Bruker AXS XFlash®Detector 4030 (with an active surface of 30 mm^2). The dead time in EDS under these conditions was less than 1%. In a study which used the 4040 model of our detector, Ritchie and coworkers showed that 10% deadtime or less was recommended for quantitative analysis [71] but warned that the situation is "not clear-cut". The Esprit software allowed definition of a number of counts rather than only a counting time. This allowed comparison of statistically equivalent points despite possible variations in current. Normalisation of the intensities by the pseudo beam current (the "system factor" as defined by Bruker) was done prior to the analyses by measuring X-ray peak intensities from a copper film placed on the metallic sample holder. This was done each time the filament is switched on and every two hours to limit the effect of varying beam current. A predefined list of elements (O, Na, Mg, Al, Si, P, S, Cl, K, Ca, Ti, Fe) was used for identification and quantification as it facilitates calculations when treating several hundred points from the same sample. For each spectrum the background was automatically modelled and subtracted, each peak was deconvoluted using a Gaussian fitting and then quantified using the $\phi(\rho z)$ matrix correction scheme with standards which include typical oxides and metals relevant to cementitious materials. They include compounds such as wollastonite, jadeite, silica and alumina.

The TEM was a FEI Tecnai Osiris™ (CIME, EPFL) with a high brightness XFEG source. The set up was optimised for cementitious materials [39]. The following settings were found to be best for imaging and EDS mappings with minimum degradation of the sample: the microscope was set to 80 kV in scanning mode (STEM) with a large spot size and adjusted to yield a low beam current (0.160 nA or less with a high gun lens). The beam was set in nanoprobe mode and scanned the sample line by line as in a SEM. Images on thin regions were acquired simultaneously in bright field (BF) and high angle annular dark field (HAADF) mode. Both contrasts are useful to observe features in the sample. EDS was carried out using a set of four windowless FEI Super-X SDD detectors integrated into the pole piece (Figure 4.1). However, only two were switched on and the sample was tilted by $\alpha = 20°$ to emulate a traditional geometry better suited for quantitative X-ray analysis. This is because by tilting the sample towards the detector this limits absorption effects due to the shadowing of the detector by the sample (Figure 4.1). Areas were selected for analysis. The count rate was quite sensitive to the thickness of the sample and ranged between 3,000 and 12,000 counts per second. The areas were scanned for 10 to 15 minutes with a low dwell time per pixel of 100 μs and with a full screen resolution of 512 pixels by 512 pixels. Drift correction was used to ensure the microscope always analysed the same area. At each pixel the software recorded the full EDS spectrum to create a spectral map, or HyperMap. We then could define polygonal objects on these HyperMaps to reconstruct spectra with sufficient counts. Only the thinnest areas were taken into consideration because quantification is only reliable in those areas (where absorption is minimal). Each spectrum was corrected for possible thermal drift in the SDD detectors by calibrating the energies to the zero-peak and the Ca peak (K series at 3.692 keV). Background correction for each spectrum was done manually and C, Cl, Co, Cu were identified for deconvolution of peaks only. The corrected spectra were quantified standardless using the Cliff-Lorimer method [72] with a thickness chosen at 150 nm as a reasonable average. Although EDS anaysis here is more qualitative because the thickness is not known, the use of atomic ratios cancels errors resulting from that unknown.

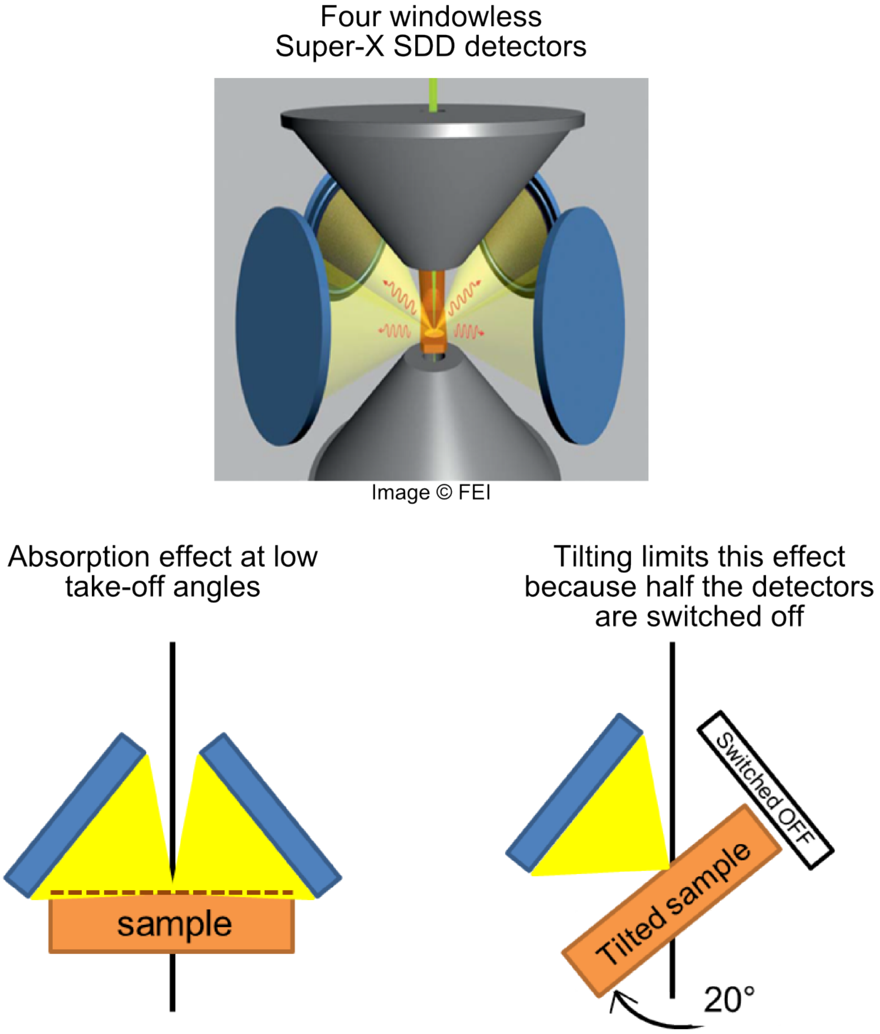

Figure 4.1: Illustration of the adopted geometry in the STEM. Using a tilting angle of 0° and all four detectors causes some X-rays to pass through material before being detected and causes unwanted absorption effects on the quantification (left). Tilting the sample by 20° and switching half the detectors off removes most of this problem and improves quantification (right).

Data acquisition

It is difficult to estimate an average composition of the C–S–H phase in a cement paste by local analysis methods. This is due to several reasons.

The first reason is the fact that hydration products do not significantly differ in atomic weight because their main constituents (Ca, Si and Al) have similar atomic numbers. While anhydrous material and large clusters of Portlandite (CH) are clearly distinct in backscattered electron images of the SEM and in images in the TEM, most hydration products appear with similar grey levels in BSE (for the SEM) and HAADF (for the STEM), even though both imaging modes are designed to highlight composition and density variations.

The second reason is the scale at which the hydration products form. The dissolution and precipitation processes favour the formation of hydration products at a very small scale ($\approx$ 10-100 nm). This is more problematic in the SEM because the interaction volume at 15 kV – estimated using CASINO for a Ca-Si substrate – has a radius of about 1-2 μm at least. Each analysis is likely to contain signal from several phases which bias the quantification result. In the TEM this problem is largely removed.

The third reason is related to the representativeness of any given sample. It is known that C–S–H has a variable composition within a sample as seen e.g. in an OPC paste observed in the TEM [9]. Averaging the composition in TEM requires a number of analyses from different areas. This is more difficult for the TEM because the samples are typically a few millimetres wide and contain only a very small fraction of observable areas which are transparent to the electron beam. The SEM is better suited to analyse areas several centimetres wide and collect significantly more analyses for a given sample.

The fourth reason is the fact that we can distinguish two C–S–H products at later ages (Figure 2.7 (b), p. 18) which differ in morphology but rarely differ in composition: the inner product (Ip) C–S–H and the outer product (Op) C–S–H. Ip C–S–H designates the product which forms with the slow reaction of clinker grains with water and which appears as a rim of reacted product. Op C–S–H is defined as the product which formed in the originally water filled space. The Ip is not always distinguishable from the Op if no apparent interface like that in Figure 2.7 (b) is observed.

Given these considerations, the following methodology was adopted to measure C–S–H composition by EDS spot analysis.

Sample representativeness was obtained by magnifying to 4000× in the SEM and 60,000× in the TEM and analysing numerous areas spread through the whole sample. As a simple step in the procedure, preliminary measurements were done on alite and belite – both of known composition (in Ca:Si atomic ratio) to verify the stability of the EDS system before analysing hydrates. This was usually impossible in the TEM because either no anhydrous material was found or because anhydrous material is significantly thicker than C–S–H regions. For the study of cementitious materials, the use of atomic ratios is common because of the problem of varying analysis totals. Atomic ratios include Ca:Si, Si:Ca, Al:Ca and S:Ca. When aluminium is incorporating C–S–H, Ca:(Si+Al) ratio is used. The calcium in ratios for C–S–H was corrected, i.e. Ca*=Ca-S when sulphate was present in the system because sulphate can be adsorbed in C–S–H [73, 74, 75]. Representation in atomic ratios also cancels errors in quantifying oxygen and removes variations in results due to variations in the beam current. When the two C–S–H products were distinguishable, the Ip and Op were measured in separate datasets in both the SEM and TEM. Points were therefore chosen manually, in such a way to maximise the number of points overall but with a limit of ≈ 25 C–S–H analysis points per SEM image. Ip rims less than ≈ 5 μm wide were considered too thin for reliable analysis. It should be possible to readily remove points of C–S–H with high analysis totals – corresponding to points with contributions from anhydrous material – e.g. above a threshold of ≈ 85%, but this was not satisfactory as this procedure tended to remove most points. Slight variations in beam current and the other reasons mentioned previously do not make this method robust.

Examples of EDS spectra of C–S–H (or C–A–S–H) are shown in Figures 4.2 and 4.3. Both show the main elements of interest (Ca, Si, Al and S) which are resolvable. There are difference in peak heights between the pure cement and the blend.

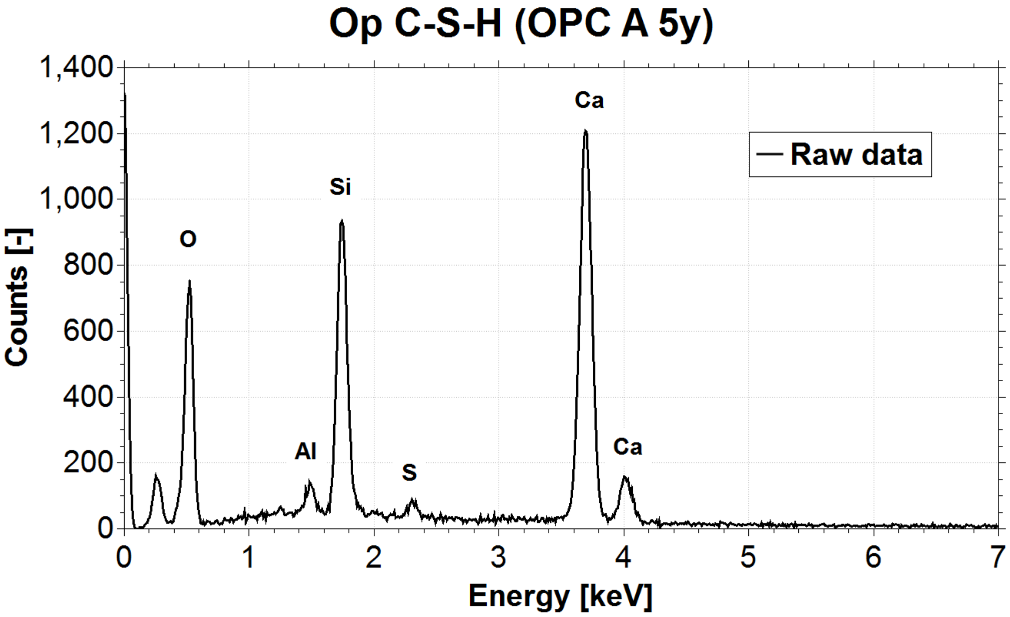

Figure 4.2: Example of a SEM-EDS spectrum of C–S–H in OPC A (5 years). The acquisition lasted 50,000 counts.

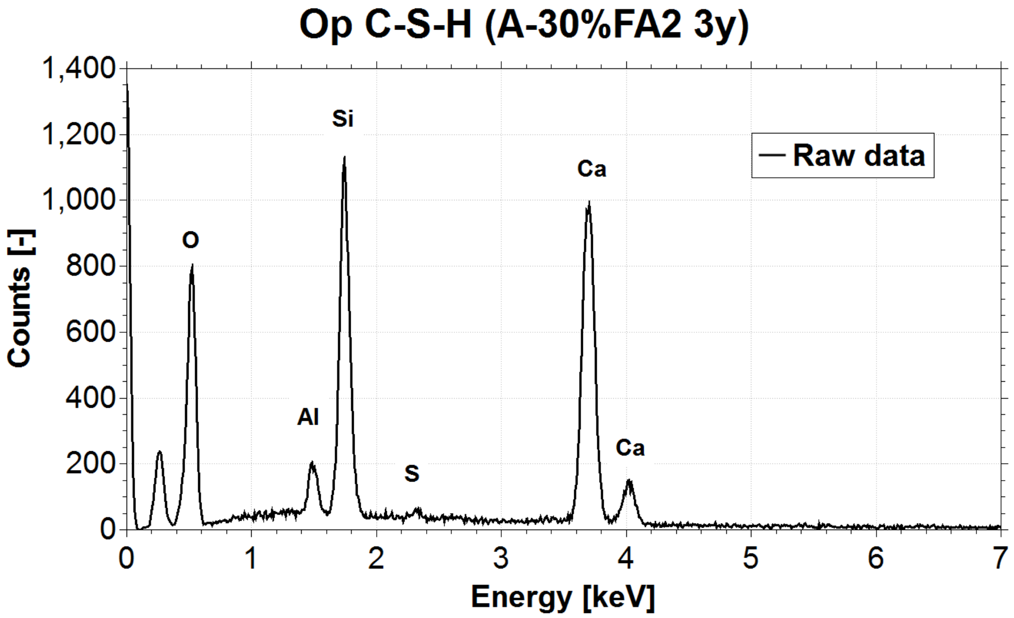

Figure 4.3: Example of a SEM-EDS spectrum of C–A–S–H in the A-FA2 blend (3 years). The acquisition lasted 50,000 counts.

Beam damage

Figure 4.4 is a backscattered electron SEM image from cement A observed with a beam current of about 0.8 nA. It was captured after short EDS point analyses at locations indicated by the circles. Despite low beam conditions, holes are observed after exposure to the electron beam. The centre of the hole turns black indicating material is removed due to damage, while the surroundings show a change in contrast. The lighter shade of grey indicates a likely charge build up and a change in the material.

In TEM, the beam was rastered (in STEM mode) to limit damage to the sample [76]. Figure 4.5 shows two HAADF images of a region of cement A. Figure 4.5 (a) is an image taken shortly after exposing the sample. We clearly observe the characteristic morphologies we can expect from C–S–H in cement paste. Even after 5 years of hydration we observe distinct fibrillar regions of outer product and a dense morphology in what resembles a small hydrated grain. After 15 minutes of exposure to the beam during EDS mapping, as shown in Figure 4.5 (b), we lose information on the morphologies which remain barely distinguishable. The microstructure has noticeably coarsened and bubbled due to beam damage. However it is noteworthy that such long exposure does not result in complete destruction of the microstructure. It is likely that the electron dose (not measured here), expressed in $e/Å^2$, was low enough to not completely degrade the sample [77]. See [78] for discussion on damage mechanisms in both SEM and TEM.

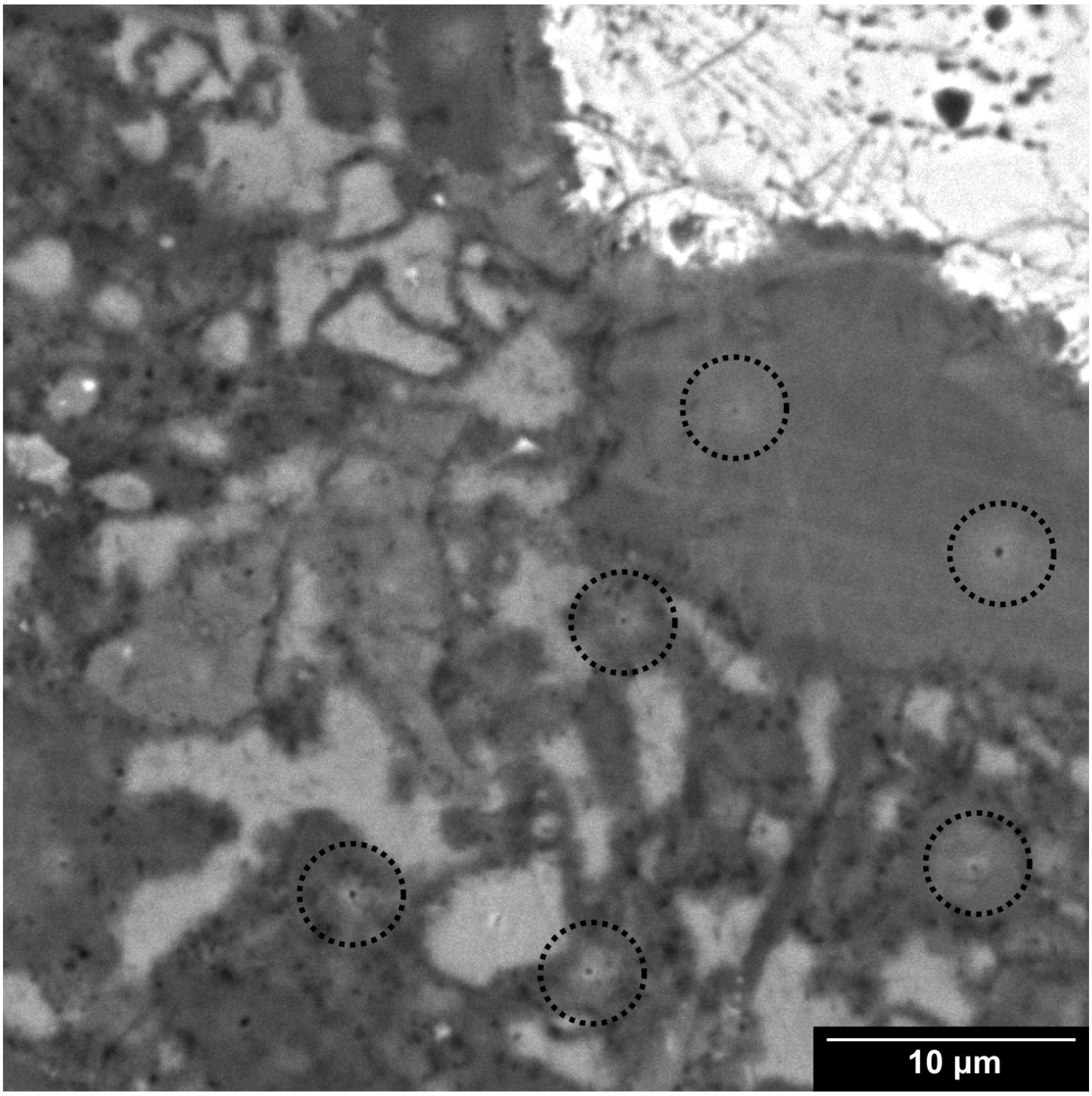

Figure 4.4: BSE image of cement A. The markings indicated by a circle are damage due to the beam dwelling at the chosen points to let the EDS detector measure characteristic X-rays during 3 seconds.

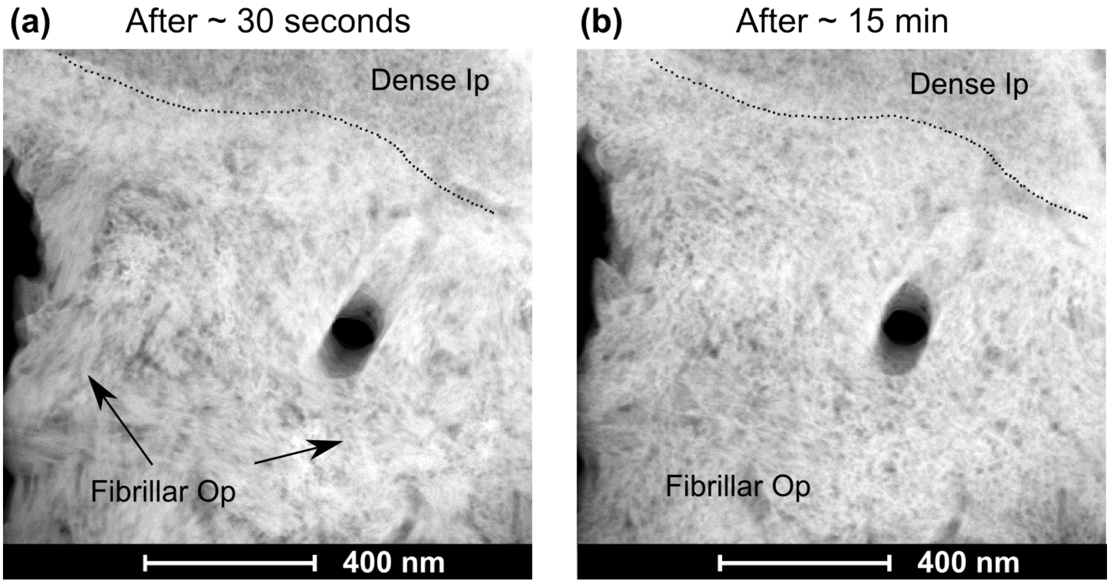

Figure 4.5: HAADF images of a thin region of cement A. (a) The image shows characteristic morphologies of C–S–H found in Portland cement. There are fibrillar regions corresponding to outer product and dense regions of inner product. There is an apparent diffuse interface between both regions. (b) The image is the same region after 15 minutes of EDS mapping with little damage but a loss of information due to bubbling of the C–S–H.

4.3 SEM-EDS data sorting

Atomic ratio scatter plots

Because of the intermixing problems described earlier, a useful representation to discriminate several phases is two dimensional scatter plots of atomic ratios [79], for example in the Al:Ca-Si:Ca and the S:Ca-Al:Ca space as illustrated in Figures 4.6 (a) and (b). Figure 4.6 (a) shows EDS analyses from the SEM taken on regions of cement A assumed to be Op C–S–H. Here the cluster of points is considered intermixed C–S–H as it contains information from both C–S–H and other Ca bearing products. The other products – shown in Figure 4.6 (a) – are Portlandite (CH) with atomic ratios of (0.00; 0.00), Ettringite (AFt) with ratios of (0.00; 0.33) and AFm (Ms, Hc and Mc) with ratios (0.00; 0.50). To discriminate the AFm phases (monosulfoaluminate from hemicarboaluminate and monocarboaluminate) the (Al:Ca; S:Ca) representation presented Figure 4.6 (b) is used. Here AFt is located at (0.33; 0.50), Ms at (0.50; 0.25) and both Hc and Mc at (0.50; 0.00).

Points are often located along tie-lines between the main cluster of points (indicated by a dashed circle) and the theoretical atomic ratio of a corresponding phase. In Figure 4.6 (a), the intermixing occurs mostly between C–S–H and CH and between C–S–H and AFt. In the Figure 4.6 (b), the different representation reveals that Ms is also present, something which was not evident from Figure 4.6 (a). The presence of both AFt and Ms were confirmed by small peaks around 9 and 10°2θ in the X-ray powder diffraction of the same sample. Points not located close to the tie lines are likely to be measurements of more than two phases. In this case, the C–S–H composition is estimated from the intersection of the manually placed tie lines. This yields Si:Ca ≈ 0.55 and Al:Ca ≈ 0.05 for the C–S–H. There is a gap between the S:Ca axis and the points Figure 4.6 (b), indicative of the presence of sulphate adsorbed on the C–S–H.

Figures 4.6 (c) and (d) show the same plots as Figures 4.6 (a) and (b) however with calcium corrected by sulphate adsorption, i.e. Ca*=Ca-S. The tie lines and dotted circles were placed at the same locations for comparison even though the theoretical atomic compositions would shift for both AFt and Ms. The cluster of points of intermixed C–S–H in Figure 4.6 (c) is clearly less scattered than without the correction (Figure 4.6 (a)). It does however not change the extreme values significantly. In this example Si:Ca ≈ 0.55 and Al:Ca ≈ 0.05, thus we obtain a Ca:Si of 1.82 and a Ca:(Si+Al) of 1.67. Corrected values are Si:Ca* ≈ 0.56 and Al:Ca* ≈ 0.05 and give Ca*:Si of 1.78 and a Ca*:(Si+Al) of 1.64.

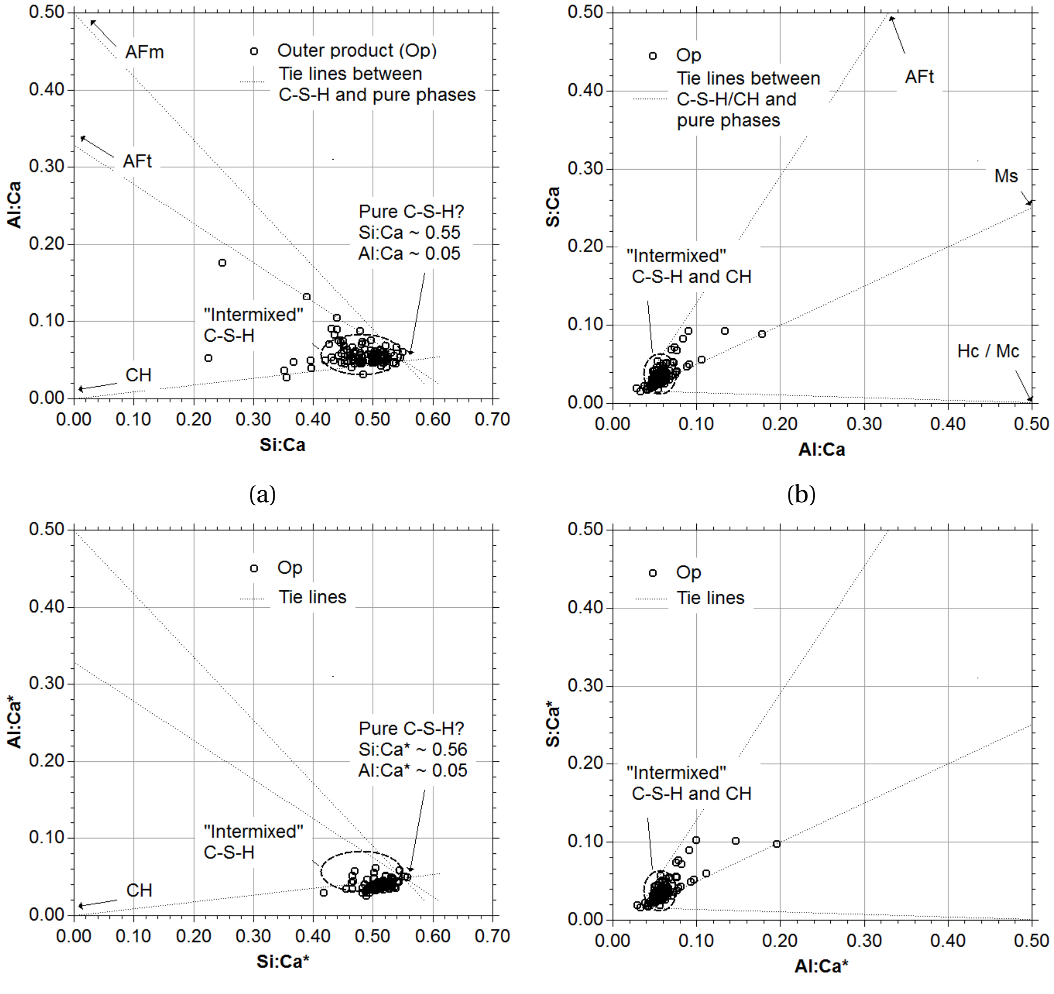

(a)

(b)

(c)

(d)

Figure 4.6: 2D scatter plots of SEM-EDS analyses of the Op C–S–H of cement A, measured with 50,000 counts per point. (a) Data with the x axis being Si:Ca and y axis being Al:Ca. (b) Same with the x axis being Al:Ca and y axis being S:Ca. (c) Same data corrected for sulphate (x axis is Si:Ca* and y axis is Al:Ca*). (d) Same data corrected for sulphate (x axis is Al:Ca* and y axis is S:Ca*).

Other representations

As we will see later, scatter plots are sufficient to estimate a C–S–H composition, but are not sufficient to show subtle variations due to the experimental parameters. Histograms and boxplots are two useful representations of atomic ratios used to describe the acquired data. As we will also see, both the intermixing of C–S–H with other phases and true variations in C–S–H are convoluted and impossible to separate in the SEM because we have no a priori knowledge of the typical degree of intermixing for any given sample. Finally, the poor statistics do not allow analysis of the data using sophisticated methods.

In box plots like on top of Figure 4.7 (a), the middle line (−) is the median value (at 50% of all values). The edges of the boxes represent the middle quartiles of the distribution. The whiskers indicate values between 5 and 95% of the distributions. Minimal and maximal values are indicated by a cross (×). The square symbol (□) indicates the mean value.

Because atomic compositions are always positive, the distributions (histograms) were assumed to be log-normal. This is evident in the box plots (e.g. Figure 4.7 (b)) which show a differing mean (□) and median (−) value.

Figure 4.7 (b) shows the data calculated as different ratios and represented as box plots. A comparison of the different ratios shows that the scatter of Ca:Si – given by the second and third quartiles – is the highest and that the scatter of Ca*:(Si+Al) is the lowest. This suggests that alumina substitution and sulphate adsorption are relevant to the atomic ratio of the C–S–H phase rather than related to other phases. Figure 4.7 (a) shows the histogram for the Ca*:(Si+Al) ratio and displays a skewed distribution which is therefore not Gaussian. This is suggested by the mean value (□) higher in Ca compared to the median value (−). The box plot is shown to scale for comparison. Because most values richer in calcium likely correspond to “intermixed C–S–H” − values impossible to distinguish from variations of “pure” C–S–H composition − it is reasonable to consider the left tail of both distributions as the probable value for “pure” C–S–H, as suggested in [80].

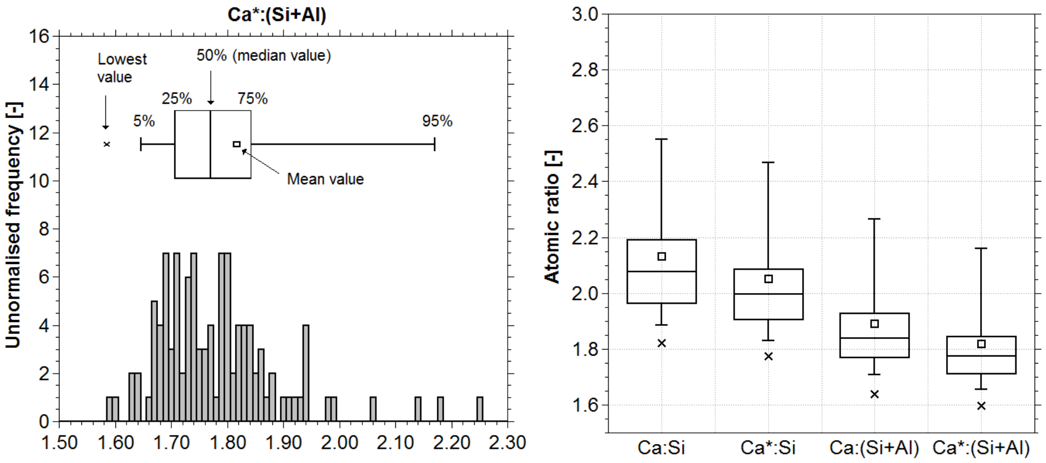

(a) (b)

Figure 4.7: Boxplot and histogram representations of SEM-EDS analyses of the Op C–S–H of cement A, measured with 50,000 counts per point. (a) The Ca*:(Si+Al) ratio represented as a histogram. The box plot of the same series is shown for comparison. In box plots, the middle line (−) indicates the median value. The whiskers indicate 5-95% of the values. The mean is indicated by (□). Outliers are given by (×). (b) Box plots of the Ca:Si, Ca*:Si, Ca:(Si+Al) and Ca*:(Si+Al) ratios.

Comparison with STEM-EDS

Before looking into details of the SEM-EDS protocol, we compare results from above with the data obtained by STEM-EDS on the same sample. Figure 4.8 shows the elemental maps for Ca and Al cumulated during 15 minutes. The map of Ca gives detailed elemental distribution on the different regions, while the map for Al is more noisy as it is only present in small amounts. After EDS acquisition the data from the HyperMap was treated. This was done by placing virtual objects (Figure 4.9 (a)) within which EDS data is cumulated from these areas to form a spectrum with sufficient statistics. Care was taken to select the thinnest regions only as calcium is easily overestimated in thicker regions because of absorption effects. Also, regions were chosen with other elements such as Mg excluded (Figure 4.9 (b)). Results from TEM – where each point was a spectrum cumulated within a chosen region – are shown in Figure 4.10 and are compared to the SEM-EDS analyses done with 50,000 counts per points. Interestingly, most points lie within the limits of the SEM points, mostly on the upper aluminium rich part of the cluster of C–S–H in both Figure 4.10 (a) and (b). These preliminary results suggest that SEM and TEM do agree quite well despite the different set ups.

From the TEM analyses (Figure 4.10 (a), with each point having different total counts), we can determine an average of Si:Ca* ≈ 0.55 and Al:Ca* ≈ 0.06 and estimate Ca*:Si of 1.82 and a Ca*:(Si+Al) of 1.64, close to those obtained by taking the edge of the SEM-EDS points (1.78 and 1.64 respectively). The TEM seems to slightly overestimate the aluminium in the system. Poor statistics on the peak for aluminium may be the main reason for this. However, the detectors

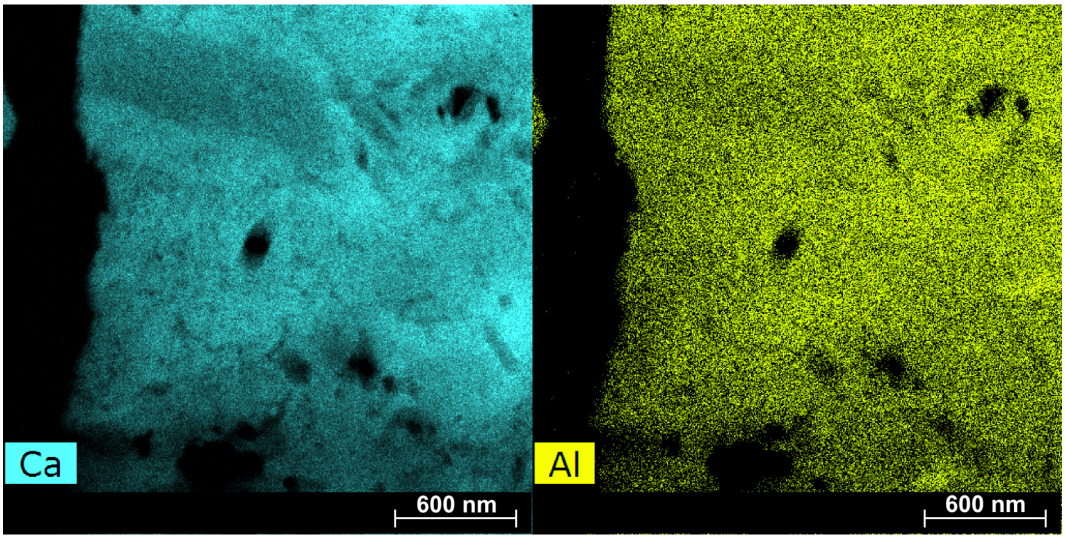

Figure 4.8: Elemental maps for Ca and Al on an electron transparent region of cement A acquired by STEM-EDS.

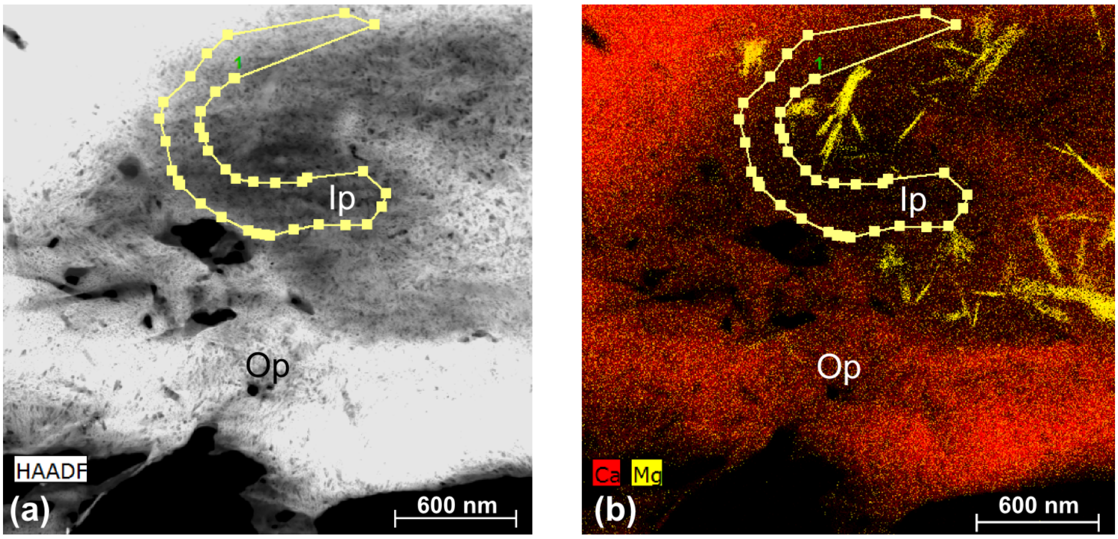

Figure 4.9: HyperMaps of cement A with objects placed to quantify the reconstructed spectra. (a) HAADF contrast showing the choice of an Ip region and an Op region. (b) Combined Ca and Mg allowing determination of pure C–S–H regions (Ip in this example).

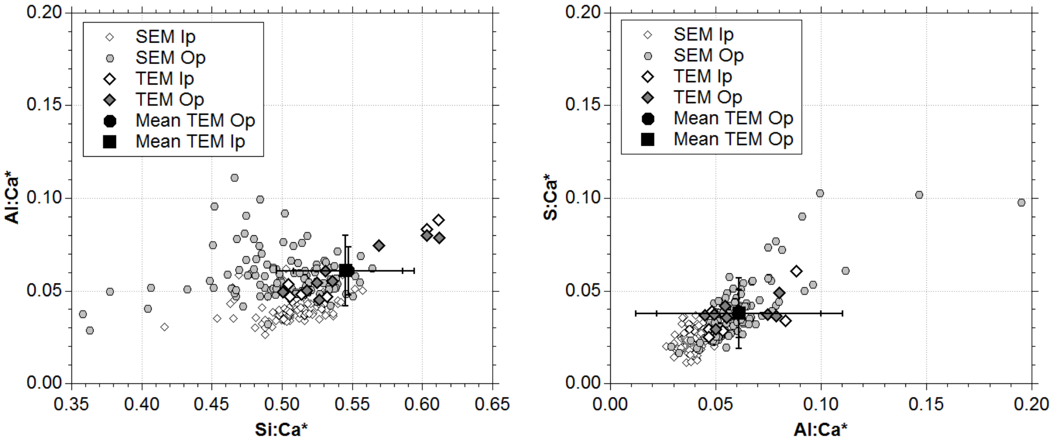

(a) (b)

Figure 4.10: Comparison between EDS analyses from STEM and SEM for cement A. The error bars are calculated from the standard deviation of the series of points. Calcium is corrected for sulphate. (a) 2D scatter plot of Si:Ca* versus Al:Ca*. (b) 2D scatter plot of Al:Ca* versus S:Ca*.

and stage have a novel geometry with large solid angles for collection which may slightly affect quantification of aluminium [81].

Estimating the "calcium silicate" ratio from the distribution of SEM-EDS points

These results and those from two other comparisons (in the following sections) between SEM and TEM support the idea of "pure" C–S–H being estimated from the lower end of "calcium silicate" distributions as shown in Figure 4.11.

The sampling of an EDS point on the surface of a bulk sample will result in the acquisition of information from an "interaction volume" far greater in size than to the beam diameter. The interaction volume radius at 15 kV in cementitious samples is approximately 1-2 μm wide. As illustrated in [80], this causes intermixed analysis of phases which is often towards calcium-rich phases such as CH. Also, chemical analyses are always positive, confined to values between 0 and 100%. Both reasons suggest that taking the log-normal representation better takes the skewing of the distribution into account.

In SEM-EDS, the "calcium silicate" ratios were therefore calculated in the logarithmic space and fitted with a Gaussian curve by means of a simple least square method. The mean (μ) and standard deviation (σ) were obtained and allowed determination of a C–S–H composition by considering the value of "pure" C–S–H as $\mu - 2\sigma$ in the logarithmic space.

For other examples, see Figure 5.19, p. 86.

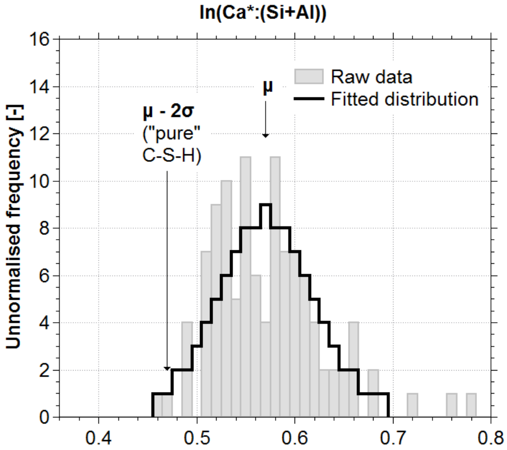

Figure 4.11: Example of the determination of a "calcium silicate" ratio from SEM-EDS data. The raw data is taken in the logarithmic space and fitted with a Gaussian curve. The mean (μ) and the standard deviation of the data (σ) are used to take the fitted value of $\mu - 2\sigma$ in the logarithmic space.

4.4 Influence of several parameters

Automated and manual analyses

The quality of the analyses is greatly improved when the user selects the areas to be analysed. Because hardened cement paste is such a heterogeneous material, user input is required to best separate contributions from anhydrous phases, CH, inner and outer product C–S–H, and other visible phases. Figure 4.12 (a) shows manually chosen analyses of cement A inner and outer product C–S–H, which are separated into two clusters of analyses. The Ip analyses are intermixed with CH, while the Op analyses intermix not only with CH but also with AFt and Ms (as seen in Figure 4.6 (a)).

Two automated sets of analyses were done on the same sample using the same counting time per point. Two scenarios were chosen to compare with manually selected points. The first considers data acquired from a single grid of 500 points recorded at 500× magnification. It is shown in Figure 4.13 (a) with data from Figure 4.12 (a). We cannot distinguish between inner and outer product, results do not show the points of lower Si:Ca* and there is a large degree of spread caused by intermixing with CH. A first approximation would therefore indicate a single composition of C–S–H with higher calcium. The second automated scenario is done at the same magnification as the manually selected points (4000×). Figure 4.13 (b) also compares the data from Figure 4.12 (a) with data from a set of $5 \times 5 = 25$ images each containing a grid of 20 points. Here the trends are almost identical to the first scenario. The points contain information from anhydrous material and mostly intermixed CH and show a lot of scatter at lower Si:Ca*. In both scenarios the quality of analyses was decreased by the fact that interfaces were not avoided and because CH was often measured directly. In Figure 4.12 (b), most points

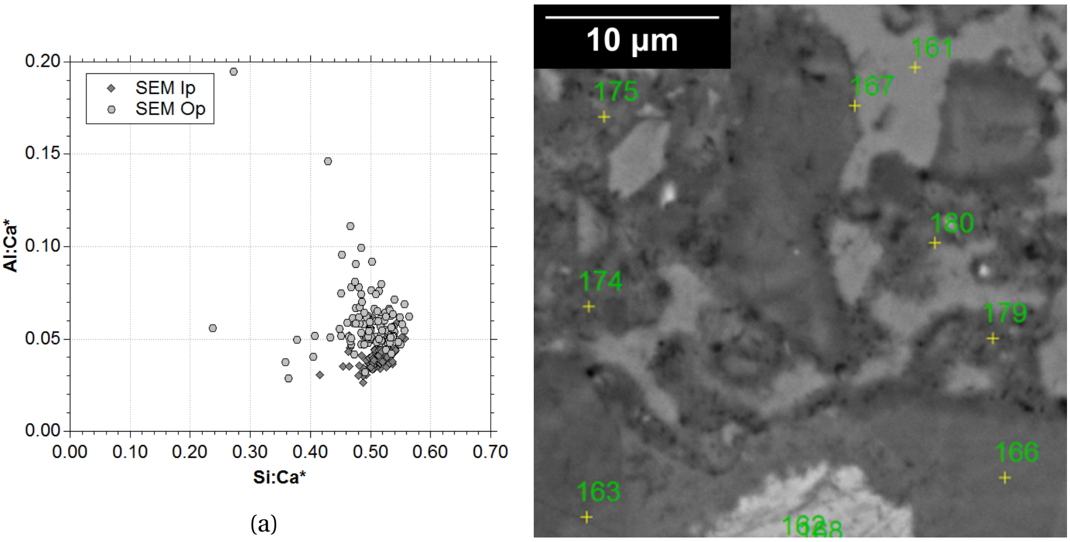

(a)

(b)

Figure 4.12: (a) Al:Ca* versus Si:Ca* plots of 90 Ip and 150 Op analyses of C–S–H from Cement A (50,000 counts per point). (b) BSE image of cement A taken at 4000× magnification. Points in these examples were placed manually. Points number 167 and 180 were intentionally placed at an interface as an example of unsatisfactory point placement.

have been manually placed at a sufficient distance from the interfaces. Points 167 and 180 however will yield a high calcium concentration because it will contain information from both CH and C–S–H. Automated analyses will therefore contain a significant proportion of such points which bias the measurements and which contain less useful data such as CH points.

It is therefore recommended to avoid automated selection of points for these reasons. A reasonable protocol is to measure at least ten different areas of interest at high magnification (at least 4000×) and well spread across the sample. No more than 10-15 points per C–S–H product points should be recorded in each region. For the TEM, it is advantageous to analyse as many thin regions as possible as the total potential analyses is limited by the total area which is electron transparent. The methodology for SEM-EDS analyses has proven to be satisfactory in obtaining a reproducible dataset for several experiments.

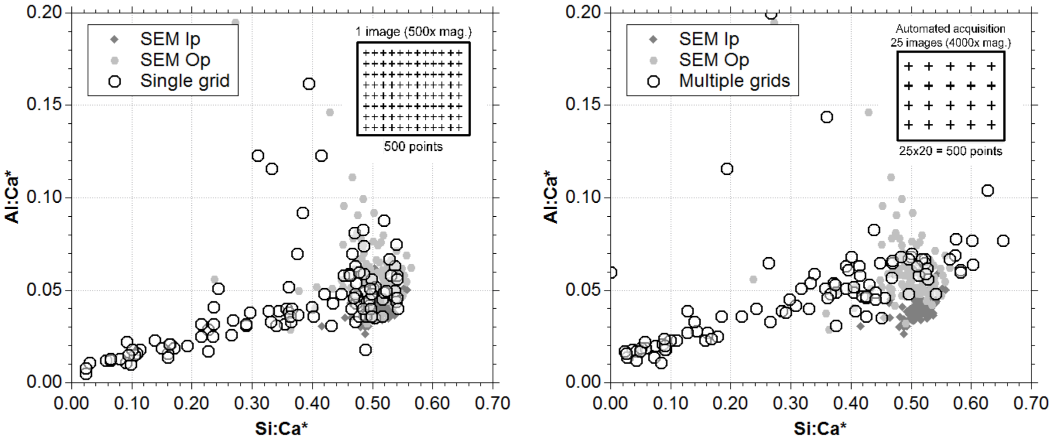

(a) (b)

Figure 4.13: Two automated grid analyses of cement A. (a) Same data as in Figure 4.12 (a), with additional data acquired from one low magnification (500×) image on which a rectangular grid of 500 points was placed prior to analysis. (b) Same data as in Figure 4.12 (a) with data from 5 × 5 = 25 images each containing a rectangular grid of 20 points. Each image was taken at 4000× magnification.

Number of measured point analyses per sample

The results in Figure 4.14 show the influence of the number of manually chosen points taken into consideration for the data treatment, both for the inner and outer product of cement A. A total of 400 points were acquired in a single session, and each set of points (100, 200 and 350 points) was chosen at random from the complete set of data. They are compared for identical conditions of 75,000 counts per points (≈ 6 seconds of counting time). Box plots show the data for both the Ip (Figure 4.14 (a)) and the Op (Figure 4.14 (b)). Both the median value and the minimum value are stable for both the Ip and Op. The mean value however is slightly sensitive to the number of analyses, and shows no correlation with the number of points. This further indicates the random occurrence of intermixing. If the minimum value is considered, Ca*:(Si+Al) ≈ 1.60 and 1.55 for the Ip and Op respectively. These results suggest that manually choosing approximately 100 points should be sufficient to estimate the atomic composition of C–S–H. The value at 95% of the data which increases with the number of points of the Op (Figure 4.14 (b)) suggests that increasing the number of points increases the chance of measuring strongly intermixed CH. The same argument does not seem to apply for the probability of measuring a "pure C–S–H" region as the bottom whisker does not depend on the number of points. The manual selection of points – based on backscattered electron images – likely has to do with the stable minimum value.

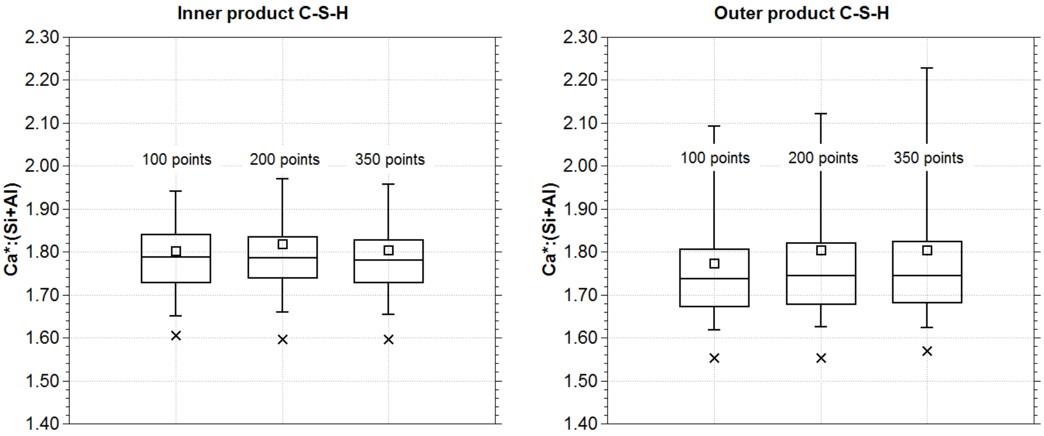

(a)

(b)

Figure 4.14: Box plots of different datasets. Influence of the number of points (100, 200 and 350) taken into consideration when representing the data from Cement A (acquired with 75,000 counts per point). The whiskers represent the 5-95% of the data. (a) Inner product. (b) Outer product.

Counting time

Figure 4.15 shows results on the influence of counting time (expressed as kilocounts per analysis point or kcp). This was varied from 20 to 300 for analyses of both the inner product C–S–H (Figure 4.15 (a)) and the outer product C–S–H (Figure 4.15 (b)). The data shows an influence of the counting time on the median value, bottom whisker (at 5%) and minimum value (×). Generally there is an increase in atomic ratio between 20,000 and 150,000 counts. Doubling the counting time from 150,000 to 300,000 does not affect the measurements in the Ip. The effect of counting time has a stronger influence on the measurements of the Op (Figure 4.15 (b)). Here the bottom whisker and minimum value increase with counting time up to 150,000 counts. The results in the Op for 300,000 differ from the trend and could not be explained. Despite the variations observed in atomic ratios, the total dose (current × exposure time) does not seem to be the most critical factor considering the order of magnitude between the lowest and highest counting time.

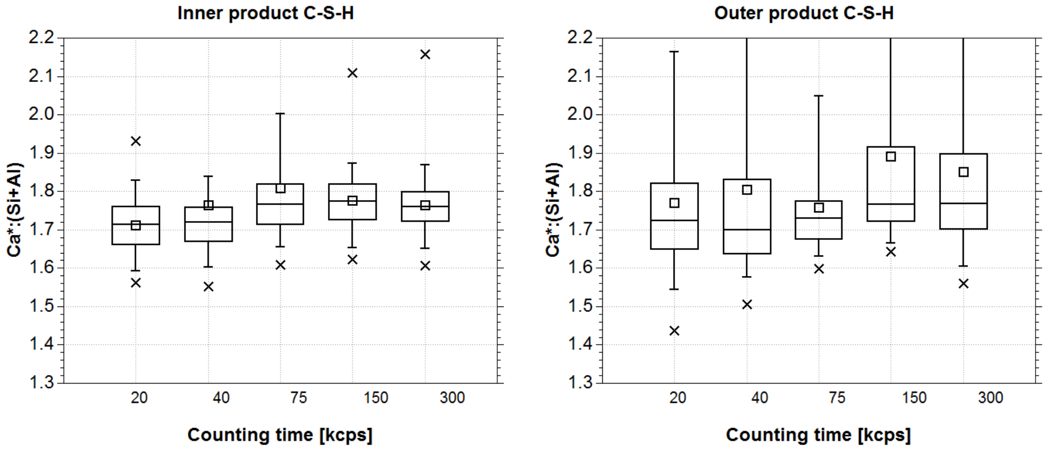

(a) (b)

Figure 4.15: Results from EDS analyses of Cement A for different counts per analysis (counting times), i.e. 20,000 to 300,000. (a) Ca*:(Si+Al) results from the Ip. (b) Ca*:(Si+Al) results from the Op.

Beam current at constant counting statistics in SEM

Because The FEI Quanta 200 SEM does not have a direct control of the current, it was increased by changing the spot size and then estimated using the system factor. Changing the spot size changes the current but also the diameter of the beam. In our SEM, the system factor given in arbitrary units is measured on a Cu film before each session. Tests showed that the system factor is related to the beam current by a factor of ≈ 8. If the factor was 5.93, the beam current is reasonably estimated by 5.93/8 ≈ 0.74 nA. Using this information, the effect of the beam current was investigated.

In a series of acquisitions made during a same session – i.e. without switching the beam off –, the spot size was varied to increase the beam current from ≈ 0.74 to 2.75 nA. Analyses were made of the Ip and Op (≈ 100 points in each product and for each current) and with constant counting statistics of 50,000 counts per analysis. Results shown in Figure 4.16 suggest that the beam current here does not have a significant effect. For one, the total dose is kept constant because the counting time was fixed by the total number of X-ray counts. Typical acquisition times were 1 second (at high current) to 4-5 seconds (at lowest current) and are likely short enough to prevent serious damage. However this is probably due to the tungsten filament electron source. Unlike field emission sources, increasing the current does not necessarily increase the current density in these experiments. When the beam of electrons is more spread out at higher currents, we do not expect significantly more damage. This is reflected here by the fact that the whiskers at 5% (bottom whiskers) do not vary.

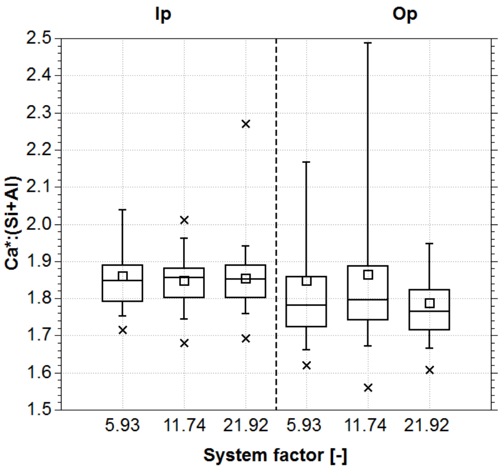

Figure 4.16: Effect of the beam current (≈ 0.74, 1.5 and 2.75 nA for system factors of 5.93, 11.74 and 21.92 respectively) at constant counting statistics of 50,000 counts per point, on measurements of cement A. It is shown for both the inner product (left) and the outer product (right).

Damage mechanisms in SEM and TEM

Discussing damage mechanisms is difficult because of the limited knowledge on the properties of C–S–H. Radiolysis is the likely dominant mechanism occurring in hydrate phases because such damage is limited by the use of a cooling stage – as it was done in a hydrated C_3S paste in [77] – or by rastering the beam. In the TEM, the crystallinity of the C–S–H only appears with limited current density. Below the threshold current density, the total dose (exposure time × current) is the determining factor. Using the same STEM (in TEM mode for this example), the crystallinity of C–S–H was qualitatively observed (Figure 4.17 (a) and (b)) in a synthetic sample of aimed Ca:Si = 1.0 prepared at 20°C and equilibrated for 180 days (sample from E. L'Hôpital). Without a cooling stage and with a beam current of ≈ 0.160 nA, the sample was quickly observed in diffraction mode before damage extinguished the faint diffraction spots after less than 20 seconds. Removal of bound water in C–S–H is also an important mechanism. In another synthetic sample (Figure 4.17 (c) and (d)), the C–S–H was prone to shrinkage after 10-15 minutes of scanning the beam (STEM mode) for EDX analysis. This shrinkage is attributed to the dreikerketten structure of C–S–H in which the interlayer spacing will change upon dehydration under the electron beam as shown by thermal dehydration of tobermorite [82, 26].

A decrease in Ca due to damage has been observed in the TEM [83] in a hydrated C_3S paste. The opposite trend is however suggested in the SEM and is not understood. Here, the results were not affected by an increase of beam current (at constant total dose). Had the experiments been done at constant counting time, we would expect more damage to occur. Also, the use of a tungsten filament with a fairly constant current density likely prevented damage to occur because the current density was not above a critical value for cement hydrates. Results

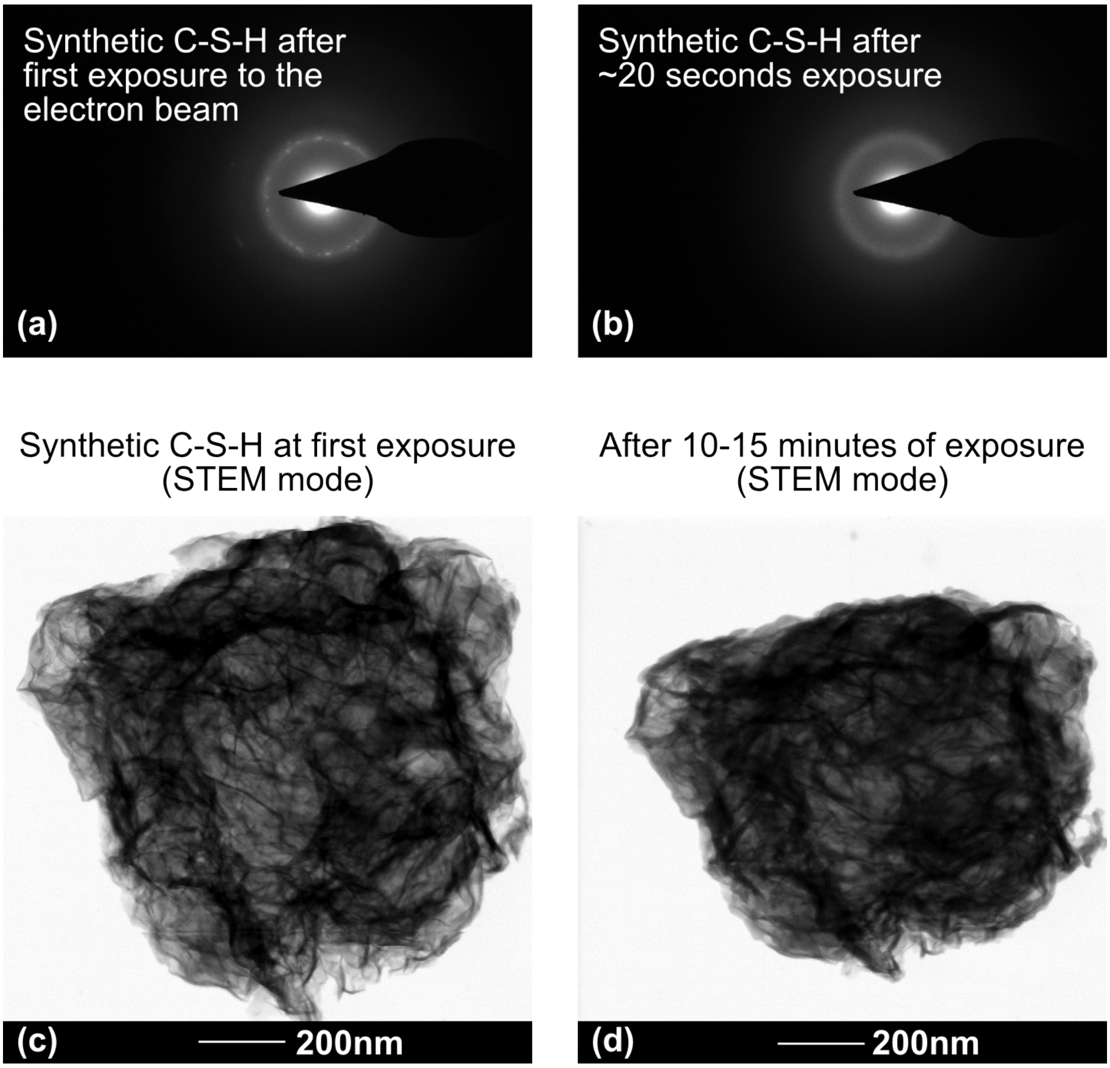

Synthetic C-S-H at first exposure (STEM mode)

After 10-15 minutes of exposure (STEM mode)

Figure 4.17: Example of diffraction and shrinkage observed by TEM and STEM. (a) Synthetic C–S–H (E. L'Hôpital) showing some diffraction spots immediately upon exposure to the beam. (b) The spots of the same sample fade as the diffraction ring is more evident after 20 seconds of exposure. (c) A similar sample shown immediately upon exposure to the beam in STEM mode. (d) The same sample as in (c) after 10-15 minutes of exposure in STEM mode. The beam current was ≈ 0.160 nA in all cases.

emphasize the need for low-dose experiments. In particular, counting time is better chosen as a fixed number of X-ray counts rather than acquisition time.

Choice of counting time

The shortest counting time (20,000 counts) shows that the peaks for Ca, Si and Al contain (with background) ≈ 6,000, ≈ 3,500 and ≈ 511 counts respectively. Because X-ray generation obeys Poisson statistics – which can be approximated by a normal distribution given the high number of counts – the standard deviation σ for a distribution having a mean value $\overline{N}$ is given by [69]

$$\sigma = \sqrt{\overline{N}} \tag{4.1}$$

The relative standard deviation $\frac{\sigma}{\overline{N}}$ is 0.013 (Ca) 0.017 (Si) and 0.045 (Al). In order to maximise the precision which increases with counting time 300,000 could be chosen. However, as standards are used and because of the problem of damage, an ideal value seems located between 40,000 and 75,000 counts in this case. A compromise of 50,000 per analysis is reasonable for the setup in our laboratory. It has the advantage of increasing the number of points acquired per session compared to the use of longer counting times.

Two other comparisons between the SEM-EDS and STEM-EDS

In order to further validate the method, SEM-EDS and STEM-EDS measurements were done on a paste of PC hydrated for 90 days and a blend of cement A with 40% of slag 8 hydrated for 5 years.

Measurements taken in both Ip and Op areas of PC are represented in Figure 4.18. Calcium corrected measurements show a very good agreement once again despite an overestimation of aluminium in STEM measurements. Both Ip and Op averages lie on the extreme values from SEM.

A blend of cement A with 40% slag 8 (hydrated 5 years) was also compared in both microscopes. We see in Figure 4.19 a good agreement between the average STEM-EDS values and the edge of the cloud of SEM-EDS points.

A comparison can be made by using unbiased values taken from the log-normal distribution of Ca*:Si and Ca*:(Si+Al). Let μ be the mean and σ the standard deviation of the fitted distributions, the value at 5% (ca. the edge of the cloud of points) is $\approx \mu - 2\sigma$. Using this method we get the following comparison for all three samples (Figure 4.20). Cement A (Figure 4.20 (a)) shows

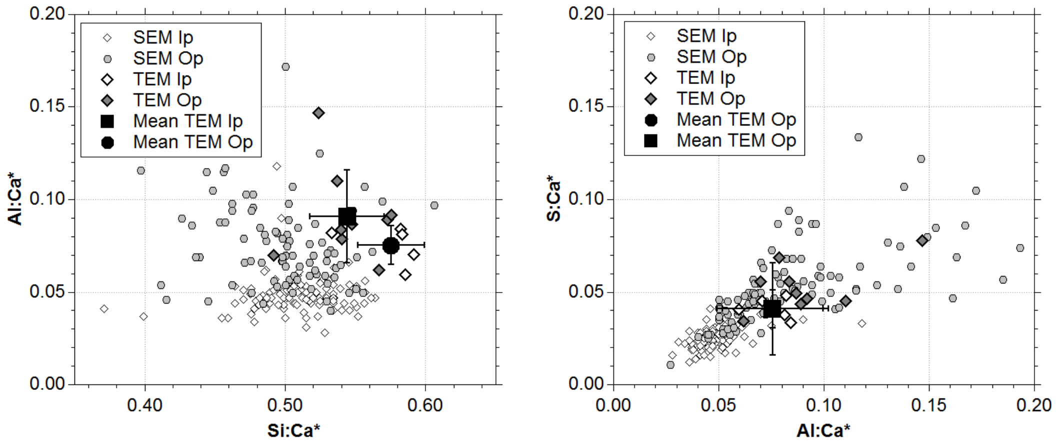

(a) (b)

Figure 4.18: Sulphate corrected data for PC (90 days). SEM-EDS points and STEM-EDS points are compared. (a) Si:Ca*-Al:Ca*. (b) Al:Ca*-S:Ca*.

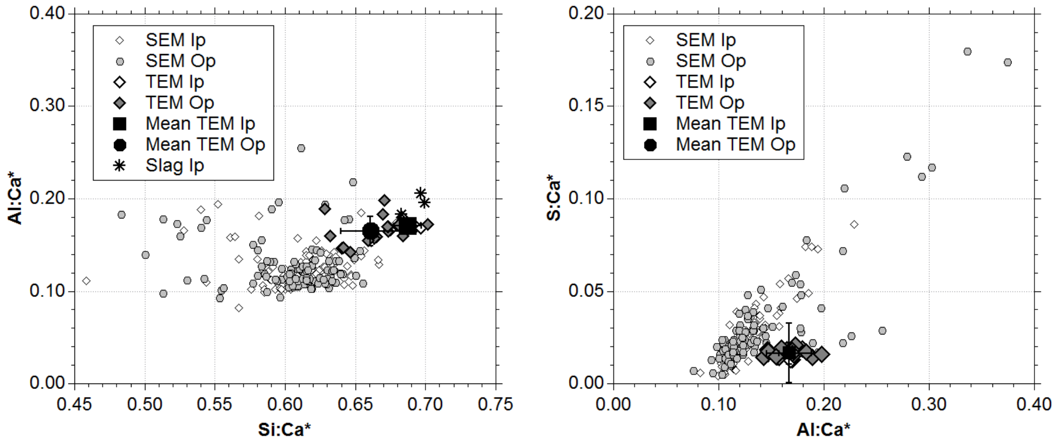

(a) (b)

Figure 4.19: Sulphate corrected data for cement A blended with 40% slag 8 (5 years). SEM-EDS points and STEM-EDS points are compared. (a) Si:Ca*-Al:Ca*. (b) Al:Ca*-S:Ca*.

an overall good correlation with a slight underestimation by the SEM of the C–S–H atomic ratio in the Op. PC (Figure 4.20 (a)) shows a good correlation despite the fact that it contains more aluminate and could have underestimated Ca*:(Si+Al) by the TEM. Cement A blended with 40% slag 8 (Figure 4.20 (c)) shows a good correlation with the Ca*:Si but the TEM likely underestimates the Ca*:(Si+Al) because of the higher alumina in the C–S–H coming from the presence of slag.

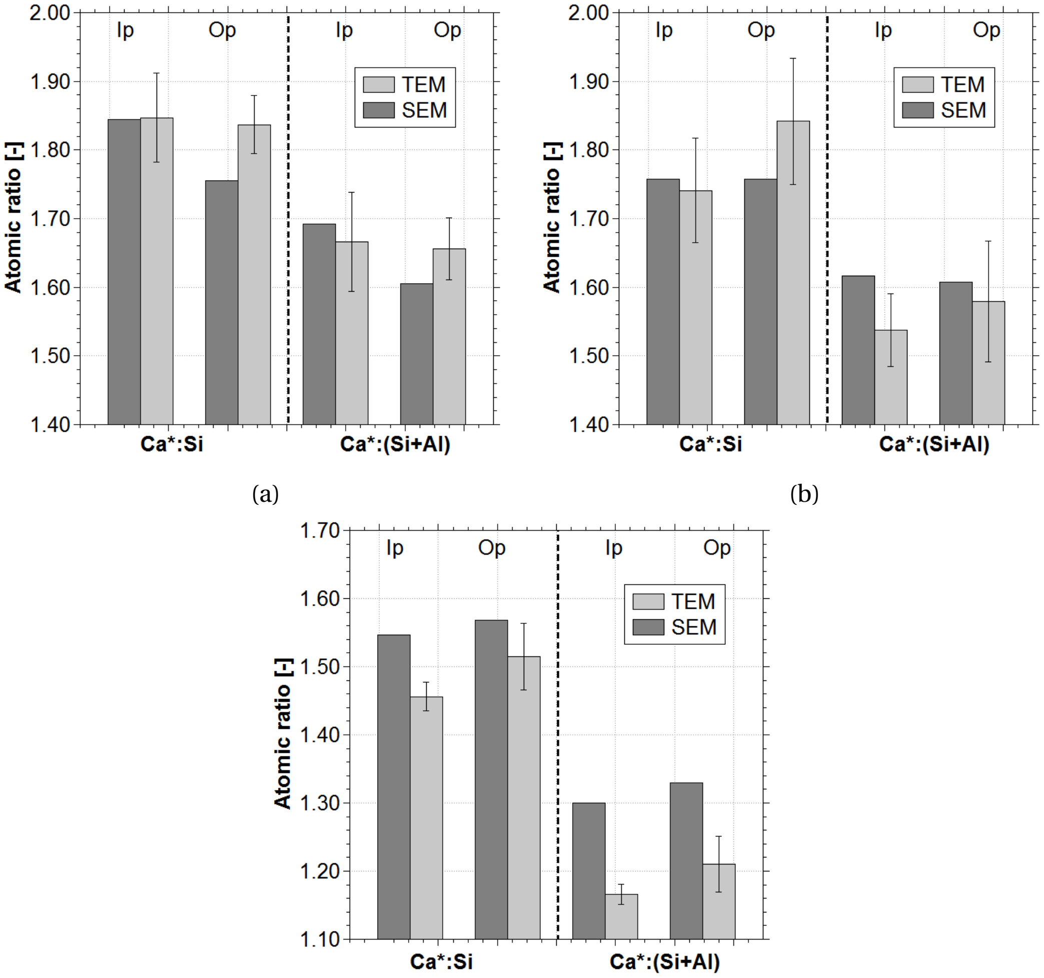

(a)

(b)

(c)

Figure 4.20: Comparison between estimated C–S–H composition (SEM) and average C–S–H composition (STEM) for three samples. (a) White cement A. (b) PC. (c) Cement A with 40% slag 8.

These examples and the example of pure cement A discussed in detail earlier show that the estimated C–S–H composition by SEM and TEM are similar. The main concern in both cases is limiting damage to the cement sample, while not hindering the quality of the data.

4.5 Summary and adopted protocol

For three matured cement pastes with water:binder = 0.4, SEM-EDS and STEM-EDS show a good correlation when the extreme value from the SEM scatter plot is considered as “pure” or not intermixed C–S–H. Another example, of a fly ash blend, can be seen in Chapter 5, Table 5.3, p. 82. The use of a simple log-normal fitting allows determination of an value similar to simply choosing the extreme value of the scatter plot. It has the distinct advantage of being unbiased when compared to a manual determination of the end point from a scatter plot, but requires a small fitting procedure. This however may only be valid in the case where intermixing occurs mostly towards calcium. In systems containing silica fume (additional Si) and metakaolin clays (additional Si and Al), the small particle size (less than a micron) often does not permit such a straightforward estimation of the C–S–H composition. Two comparisons shown in Figures 4.21 (a) and 4.21 (b) show that the correlation between STEM and SEM mainly depends on the degree of reaction of the fine SCM particles in the case of silica fume. In Figures 4.21 (a) less silica fume has likely reacted so the Op analyses are strongly intermixed with pure silica fume. The analyses from SEM are all biased towards high Si:Ca* ratios. In the Figure 4.21 (b), it appears that more silica fume has reacted. The high Al:Ca* could be due to poor statistics on Al in this sample which contained very little of it. The STEM analyses fall somewhat in the middle of the Op analyses from SEM which contain information both from low Ca*:Si C–A–S–H and unreacted silica fume particles. These examples show that such a strong degree of intermixing cannot be dealt with without knowledge from other techniques, e.g. ^{29}Si MAS NMR which could quantify the degree of reaction of silica fume.

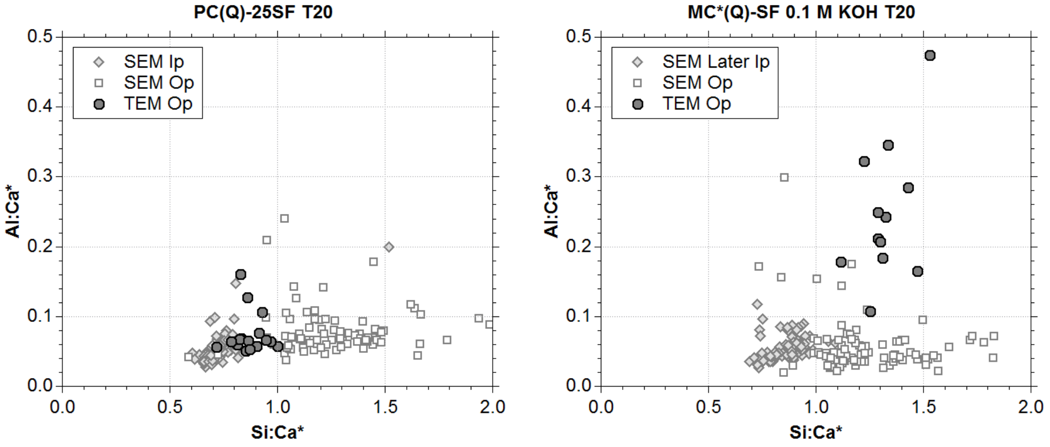

(a) (b)

Figure 4.21: Examples of EDS analyses in silica fume blends obtained by SEM and TEM. (a) Comparison between analyses from the SEM and TEM in a cement-silica fume blend. The STEM analyses of the Op fall on the low end of the Si:Ca* distribution. (b) A similar comparison in which the Op measured by STEM falls somewhat in the middle of the Op analyses obtained by SEM. The high Al:Ca* values could be due to the low amount of alumina in the system, the quantification of which is less precise because of low counting statistics in the STEM.

Generally, the study in SEM and TEM of the C–S–H phase from cementitious materials is not a straightforward process and must be done with some precaution. The conditions of observation were optimised and discussed for a white cement sample hydrated for five years at room temperature. Guidelines for a satisfactory protocol were highlighted and are summarised here.

- Cementitious materials should be studied in polished sections [63], not fractured surfaces which induce errors in quantification as seen in [64, 65].
- TEM samples should similarly be ion-thinned to minimise absorption effects due to varying thicknesses.
- The beam current in a standard SEM should remain in the range 0.7-1.0 nA to minimize damage and effects on the analyses. The damage is likely to be more critical in field emission sources which produce more focused beams, i.e. higher current density. This can be limited by slightly defocusing the beam.
- Exposure time is dependent on the SEM and EDS detector. The exposure time should be set up with respect to the total electron dose. Rather than setting an acquisition time, the counting time should compensate for variations in beam current. This is done by fixing a total number of X-ray counts as the criteria for stopping an analysis.
- Compositions should be expressed in atomic ratio in order to remove errors on oxygen quantification and water content which decrease the analysis totals. Oxygen is therefore best estimated by stoichiometry. Because of substitution of silica by alumina and sulphate adsorption occurring in C–S–H, a proper expression for the “calcium silicate” ratio is (Ca-S):(Si+Al).
- Ratio plots are a convenient way to get an overview of the intermixed phases present in the sample. Box plots and histograms are useful to show the distribution of values in order to determine an unbiased value of “pure” C–S–H by considering the lower edge of “calcium silicate” ratios.
- The TEM was optimised for the observation of cements and used in scanning mode (STEM) to limit damage. The overestimation of aluminium in the present TEM is due to low statistics on aluminium and possibly to the novel SDD setup. It should be improved in the near future. Data in Chapter 5, Section 5.3 does show that the Al:Si is sometimes estimated to be double in the STEM, but this overestimation does not seem constant for a straightforward correction (it could also be due to strong local concentration variations).
- The estimation of C–S–H atomic composition relies on data acquired by manual choice of the regions of interest (particularly the inner and outer product C–S–H). Points should be measured in many zones across the sample and at sufficiently high magnification (at least 4000× in our setup). Automated point analyses are of limited interest because

CH and interfaces are measured. Automated analyses also cannot distinguish Ip and Op C–S–H.

5 Systems still containing Portlandite

5.1 Introduction

This chapter focusses on results from paste samples still containing Portlandite (CH) and hydrated with a low solution:binder ratio of 0.4. The results show the composition of C–S–H estimated by EDS and the corresponding amount of CH determined by TGA. The C–S–H morphology as observed in the TEM will also be shown for a selection of the samples.

In the first part (Section 5.2), we will deal with the comparison between the grey cement (PC) and alite (MC) hydrated for 90 days at different temperature (10, 20 and 38°C) and, in the case of alite, with increasing amounts of potassium hydroxide (0, 0.1, 0.5 M KOH) to emulate a model cement with realistic amounts of alkali.

The second part (Section 5.3) deals with matured systems which are binary blends made with cement and 40% slag, 30% fly ash and 10% silica fume (see Section 3.1 in Chapter 3). The blends have reacted for 5 years (cements and slag blends) and 3 years (cements with fly ash, cements with silica fume).

5.2 OPC and alite pastes

Comparison between alite and OPC

Microstructure of the pastes. Figure 5.1 shows the similarities and differences between a grey cement and alite paste (0.5 M KOH). The typical heterogeneous microstructure of the OPC B can be seen in Figure 5.1 (a) with unreacted grains showing high electron backscattering (white grey levels). CH (in light grey) is dispersed in the sample and C–S–H (dark grey) forms most of the matrix. CH can appear as platelets (dashed box) [84]. Black indicates the presence of porosity. Another view with higher magnification (Figure 5.1 (b)) illustrates the presence of unreacted alite around which inner product (Ip) C–S–H has formed and outer product (Op) C–S–H which formed within the originally water-filled space. Op C–S–H is highly intermixed with other phases such as AFt and AFm phases. Also, the Op appears more porous than the Ip.

Figure 5.1 (c) shows the microstructure of alite (0.5 M KOH) hydrated for 90 days. Here large clusters of CH form, and seem to hinder the hydration of grains which are surrounded by CH [84, 85]. No platelets seem to from. The difference between the Ip and Op regions is more contrasted (Figures 5.1 (d)) because the Op seems more porous compared to the grey cement. The very small hydrated grains are easier to observe because one can notice the thin layer of Op C–S–H which grew from the surface of the alite grain (see example in the dashed square). Small grains like this example often have small hollow shells in the centre [84]. These form in cement pastes but are not clearly visible in the grey cement (Figure 5.1 (b)). In this sample there is porosity between the Op regions and between the Op C–S–H and CH regions.

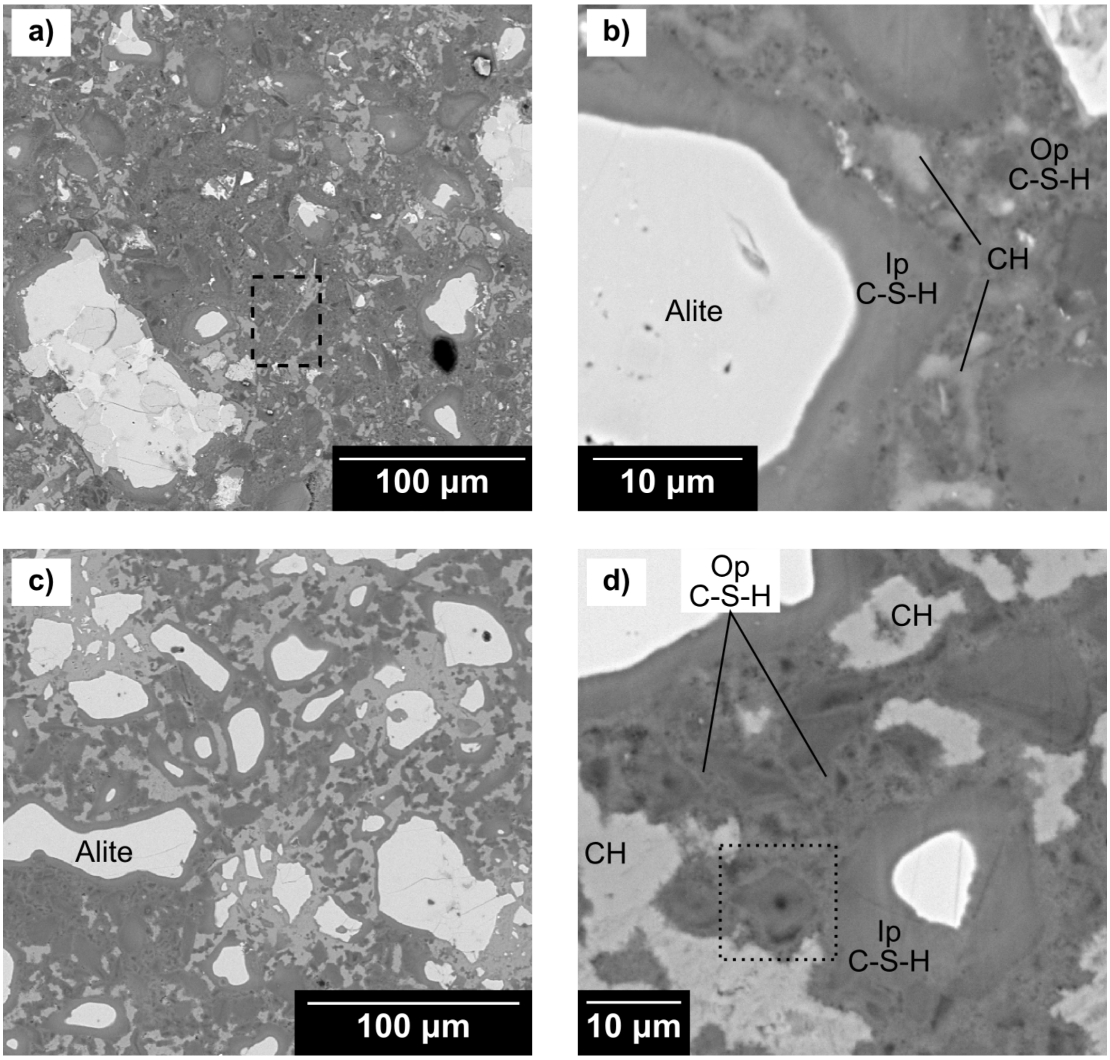

Figure 5.1: (a) BSE image of OPC B (90 days, 20°C, w:c = 0.4). (b) Higher magnification image of the same sample. (c) Alite paste (0.5 M KOH, 90 days, 20°C, w:c = 0.4). (d) Same paste at higher magnification.

Morphology of the C–S–H. The morphology of the C–S–H was also studied by TEM (in scanning, or STEM mode). Figure 5.2 (a) shows the PC sample with packets of fibrillar C–S–H with typical directional morphology (indicated by white arrows), dense Ip in the outer part of the small grain (between dashed lines) and the inner part of the grain resembling fine foils. Relics of AFt (or AFm) such as that indicated by a black arrow can be seen. Here the fibrils seem to fan out as it was noticed previously [9].

The same alite sample shown previously with 0.5 M KOH (Figure 5.2 (b)) shows similarities with the cements. Dense Ip and fibrillar Op are observed. However, the fibrils seem to grow in straight packets rather than fan out like in the OPC systems [examples of C–S–H in C_3S e.g. Fig. 25 in [8], Fig. 6 (a) in [21] and images from early age samples in [39]].

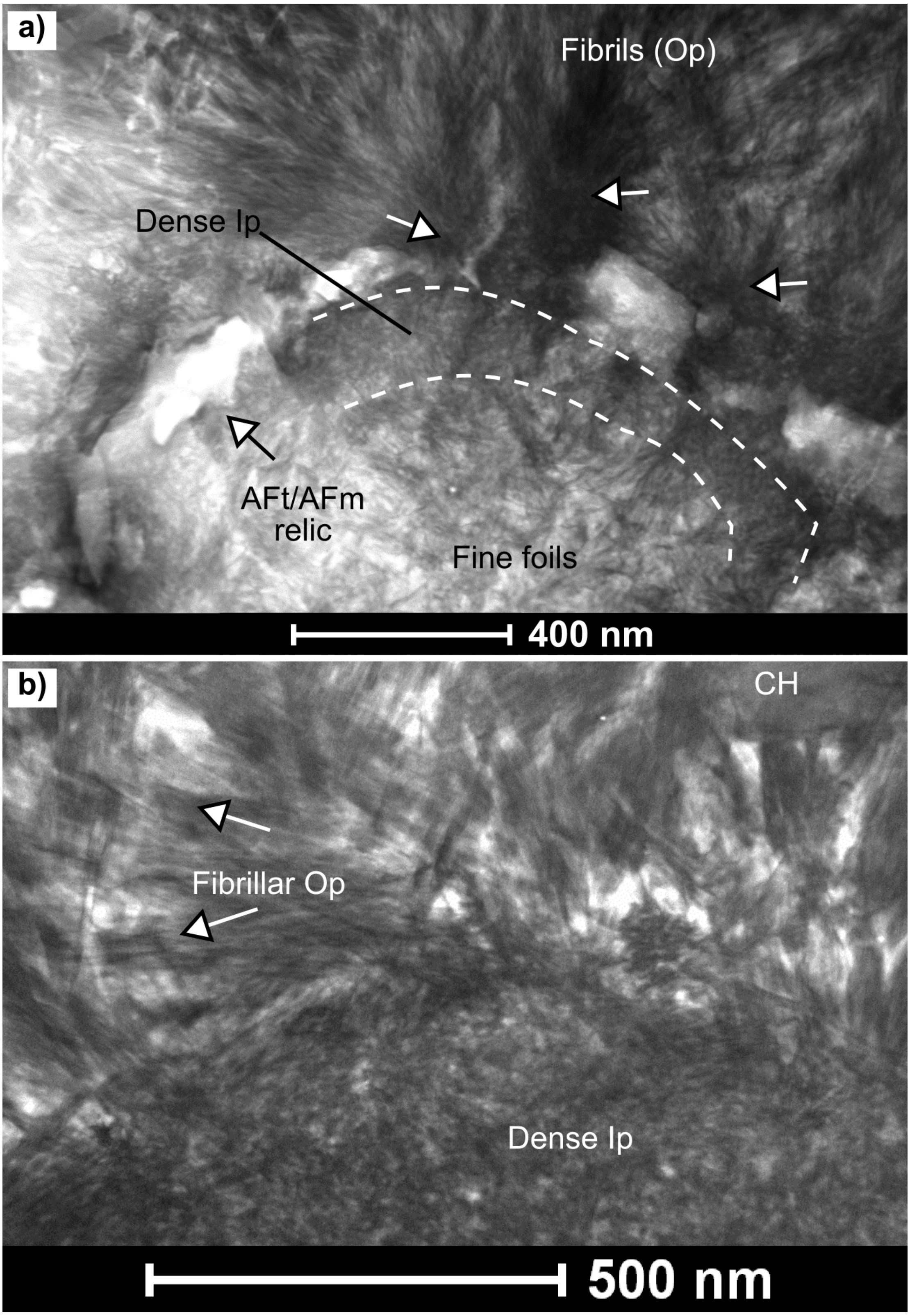

Figure 5.2: (a) BF image of PC T20 (90 days, 20°C, w:c = 0.4). (b) Alite (0.5 M KOH, 90 days, 20°C, w:c = 0.4) paste.

Composition of the C–S–H. The Ip and Op C–S–H composition were estimated for the alite hydrated with 0.5 M KOH and compared to the grey cement (Figure 5.3). Here we see that despite the correction of calcium by sulphate, the amount of calcium in the atomic composition of C–S–H in plain alite with same water:binder = 0.4 is consistently lower than in cement. Ca*:Si ≈ 1.60 for both Ip and Op, while Ca*:Si ≈ 1.80 for the C–S–H in the PC system shown here. The large error bars are due to the fact that intermixing is usually higher in the Op where CH phases are also measured within the interaction volume in the SEM. In cement the intermixing can also occur with AFt and AFm. When alumina incorporation is taken into account, the C–S–H, or C–A–S–H in alite has Ca*:(Si+Al) ≈ 1.50 compared to Ca*:(Si+Al) ≈ 1.60-1.65 in the PC. There is no difference between the composition of the Ip and Op of the PC.

The sulphate may play a role in explaining some of the differences in morphology given the fact that they are strongly adsorbed at early age [37] and because of results on early age alite pastes show “flower” shaped C–S–H particles in fractured surfaces observed by secondary electron imaging [86]. The sulphate may have an impact on the composition, either because the 1:1 correction may not exactly correspond to reality or because another mechanism is causing the cement to have a higher Ca*:Si ratio. For example, assuming that sulphate hinder the growth of CH [87] and therefore decrease the final amount observed in the paste, the Ca*:Si would have higher values because there is an intimate link between CH growth and the growth of C–S–H [88, 39]. The results on alite-silica fume blends presented in Chapter 6 actually suggest that the combined presence of gypsum and aluminate may have an effect on the Ca:Si ratio of C–S–H formed from hydrated alite and increase the Ca:Si while decreasing the total CH present.

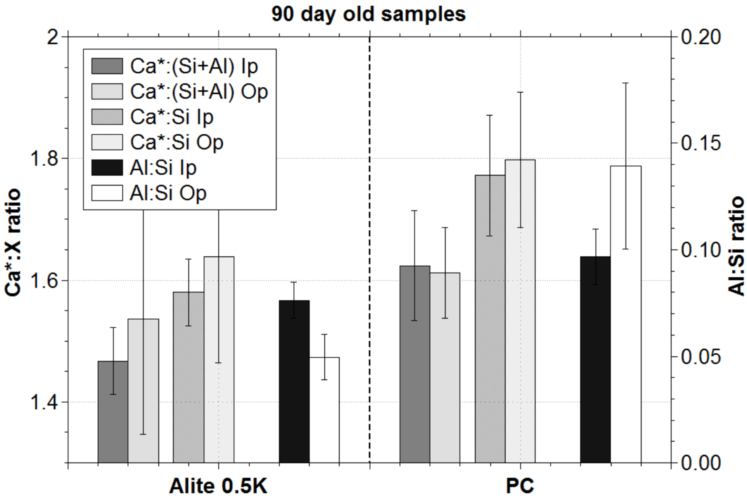

Figure 5.3: Comparison of Ca*:Si (Ca* = Ca-S) and Ca*:(Si+Al) in non-blended pastes hydrated at 20°C water:binder = 0.4. The alite paste was hydrated with 0.5 M KOH.

Influence of temperature on alite and PC reference systems

Alite (0.5 M KOH) and grey cement samples hydrated at 10, 20 and 38°C and are compared in the SEM (Figure 5.4). In the alite systems with 0.5 M KOH, temperature does not seem to have a particular effect. The high porosity of the sample hydrated at 20°C (Figure 5.4 (c)) and seen in Figures 5.6 (e) is qualitatively similar to that in the samples hydrated at 10°C (Figure 5.4 (a)) and 38°C (Figure 5.4 (e)).

In the grey cement series, the temperature has no visible effect on the porosity of the system. (Figures 5.4 (b), (d) and (f)).

A closer look at the histograms of the grey levels in the SEM images of the alite shows that the C–S–H relative brightness as defined in [89] increases from ≈ 0.45 in alite at 10 and 20°C to ≈ 0.50 in the same sample at 38°C. In the grey cement, the same relative brightness does not increase significantly. Values for 10, 20 and 38°C are 0.510 ± 0.009, 0.524 ± 0.008 and 0.526 ± 0.011 respectively. For alite, the increase in C–S–H relative brightness at 38°C suggests that the C–S–H is denser. For the PC samples, all relative brightness values lie within the standard error of the mean value and do not suggest an increase in C–S–H density as in [89]. However, the range of temperatures is smaller than in [89]. The low reactivity of the grey cement and the fact that the water was initially at room temperature can also explain the very small changes.

In both series, the distribution of CH did not change noticeably with temperature. The amount of CH does not vary with temperature either, assuming an error of ± 1% on TGA measurements.

The composition of C–S–H in pure alite and PC does not appear to vary with temperature as shown previously in [89] for cement pastes hydrated from 5 to 60°C. The alite (MC) composition is Ca*:Si ≈ 1.60 and Ca*:(Si+Al) ≈ 1.50 (Figure 5.5 (a)), and is Ca*:Si ≈ 1.70-1.80 and Ca*:(Si+Al) ≈ 1.60 for the grey cement (PC) (Figure 5.5 (b)). The systematic difference in composition between alite and grey cement is also observed at lower and higher temperatures.

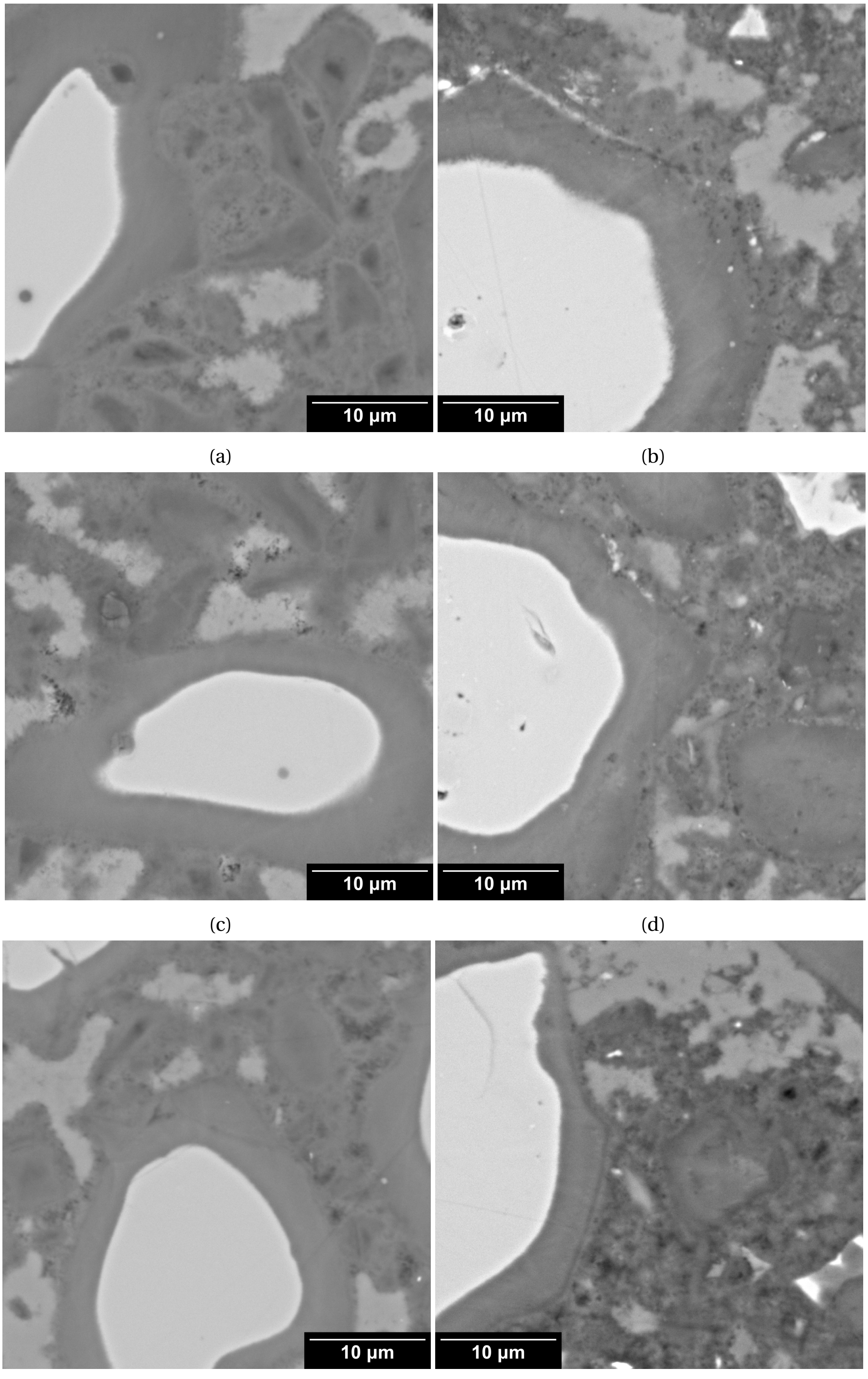

(a) (b)

(c) (d)

(e) (f)

Figure 5.4: SEM images of pastes (matured 90 days with solution:binder = 0.4) of alite (0.5 M KOH) hydrated at (a) 10°C, (c) 20°C, (e) 38°C and of PC hydrated at (b) 10°C, (d) 20°C and (f) 38°C.

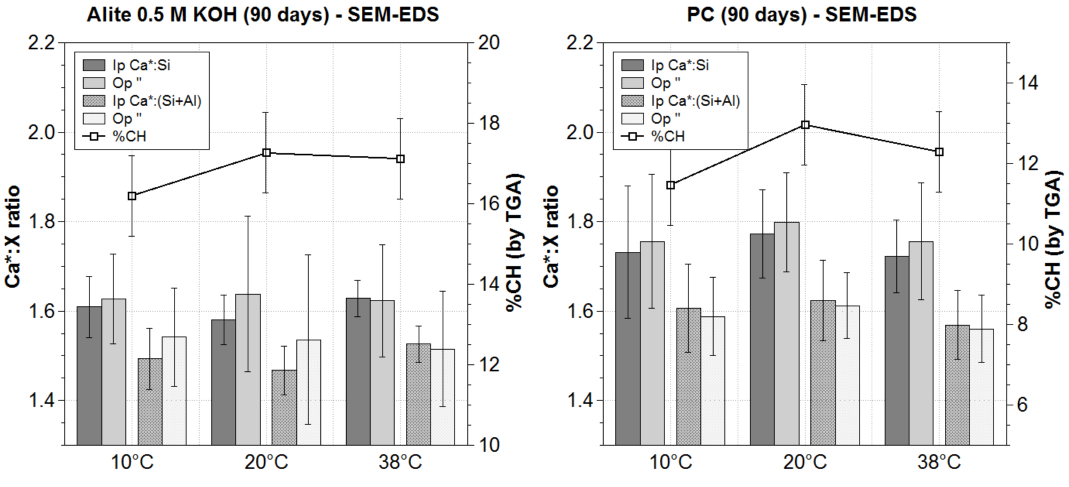

(a)

(b)

Figure 5.5: Ca*:Si and Ca*:(Si+Al) of pastes (matured 90 days with solution:binder = 0.4) of (a) alite (0.5 M KOH) hydrated at 10, 20 and 38°C and (b) PC hydrated at the same temperatures.

Influence of alkali on alite hydrated at 20°C

Figure 5.6 shows both SEM and TEM images for the samples, with Ip and Op in each image. Three samples containing 0 M KOH (Figures 5.6 (a), (b)), 0.1 M KOH (Figures 5.6 (c), (d)) and 0.5 M KOH (Figures 5.6 (e), (f)) show slightly different Op regions, however with no possible assessment of the effect of alkali on the space-filling ability of the fibrils. The case of alite with 0.5 M KOH (Figures 5.6 (e), (f)) for example shows that the fibrils observed by TEM do not fill the entire space. This is reflected in the SEM image where the regions between alite grains or between CH and alite grains appear darker. For any given sample, the observations by SEM correspond well to those in TEM in terms of apparent porosity observed in the SEM and the space-filling ability of fibrils observed in the TEM.

The composition of C–S–H (Figure 5.7) seems to be slightly affected by the presence of alkali with values of Ca:Si ≈ 1.50 for pure alite and ≈ 1.60 in presence of 0.1 and 0.5 M KOH. Here the final amount of CH was ≈ 19% in absence of alkali compared to about 17% for alite with alkali. In the case where more CH formed, the Ca:Si was lower. However the differences here are barely significant.

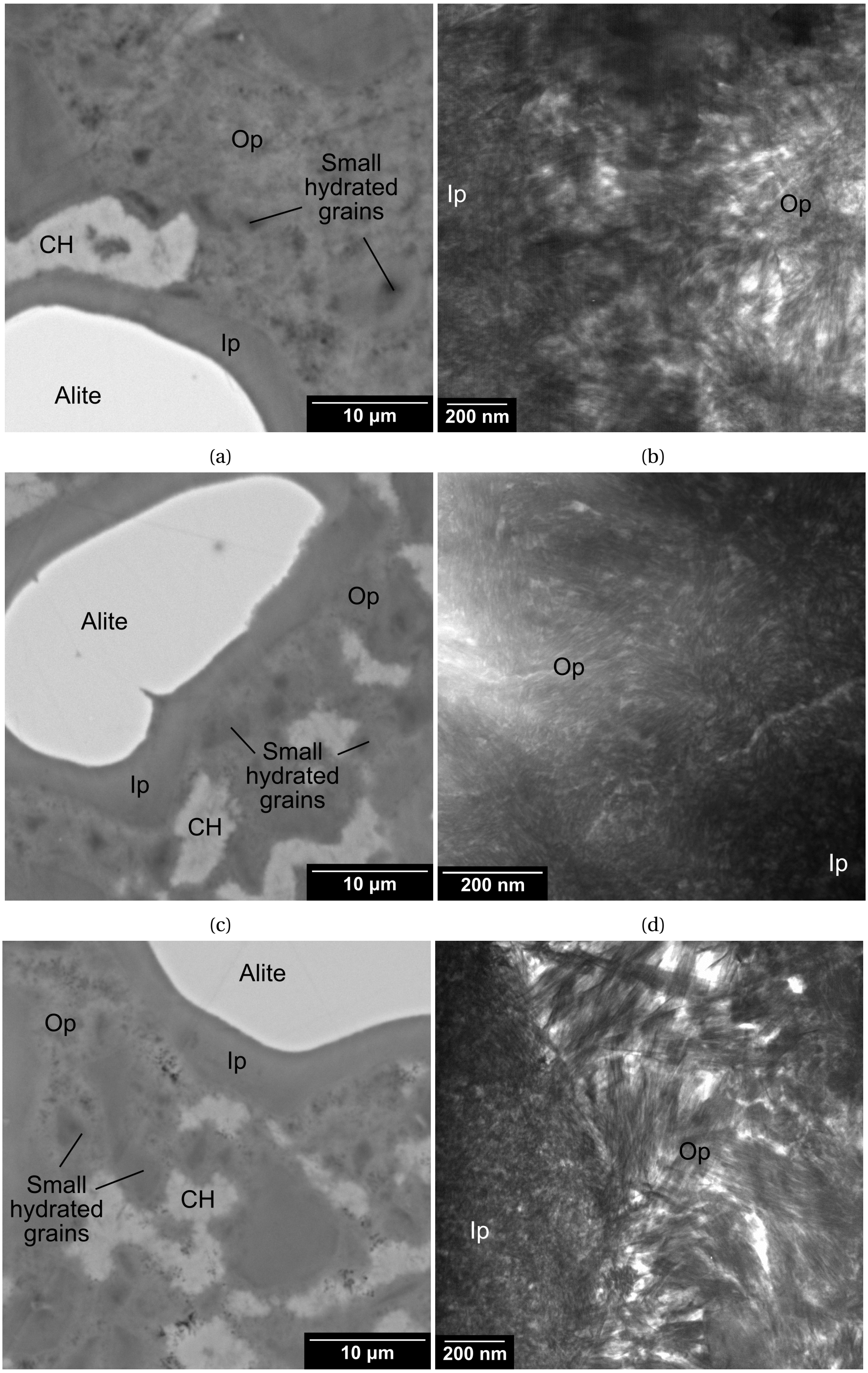

(a) (b)

(c) (d)

(e) (f)

Figure 5.6: SEM images of alite with (a) 0 M KOH. (c) 0.1 M KOH. (e) 0.5 M KOH. TEM images of the same sample with (b) 0 M KOH. (d) 0.1 M KOH. (f) 0.5 M KOH.

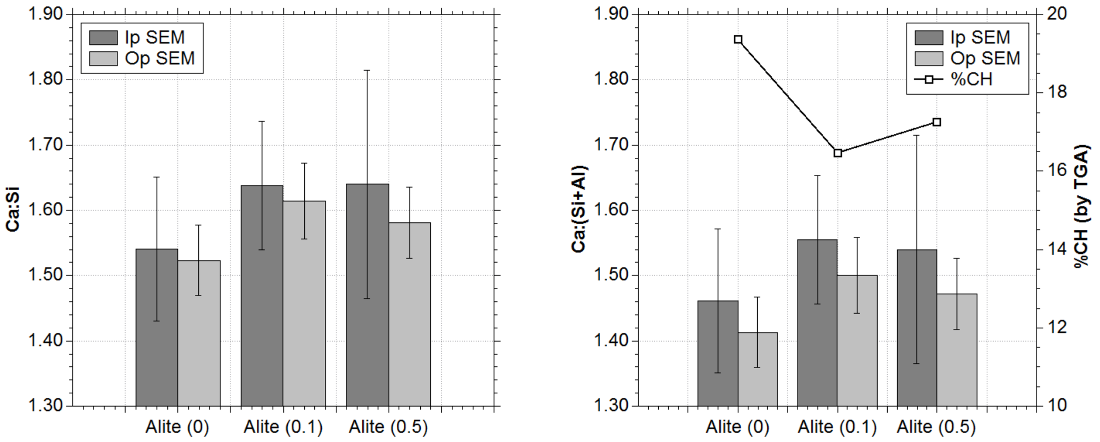

(a) (b)

Figure 5.7: (a) Ca:Si ratio of the Ip and Op C–S–H in alite with 0, 0.1 and 0.5 M KOH. (b) Ca:(Si+Al) ratio of the same samples.

Alumina content in C–A–S–H for alite and PC reference systems

The Al:Si ratio in the C–S–H (or C–A–S–H) phase was determined from the EDS points and taken as the mean of the distribution of points (Figure 5.8). It was considered a normal distribution and the error bars show the variability in results expressed as ± σ (standard deviation).

The alite systems show that the Al:Si ratio is lower in the Op than the Ip while the opposite occurs in the cement, the Ip has a lower Al:Si ratio than the Op. The only source of alumina for alite systems being the alite itself, alumina may more easily enter C–S–H in the inner product regions.

For alite (Figure 5.8 (a)), the Al:Si in the Ip is ≈ 0.07-0.08 and ≈ 0.05 in the Op. Only the sample hydrated with 0.5 M KOH and at 38°C has similar Al:Si in both the Ip and Op. Overall the ratio is constant in pure alite systems. Knowing that the total Al:Si in the alite preparations was ≈ 0.05, the results are consistent with only slightly higher values in the Ip.

Figure 5.8 (b) shows results for alumina in the PC samples which hydrated at the three temperatures. Here the alumina in Op C–S–H is greater in the Op in all samples. The PC series shows Al:Si of ≈ 0.10-0.11 in the Ip and ≈ 0.14-0.15 in the Op. The increased alumina content in the Op C–S–H is likely to be linked to the aluminate phases present in the raw clinker and the presence of aluminate hydrates (AFt, AFm) finely intermixed in the Op. Also, the higher Al:Si in the Op could be linked to the initial increase in aluminium concentration available in solution during the massive growth of Op C–S–H at early age. As it will be shown in Section 5.3, the alumina in C–S–H seems to be correlated to all available sources of alumina as seen in matured systems.

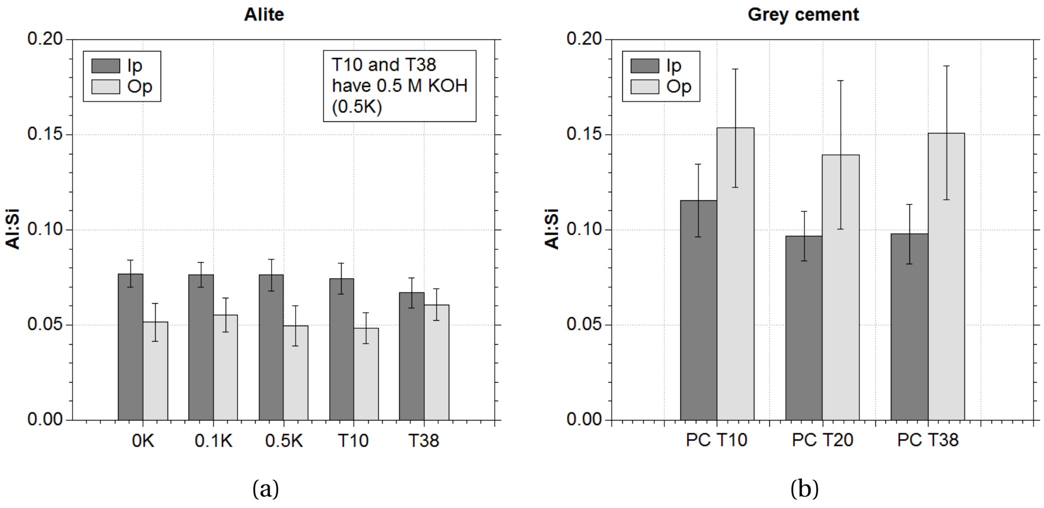

(a) (b)

Figure 5.8: Al:Si of pastes (matured 90 days with solution:binder = 0.4) of (a) alite (0, 0.1, 0.5 M KOH) hydrated at 10, 20 and 38°C and (b) PC hydrated at the same temperatures.

Summary on pure alite and PC pastes

We have compared the microstructure of alite and OPC pastes of solution:binder = 0.4 hydrated for 90 days. The morphology and composition of the C–S–H were characterised by SEM-EDS and STEM.

Alite pastes appear more porous in the SEM and TEM microstructure compared to cement and shows large clusters of CH and no platelet shaped particles. Alite systems have fibrillar Op C–S–H which does not appear to fill space as efficiently as the PC systems and which forms in straight packets. Small grains (less than ≈ 10 μm) show hollow shells. Temperature has no effect on the composition of C–S–H. Alkali may slightly increase the Ca*:Si compared to pure alite without alkali where the Ca:Si is ≈ 1.50 instead of 1.60 in all other alite pastes, however this was not verified in more than one sample per series. Temperature and alkali have no quantifiable effect on porosity in these samples. Alite has C–S–H with a lower Ca*:Si (and Ca*:(Si+Al)) than PC. The roles of both sulphate and aluminate phases may be central in explaining the higher Ca*:Si ratio in cement, the fibrils which fan out in cement and the different growth of CH which forms platelets in its presence in cement samples. Results from recent work [86, 90] on early age samples support this view. In their samples, “flower-like” morphology appear in SE (secondary electron) imaging of hydrated alite or clinker grains in presence of sulphate in solution. It was also showed [90] that the depletion of gypsum was responsible for a change in morphology seen in the SEM.

Cement pastes show fibrillar structures for the Op which fan out compared to alite pastes. The distribution of CH is unlike alite where clusters of CH are smaller and more finely distributed. The microstructure is more complex and appears to have used space more efficiently. The Ca*:Si and Ca*:(Si+Al) is higher than in alite.

In pure alite, the alumina is more incorporated in the Ip of alite. More alumina incorporates the Op of cement. Temperature does not affect the composition of the C–S–H with the exception of the Al:Si in alite which is similar in both the Ip and Op at 38°C. The observed differences seem linked to the mobility and overall availability of aluminate phases.

5.3 Matured systems with SCMs

The following blends are matured samples from previous work in our laboratory [36]. They were left to react up to 3-5 years under water at room temperature (≈ 20°C).

Summary on raw materials and blends

The raw materials are shown in a simplified Ca-Si-Al ternary diagram (Figure 5.9). Here are shown the five blends which are – aside from the references with 100% cement A,B or C, – cement with 40% of slag 01 or slag 08, cement with fly ash 01 or fly ash 02 and cement with 10% silica fume. See complete list of materials and samples in Chapter 3, Section 3.1, p. 25).

The C–A–S–H in series A (white cement binary blends)

Images of the microstructure of binary blends seen by SEM are similar regardless of the cement used and will not all be shown. Microstructural results will be shown for the series A. The composition of the C–A–S–H (C–S–H with alumina) will however later be shown for all three series A, B and C.

Microstructure by SEM. Figures 5.10 and 5.11 show the microstructure of binary blends made with cement A and different SCMs. In all blends the appearance of the Op is qualitatively different from that of the OPC reference shown in Figures 5.10 (a) and (b). This is more evident from the images at higher magnification shown in Figures 5.10 (b), (d) and (f) and Figures 5.11 (b), (d) and (f). While not measured here, it is known that the porosity can be refined by the presence of SCMs even though the total amount of porosity increases. An example can be found e.g. in [91].

Both blends with slag 1 and slag 8 shown in Figures 5.10 (c)- (d) and Figures 5.10 (e)- (f) respectively. They contain numerous angular slag grains which have reacted to a certain extent, forming rims of Ip in a similar manner to that of cement clinker. As in cement clinker after several months, small slag grains may have completely reacted. The Ip in slag grains is darker than in clinker essentially because it is finely intermixed with hydrotalcite-type phases [40]. CH is present in large amounts in the microstructure.

With 10% of added silica fume, (Figure 5.11 (a)) the consumption of CH is obvious when comparing to the cement reference (Figure 5.10 (a)). Some CH is still present as small finely

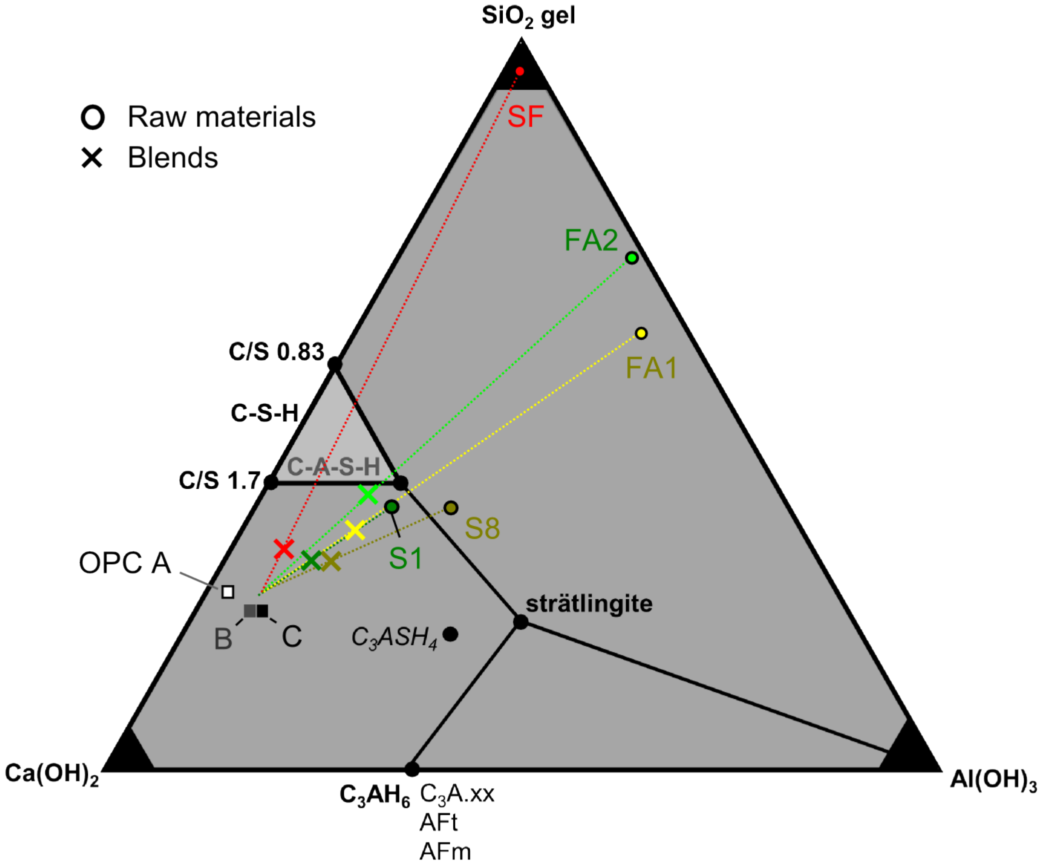

Figure 5.9: Ternary diagram with the matured samples and raw materials. The three OPCs and five SCMs are indicated by circles and the blends are indicated by crosses along the dotted lines corresponding to each binary blend.

dispersed clusters. There are numerous small hydrated grains which have a darker core.

The microstructure of blends with fly ash 1 and 2 shown in Figures 5.11 (c)- (d) and Figures 5.11 (e)- (f) respectively. The microstructure is rather complex due to the fact that fly ashes are often a mixture of several classes of particles. This is already apparent when observing the different grey levels in fly ash grains. The typical round shaped particles are seen throughout the matrix and some have reacted. The large particles seem to have a rim of Ip which is unfortunately too thin to analyse in the SEM. Fly ash particles can appear hollow. There are no significant differences between the fly ash 1 blend and the fly ash 2 blend.

Morphology of C–A–S–H by TEM. Three samples from the series with cement A were studied by TEM (in STEM mode). STEM images are shown in Figures 5.12 and 5.13. An image (in HAADF contrast) of the OPC A sample is shown for reference in Figure 5.12 (a) where both the dense Ip and fibrillar Op C–A–S–H are shown. In the blends, we observe both the fibrillar and foil-like morphology. Fibrils form on the original clinker grains and on the surfaces of SCM particles. Fine foil-like morphologies are observed far from the clinker surfaces, within clinker Ip regions and within slag grains. Coarser foils are observed in the fly ash grains.

Figure 5.12 (b) shows fibrillar Op in the OPC A blended with 40% of slag 8. The fibrils grew from the surface of a clinker grain (as seen by the presence of AFt or AFm relics) while the Op in Figure 5.12 (c) − which formed not at the interface of the clinker grain to the bottom left of the fibrillar region of Figure 5.12 (b) − mostly has a very fine foil-like morphology similar to the morphology of small hydrated grains in OPC. EDS analyses of both regions showed differences in C–A–S–H composition. Figure 5.12 (d) of the same sample shows a small hydrated slag grain in which the compositional gradients were made visible by using the Mg map (Figure 5.12 (e)). We can observe the presence of Mg-rich regions (dark spots and the outer part of the slag grain), hydrotalcite-like phases ("HT" in the image) and fine directional foil-like Ip in the centre of the slag grain. Here the Mg map allows choice of the pure C–A–S–H region from the centre. Fibrillar Op was often observed at the surface of the slag grains.

The blend containing OPC A and 30% of fly ash 2 also shows fibrillar Op at the interface of hydrated clinker grains (Figure 5.13 (a)). Here the approximate location of the surface of the once present anhydrous clinker grain is marked by a dashed line. Close to this interface the Ip appears to have a dense morphology. Towards the inner part of the grain (on the right side) the morphology changes to fine foil-like. Figure 5.13 (b) shows fibrillar Op C–A–S–H which grew outwards from the surface of the fly ash grain, while the Ip of the fly ash has coarser foil-like morphology. Here the composition of fibrils and fine foils differed. The Ip from fly ash grains was very variable, likely due to the variable composition of the fly ash anhydrous material.

Differences in C–A–S–H compositions by STEM. Results from the STEM sometimes appear to overestimate the amount of alumina (this is discussed in Chapter 4). However, the Ca*:Si correspond quite well for the three matured systems.

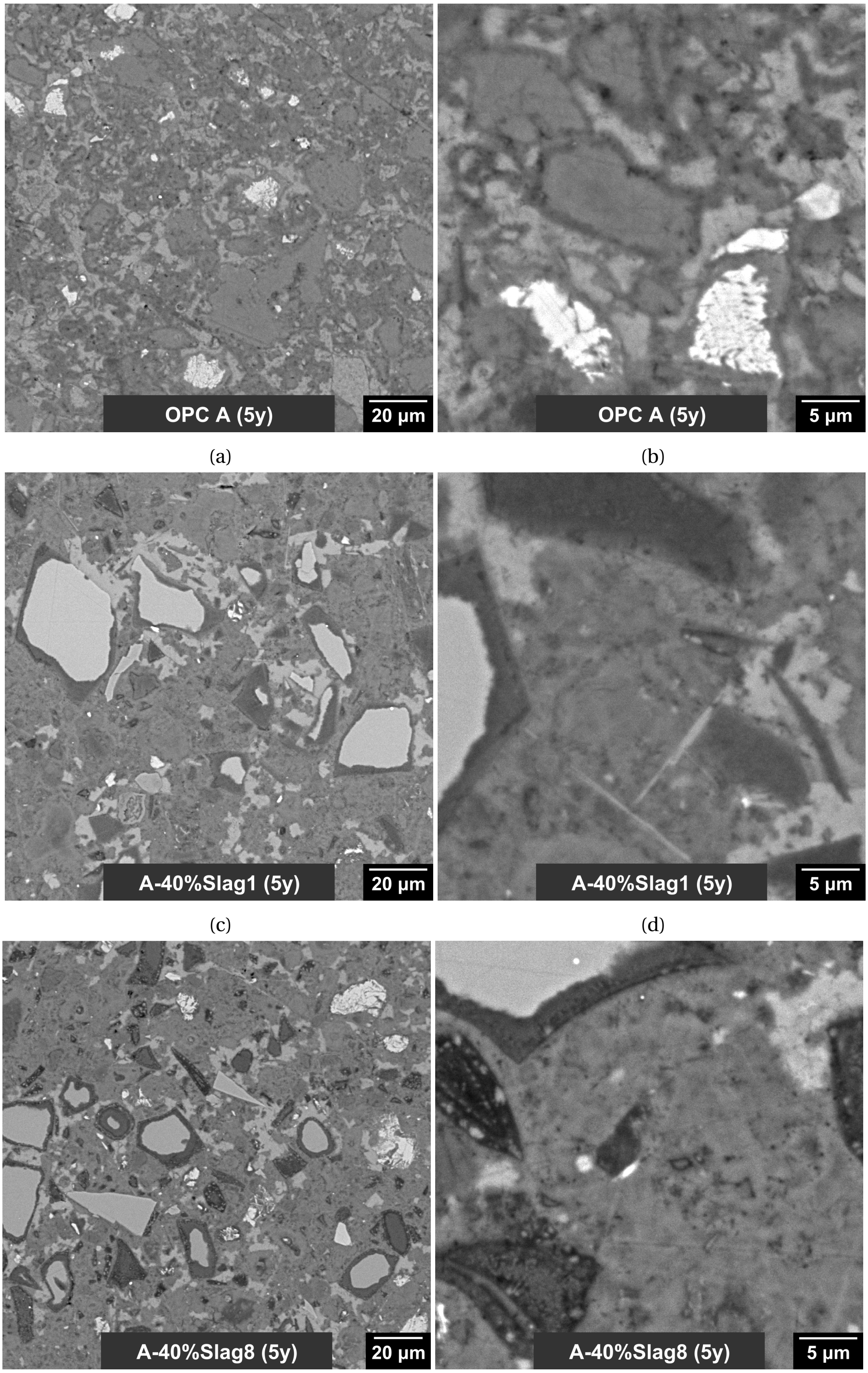

(a) (b)

(c) (d)

(e) (f)

Figure 5.10: SEM images of the series of cement A (A, A-S1, A-S8). Samples from V. Kocaba. (a)- (b) 100% OPC A (5y). (c)- (d) OPC A-40%S1 (5y). (e)- (f) OPC A-40%S8. (5y)

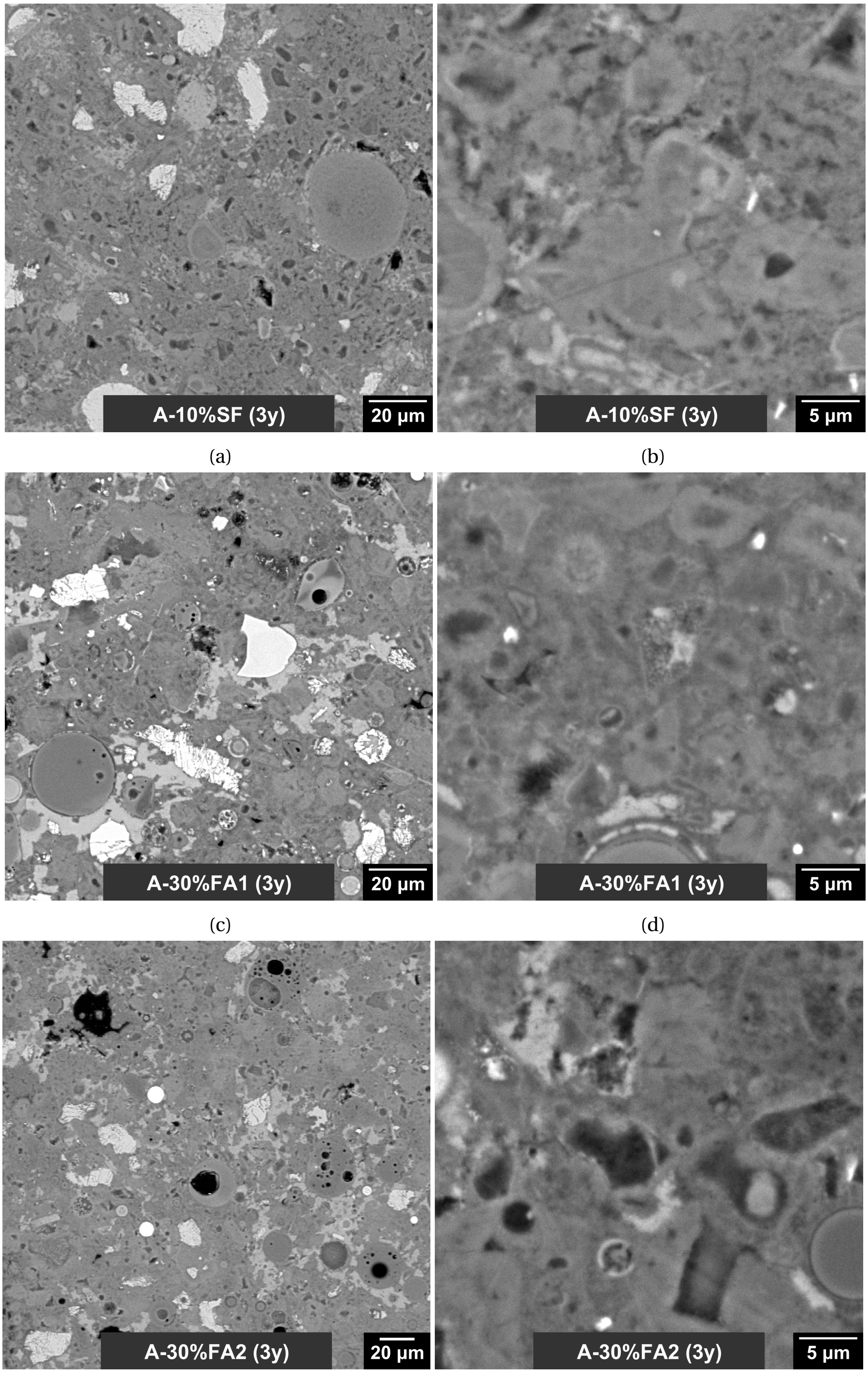

(a) (b) (c) (d) (e) (f)

Figure 5.11: SEM images of the series of cement A (A-SF, A-FA1, A-FA2). Samples from V. Kocaba. (a)- (b) OPC A-10%SF (3y). (c)- (d) OPC A-30%FA1 (3y). (e)- (f) OPC A-30%FA2 (3y).

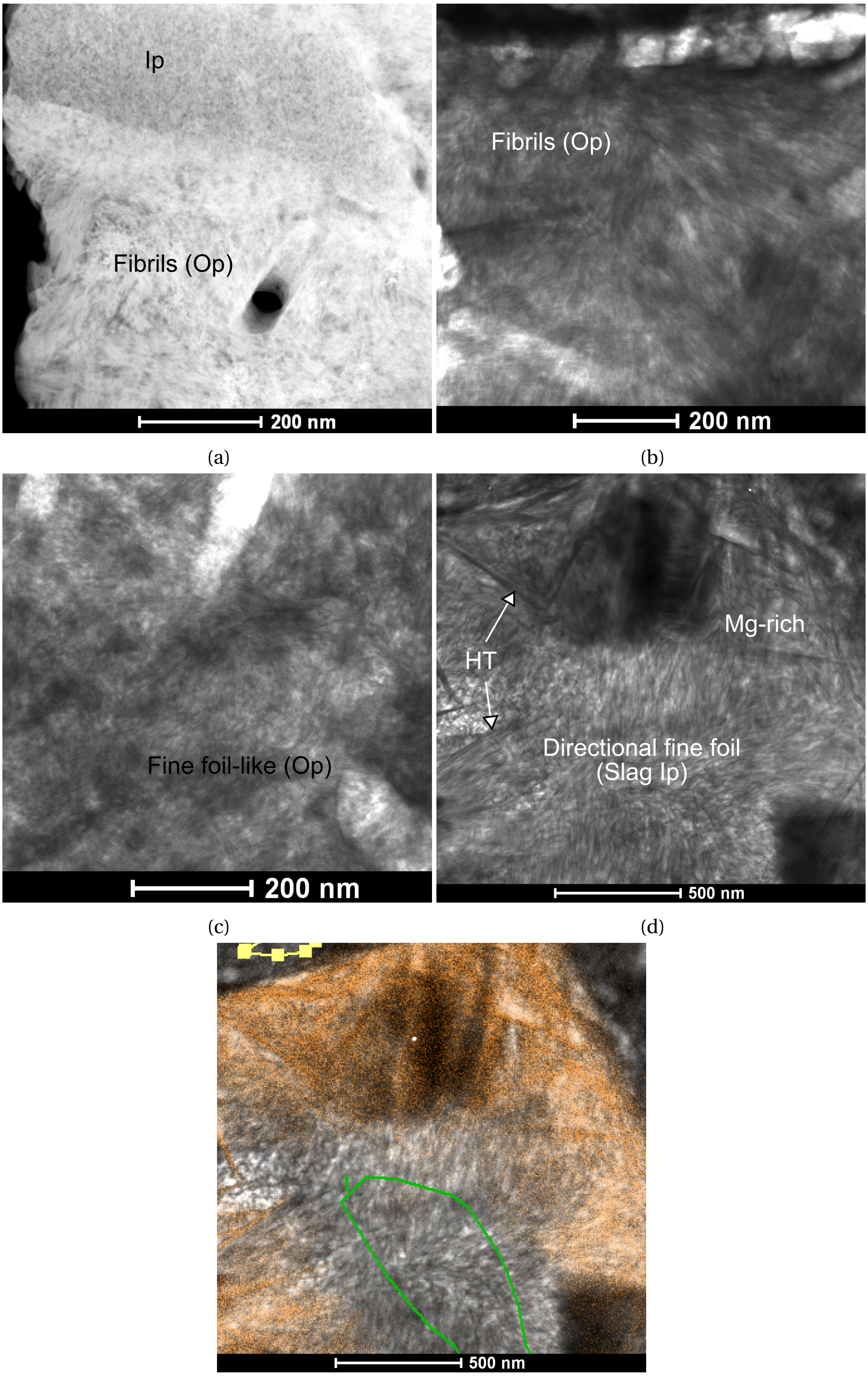

(a) (b)

(c) (d)

(e)

Figure 5.12: STEM images of OPC A and A-S8. (a) OPC A (HAADF). (b) Op C–S–H region of A-S8. (c) Op region containing fine foil-like C–S–H. (d) Ip region of a small hydrated slag grain of A-S8. (e) The Mg EDS map of the small hydrated slag grain. The green line shows the area of pure C–A–S–H.

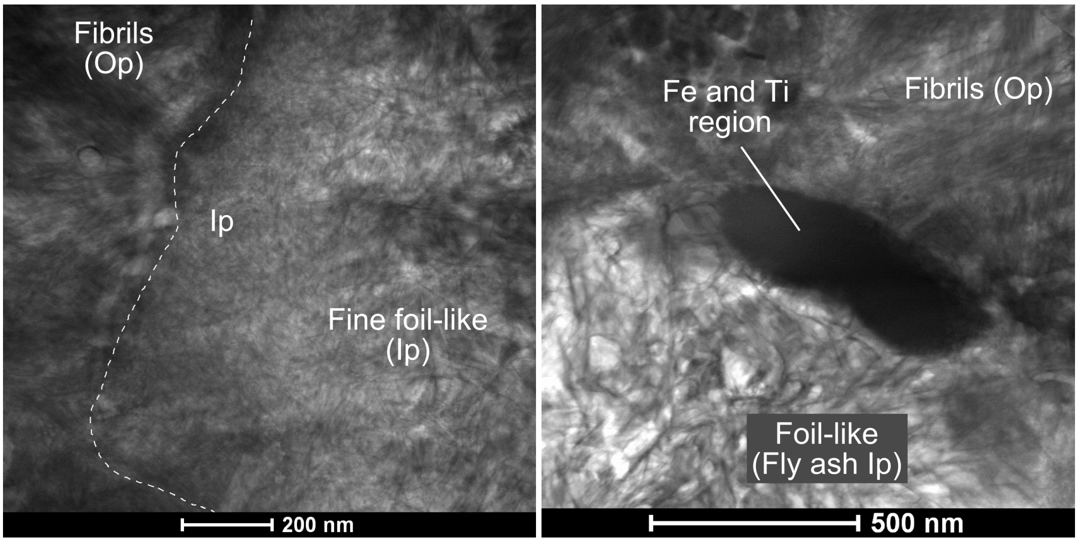

(a) (b)

Figure 5.13: STEM images of A-FA2. (a) Ip/Op interface region (from the hydration of clinker) in the A-FA2 blend. (b) The Ip region of a fly ash grain surrounded by fibrillar Op in the A-FA2 sample.

Given the nature of TEM samples, the statistics are rather poor because only one sample was prepared for each system. An average of 2-10 EDS "points" (areas) per type of C–A–S–H were quantified to estimate the composition. However because care was taken to use only thin regions for analysis, the differences in atomic composition should be reliable.

The composition of the C–A–S–H is tabulated for the three samples studied by STEM-EDS. Figure 5.14 and Figure 5.15 shows the Ca*:Si and Al:Si respectively for the three samples in a bar chart representation. They show that the composition of fibrils is generally of Ca*:Si = 1.50 or higher. The foils have Ca*:Si which range 1.30-1.50. The Al:Si in fibrils reaches a maximum Al:Si of ≈ 0.25-0.30. Only in foil-like regions does the Al:Si reach ≈ 0.40-0.50. The values of Al:Si obtained by STEM-EDS in foil-like regions are sometimes high compared to values by SEM-EDS. Local variations in composition are not excluded and could bias results. All compositions are compatible with a tobermorite structure. In the case of infinite chains where every bridging silicate is substituted by an aluminium, we obtain 1/2 = 0.50.

In OPC A (Table 5.1), the fibrils and Ip such as those seen in Figure 5.12 (a) have Ca*:Si ≈ 1.80-1.85.

The slag blend (Table 5.2) shows that the fibrils and Op fine foils – as seen e.g. in Figure 5.12 (b) and Figure 5.12 (c) respectively – have Ca*:Si ≈ 1.53, significantly lower than in the pure cement. In the Ip of the slag measured free from intermixing with Mg-bearing phases (Figure 5.12 (d)), the Ca*:Si is lower (≈ 1.44) and has slightly more alumina (higher Al:Si).

In the blend with fly ash, the Ca*:Si of the Op measured in the SEM is ≈ 1.40 while the STEM can distinguish two types of Op which have a different composition. Op fibrils like those in Figure 5.12 (a) have a ratio of ≈ 1.52 and fine foil-like Op has Ca*:Si ≈ 1.29. The clinker Ip C–A–S–H has a Ca*:Si ≈ 1.43 wether the morphology is dense or fine foil-like. The fine foils have higher Al:Si. The foil-like Ip from the fly ash also has a low Ca*:Si (≈ 1.35) but with the highest Al:Si.

Table 5.1: Composition of the C–A–S–H in OPC A

OPC A	**Ca*:Si**	**Std. dev.**	**Ca*:(Si+Al)**	**Std. dev.**	**Al:Si**	**Std. dev.**
Ip (SEM)	1.88	0.05	1.73	0.05	0.08	0.01
Ip (TEM)	1.81	0.19	1.62	0.21	0.12	0.03
Op (SEM)	1.85	0.07	1.66	0.06	0.11	0.01
Op (Fibrils)	1.84	0.13	1.66	0.13	0.11	0.02

Table 5.2: Composition of the C–A–S–H in A-S8

A-S8	**Ca*:Si**	**Std. dev.**	**Ca*:(Si+Al)**	**Std. dev.**	**Al:Si**	**Std. dev.**
Ip (SEM)	1.55	0.05	1.30	0.04	0.19	0.01
Ip (TEM)	1.46	0.02	1.17	0.02	0.25	0.01
Ip Slag (TEM)	1.44	0.02	1.13	0.03	0.28	0.01
Op (SEM)	1.57	0.04	1.33	0.03	0.19	0.01
Op (Fine foil)	1.54	0.04	1.23	0.07	0.25	0.04
Op (Fibrils)	1.52	0.05	1.21	0.04	0.25	0.02

Table 5.3: Composition of the C–A–S–H in A-FA2

A-FA2	Ca*:Si	Std. dev.	Ca*:(Si+Al)	Std. dev.	Al:Si	Std. dev.
Ip (SEM)	1.44	0.03	1.25	0.04	0.15	0.01
Ip (TEM)	1.43	0.10	1.09	0.04	0.31	0.05
Ip FA (TEM)	1.35	0.06	0.89	0.04	0.52	0.01
Op (SEM)	1.40	0.06	1.22	0.05	0.16	0.02
Op (Fine foil)	1.29	0.06	0.92	0.08	0.40	0.07
Op (Fibrils)	1.52	0.09	1.20	0.08	0.27	0.07

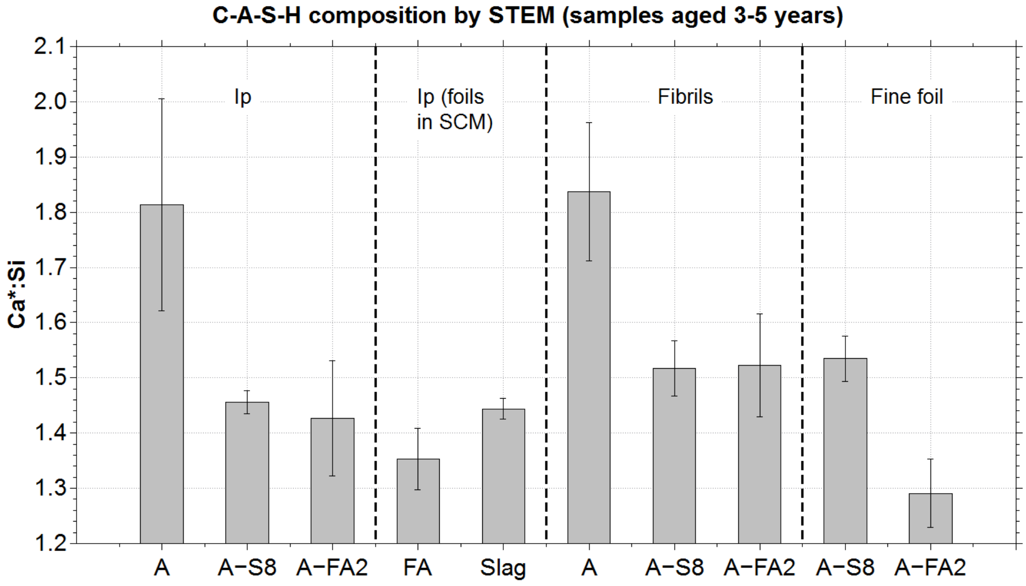

Figure 5.14: TEM data from three blends (hydrated 3-5 years), as bar charts. The Ca*:Si ratio is shown.

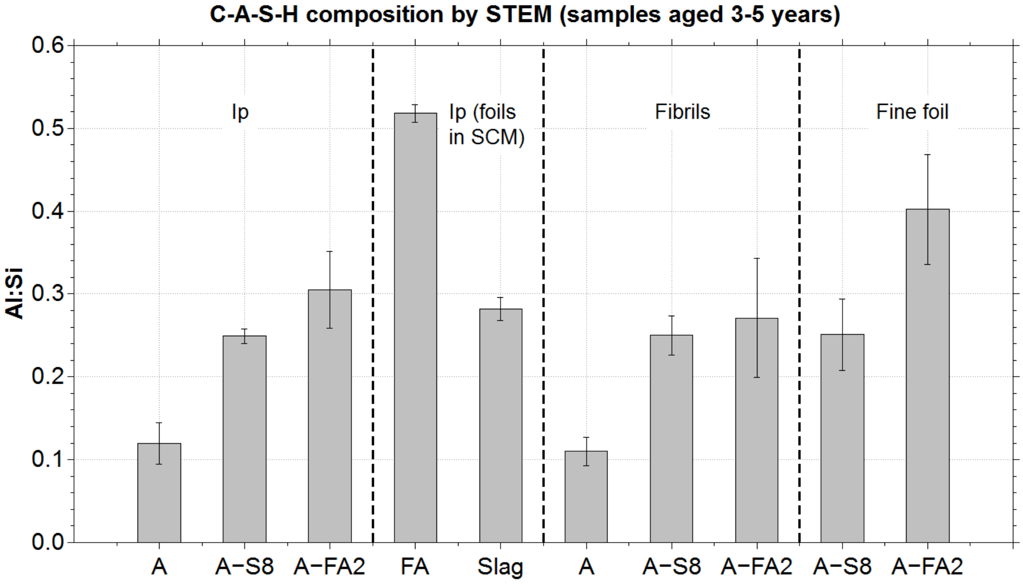

Figure 5.15: TEM data from three blends (hydrated 3-5 years), as bar charts. The Al:Si ratio is shown.

Portlandite content in matured systems measured by TGA

The amount of CH present at later age in these paste samples is shown in Figure 5.16. The amount of CH in pure cement seems related to the amount of alite present. OPC B, with lower alite content has about 11% compared to ≈ 15% and ≈ 18% in OPC C and OPC A respectively, both of which have high alite content.

Because SCMs can enhance the nucleation and growth of initial C–A–S–H (the “filler effect”) and then react to form additional C–S–H phases (with or without consuming CH), the CH content is normalised to the anhydrous cement content (the fraction of cement in the raw mix before hydration) to better compare systems with different levels of substitution. Such results are also given in Figure 5.16.

Here we see that the slag systems – the slag being a mostly hydraulic SCM – produce similar or higher normalised amounts of CH compared to pure OPC.

Fly ash samples are pozzolanic compared to the slags because the normalised CH content is lower than that of OPC. No significant differences in final amount of CH exist between both siliceous fly ashes even though they do differ in composition (FA2 is richer in silica while FA1 has more calcium).

The impact of the materials here is therefore a strong function of the amount of reactive silica and alumina but not only. The fineness of the materials also likely has a crucial impact. The silica fume causes a high consumption of CH for only 10% replacement. This is in part because it has a mean particle diameter of typically less than a μm and can significantly react at earlier ages than the SCM particles in slag and fly ash blends (see Figure 6.1 in Chapter 6, p. 94).

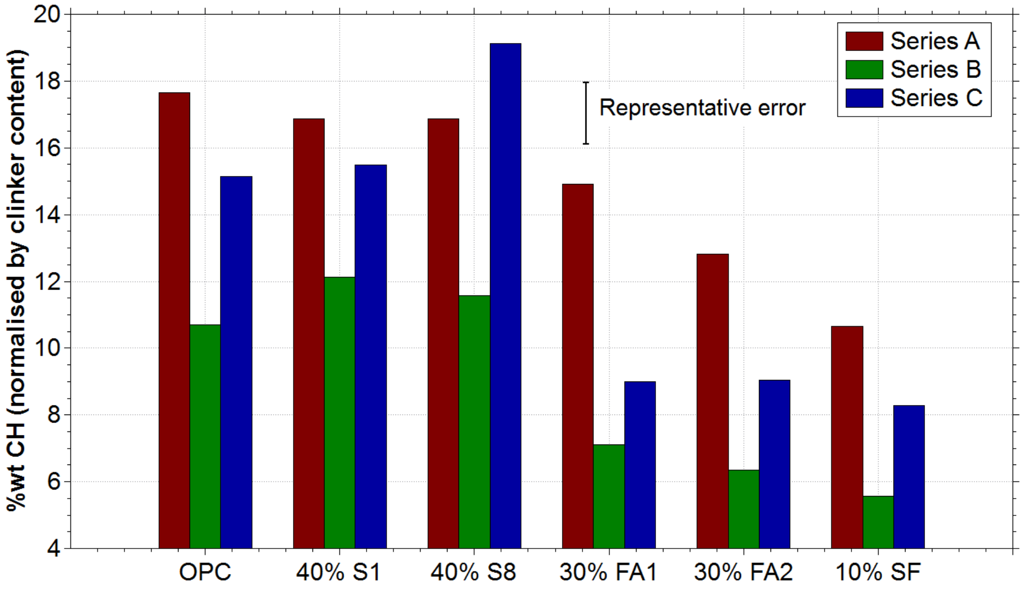

Figure 5.16: Normalised CH content in matured systems, from TGA data. The three series are shown.

Composition of the C–A–S–H in matured systems by SEM-EDS

Previous results (Figure 5.17) showed that in slag blends of water:binder = 0.4, the composition of C–A–S–H is stable from 28 days onwards. Ca:(Si+Al) drops from ≈ 2.00 to ≈ 1.50 in presence of 40% slag. The C–A–S–H composition there was estimated using the average of the cloud of points as it was done before and therefore overestimates the “calcium silicate” ratio.

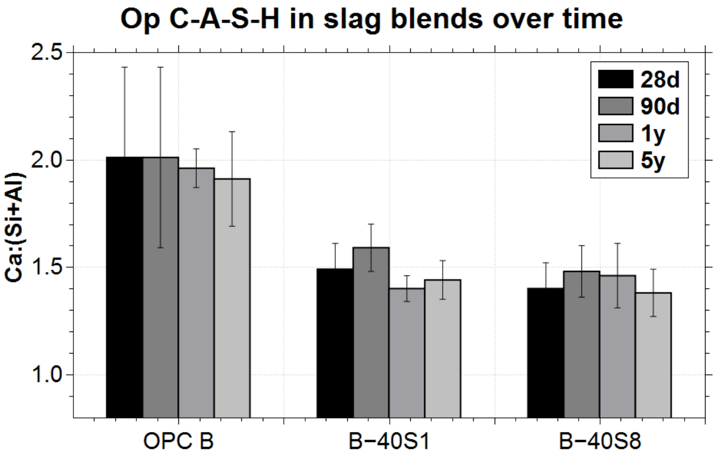

Figure 5.17: C–A–S–H composition in slag blends over time. (from V. Kocaba)

To estimate the composition on newly analysed samples, the bias for the “intermixed” C–A–S–H composition was considered towards Ca, as shown by scatter plots of the Ip C–A–S–H of samples OPC A, A-S8 and A-FA2 in Figure 5.18 (a). Figure 5.18 (b) shows that intermixing occurs with monosulfoaluminate AFm (Ms) for both blends, and is consistent with XRD patterns (Figure 5.22). The methodology from the previous chapter could therefore be applied.

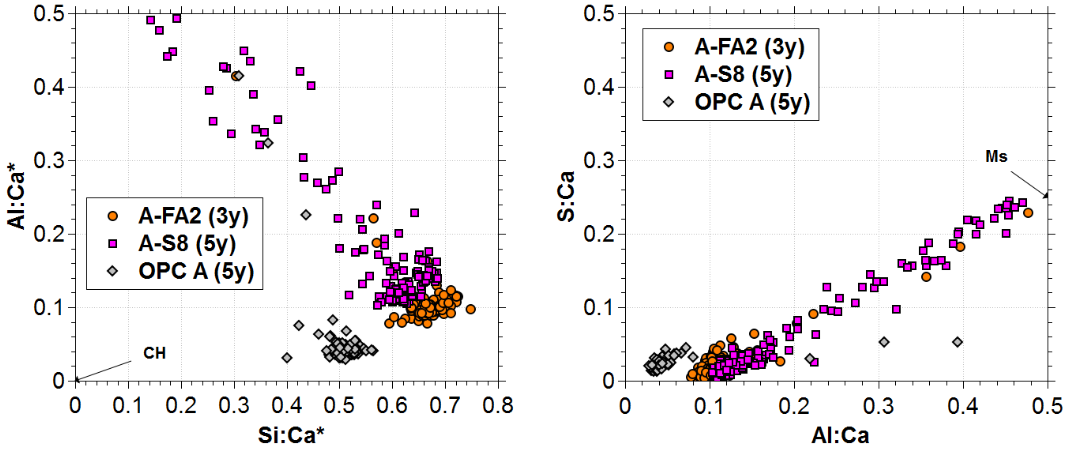

(a) (b)

Figure 5.18: SEM-EDS scatter plots from 3 samples of series A. (a) Si:Ca* vs. Al:Ca*. (b) Al:Ca vs. S:Ca (uncorrected Ca).

The SEM-EDS points were taken in the logarithmic space as illustrated in the three examples in Figure 5.19. The data was fitted by a simple normal distribution (μ is the mean and σ is the standard deviation) from which the value of "pure C–A–S–H" was obtained by taking $\mu - 2\sigma$ in the log-normal space. Atomic ratios were taken from this value of the different "calcium silicate" ratios.

Results from optimised SEM-EDS point analyses are shown in Figures 5.20, 5.21, 5.23 and 5.25 for the three series: series A (red), series B (green) and series C (blue).

The inner product (Ip) and outer product (Op) of the C–A–S–H were measured by SEM-EDS point analyses. In Figures 5.20 and 5.21, the Ca*:Si and Ca*:(Si+Al) ratios were determined from the lower values of their distribution of values (see Chapter 4) and are shown as a function of relative consumption of CH compared to OPC (as measured by TGA), with the errors on atomic ratios as standard deviation of the distribution of points and about 1% error on TGA measurements.

Here we can observe that for both the Ip and Op C–A–S–H, Figures 5.20 (a) and (b), there appears to be some overall trend where the decrease in Ca*:Si is mostly correlated to the relative consumption of CH. Such trend is not as clear for Ca*:(Si+Al). Values of Ca*:Si in Figures 5.20 (a) and (b) range from a highest of ≈ 1.60 down to ≈ 1.30 compared to ≈ 1.70-1.90 in pure OPC. This is occurring similarly in the Ip and Op. When the composition of C–A–S–H includes alumina as in Figures 5.21 (a) and (b), given as Ca*:(Si+Al), the upper limit value is

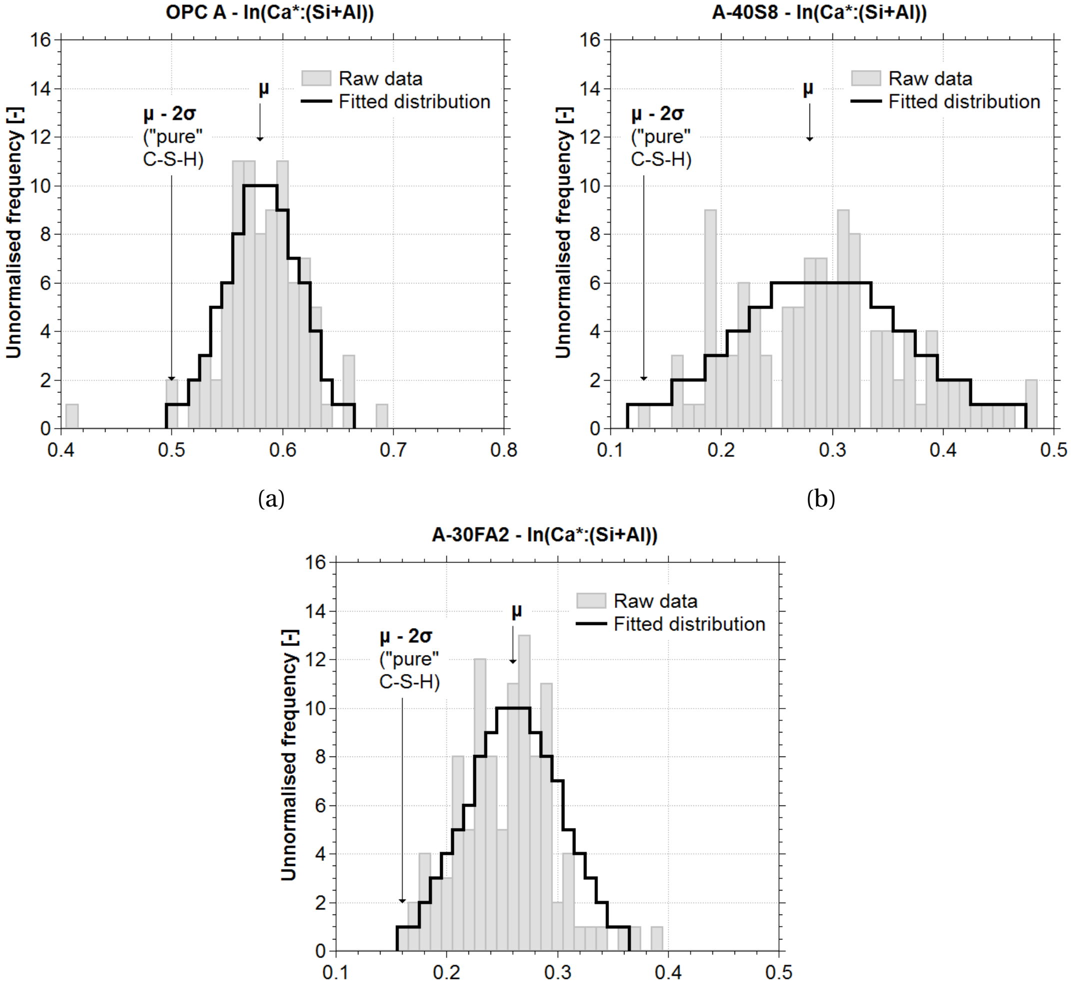

(a) (b) (c)

Figure 5.19: Histograms of SEM-EDS data from 3 samples of series A. The data is Ca*:(Si+Al). (a) OPC A 5y. (b) A-S8 5y (c) A-FA2 3y.

≈ 1.40 and the lowest ≈ 1.0-1.1. Here the values for OPC are ≈ 1.65-1.70. The exception of ≈ 1.40 in the Op C–A–S–H of OPC C could not be explained. Overall, the persistence of CH does not prevent the C–A–S–H from reaching overall final values for Ca*:Si and Ca*:(Si+Al) lower than in OPC.

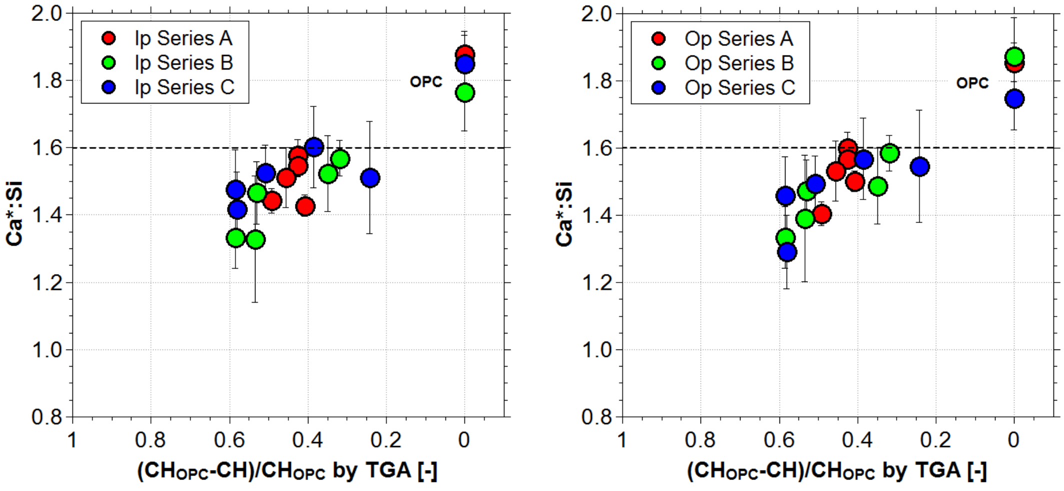

(a) (b)

Figure 5.20: Composition of C–A–S–H (Ca*:Si ratio) in the three series measured by SEM-EDS. The values are taken from the lower edge of the distribution and shown as a function of relative decrease in amount CH compared to OPC. The error bars are the standard deviation of the distribution of the data. (a) Ca:Si corrected for sulphate (Ca*:Si) in the Ip C–A–S–H. (b) Ca*:Si in the Op.

XRD patterns in all matured paste samples (see Figure 5.22 for series A) did not show the presence of any crystalline CASH phases such as strätlingite. The C–A–S–H is therefore considered to contain the whole amount of alumina measured by SEM-EDS. Figure 5.23 shows the Al:Si in the Ip C–A–S–H in Figure 5.23 (a) and the Op C–A–S–H in Figure 5.23 (b) as a function of the total Al:Si in the anhydrous mix (from XRF data). The black dashed line indicates the 1:1 line. There seems to be a good correlation between the total alumina and the amount incorporated in the final C–A–S–H product. The scatter is more important for the series B (especially in the Ip C–A–S–H) which cement B contained the most aluminate phase in the clinker. In both the Ip and Op, the amount of alumina in the C–A–S–H increases more or less linearly with the Al:Si of the cement and SCM combined, however below the 1:1 line which represents complete incorporation of alumina into C–A–S–H. Figure 5.24 shows the XRD counts for Ettringite and monosulfoaluminate which appear to increase as a function of total Al:Si. This could indicate that the amount of alumina in solution could directly impact the amount in C–A–S–H, irrespective of whether the aluminium comes from the clinker or the SCM. Also, it appears that the alumina from solution distributes itself both between C–A–S–H and other phases. This could be related to Fig. 7 in [92], where the amount of alumina in solution directly influences the amount in C–A–S–H, whether it is synthetic or in pastes with fly ash or Portlandite-free blends. However, such systems were not adjusted for sulphate, so it is possible that the aluminium

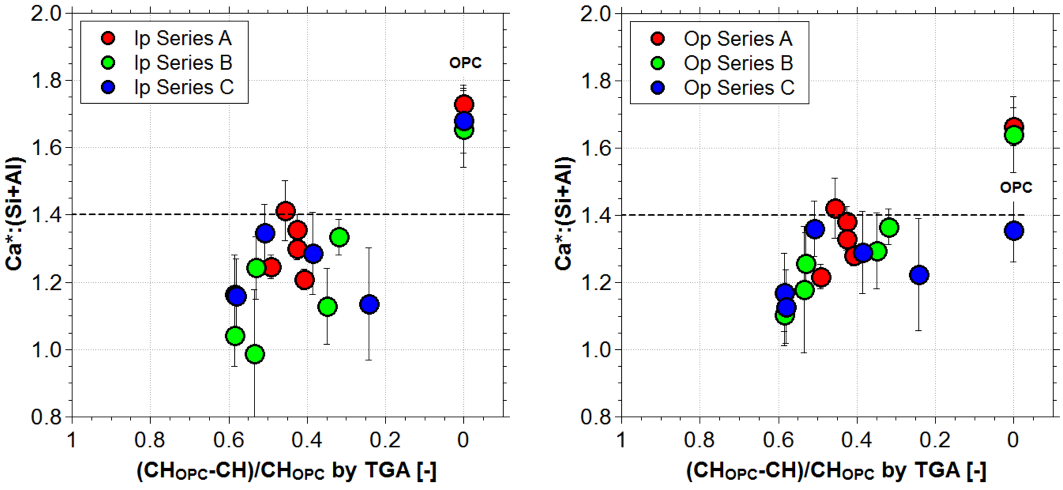

(a)

(b)

Figure 5.21: Composition of C–A–S–H (Ca*:(Si+Al) ratios) in the three series measured by SEM-EDS. The values are taken from the lower edge of the distribution and shown as a function of relative decrease in amount of CH compared to OPC. The error bars are the standard deviation of the distribution of the data. (a) Ca*:(Si+Al) in the Ip. (b) Ca*:(Si+Al) in the Op.

incorporation is in fact mostly from the SCMs.

When the Al:Si is plotted against the Ca*:Si (Figure 5.25), we observe a range of possible C–A–S–H compositions for both the Ip (Figure 5.25 (a)) and the Op (Figure 5.25 (a)) which span Ca*:Si ≈ 1.30-1.90 and Al:Si ≈ 0.05-0.30 for cements blended with 40% of slag, 30% of fly ash and 10% of silica fume cured under water with water:binder = 0.4 at room temperature. Results here suggest – as shown by Richardson [14] – that the C–A–S–H with lower Ca*:Si values are able to accommodate more alumina in the C–A–S–H. The highest Al:Si value was ≈ 0.28 for Ca*:Si ≈ 1.32. This is somewhat in accordance with a series of C–A–S–H samples (from E. L'Hôpital) where the maximum Al:Si in C–A–S–H made in alkaline solutions was ≈ 0.25 for a Ca:Si ≈ 1.00.

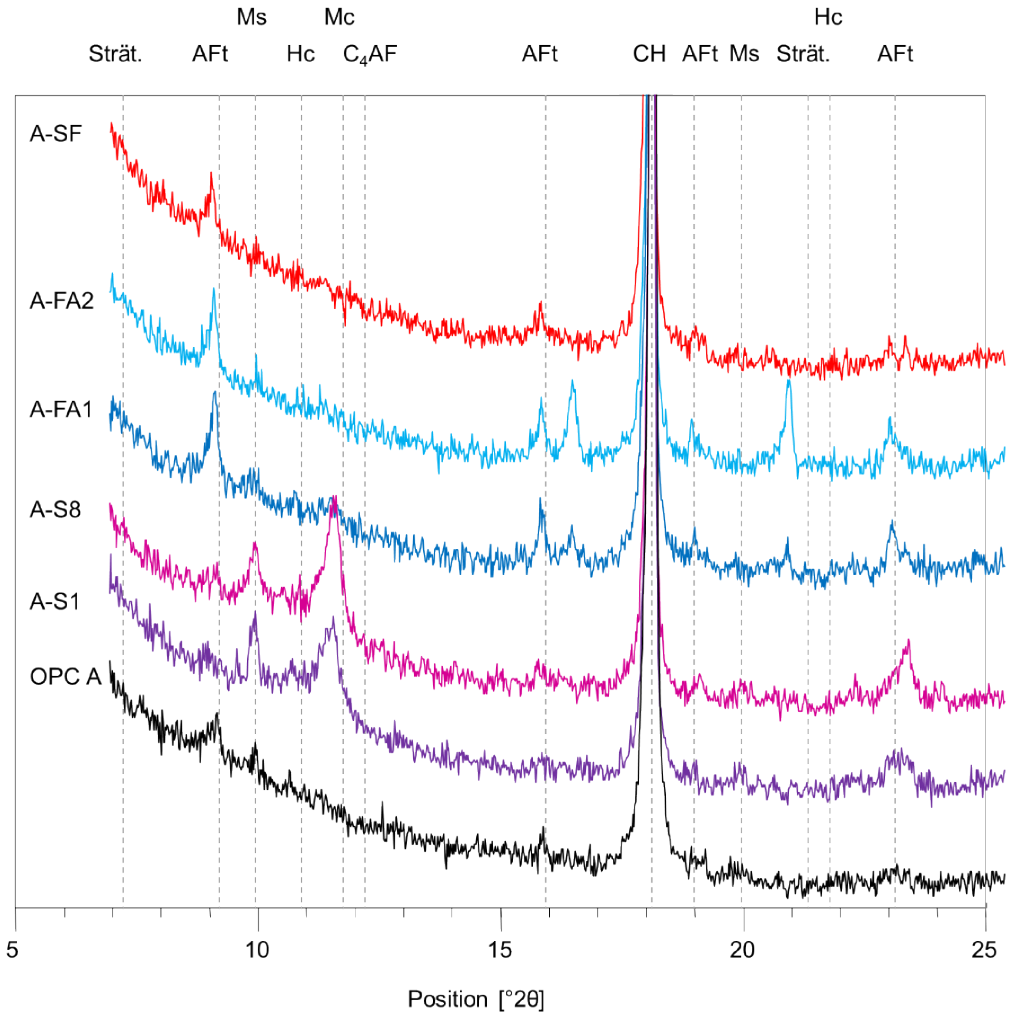

Figure 5.22: XRD patterns for series A.

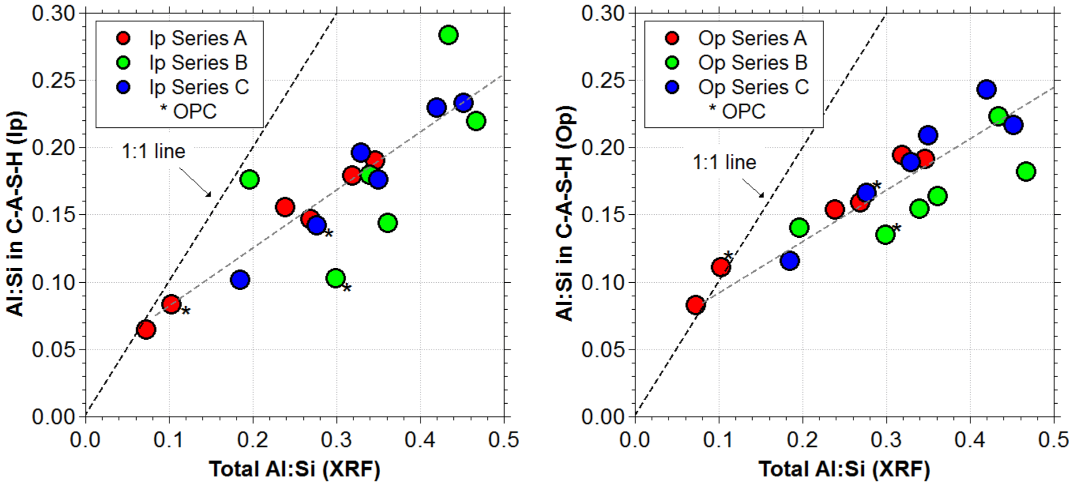

(a) (b)

Figure 5.23: Composition of C–A–S–H in the three series measured by SEM-EDS. Al:Si is shown as a function of the total amount of Al:Si in the anhydrous phases (cement and SCM). (a) Al:Si in the Ip C–A–S–H. (b) Al:Si in the Op.

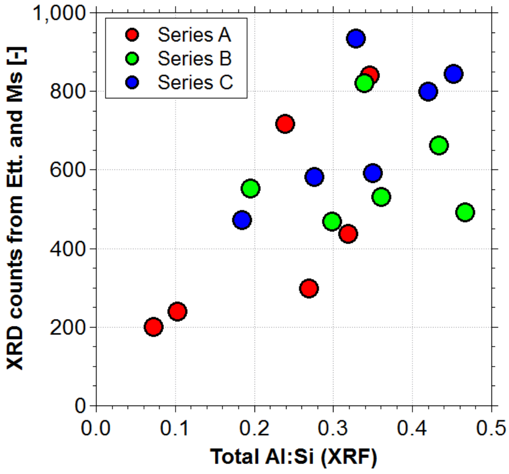

Figure 5.24: XRD total counts from Ettringite and monosulfoaluminate peaks as a function of total Al:Si.

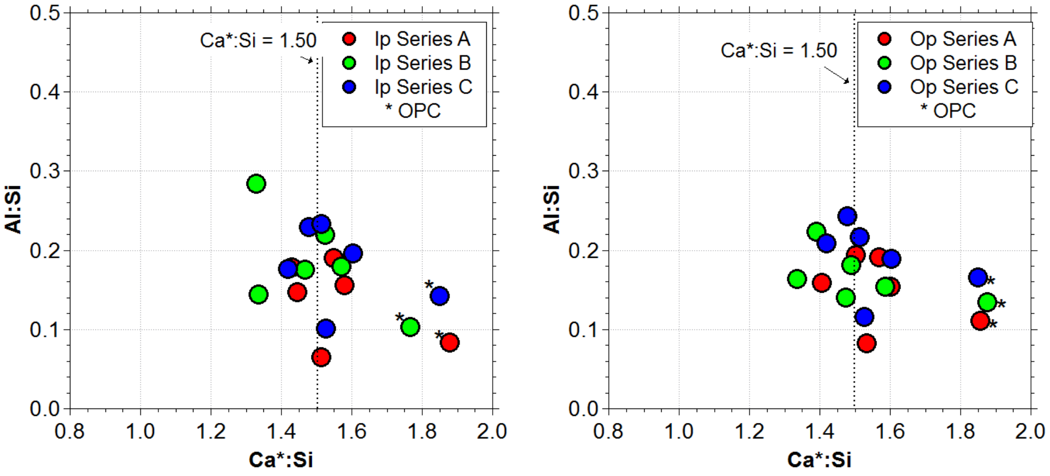

(a)

(b)

Figure 5.25: Composition of C–A–S–H in the three series measured by SEM-EDS. Al:Si is shown as a function of the Ca*:Si in C–A–S–H. (a) Al:Si in the Ip C–A–S–H. (b) Al:Si in the Op.

Summary on matured systems

Matured paste samples from a previous project prepared with three cements blended with five supplementary cementitious materials (SCMs) were studied after being left to mature for 3-5 years, cured under water and with an initial water:binder ratio of 0.4, in the laboratory in sealed containers and at room temperature.

The SCMs used were two slags at a 40% substitution level of the cement, two fly ashes at 30% substitution level of the cement and a silica fume at 10% substitution level of the cements. All five materials had different calcium, silica and alumina contents.

Based on SEM images shown for the series A (and for the other series as well), the microstructure is impacted by the presence of the SCMs. The Op appeared more homogeneous compared to the cement reference with smaller pores visible in the SEM images.

Two binary blends of slag or fly ash with cement A were examined by TEM. Two morphologies were observed: the fibrillar C–A–S–H and the foil-like C–A–S–H. There is a difference between the fibrillar-like morphology typical of OPC pastes hydrated in normal conditions and fine or coarse foil-like morphologies observed in blends. The fibrillar morphology persisted after years of hydration and was systematically present either at the original surface of the clinker grain or at the surface of SCM particles. The foil-like morphology could be seen in these systems either further within inner-product regions of clinker grains or inside reacted grains of SCM. Foil-like morphology occurring in regions other than clinker Ip regions showed equivalent or lower Ca*:Si and increased Al:Si when compared to fibrillar Op regions. It is unclear how much alumina can incorporate in the C–A–S–H without other phases precipitating (see Appendix, p. 131). Foil-like morphology is likely the C–A–S–H which formed after the initial growth of fibrillar C–A–S–H.

The correlation between SEM and TEM results were satisfactory for Ca*:Si (when alumina was not included in the results). It was observed that fibrillar C–A–S–H has a composition of Ca*:Si ≈ 1.50 or greater. Foil-like C–A–S–H here had Ca*:Si ≈ 1.30-1.50.

The relative consumption of Portlandite appeared quite similar overall for each SCM irrespective of the type of cement used. The impact on final amount of CH does depend on the amount of reactive calcium, silica, and alumina. It also depends on the nature of the SCM, its fineness, amorphous content and other factors.

For all three series, SEM-EDS results showed that the C–A–S–H composition is changed. It appeared that the Ca*:Si decreases with the relative consumption of CH (compared to OPC). The correlation was not so clear for Ca*:(Si+Al). Despite the persistence of CH, the Ca*:Si showed values ≈ 1.30-1.60 and Ca*:(Si+Al) ≈ 1.00-1.40, all significantly below values for pure cement. The Al:Si in C–A–S–H was seen to increase linearly with the amount of Al:Si present in the anhydrous mix and could reach almost 0.30 in C–A–S–H which had the lowest observed Ca*:Si of ≈ 1.30.

6 The C–S–H in pastes with increasing additions of silica fume

6.1 Introduction

Silica fume is added in rather small amounts in practice because it has a very strong impact on binders. Particles of silica fume have very small sizes, with 95% of the particles smaller than a μm. They are highly amorphous and mainly composed of SiO_2. Small additions of silica fume are beneficial to concrete for several reasons. They increase cohesion and reduce bleeding, enhance mechanical properties and improve durability because of reduced permeability [93].

The hydration of OPC at early age is enhanced even before it reacts chemically as it provides high surface area. This enhancement at early age is the “filler effect”. Silica fume − like other pozzolanic SCMs − can react with CH to form C–S–H. Recent results from A. Muller [88] are shown in Figure 6.1 and show that silica fume reacts from the first day (in a white cement-10% silica fume blend, water:binder = 0.4).

The final Ca:Si of the C–S–H in blends with silica is lower compared to that in OPC. Groves and coworkers showed that the Ca:Si could reach values down to ≈ 0.80 [94]. They also showed by TEM that the morphology of C–S–H is changed in presence of silica fume in blends hydrated at 40°C [94]. The C–S–H generally has a foil-like morphology which differs from the fibrillar morphology in OPC [95]. The silicate chains of C–S–H condense to form longer chains than non-blended systems. Thermodynamic calculations have also shown that both the phase assemblage and pore solution are also affected by the addition of silica fume (see Fig. 5 in [5]), particularly at additions of ≈ 40-50%.

In this chapter, silica fume was added in large amounts to alite (model cement) and PC pastes to change the composition of the C–S–H formed and to better understand the relation between its morphology and composition, and how the pozzolanic reaction (consumption of CH) changes its composition in realistic systems, i.e. in pastes of low solution:binder ratio.

Four series of samples with solution:binder = 0.4 were cast at 10, 20 and 38°C (cf. p. 26). There was an early age series with cement (PC) and 10, 25 and 45% of silica fume (SF) hydrated

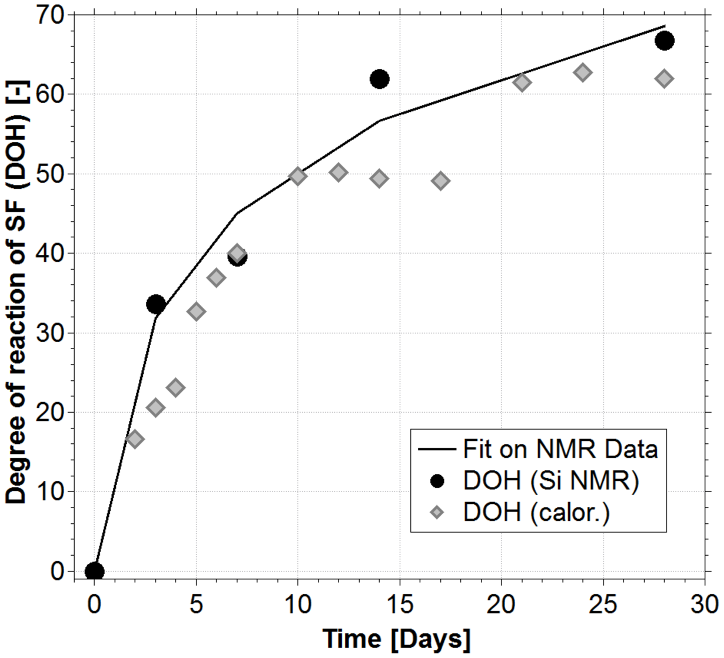

Figure 6.1: Degree of reaction of silica fume – measured with two techniques – in a white cement-10% silica fume blend. Reproduced from [88].

from 1 to 28 days. This is the PC2 series. Three later age series were cast and studied after 90 days of hydration. One of these series (PC(Q) series) was made with PC, quartz and silica fume to maintain the same PC:SF ratio as in the early age series (except the blend with 45%SF which is still without quartz). Two series were made with alite and silica fume. The first was made with alite, quartz and silica fume (MC(Q)-SF series), and the second was made with alite, aluminate, gypsum and silica fume (MC*(Q)-SF series) to have two "model cements". In the systems with alite, 0, 0.1 and 0.5 M of KOH was included in the solution. More details can be found in Chapter 3, Section 3.2, p. 26.

6.2 Estimation of the C–S–H composition in silica fume blends

Unless stated otherwise, the composition of the Ip C–S–H was estimated by SEM-EDS using the mean of the distribution of analyses, not the value at the lower edge of Ca:X distribution. The Ip and Op C–S–H analyses in the matured systems characterised in Chapter 5 were biased towards high Ca:Si ratios (because the intermixing in SEM-EDS was mostly with CH), as seen in detail in Chapter 4. Here SEM-EDS analyses of the Op C–S–H in blends with silica fume also have a strong bias towards very low Ca:Si. Results on the two blends characterised in the STEM (Figure 4.21, p. 59) suggest that the intermixing here is mainly influenced by the degree of hydration of the silica fume. The value measured by STEM can be towards the highest measured Ca*:Si or around the mean. Because the degree of reaction of the silica fume was not measured here, there is no way of suggesting a preferred estimation of the Op C–S–H. For this reason, the study on the C–S–H pastes with silica fume will focus exclusively on the Ip C–S–H.

6.3 Hydration of silica fume blends at early age (1-28 days)

Pure cement

In the PC2 samples (pure cement), we observe the typical characteristics of the microstructure at early age as seen by SEM. In Figure 6.2 (a), Hadley grains about 1 μm thick appear at 1 day of hydration at 20°C and are mostly gone by 3 days of hydration except for small grains as seen in Figure 6.2 (b). At 6 days, in Figure 6.2 (c) Hadley grains are no longer observed. In the samples hydrated at 10°C or 38°C, the Hadley grains persist at the most until 3 days and are of similar size.

Data from TGA seen in Figure 6.3 shows that the amount of CH reaches $\approx$ 12% in the cement regardless of the temperature. Temperature seems to only accelerate its formation. Its distribution does not appear to be influenced by temperature either. The microstructures in Figure 6.4 show no visible difference irrespective of the hydration temperature of 10, 20 or 38°C. The formation of inner product is first observed at 6 days at 10°C, 3 days at 20°C and at 1 day at 38°C.

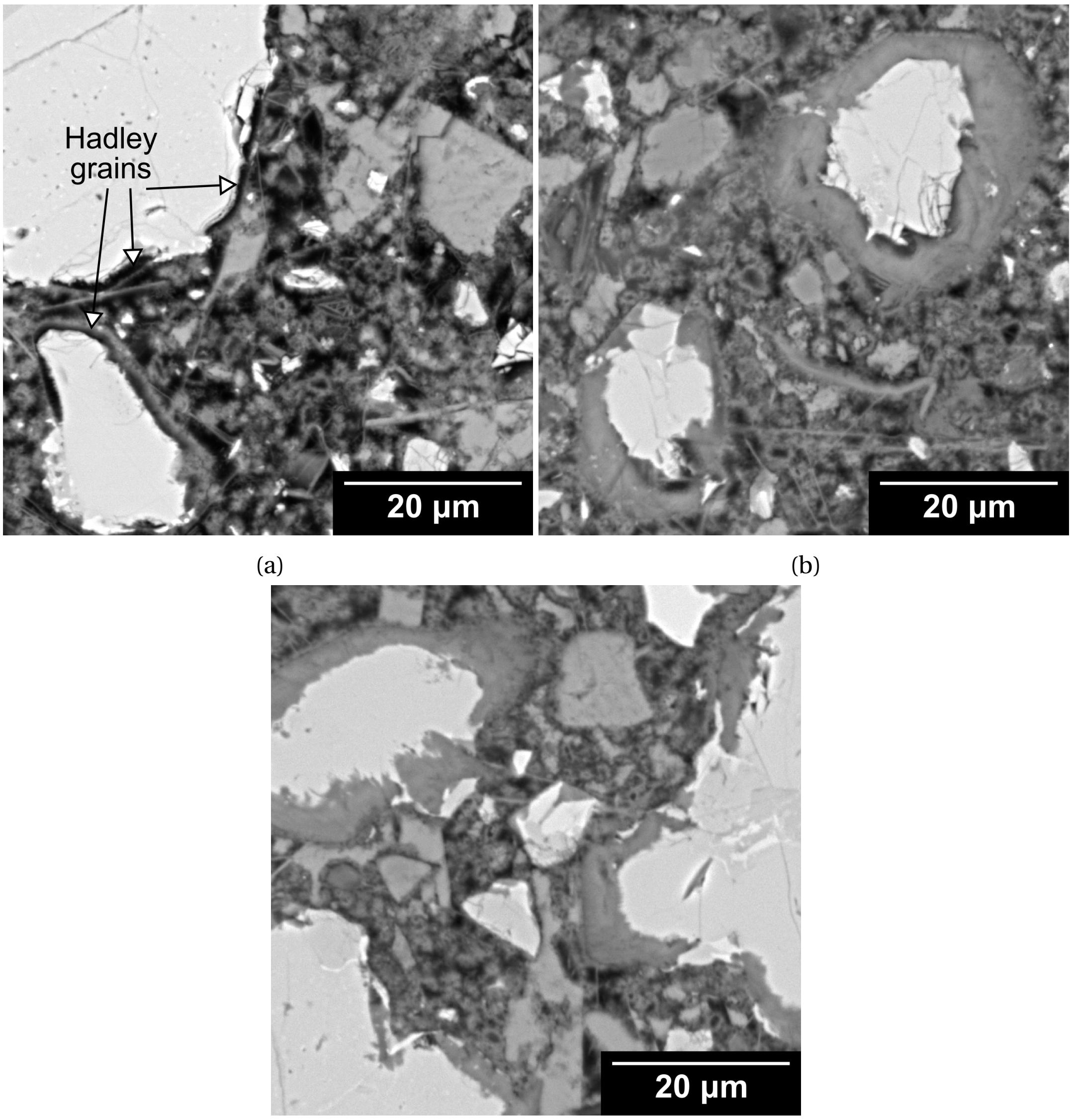

(a)

(b)

(c)

Figure 6.2: Early age SEM images of the PC2 hydrated at 20°C. (a) After 1 day of hydration. (b) After 3 days of hydration. (c) After 6 days of hydration.

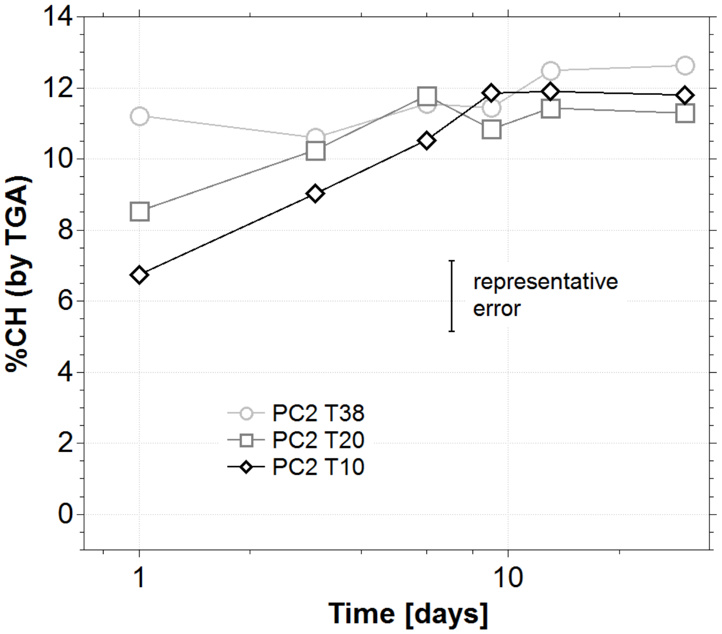

Figure 6.3: %CH in PC2 pastes hydrated at 10, 20 and 38°C.

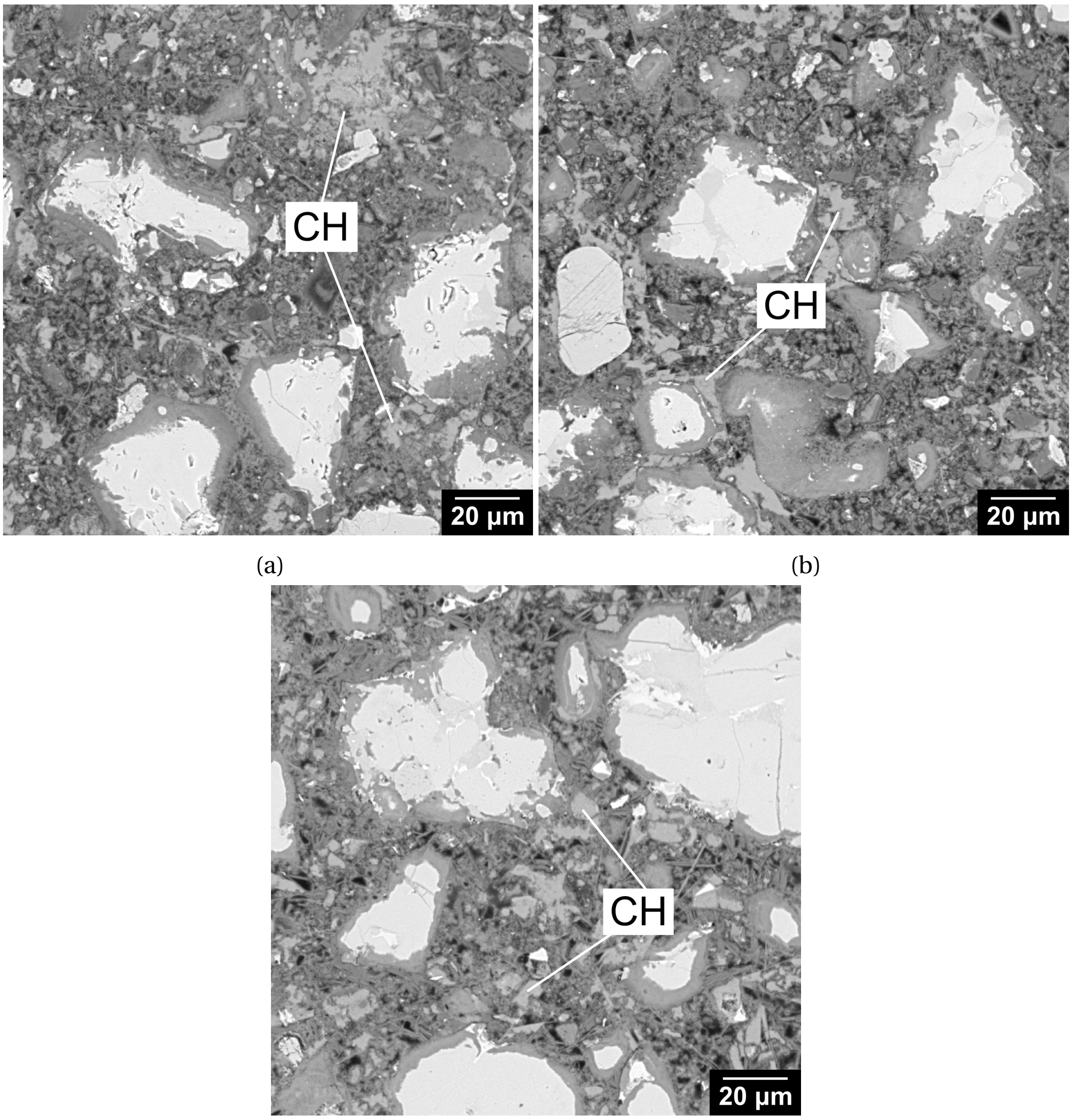

(a)

(b)

(c)

Figure 6.4: SEM images of the microstructure of PC2 pastes at 13 days for three temperatures. (a) Paste hydrated at 10°C. (b) Paste hydrated at 20°C. (c) Paste hydrated at 38°C.

Pastes of cement with silica fume

Early hydration kinetics. The normalised heat release in pastes hydrated at 20°C up to 36 hours are shown in the isothermal calorimetry curves of Figure 6.5. The presence of silica fume does not cause any significant change in the induction period as noted previously by Dobson and coworkers [95]. Once the reaction begins, there are significant differences. One one hand, the PC2 (pure cement) shows two peaks for the silicate and aluminate reaction respectively which occur between 6 and 14 hours. The peaks are relatively low with maximum heat flow of ≈ 3 mWg^{-1}. On the other hand, when silica fume is added, the increasing substitution of cement by silica fume at constant water:binder causes the slope of the acceleration period to steepen and enhances the reaction of the aluminate phases. The heat flow during the aluminate reaction reaches up to ≈ 12 mWg^{-1}. The shape of the curves strongly resemble those obtained in alite-C_3A-gypsum systems [59, 96] where the amount of gypsum was reduced in alite-C_3A blends without causing undersulfation. It is possible – but only speculatively – that the effect of replacing cement with silica fume has a very similar effect to reducing the amount of gypsum. In other words, the silica fume seems to cause an apparent reduction in available sulphate which is consistent with the fact that initially high Ca:Si C–S–H should form and which can adsorb sulphate in great amounts [97] in order to compensate for overcharging of the C–S–H surface [74]. Only over time would the system release sulphate back into solution and make it available again.

Impact of temperature on pozzolanic reaction. The normalised TGA data from Figure 6.6 shows that there is a net consumption of CH at 28 days in all systems except for the PC2-10SF series hydrated at 10°C. When comparing the data at 10, 20 and 38°C (Figures 6.6 (a), (b) and (c) respectively) it is seen that increasing the temperature causes both the highest and final value of %CH to decrease and to occur earlier in time. Also, increasing the amount of silica fume at any given temperature causes the same effects because more silica fume has likely reacted. At very high additions of ≈ 40-50% the degree of reaction is probably lower. It was observed that in other samples of similar water:binder ratio, only up to 75% of the silica fume reacts [98].

Values of normalised %CH observed at 1 day in most blends are lower than in the pure cement samples. This suggests two possible things. It can be that the silica fume indeed has already begun reacting as suggested by Figure 6.1. It could also be that the presence of silica fume is impacting the growth of CH already at that point. The amount of CH at 1 day is lowered with increasing additions at all temperatures.

Impact of silica fume on the microstructure. The impact of silica fume is also evident in the microstructures of blends with increasing additions. The distribution and morphology of CH in silica fume blends is very different compared to PC2 pastes. Examples of samples hydrated at 20°C are given in Figure 6.7. In Figure 6.7 (a), we observe that in pure cement the CH forms

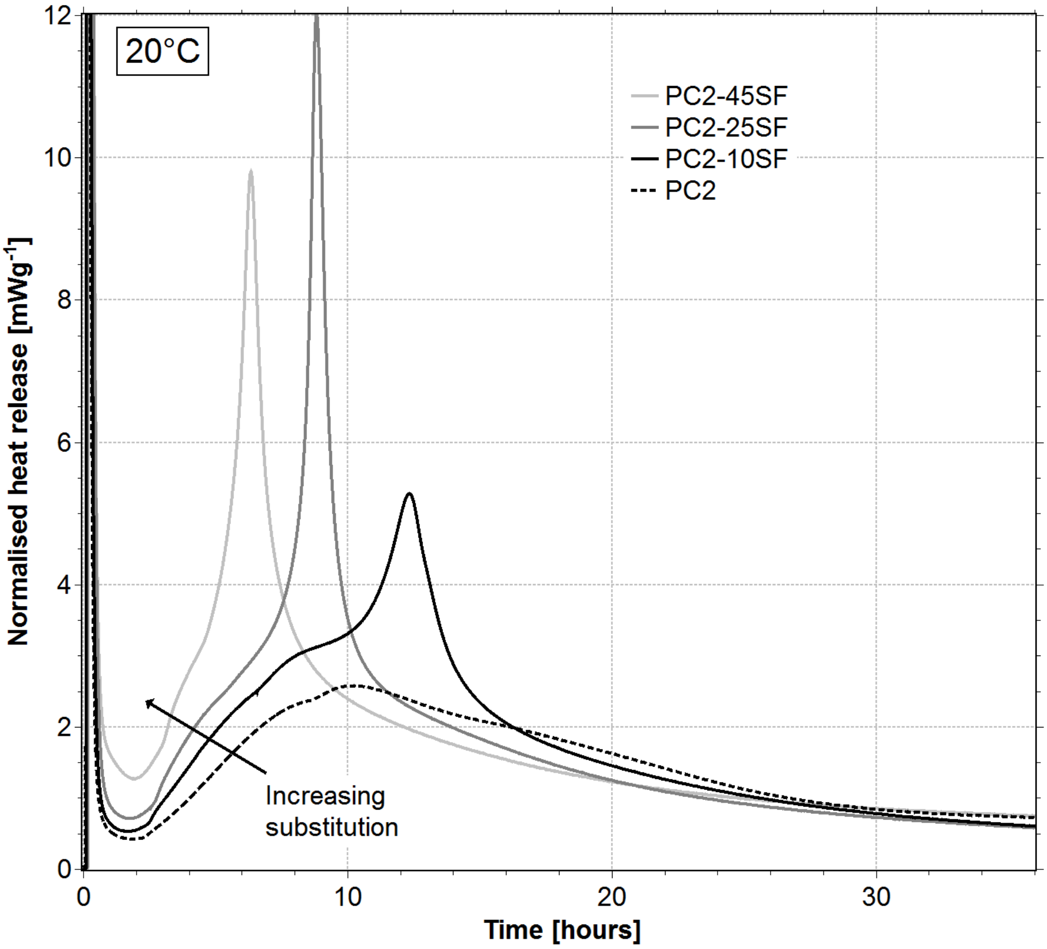

Figure 6.5: Isothermal calorimetry of early age silica fume blends hydrated at 20°C. Data of the heat flow is shown normalised to the amount of anhydrous cement and during the first 36 hours.

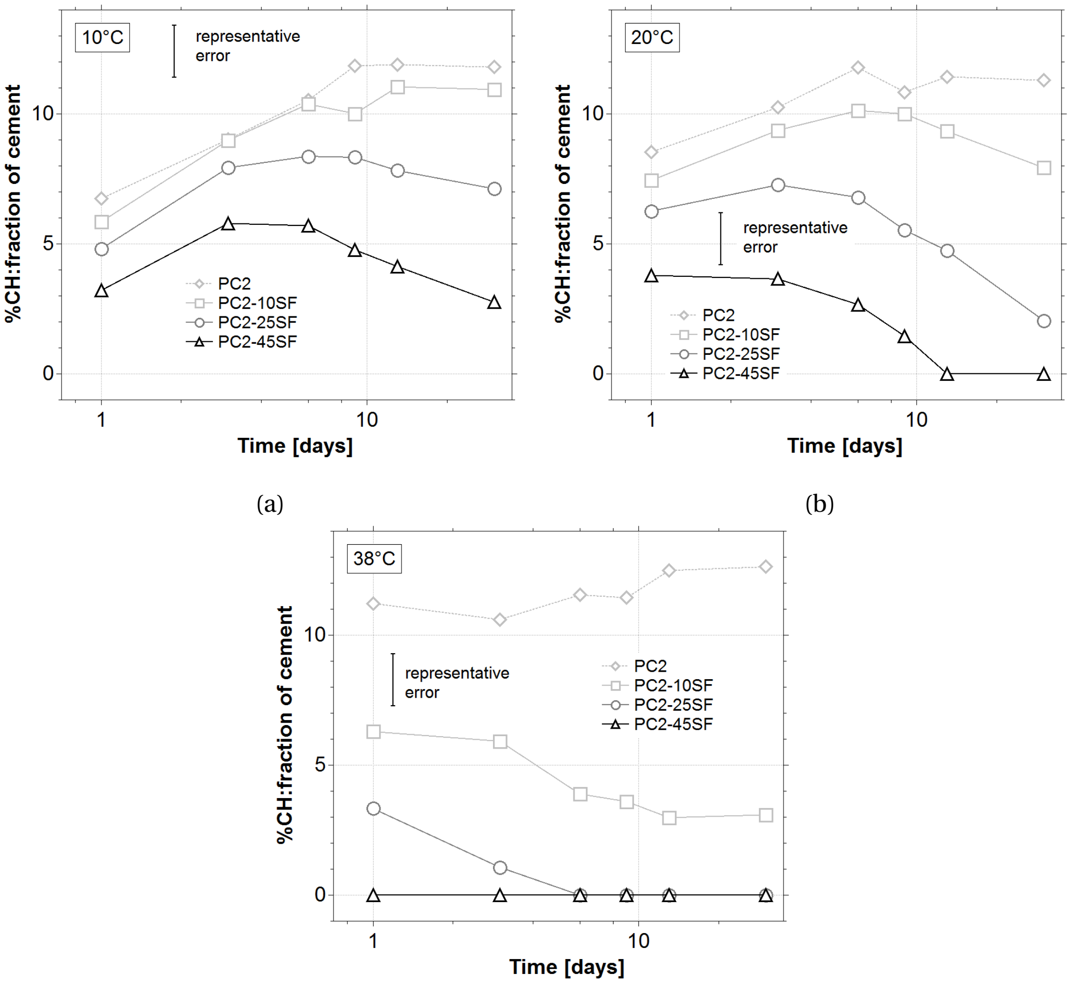

(a)

(b)

(c)

Figure 6.6: Evolution of normalised %CH in silica fume blends at different temperatures. Data from TGA with normalisation to the fraction of cement in the initial mix. (a) Hydration at 10°C. (b) Hydration at 20°C. (c) Hydration at 38°C.

as agglomerates and only few as platelets. When cement is replaced by 10, 25 and 45% of silica fume (Figures 6.7 (b), (c) and (d) respectively) the microstructure appears denser because of the presence of the fine particles of silica fume and the CH mostly forms as thin platelets and with only a few agglomerates. Hadley grains appear larger and persist often longer than in pure cement depending on temperature. Hollow shells persist up to ≈ 6 days at 10°C, ≈ 3-6 days at 20°C and ≈ 1 day at 38°C. CH also agglomerated around clinker grains sometimes surrounding it entirely (see dashed boxes in Figure 6.7) or part of it (see Figure 6.8 (e) for example). A particularly unusual texture of the CH distribution is the occurrence inside the shells.

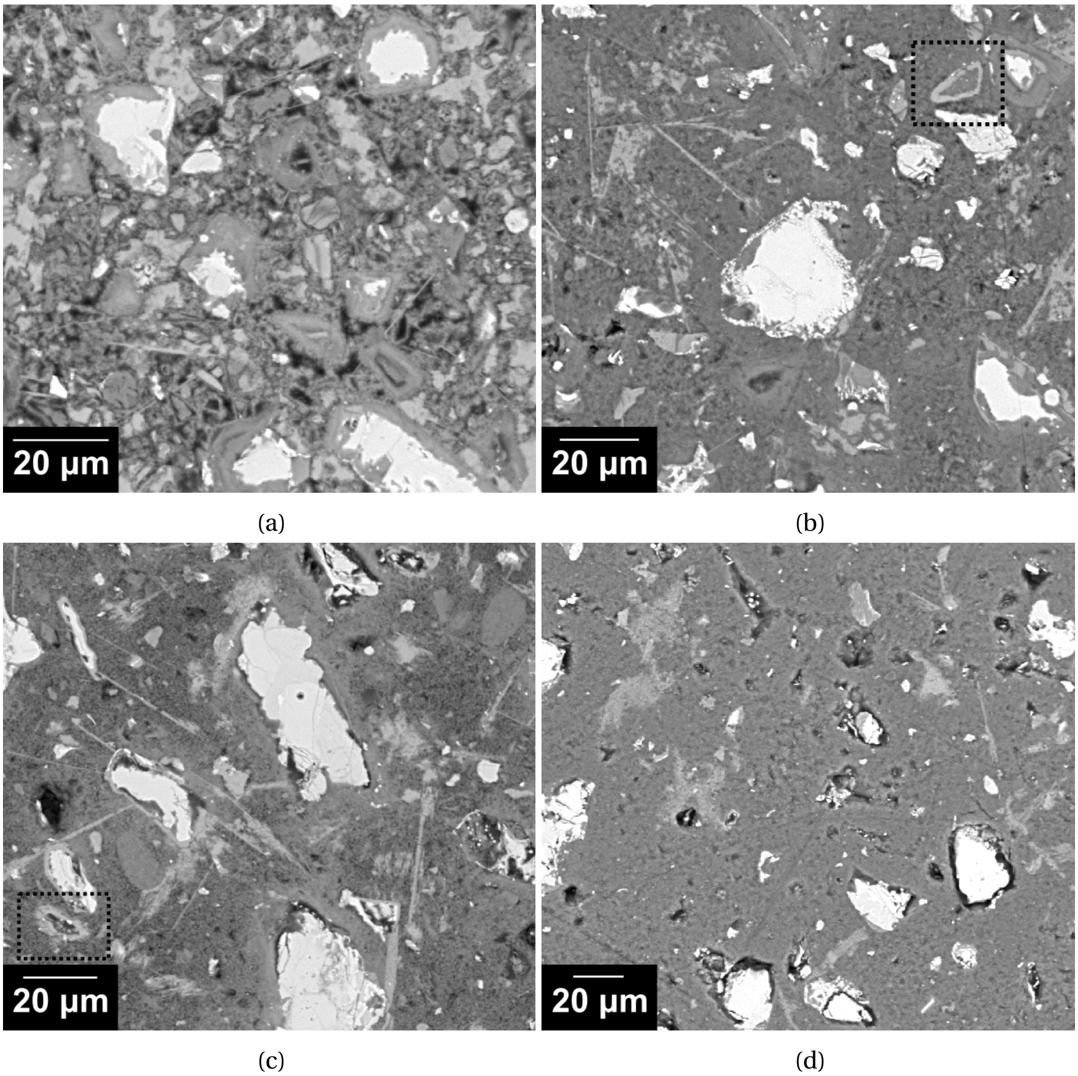

(a) (b)

(c) (d)

Figure 6.7: SEM images of pastes with increasing additions and hydrated at 20°C. Dashed boxes show grains surrounded by CH. (a) PC2 paste hydrated for 6 days. (b) PC2-10SF paste hydrated for 9 days. (c) PC2-25SF paste hydrated for 3 days. (d) PC2-45SF paste hydrated for 3 days.

Figure 6.8 shows SEM images of the PC2-25SF series at 1, 6 and 13 days for the three temperatures. When TGA data indicates CH is still present, it is present as platelets and as rims around clinker grains. CH appears to have formed in the Hadley grains. Initially, inner product C–S–H with a high Ca:Si forms while CH is still present, for example in Figures 6.8 (c), (e) and (g). When CH should be completely consumed like in Figure 6.8 (f), the rim appears to be fading as CH is consumed by pozzolanic reaction with silica fume. The PC2-25SF hydrated at 38°C, as well as all other blends of cement or alite hydrated at 38°C with silica fume additions, show that there is porosity at the interface. See Figures 6.8 (h) and (i) for example for the "imperfect interface". This could be due to accumulation of silica fume particles at the surface which react more rapidly at higher temperature to form denser C–S–H products. This could be a reason for such a porous region.

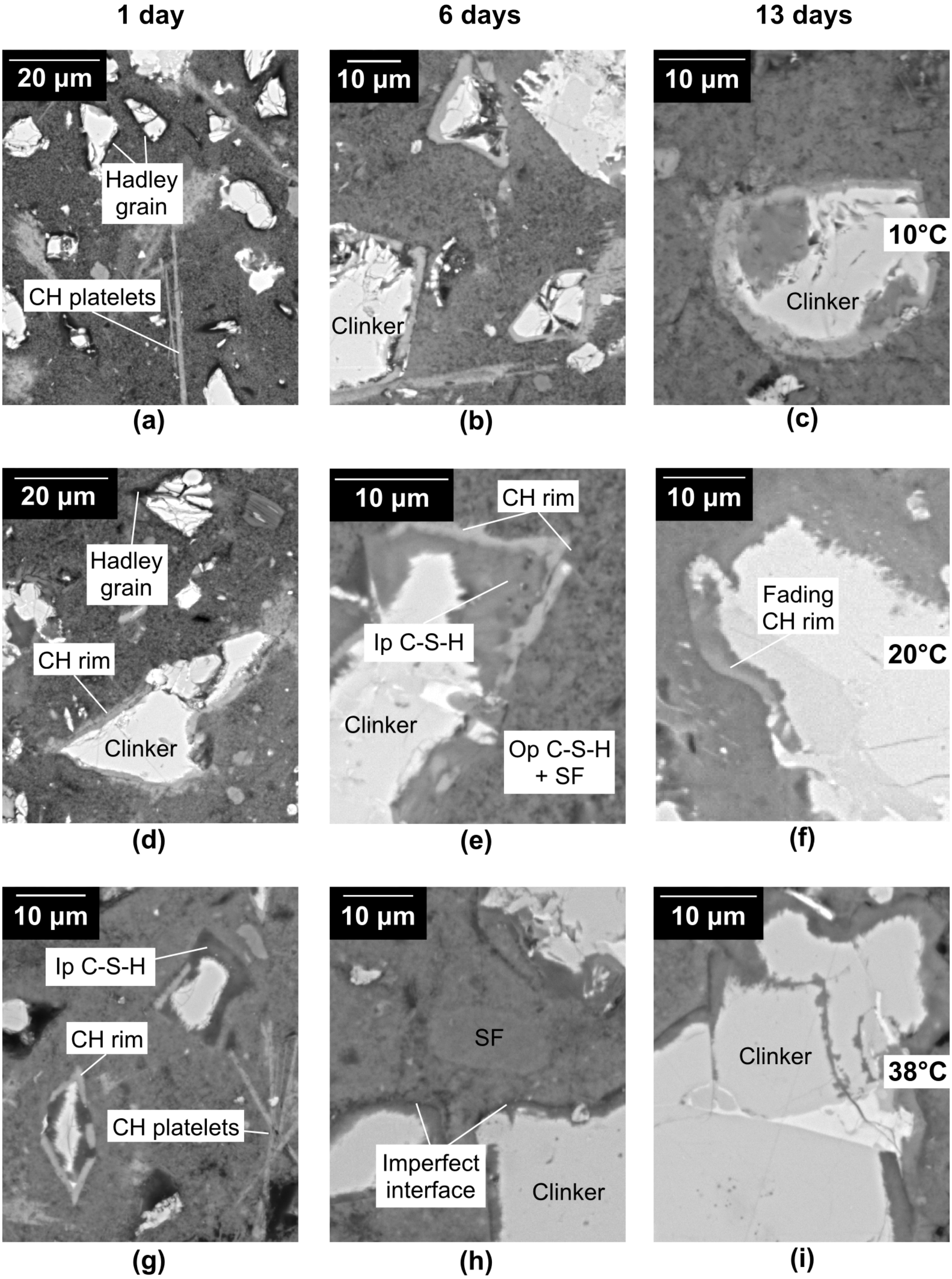

Figure 6.8: Microstructure evolution by SEM of the PC2-25SF series at 1, 6 and 13 days hydrated at 10, 20 and 38°C. (a), (b) and (c) are images from the 10°C series. (d), (e) and (f) are images from the 20°C series. (g), (h) and (i) are images from the 38°C series.

6.4 Matured samples containing silica fume (hydrated for 90 days)

Morphology and composition of the C–S–H in the SEM

Most cement-silica fume blends from this study which hydrated for 90 days, as well as blends from other projects, showed the existence of two distinct rims of Ip C–S–H which have a different grey level and composition. In the examples where an analysis was possible, the Ca:Si was often lower in the innermost Ip C–S–H ("Later Ip") as compared to the outermost Ip C–S–H ("Early Ip"). The outermost C–S–H showed a slightly higher Ca:Si, which is counterintuitive at first hand. An example of this in sample PC(Q)-25SF T10 is given in Figure 6.9 (a) where a region containing both Ip regions is observed. The EDS map of the region is shown in Figure 6.9 (b) where the Later Ip rim has a slightly lower Ca:Si. When comparing both Ca and Si maps (Figures 6.9 (c) and (c) respectively), it is the decrease in calcium which explains the difference in composition. The silica is constant over both Early Ip and Later Ip regions. The cracks which appeared over time and shown in Figure 6.9 (c) are located precisely at the interface between the two Ip regions and suggest that they are indeed different in nature because differential shrinkage of the C–S–H could have occurred.

Ip rims in alite blends. In alite-silica fume blends (model cement-silica fume blends) shown in Figure 6.10, the two inner product regions are well defined regardless of temperature, amount of alkali and presence of both gypsum and aluminate. In MC(Q) samples shown in Figures 6.10 (a), (b), (c) and (g) which do not containing gypsum nor aluminate, the Early Ip rims are thicker than the MC*(Q) samples which contain gypsum and aluminate as part of the model cement. In the MC*(Q) samples shown in Figures 6.10 (d), (e), (f) and (h) the Early Ip rims are noticeably thinner.

The Ca:Si ratio was measured in both Ip regions (Figure 6.11). Here the Later Ip always had a slightly lower Ca:Si, despite the product being closer to the original alite grain which is rich in calcium. Intermixing of phases could not have occurred to bias the results towards higher calcium. The MC(Q)-SF series, without gypsum and aluminate, had overall lower Ca:Si ratios and more remaining CH than the MC*(Q) series which contained gypsum and aluminate. In the MC*(Q) series, the Ca:Si was overall higher and only one sample had CH remaining.

Ip rims in PC blends. In cement-silica fume blends, the Early Ip rim was not always visible and measurable. Examples from Figures 6.12 (a), (b), (d) and (e) are the clearest in showing the existence of two distinct Ip rims of C–S–H. It can be observed the presence of a slightly lighter Ip C–S–H in the outer region of the hydrated clinker grain. In the inner most part of the Ip hydrates a darker Ip C–S–H formed. Figure 6.12 (c) had dark areas too small to analyse. In Figures 6.12 (f), (g), (h) and (i) the features are not distinct.

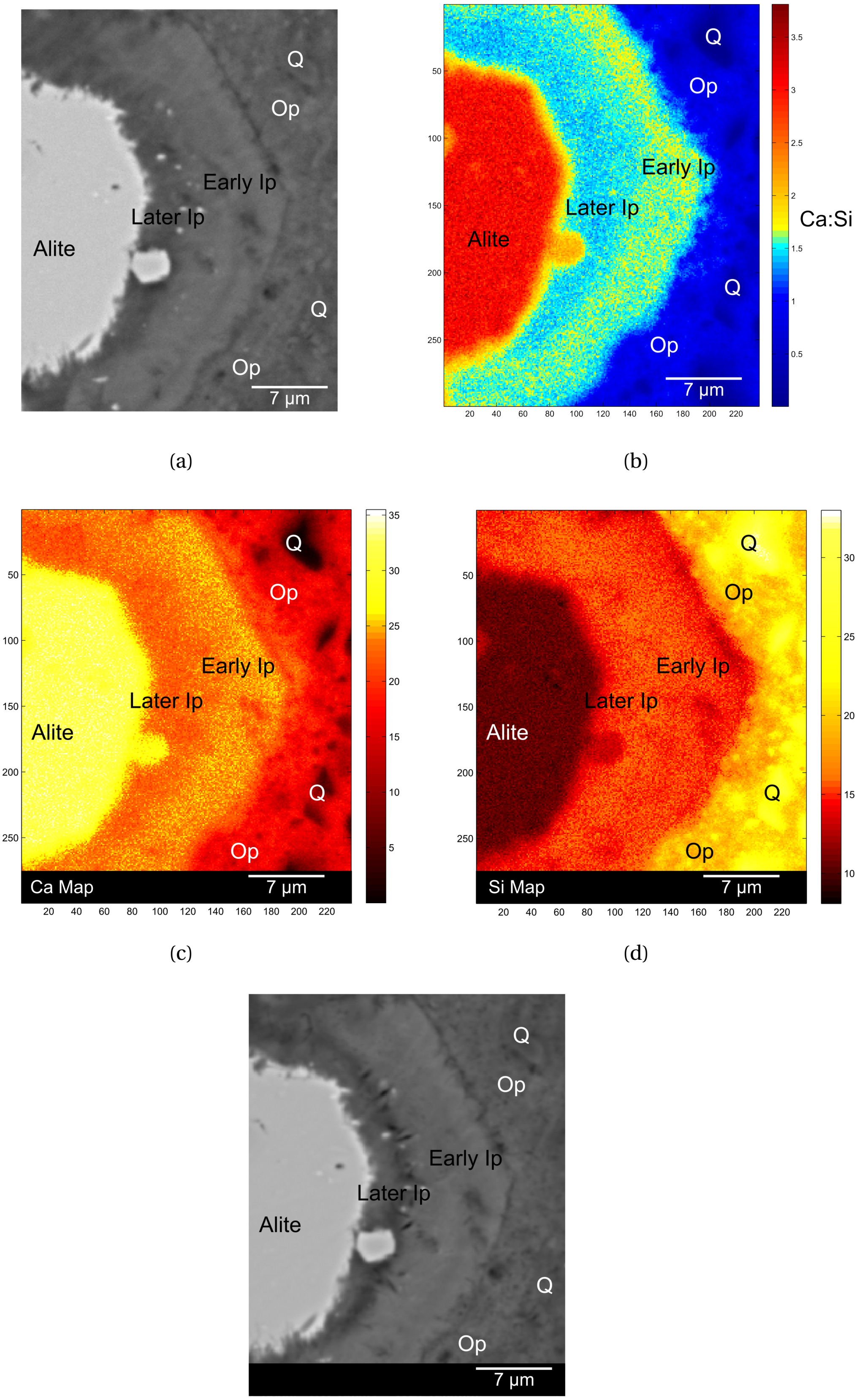

(a)

(b)

(c)

(d)

(e)

Figure 6.9: Region of PC(Q)-25SF T10 sample analysed by SEM-EDS mapping. The beam current was ≈ 1.2-1.4 nA (spot size 6). (a) SEM image before EDS mapping. (b) Quantified EDS map of the region. (c) Quantified Ca Map. (d) Quantified Si Map. (e) SEM image after the acquisition of EDS data during two hours.

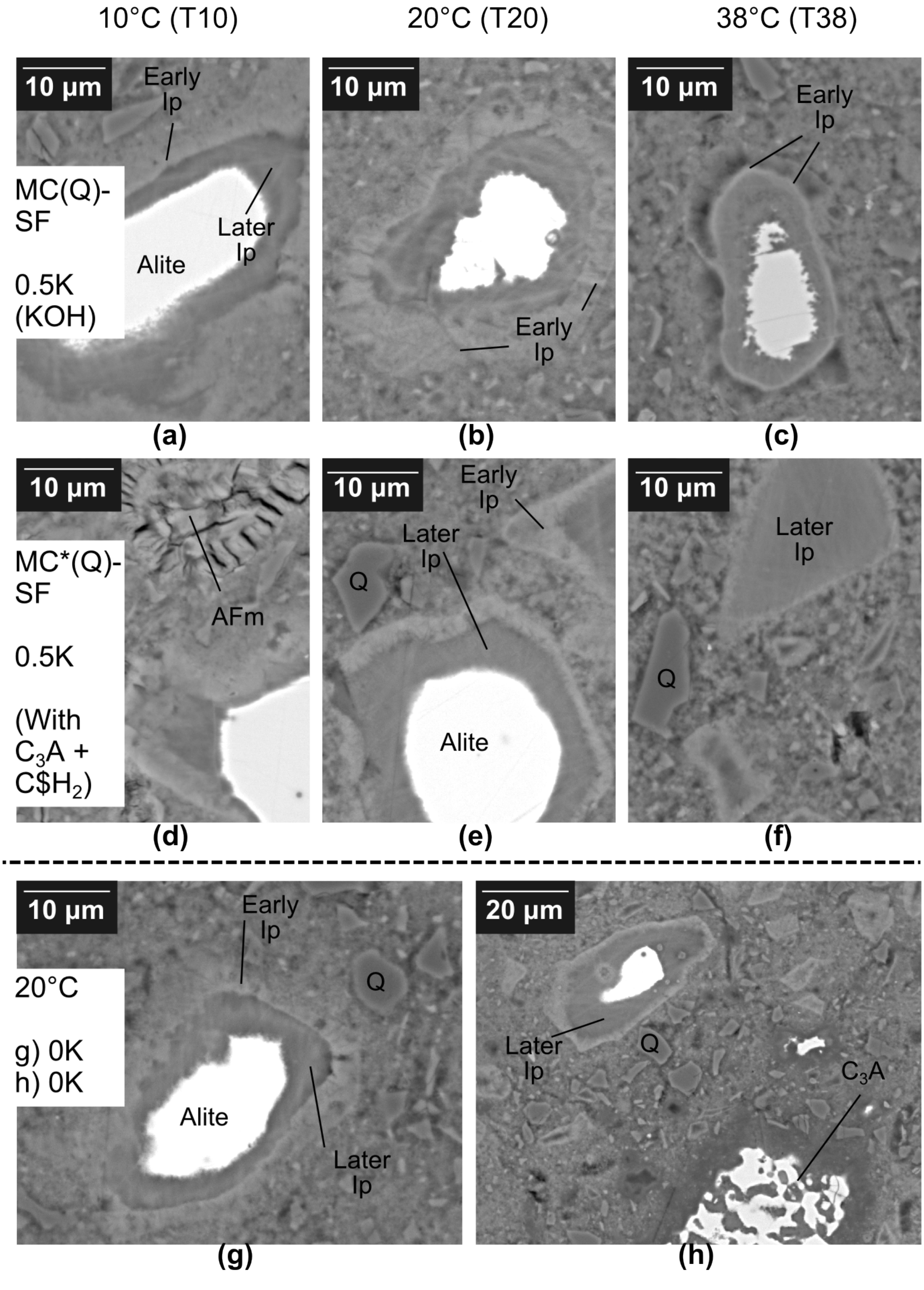

Figure 6.10: Microstructure by SEM of matured alite-silica fume samples showing two well-defined inner product regions. For example, T10 indicates hydration at 10°C, 0K indicates 0 M KOH and MC*(Q) indicates alite with gypsum and aluminate as well as quartz (MC(Q) indicates only alite with quartz.). (a) MC(Q)-SF 0.5K T10 sample. (b) MC(Q)-SF 0.5K T20 sample. (c) MC(Q)-SF 0.5K T38 sample. (d) MC*(Q)-SF 0.5K T10 sample. (e) MC*(Q)-SF 0.5K T20 sample. (f) MC*(Q)-SF 0.5K T38 sample. (g) MC(Q)-SF 0K T20 sample. (h) MC*(Q)-SF 0K T20 sample.

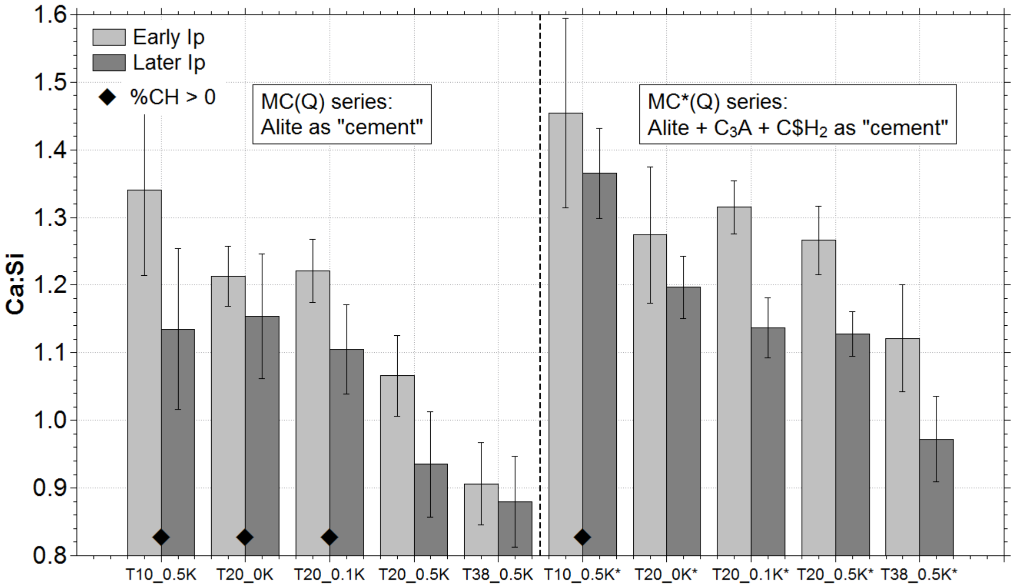

Figure 6.11: Ca:Si measured in both Ip C–S–H regions of alite-silica fume blends.

Discussion on the origin of the two Ip rims. The origin of the two rims is linked to the hydration of clinker at different times. The pore solution appears to be the determining factor in which type of solids form. As it can evolve over time, this can explain the observation of two C–S–H rims with slightly different Ca:Si.

The Early Ip was either Ip C–S–H formed with high Ca:Si which was converted to a C–S–H with low Ca:Si or a CH rim converted to C–S–H. The presence of two Ip regions with a lower Ca:Si in the innermost region was not observed in all PC systems. However in the alite blends, it was thinner in presence of aluminate and gypsum. The absence in several PC samples could therefore be due to the high aluminate in this cement.

This change in Ca:Si occurring in the Ip regions suggests that at some point in time the conditions of formation changed and the outermost Ip – may it be originally be CH or Ip C–S–H from the hydration of the cement – was transformed to reach a lower Ca:Si. However, the innermost Ip begins to form directly with a Ca:Si lower than the outermost at any given time. The outermost Ip was therefore considered “Early Ip” and the innermost Ip is considered “Later Ip” to illustrate the logical sequence of events occurring in these systems. Unfortunately, it was not possible to observe these two products in the STEM because the probability of observing an inner product is low in blended systems. The way damage occurred in the EDS mapping of an Ip region could be evidence of the possible different nature of the two Ip rims.

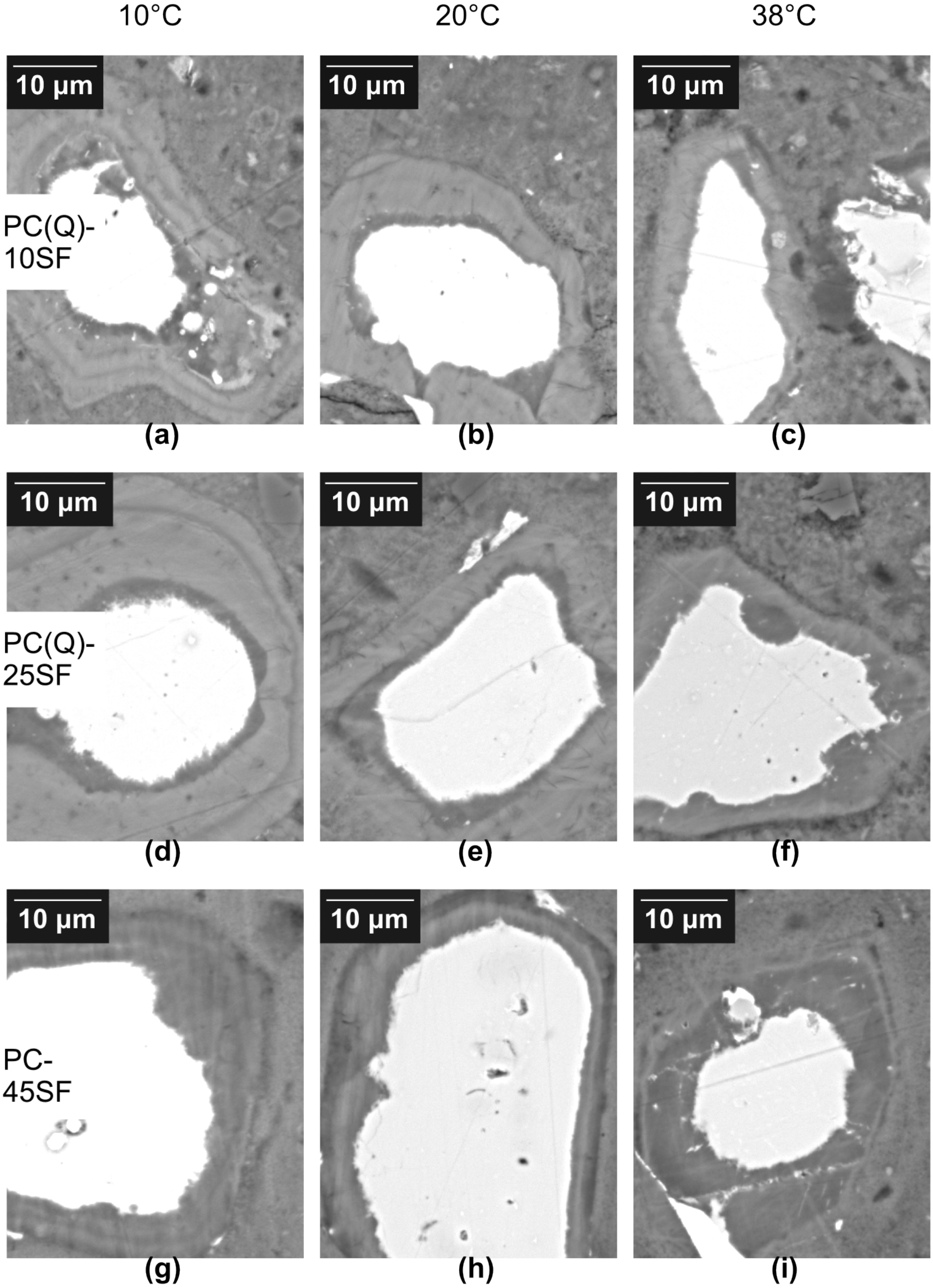

Figure 6.12: Microstructure by SEM of matured cement-silica fume samples hydrated at 10, 20 and 38°C. (a), (b) and (c) show the PC(Q)-10SF series. (d), (e) and (f) show the PC(Q)-25SF series. (g), (h) and (i) show the PC-45SF series.

Morphology of the C–S–H in STEM

The morphology of the C–S–H was studied by STEM in three samples, a sample from another study [88] containing 90% white cement and 10% silica fume sealed cured at room temperature with water:binder = 0.4, the PC(Q)-25SF T20 sample and the MC*(Q)-25SF T20 sample.

It was observed in the white cement-silica fume blend that after 28 days the Op was mostly fine-foil like (Figure 6.13), with a composition ranging from 1.35 to 1.45 despite the presence of ≈ 20% CH. One region (Figure 6.14) showing a small hydrated alite grain contained fibrillar C–S–H at the original grain interface. The Ip which formed during the first hours of hydration appeared dense. The centre of the small grain appeared less dense and foil-like, as seen previously in a cement hydrated with w:c = 0.4 and at 20°C [9] and in Figure 5.2 (a) of Chapter 5. In this region the Ca:Si varied between 1.60 and 1.70, for both the fibrillar Op around the alite grain and the Ip from the alite grain. The value for Ca:Si is closer to that of the pure cement – reported at ≈ 1.70 [99].

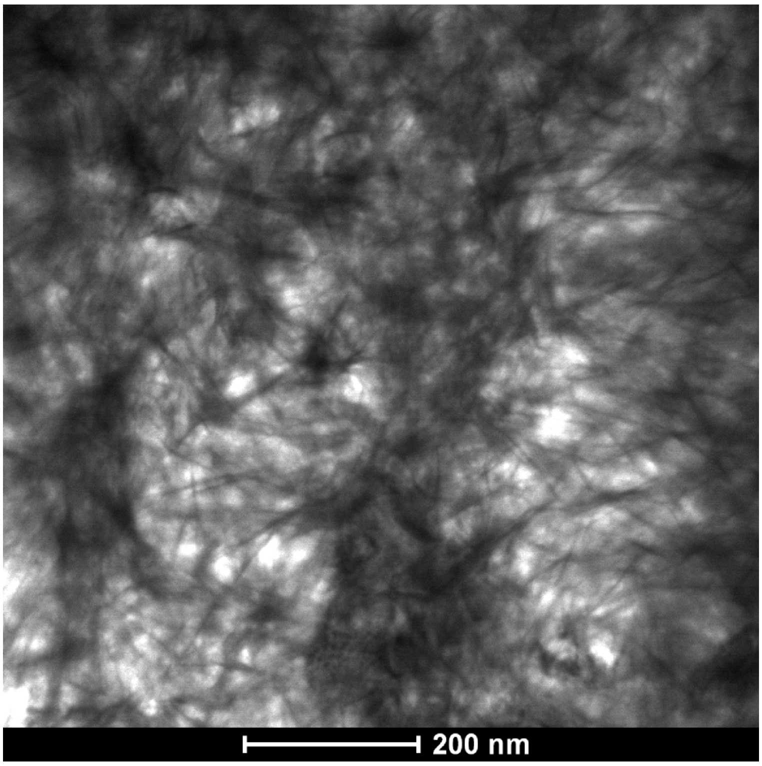

Figure 6.13: STEM image of the Op region of the sealed cured sample with white cement and 10% silica fume. A fine foil-like morphology is observed.

The C–S–H was observed in two blends with higher additions (25% silica fume). The PC(Q)-25SF sample hydrated at 20°C is shown in Figure 6.15 (a) to have both fibrillar and foil-like morphologies in outer regions containing quartz and silica fume grains which are better revealed by the EDS map of the same region shown in Figure 6.15 (b). Here the quartz and the silica fume grains both have contributed to the initial formation of fibrillar C–S–H as

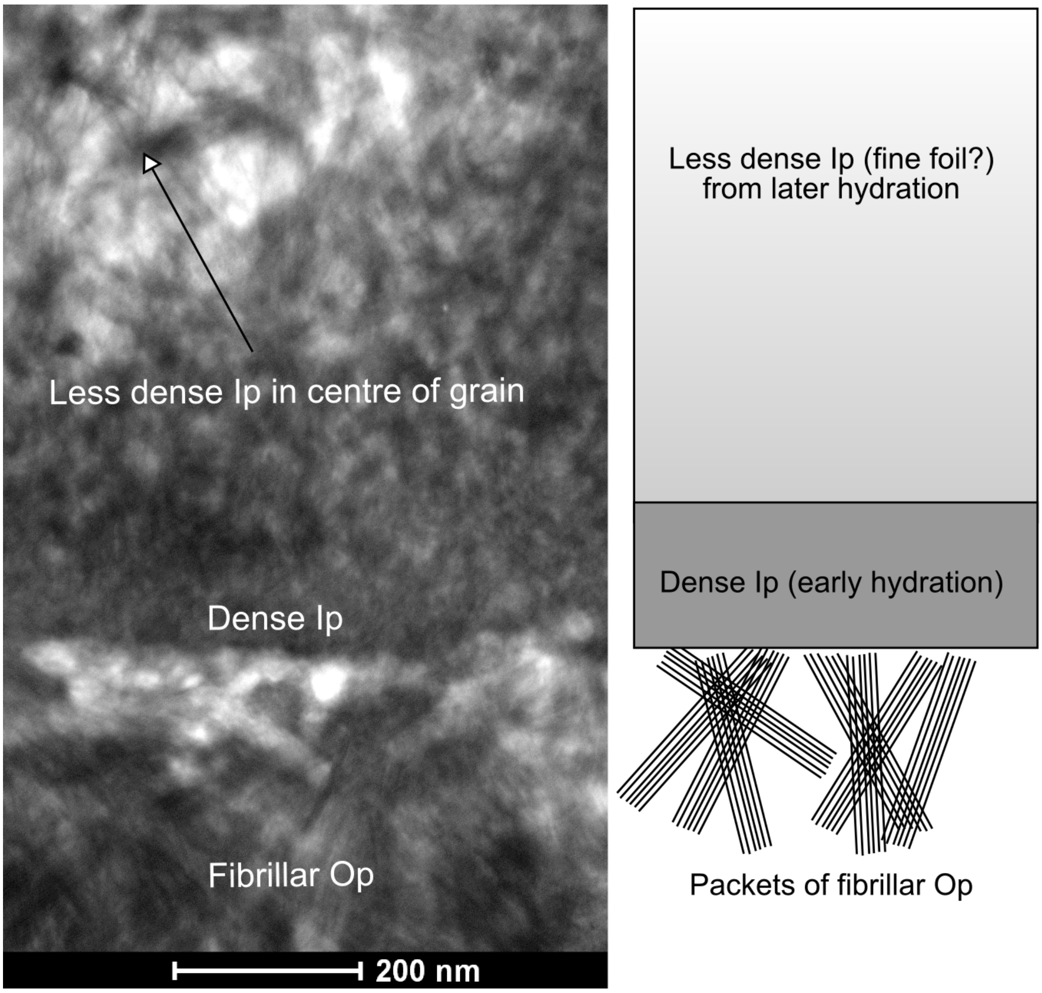

Figure 6.14: STEM image of the Ip region of the sealed cured sample with white cement and 10% silica fume. Here fibrillar Op, dense Ip and fine foil-like Ip are observed.

they provided surfaces for their nucleation and growth. Despite the high replacements, they persisted but are somewhat confused with foil-like C–S–H which exists intermixed with the fibrillar C–S–H. Packets of fibrils seem to growth outwards from the silica fume particles. Figure 6.15 (c) shows a fine foil-like region (probably Op) of C–S–H. The Ca:Si by STEM was ≈ 1.18 and the foils are coarser than in the Op C–S–H of the sealed cured sample of Figure 6.13.

Figure 6.15 (d) shows an Op C–S–H region of the MC*(Q)-25SF model cement sample hydrated at 20°C. Here the foil-like C–S–H is the most coarse compared to previous samples and has the lowest Ca:Si of ≈ 0.82.

A sample from E. L'Hôpital with aimed Ca:Si = 1.00 and Al:Si = 0.03 was provided for comparing the morphology with the paste samples. The paste sample of Figure 6.15 (c) shows resemblance for broadly similar Ca:Si and Al:Si of the C–S–H. The sample of Figure 6.15 (d) shows a striking similarity to the foil-like morphology in the synthesised sample as well. Pastes samples here show essentially the same morphology in paste samples compared to synthetic systems equilibrated for at least 6 months and with a high solution:solid ratio of 45.

Comparing the three paste samples, it appears that in systems with low solution:binder ratio the C–S–H of systems highly blended with silica fume forms with similar characteristics compared to those made in dilute conditions. The foil-like morphology appears more coarse when the Ca:Si decreases and suggests that the C–S–H formed here is at equilibrium with the solution at a given place and time.

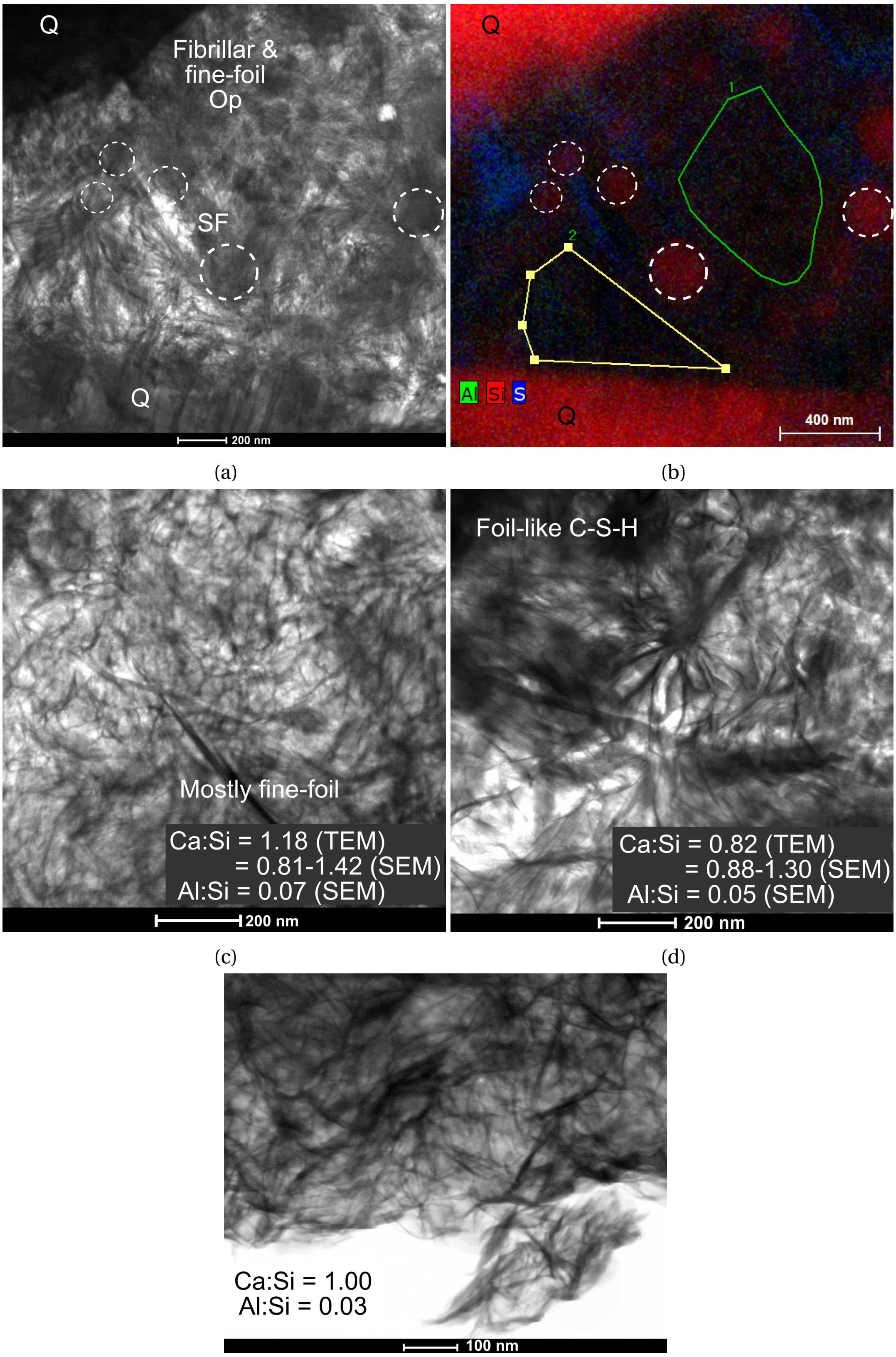

(a) (b) (c) (d) (e)

Figure 6.15: Comparison between blends and synthetic samples observed by STEM. (a) PC(Q)-25SF T20 sample showing both fibrillar Op and foil-like Op C–S–H regions. (b) EDS map of the PC(Q)-25SF T20 sample revealing the presence of unreacted silica fume particles. (c) Foil-like Op C–S–H in the PC(Q)-25SF T20 sample. (d) Foil-like Op C–S–H in the MC*(Q)-25SF T20 sample. (e) Synthetic C–S–H from E. L'Hôpital with aimed Ca:Si = 1.00 and Al:Si = 0.03 prepared at 20°C.

Composition of the C–S–H in silica fume pastes samples

The time evolution of the C–S–H composition is shown for the three temperatures in Figure 6.16 when the analysis of an the Ip was possible. Figures 6.16 (a), (b) and (c) show for 10, 20 and 38°C respectively that the Ca:Si decreases with the %CH and with time as suggested by the lines between successive points of a same series. The data shown as the grey series in Figure 6.17 suggests an overall trend for decreasing Ca:Si with the consumption of CH. In this early age series the highest Ca:Si in absence of CH is ≈ 1.50 and the lowest Ca:Si here in absence of CH is ≈ 1.0.

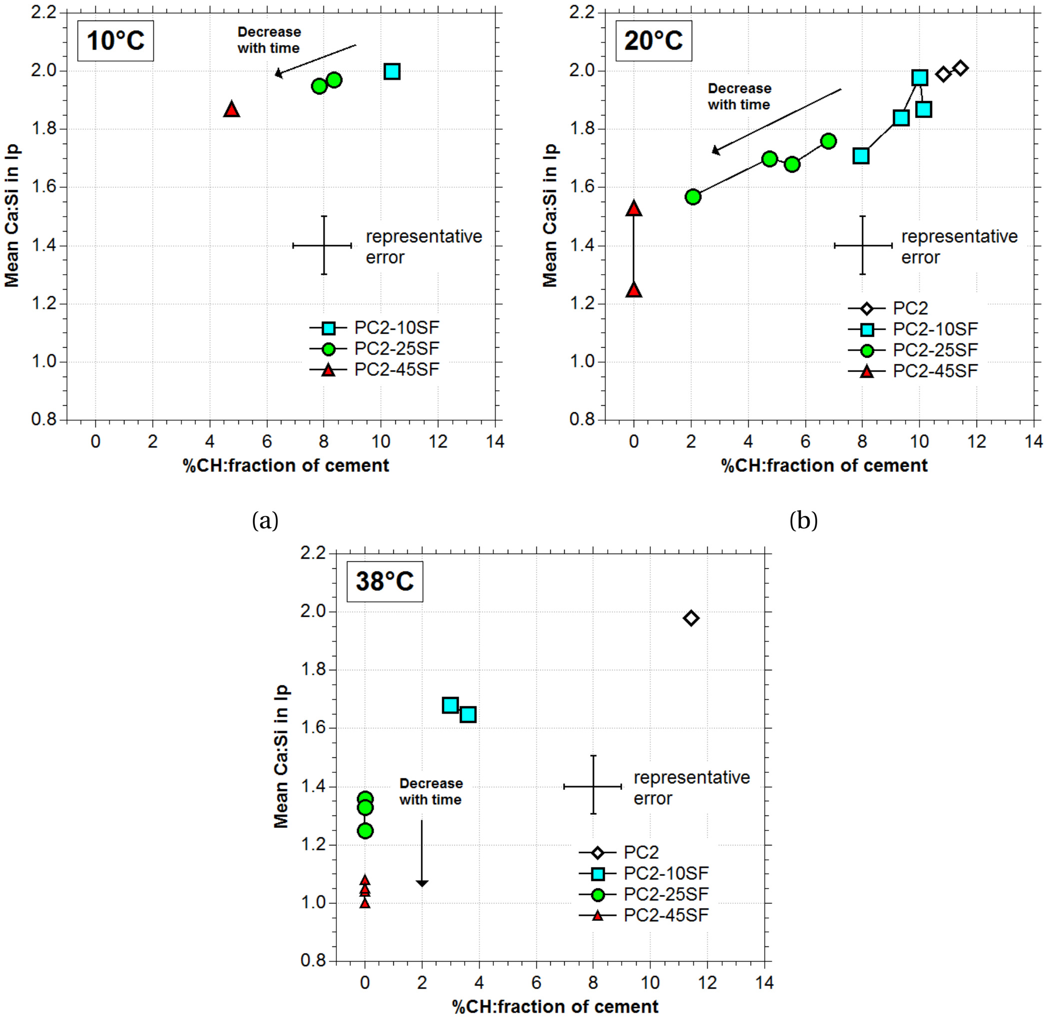

(a) (b)

(c)

Figure 6.16: Comparison between determined CH content and estimated Ca:Si in the Ip C–S–H of early age samples. (a) Series hydrated at 10°C. (b) Series hydrated at 20°C. (c) Series hydrated at 38°C.

The data from Figure 6.16 is shown in Figure 6.17 with data from the matured cement and alite systems hydrated for 90 days. Here we observe very similar decreasing trends from high Ca:Si at high %CH to very low Ca:Si when CH is entirely consumed. The PC(Q) series had quartz which increased the effective water:cement ratio and showed the same trend as the early age series but slightly shifted down. The Ca:Si decreases with the amount of CH from ≈ 1.9-2.0 to ≈ 1.3-1.4 when %CH reaches zero. The lowest value is also Ca:Si ≈ 1.0.

The MC(Q) system containing alite, quartz and silica fume – but without gypsum and aluminate – decreases from Ca:Si ≈ 1.60 with ≈ 17% of CH to ≈ 1.0-1.2 when %CH reaches zero. The lowest value is Ca:Si ≈ 0.90. Most samples from the MC*(Q) series – which contain gypsum and aluminate – have no CH but have Ca:Si values closer to the blends of cement and silica fume (see dashed circle). The highest Ca:Si in absence of CH here is ≈ 1.40-1.50. The lowest Ca:Si is ≈ 1.0-1.1.

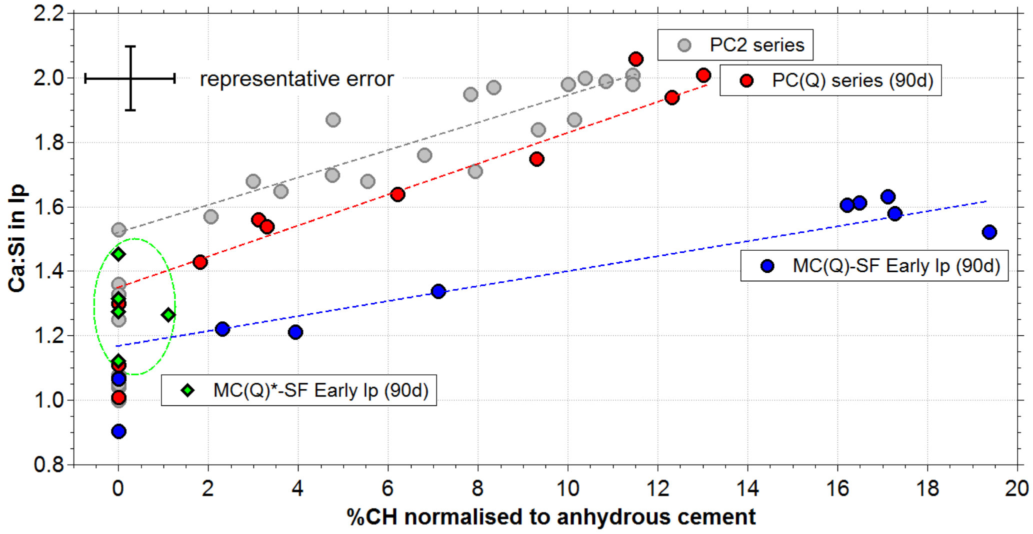

Figure 6.17: Ca:Si compared to %CH in all silica fume blends.

6.5 Summary on the impact of silica fume on the morphology and composition of C–S–H in pastes

The results from this chapter show that the microstructure development of paste samples is strongly affected by the addition of small to large amounts of silica fume.

At early age, the size and persistence of Hadley grains and the morphology of CH agglomerates were changed compared to pure cement. Silica fume particles which can deposit around the clinker grains in the Hadley grains and rapidly react, particularly at 38°C where porosity exists between the Op and the Ip. The pozzolanic properties of the silica fume were shown by the decrease in Ca:Si in the Ip with the consumption of the CH. Fibrillar C–S–H formed initially on the surface of clinker and quartz particles and persist over time. They are highly intermixed with foil-like C–S–H and show no difference in composition in the STEM analyses.

The presence of dispersed silica causes the microstructure to appear much denser than the pure cement.

At later times two rims of Ip were observed with different Ca:Si. The outermost rim was well observed in alite systems and were more pronounced in absence of gypsum and aluminate. There can be differences between the Ip and Op C–S–H in terms of morphology and composition. The evolution of the solution over time plays an important role on the formation of solids. Fibrillar C–S–H formed while the solution was dominated by the initial reaction of the cement while the foil-like C–S–H can form as soon as the silica fume has affected the pore solution.

There are two regimes of change of composition of the C–S–H. In Chapter 5 the decrease in Ca:Si is overall limited by the presence of CH and numerous regions of fibrils are observed. Here − once CH is consumed − the C–S–H is able to reach low Ca:Si which are not far from the value for pure tobermorite structures and have foil-like morphology throughout most of the sample.

7 Discussion

7.1 Summary of C–A–S–H in pastes

Results from this Ph.D. work underlines the importance of understanding the history of what occurs in pastes of water:binder ratio of 0.4, i.e. low water:binder.

In pure cement pastes, there is a massive growth of fibrillar Op C–A–S–H from the surface of clinker grains which occurs when CH begins to precipitate. The precipitation of CH begins once the solution is highly supersaturated with respect to Portlandite. In blends, the system begins mostly as a pure OPC, with surfaces providing additional surface for fibrillar C–A–S–H to grow. Only once the conditions in solution favour the release of species from the SCM(s) into solution does the system begin to form C–A–S–H with lower Ca:Si (which can have a foil-like morphology) and consume CH (for pozzolanic SCMs). Over time, the Ca:Si of the initial C–A–S–H decreases towards a lower value. The decrease of Ca:Si is expected to occur more easily at high water:binder ratio.

The comparison of alite and cement pastes in Chapter 5 showed the C–A–S–H forms with a fibrillar morphology, as shown previously [32, 8, 44, 21]. The Ca*:Si (Ca* = Ca - S) in cement ranged ≈ 1.80-1.90. The Ca*:Si in alite was lower, ≈ 1.50-1.60, but still within the expected range of Ca:Si (1.50-2.00) in presence of Portlandite based on solubility experiments, e.g. [27].

The results presented in Chapter 5 and Chapter 6 have shown that the C–S–H (or C–A–S–H) phase which is formed in blended pastes of low water:binder ratio has variable composition and morphologies.

In Chapter 5 results from blended systems containing CH suggest that the decrease of Ca:Si is limited to about ≈ 1.30. In these systems the fibrillar morphology dominated and foil-like regions were rarer. In Chapter 6, systems contained little or no remaining CH and showed that the decrease in Ca:Si is possible below ≈ 1.30. In these systems foil-like morphologies were predominant.

The composition and morphology are strongly linked. In the pastes samples, the fibrillar morphology had Ca:Si ≈ 1.50 or higher, while foil-like morphology had Ca:Si only up to ≈ 1.50. Figure 3.2 (p. 32) also showed that the foil-like morphology is coarser at lower Ca:Si ratios.

Fibrils form during the early stages of hydration of alite and OPC. They are also present in blends with SCMs where they most likely correspond to the initial reaction of the alite or OPC. This is strongly suggested by the fact that fibrils always seem to originate from the original surfaces of clinker or alite grains. They were also observed to grow from the surface of quartz grains in a OPC-quartz-silica fume blend. The presence of SCM particles also can provide a surface from which fibrils could initially grow. The fibrillar C–S–H persisted after at least five years here, and have been observed after 20 years in an OPC paste [57]. The fibrillar-like morphology persisted despite the decrease in Ca:Si in blended systems from this study.

Foils have a 2-dimensional morphology rather than 1-dimensional growth morphologies of the fibrils. In pure cement samples, they usually have similar Ca:Si to Op fibrils when they form in small cement grains. In presence of SCMs, foils can form within the Ip of clinker and SCM grains. Foils were also observed in the Op region of blends. They have lower Ca:Si within SCM grains. Because of the presence of fibrils in several systems with SCMs, the foil-like morphology does not seem related to the initial reaction of the OPC but rather to the reaction of SCM particles which normally begins after the reaction of the alite or cement.

Based on these observations and work from other past and present projects, the following ideas on C–S–H are formulated.

7.2 Indications of a tobermorite-“mobile calcium” model for C–S–H

Most researchers agree on a defect-tobermorite model to explain the variation of Ca:Si between 0.83 and 1.50. It is based on two mechanisms: the removal of bridging tetrahedra and the replacement of two protons by a calcium ion. The debate on the most suitable model for describing C–S–H is related to Ca:Si over ≈ 1.50 where two viewpoints apply to explain how the Ca:Si is further increased. Richardson [21] showed that most models either encompass a tobermorite/jennite viewpoint or a tobermorite/“solid-solution CH”, which in fact pertains not to the presence of microcrystalline CH but rather to the presence of Ca−OH groups in the C–S–H interlayer at higher Ca:Si.

It is interesting to note that in his 2004 review paper [21], Richardson mentioned that *“In some systems, the data can only be accounted for on the T/CH structural viewpoint, whilst in others, both the T/CH and T/J viewpoints could apply”* when discussing the applicability of both viewpoints to paste samples of low water:binder ratio. This suggests that even in paste samples, a tobermorite/“solid-solution CH” model could generally be appropriate. The experimental evidence that calcium is mobile in C–S–H of Ca:Si ≥ 1.00-1.30 was already discussed in Chapter 2 with respect to leaching and carbonation experiments. This is further supported by recent work.

Recent results from two independent studies by A. Bazzoni on hydrated C_3S [39] and by A. Muller on a cement paste [88] further support the idea of highly mobile calcium in C–S–H. The results of these studies indicate (Figure 7.1) that increasing the water:binder ratio in the range ≈ 0.30-0.80 causes an increase in the amount of precipitated CH and a decrease of the Ca:(Si+Al) of the C–S–H phase. The Ca:(Si+Al) in C–S–H could be significantly lower, ≈ 1.50-1.60 instead of ≈ 1.70-1.80 and was confirmed by three different characterisation techniques.

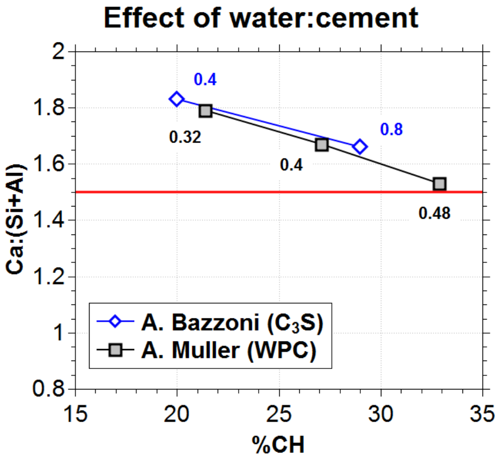

Figure 7.1: Effect of water:cement on Ca:Si and %CH.

7.3 Is C–A–S–H at equilibrium in realistic pastes?

Highly variable Ca*:Si and Al:Si in Ip C–A–S–H

The composition of the Ip C–A–S–H in all blends studied during this Ph.D. work is shown in Figures 7.2, 7.3 (cement pastes) and 7.4 (alite pastes). For the silica fume blends, the Later Ip is shown here, not the Early Ip. Al:Si is shown as a function of Ca*:Si (Ca* = Ca - S). Some samples containing metakaolin are also included and are most of the points on the upper left part of the figures (values of Al:Si ranging ≈ 0.25-0.40) but contain monosulfoaluminate and other AFm phases such as strätlingite which complicated the analysis of the C–A–S–H (see the Appendix, p. 131).

In the pastes studied, the overall range of Ca*:Si ≈ 0.90-2.00 and the range of Al:Si ≈ 0.05-0.30. The points with Al:Si ≈ 0.35-0.40 are considered more doubtful based on recent ^{27}Al and ^{29}Si MAS NMR results [100] on white Portland cement-metakaolin blends where the ratio did not reach such high values.

The presence of CH (Figure 7.2) occurred generally for Ca*:Si = 1.30-2.00 with the exception of three alite-silica fume pastes (Figure 7.4) where the Ca*:Si ≈ 1.10-1.15. From results on the consumption of CH by pozzolanic reaction with silica fume (Figure 6.17, p. 115) it was estimated that the Ca*:Si of Ip C–A–S–H (of Early Ip in the case of alite blends) at the point where CH should not be present in pastes was Ca:Si ≈ 1.20-1.50.

Compared to solubility data like that in e.g. Figure 2.5, p. 14, it appears that the conditions in pastes of low water:binder ratio limits the consumption of CH and favours the decalcification of the C–A–S–H. This is observed by the lowest Ca*:Si = 1.20 at the point where CH should be absent which is lower that what is frequently observed in other preparations where Ca*:Si = 1.50 or sometimes higher. The fact is blended systems always begin by forming high Ca*:Si C–A–S–H and then favour the possible consumption of CH and the formation of low Ca*:Si C–A–S–H.

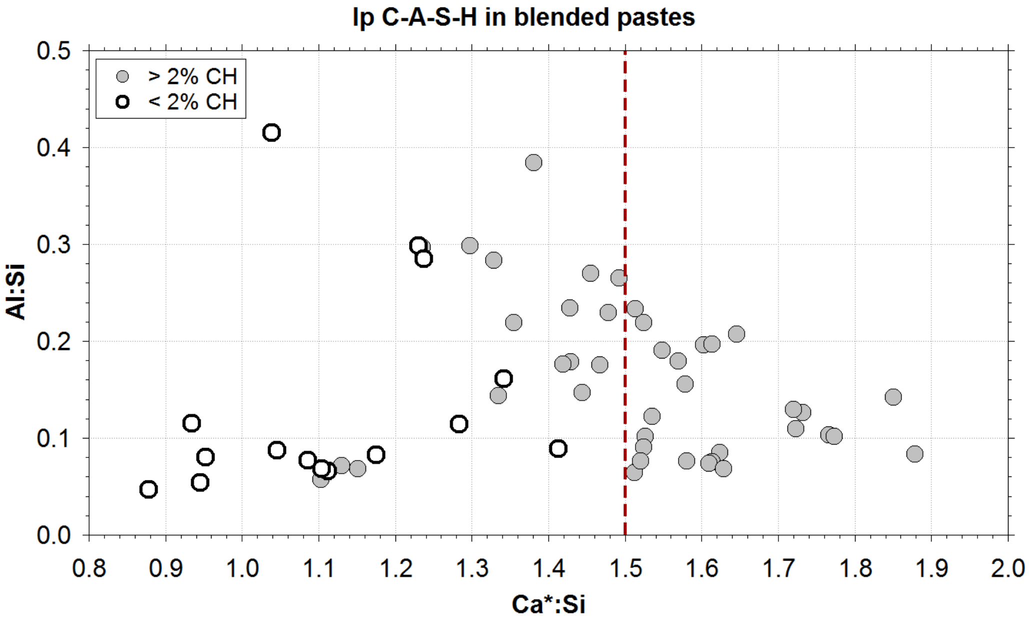

Figure 7.2: C–A–S–H composition in blended pastes (all samples). Points of samples with less than 2% normalised CH are bolder to indicate systems which are mostly free from Portlandite.

The reason for the persistence of CH is probably not linked to the availability of water in the pore structure but rather the fact that CH has a low surface area per volume compared to C–S–H for example. This should be further explored.

Figures 7.3 (cement pastes) and 7.4 (alite pastes) allow comparison of both sets of data. The possible composition in alite blends are in lower Ca*:Si regions compared to cement. Blends with slag and fly ash are somewhat restricted to Ca*:Si ≈ 1.30 or higher and to a maximum Al:Si ≈ 0.30. Silica fume and metakaolin blends were appropriate to reach C–A–S–H compositions farthest from that in OPC. Temperature and substitution levels, when both are increased, favour the reaction of SCMs which further lowers Ca*:Si (and increases Al:Si when alumina is present).

As mentioned briefly in the appendix, it is unclear how alumina may limit or not the decrease in Ca*:Si. It cannot be excluded that alumina limits the dissolution of silicate phases.

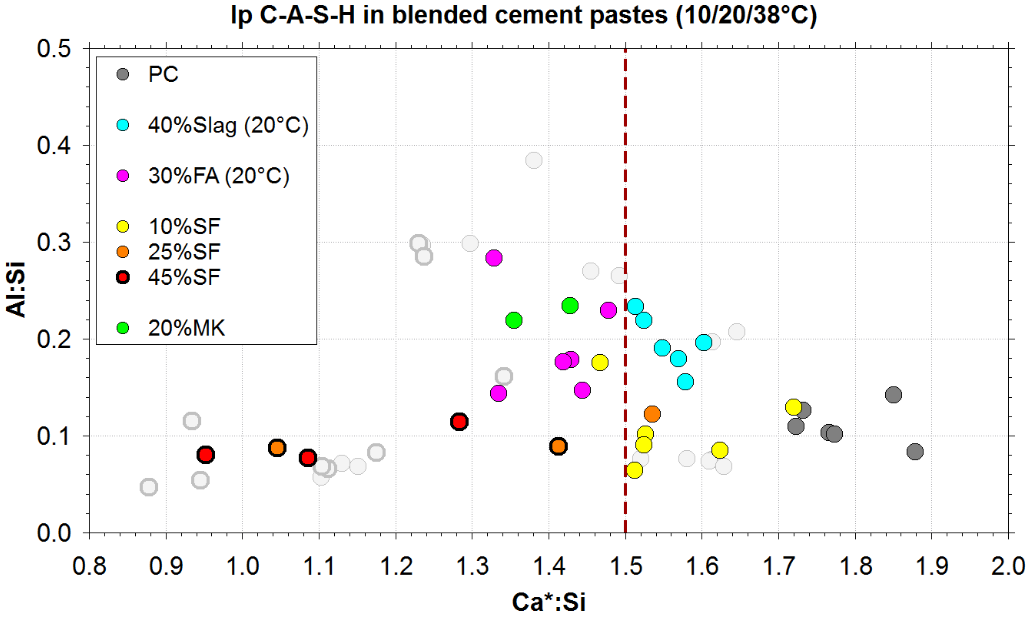

Figure 7.3: C–A–S–H composition in blended cement pastes. Points of samples with less than 2% normalised CH are bolder to indicate systems which are mostly free from Portlandite.

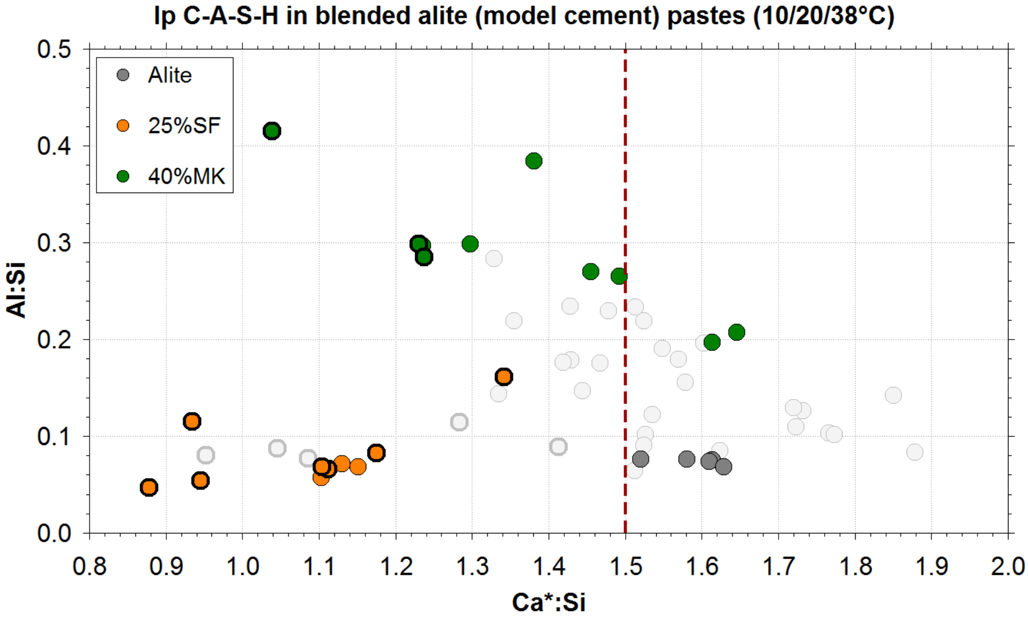

Figure 7.4: C–A–S–H composition in blended alite pastes. Points of samples with less than 2% normalised CH are bolder to indicate systems which are mostly free from Portlandite.

Decalcification as a dominant mechanism

Results from this thesis have shown that the impact of SCMs was significant on the final composition and morphology of C–A–S–H in pastes of low water:binder ratio, and that there are indications of interactions between CH and C–A–S–H. The main interaction appears to be decalcification of C–A–S–H, while consumption of CH is limited under some conditions.

When fibrillar C–A–S–H had initially formed – and assumed to be with a high Ca*:Si of 1.70-1.80 based on results on the Ip of silica fume blends – they were decalcified to reach values of Ca*:Si as low as 1.50 and persisted in blends still containing CH. This could be related to fast C–S–H precipitation during the first hours of cement hydration (in the presence of high calcium concentrations in solution) and later a slow conversion of the C–S–H to a thermodynamically more stable C–S–H with a Ca:Si of ≈ 1.50. In such systems foil-like C–A–S–H of Ca*:Si ≈ 1.30-1.50 co-existed with fibrillar C–A–S–H. Here the fibrillar morphology was not destabilised by the removal of calcium as also observed in carbonation experiments. Such results do not strongly support the idea of calcium being part of a jennite-like structure, in which calcium would not be readily “leached”.

When CH was still present in paste samples, the lowest Ca:Si in C–A–S–H was ≈ 1.30, while silica fume blends had C–A–S–H with Ca:Si as low as ≈ 0.90 after CH was entirely consumed by pozzolanic reaction. In silica fume blends, the highest measured Ca:Si in absence of CH was ≈ 1.20-1.50. This suggests that the presence of CH is a limiting factor in forming C–A–S–H with very low Ca:Si. It could indicate that as with data presented in solubility curves (e.g. Figure 2.5, p. 14), there may exist some local equilibrium in pastes at the point of saturation of CH in solution where the corresponding C–A–S–H would have a Ca:Si ≈ 1.20-1.50, rather than being precisely at Ca:Si = 1.50.

Morphology of the C–A–S–H phase

Results presented in this work further confirms that the foil-like morphology of C–A–S–H is the stable form for Ca:Si ≈ 1.50 or less. As seen in Figure 3.2, p. 32, the coarseness appears to correlate to the Ca:Si ratio as fine foil-like morphologies appeared at ratios ≈ 1.30-1.50 while better defined foils, with a “coarser” appearance in TEM, had values ranging 0.80-1.20.

High Ca:Si C–S–H – observed here in the Op with fibrillar morphology – has a very strong link to the growth of CH. It is still not clear if the growth CH is directly responsible for the directional morphology or if the activities of calcium and silica in solution are responsible for their formation. Foils of Ca:Si ≈ 1.70 have been observed by Richardson [15, 21] who described the Op C–S–H in a white cement paste activated with 5 M KOH to be “crumpled-foil Op C–S–H” in a sample containing microcrystalline C–S–H. Recent TEM images from E. Tajuelo [55] of controlled hydration of C_3S showed somewhat fibrillar C–S–H of Ca:Si ≈ 1.75 which had grown just over the point of calcium saturation with respect to CH. Ongoing work by A. Kumar [56] has also shown that synthetic C–S–H of Ca:Si ≈ 1.90 may be prepared in less than a few hours in specific conditions and with foil-like C–S–H morphology. Here no CH had precipitated.

When CH is absent, paste samples appear closer to equilibrium. In the scope of the current work, synthetic samples of aimed Ca:Si = 1.00 prepared by E. L'Hôpital showed foil-like morphology (Figure 7.5) which are very similar to the silica fume blends (e.g. images from Figure 6.15, p. 113). Here the preparation times were of at least six months and can be assumed to be at equilibrium. This suggests that the pastes with no more CH are better able to form C–A–S–H with the more stable foil-like morphology of low Ca:Si C–A–S–H.

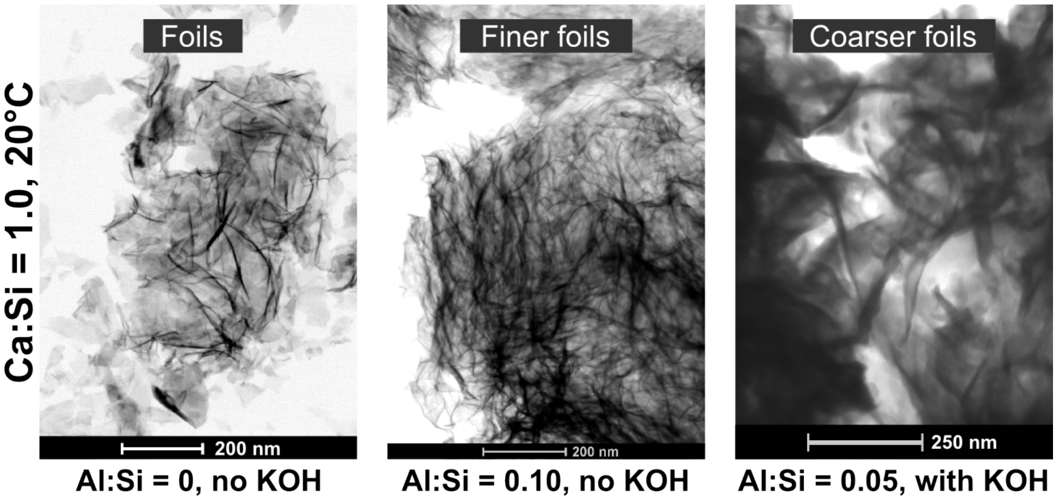

Figure 7.5: C–A–S–H morphologies observed in synthetic samples.

It is not clear to what extent the two main morphologies in fact represent a unique C–S–H phase. If one reasons in terms of small building blocks (monomers and dimers are dominant during early hydration, e.g. [24]), those building blocks likely do not stack well and cause defects. Nothing would prevent them from arranging into different morphologies. This could be a reason why there exists a spectrum of morphologies (thin or thick fibrils, fine to coarse foils) which are curves due to stacking defects. This is unlike synthetic tobermorite which appears as platelets (e.g. [101]).

Importance of the pore solution

Much of the work on the chemical stability of C–A–S–H is done in dilute conditions because it is impossible to otherwise control the solution. Pore solution extraction from paste samples can be used to determine the concentration of the different species during the first months, and with greater difficulty after the first year depending on the initial water:binder ratio. It can then be linked to the solid phases and thermodynamic modelling [3].

Results on the silica fume blends showed the existence of two Ip C–S–H rims. It is most likely that the existence of both regions are due to the time evolution of the pore solution.

Unpublished results from B. Lothenbach [98] on silica fume blends and results of F. Deschner from fly ash blends [102, 103] show than not only are there large variations over time, but that the temperature can have a significant impact on the pore solution in pastes.

The comparison between the two sets of alite-silica fume blends (see Figure 6.11, p. 108) revealed that the Ca:Si of the C–A–S–H is affected by the presence of gypsum and aluminate in the raw mix. These are certainly affected by the pore solution which is changed in presence of sulphate and aluminate ions.

In general, it appears that in cement paste, the activity of the ionic species in solution – particularly that of Ca^{2+} in the local environment – dictates the formation of the solids which then tend to persist. It was discussed earlier how the activity of calcium can change the formed morphology e.g. in dilute reaction of C_3S.

Knowing this, it seems that the equilibrium exists between the pore solution and the solids which should form. What complicates matters is that as long as material can dissolve, true equilibrium cannot be reached because the pore solution will constantly evolve. It could very well be that a better understanding of the pore solution will significantly help bridge the gap between the knowledge on the behavior of dilute systems and what is occurring in the very constrained conditions of pastes of low water:binder ratio.

7.4 Influence of alumina

In the matured series of samples, it appeared that Al redistributes between C–A–S–H and other phases. As suggested by previous work, more Al could enter C–S–H for lower Ca:Si. This is not contradicted by the points of C–A–S–H composition in Figure 7.2.

This point is not discussed further because results from the metakaolin blends – shown in the Appendix, p. 131 – are complicated to interpret, both from a compositional and morphological point of view. The overall Al:Si could reach values of ≈ 0.5 and were considered highly doubtful. Also, the morphology is very fine-scale and somewhere between fibrils and fine foils, but not as well defined as in other blends. It appeared that the products forming in the Op regions are either highly intermixed even at the scale of the TEM or there could maybe be a solid solution occurring between C–A–S–H and other “CASH” phases. It is therefore unclear how very high concentrations of alumina in solution could destabilise the C–A–S–H to form other phases. For these reasons the reader is referred to the summary of results in the Appendix p. 131.

8 Conclusions and perspectives

The thesis aimed to better understand the link between C–A–S–H composition and morphology in realistic pastes and to compare results on synthetic preparations.

8.1 Methodology for assessing the C–A–S–H composition by SEM-EDS

A detailed study on the parameters influencing the results obtained by SEM-EDS was done on a white cement sample hydrated for five years (water:binder = 0.4, 20°C). It was found that a good correlation between results from intermixed points measured by SEM-EDS and measurements of pure C–A–S–H obtained by STEM-EDS were possible. This relies on several conditions.

- The use of experimental parameters which minimize damage to the sample. They include low current, low current density and low exposure times.
- The manual choice of points. This allows to separate contributions from the Ip and Op C–A–S–H, to avoid interfaces and optimise the acquisition time to record mostly "useful measurements" which is important for the data treatment.
- The consideration of atomic ratios, with and without correction by aluminium substitution and sulphate adsorption. This facilitates comparison between different systems.
- The use of complementary representations which include 2D ratio plots, frequency histograms and box plots. They allow to identify other phases intermixed with C–A–S–H and apply very simple data treatment.
- The consideration of the "least-intermixed" measurements which is backed-up by STEM-EDS measurements of pure C–A–S–H. In many cases the disadvantage of intermixing in SEM-EDS can be overcome and permits the analysis of larger areas compared to TEM

and a higher number of samples for a same amount of time. This is more problematic in the Op of silica fume and metakaolin blends.

8.2 Pastes still containing Portlandite

OPC and alite pastes

Comparison between alite and OPC showed that the main features are similar in both pastes. The formation of Ip and Op was observed. The Op was fibrillar in both cases. Temperature had no visible effect on the composition of the C–S–H. Alkali did not have any significant effect either. However there were differences between both types of reference systems.

- The Ca*:(Si+Al) ratio (with Ca* = Ca - S) was systematically lower in alite compared to pure cement. In alite Ca*:Si was ≈ 1.50-1.60 compared to ≈ 1.80 in cements. This could be related to the presence of aluminate phase and sulphate.
- In alite, the Op forms in straight packets, while in OPC, it fans out (see Figure 5.2, p. 66). This seems also linked to aluminate and sulphate as suggested by results from other projects in our laboratory.

Matured systems with SCMs

Characterisation of matured systems still containing Portlandite showed that the presence of SCMs has a big impact on the composition and morphology of the C–A–S–H. Three cements were blended with five SCMs and hydrated for several years.

In such systems the relative consumption of CH seemed to depend mostly on the SCM. The relative consumption was almost identical for all three cements used here.

The Ca*:Si in such pastes showed values of ≈ 1.30-1.60 and Ca*:(Si+Al) ≈ 1.00-1.40, all significantly below values for pure cement. The Al:Si in C–A–S–H was higher than in OPC and correlated quite well to the total Al:Si.

In binary blends with slag, fly ash and 10% silica fume, the Op C–A–S–H appeared more homogeneous in polished sections for SEM. Three samples examined by STEM showed the following morphology and composition.

- Fibrillar Op C–A–S–H was present in large amounts even after 3-5 years. They had formed on the surface of clinker or SCM grains. Their composition in two blends was Ca*:Si ≈ 1.50-1.60, lower than ≈ 1.80 in pure cement.
- Foil-like C–A–S–H formed in the originally water-filled space, inside clinker grains or inside SCM grains. Their composition ranged Ca*:Si ≈ 1.30-1.50. They contained more

alumina than the fibrils.

8.3 Silica fume blends

As observed by isothermal calorimetry at 20°C, silica fume affects the kinetics of the early age reaction of OPC by accelerating the silicate reaction and enhancing the aluminate reaction.

The microstructure as seen by SEM is strongly changed by the presence of small to large amount of silica fume additions. In pastes of water:binder = 0.4, the Op appeared dense by the presence of silica fume particles. Hadley grains − typical of OPC − were larger and persisted longer before being filled with products. CH formed mostly as platelets rather than large agglomerates. When it agglomerated it did so around clinker or alite grains to for a CH rim which did not necessarily cover the whole of the grain.

The microstructure at 90 days is dominated by foil-like C–A–S–H which bears strong resemblance to synthetic preparations. In one system, fibrillar C–A–S–H appeared to have formed on quartz particles. Based on three samples studied by STEM, the composition of the C–A–S–H and the morphology seem to be related. Foils with Ca:Si ≈ 1.30-1.40 are finer than those with values down to 0.90 which have a coarser appearance.

The silica fume blends have a foil-like morphology which is essentially the same as in synthetic samples from E. L'Hôpital with aimed Ca:Si = 1.0.

The pozzolanic reaction was followed over time. The decrease in CH was accompanied by a decrease in Ca:Si of the C–A–S–H from the Ip regions. Around ≈ 1.20-1.50 (depending on the set of samples) CH no longer was detected. Then values of Ca:Si reached as low as 0.8. Temperature accelerated this reaction but the trend was similar.

Characterisation of the Ip C–A–S–H in all blends from this work as well as from other projects revealed that there are often two Ip regions. When they were clearly visible and separately measurable, the innermost Ip had a lower final Ca:Si than the outermost Ip (a difference of Ca:Si ≈ 0.10-0.20). The outer rim is mostly C–A–S–H from the initial OPC hydration − with high Ca:Si − or the CH rim which were converted to lower Ca:Si C–A–S–H. It was referred to as "Early Ip". The innermost Ip, which appeared darker in SEM rim is hypothesised as being low Ca:Si C–A–S–H which forms when the solution directly favors its formation. It was referred to as "Later Ip". In alite systems the rims were always visible, while they were not always observed in OPC blends.

A comparison between the model systems (alite and silica fume) containing gypsum and aluminate and those without showed that the composition of the C–A–S–H and the amount of CH were different. In absence of gypsum and aluminate the final Ca:Si was lower and CH was present in several samples. In presence of gypsum and aluminate, only one sample still had CH and the Ca:Si was higher.

8.4 Discussion on the stability of C–A–S–H in cement pastes

The range of compositions for C–A–S–H was found to be Ca*:Si = 0.80-1.90, with a reliable maximum observed Al:Si of ≈ 0.30.

The results from this thesis and those from other studies strongly suggest that the calcium from the C–A–S–H phase is mobile for ratios of Ca:Si ≥ 1.00-1.30 and could point to a tobermorite/"solid-solution CH" model as defined in [21] rather than the coexistence of two types of C–A–S–H phases in a same sample. This could be the reason we can observe a spectrum of morphologies.

In paste samples of low water:binder, it appears that the consumption of CH are strongly linked. When the decrease in CH is limited, it appears that the decrease iin Ca*:Si is also limited. Once CH is consumed, the system is able to reach far lower Ca:Si.

It could be that a sound knowledge of the phase in both dilute conditions and paste samples will come from better understanding the impact of the pore solution on the composition and morphology of the solids.

8.5 Perspectives

The thesis has brought new insights into the relation between the composition and morphology of the C–A–S–H in realistic pastes of low water:binder ratio and shown important points to consider in pastes which are different than synthetic preparations. The importance of the pore solution was highlighted in the discussion and may become central in bridging the gap between the knowledge on dilute reaction and the knowledge on paste samples.

It would therefore be interesting to study the pore solution in similar systems to complement the current study and obtain more information on the evolution of C–A–S–H formation over time.

The effect of temperature was not examined by STEM and could provide valuable insight into the impact it has on the morphology.

In Figure 7.2, there is an area between the composition of C–A–S–H of silica fume blends and that of metakaolin blends which could be explored e.g. by formulating ternary blends of cement (or alite) with both metakaolin and silica fume as replacements.

Because of difficulties in estimating the composition of C–A–S–H by SEM-EDS in metakaolin blends and the variability of Al:Si in STEM-EDS, the results on those mixes should be further investigated. ^{27}Al and ^{29}Si MAS-NMR experiments would have been interesting to provide another measurement of the Al:Si in such samples, provided the deconvolution is possible.

During the final C–A–S–H workshop held at Empa in Dübendorf, Switzerland on May 5th and 6th 2014, it became obvious that renewed collaborative efforts can go a long way in sharing expertise for the numerous techniques and converging towards a better knowledge of the C–A–S–H phase. This should be emphasised for the research in cement chemistry which has become extremely multidisciplinary over the last decades with new and better materials characterisation methods.

A Data on blended pastes containing metakaolin

Three series of samples were prepared with water:binder ratio of 0.4 and hydrated for 90 days. There were two model cement systems based on alite and metakaolin. One series was prepared with alite and metakaolin (MC-MK) while a second also contained aluminate and gypsum (MC*-MK). A series with cement and metakaolin was also prepared (PC-MK). Some gypsum was added to the cement-metakaolin mixes to try and properly sulphate the mix and limit the reaction of aluminate during the first hours.

Results were complicated to interpret because the high possible amount of aluminium in solution. This was caused by the reaction of metakaolin which favours the formation not only of C–A–S–H but monosulfoaluminate and more crystalline "CASH" phases such as strätlingite. This was observed in a previous project [91] where intermixing of phases seem to occur between unreacted metakaolin, strätlingite, monosulfoaluminate and the elusive C–A–S–H phase at the lowest values for Al:Ca. It was reasonably estimated at the "least intermixed" edge of all the points. The same procedure was applied here by using the appropriate values from the fitted distributions as it will shown in the two main situations. Contrary to bedore, the Al:Si was determined by taking (Al:Ca*):(Si:Ca*).

A.1 Microstructure development

At the scale of the observations which can be made by SEM on polished sections, it is clear that the substitution of cement by metakaolin has a big impact on the microstructure of the paste. The overall reaction of the anhydrous grains for 90 days of hydration was qualitatively lower than in pure systems and silica fume systems.

In cement-metakaolin blends shown in Figures A.1 (a)- (b) and (c)- (d) – for replacements of 20% and 40% respectively – the outer regions is filled with unreacted metakaolin particles and C–A–S–H and show a strong or complete consumption of CH. The inner product C–A–S–H regions have formed around the clinker grains. The outer region has a somewhat "messy" appearance but on a very small scale. In Figures A.1 (e)- (f) the outer region has a coarser appearance with what seems to be platelet-shaped phases which prevented the formation of inner product C–A–S–H. The grain on the bottom-right of Figure A.1 (f) is clearly devoid of inner product C–A–S–H. Few regions of apparent inner product where analysed but where not C–A–S–H, as further suggested in Figures A.9 (a)- (b).

Alite blends with metakaolin not containing C_3A and gypsum took a few days to a week to form a cohesive paste. The longest time a paste took to set was with no alkali and low temperature. When C_3A and gypsum were part of the formulated mix, the paste could set in less than a day like the cement blends. In alite blends shown in Figures A.2 (a)- (b) and (c)- (d), we observe a similar microstructure. The outer product region is “messy”, and inner product regions have formed. While the blend in Figures A.2 (a)- (b) contained no C_3A and gypsum, the blend in Figures A.2 (c)- (d) contained both C_3A and gypsum. C_3A did not completely react. Figures A.2 (e)- (f) show the same blend but hydrated at higher temperature. The outer-product region is very heterogeneous and was composed mainly of monosulfoaluminate and strätlingite.

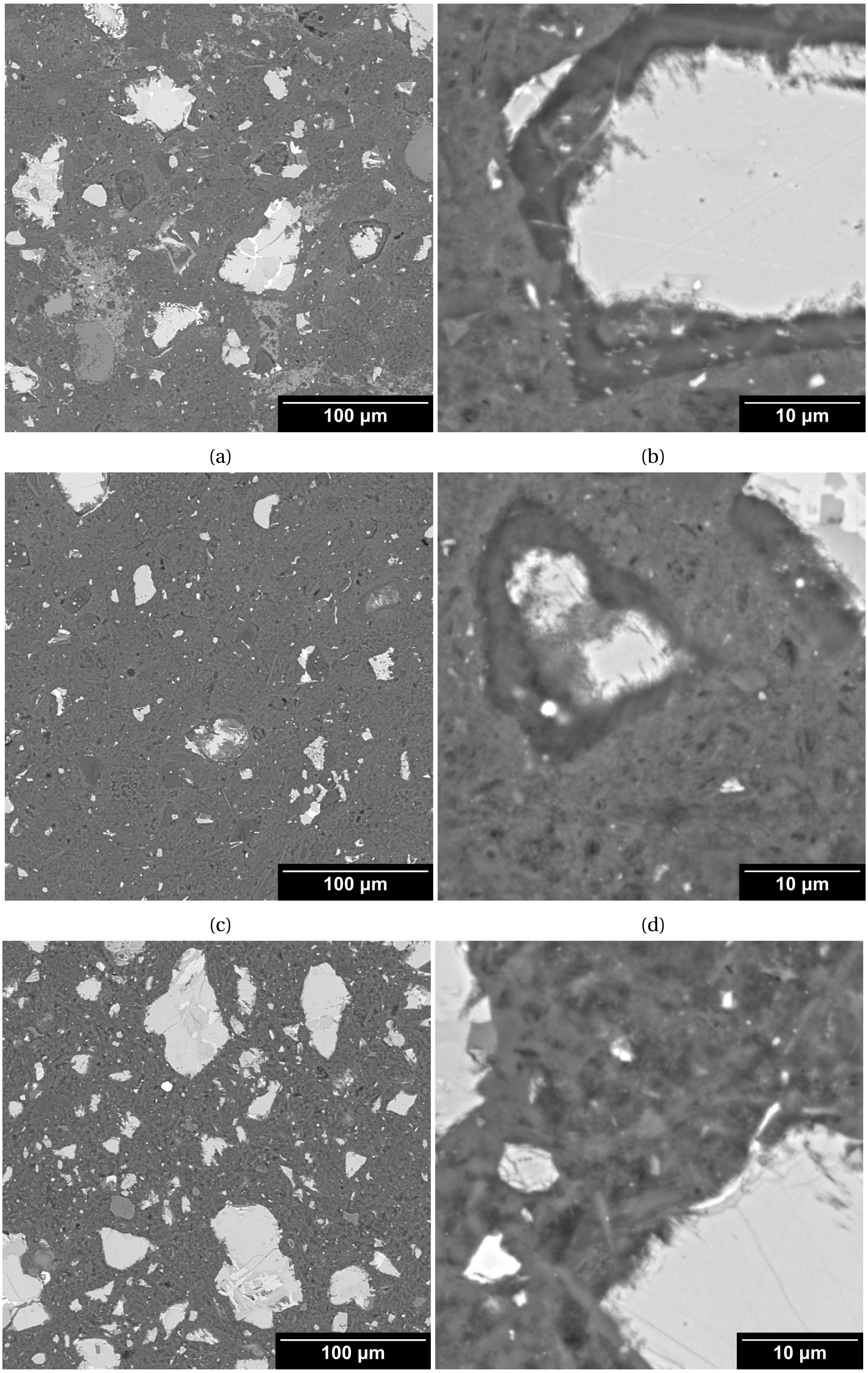

(a) (b)

(c) (d)

(e) (f)

Figure A.1: SEM images of the cement-metakaolin blends. (a)- (b) PC-20MK T10. (c)- (d) PC-40MK T20. (e)- (f) PC-20MK T38.

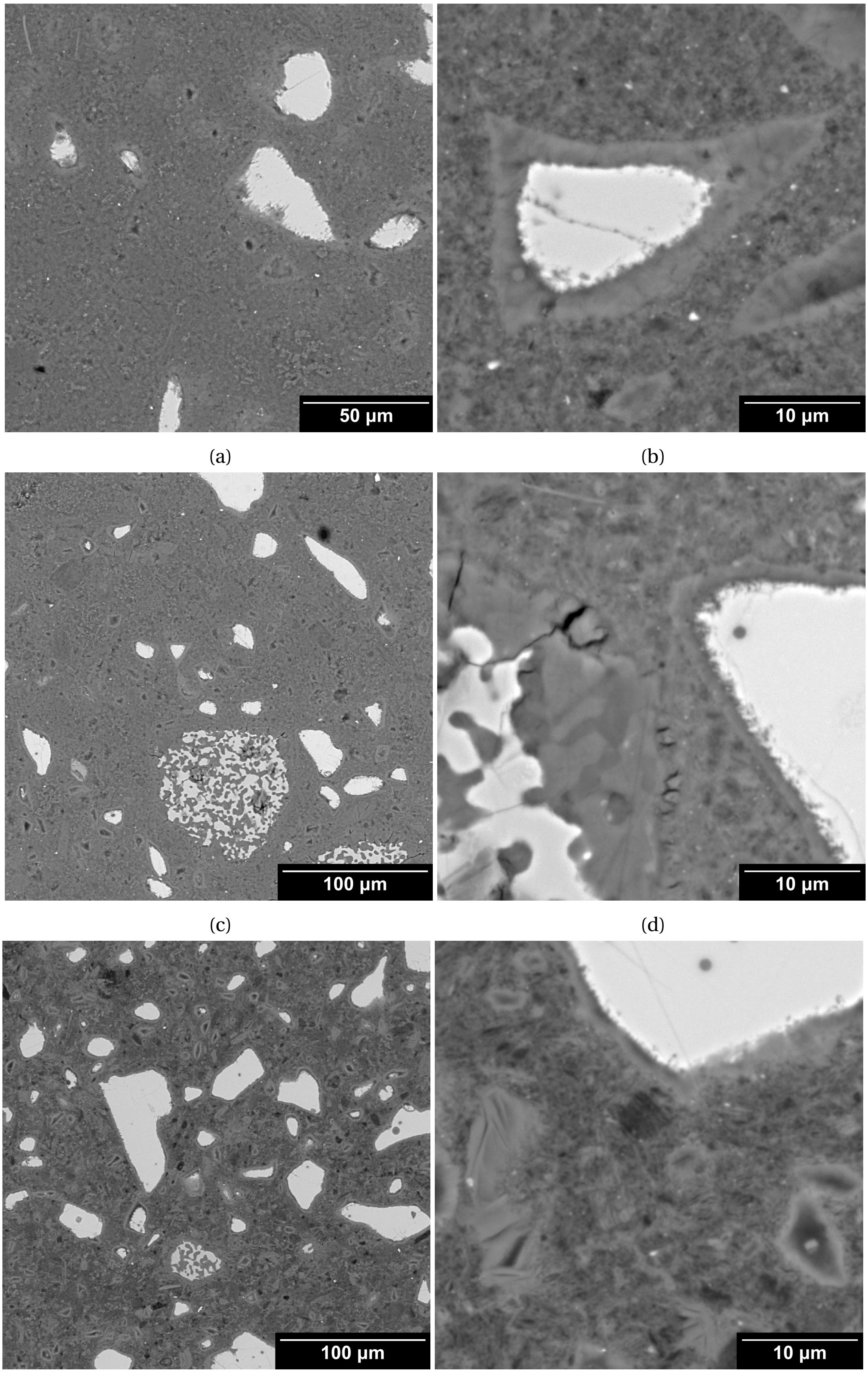

(a) (b)

(c) (d)

(e) (f)

Figure A.2: SEM images of the alite-metakaolin blends. (a) - (b) MC-MK T20 with no alkali. (c) - (d) MC*-MK T20 0.5 M KOH. (e) - (f) MC*-MK T38 0.5 M KOH.

A.2 Morphology of the C–A–S–H

There appears to be a change in morphology in blends with metakaolin compared to the systems with only OPC or alite. In Figure A.3, the microstructure of the PC-20MK T20 cement blend is very heterogeneous and shows the presence of unreacted metakaolin particles (see Figure A.4 for a map which illustrates this), regions with somewhat fibrillar C–A–S–H which grew outwards from a small surface, and a fine-scale foil-like morphology in the Op regions. SEM-EDS analyses suggested that C–A–S–H was intimately mixed with AFm phases. STEM-EDS suggests the same thing. The Al:Si was very high, often ≈ 0.35-0.40 regardless of the size of the chosen area for quantification.

In the alite-metakaolin blend (sample MC*-MK T20 0.1 M KOH, Figure A.5), things are less clear in terms of morphology. It appears somewhat fibrillar or somewhat foil-like. The quantification by EDS gave a Ca*:Si in analysed areas ranging ≈ 1.00-1.20 and an Al:Si ratio of ≈ 0.45-0.90. Areas of strätlingite were found (Figure A.6) but did not stand out morphologically. Strätlingite appears to not form in well defined regions of the microstructure unlike in synthetic preparations (Figure A.7) where platelets of strätlingite were observed to form in between packets of foil-like C–A–S–H.

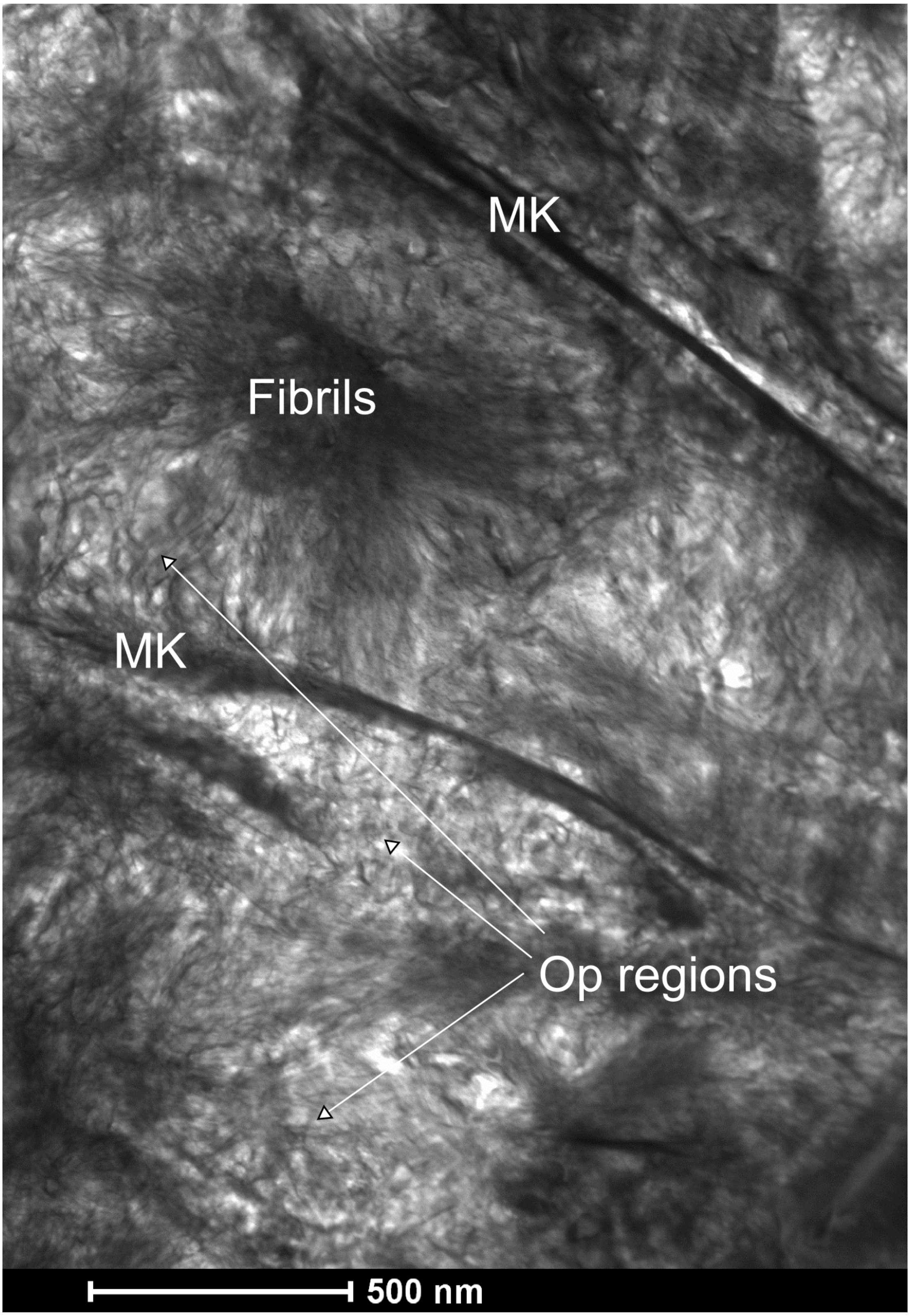

Figure A.3: BF STEM image of the PC-20MK T20 blend.

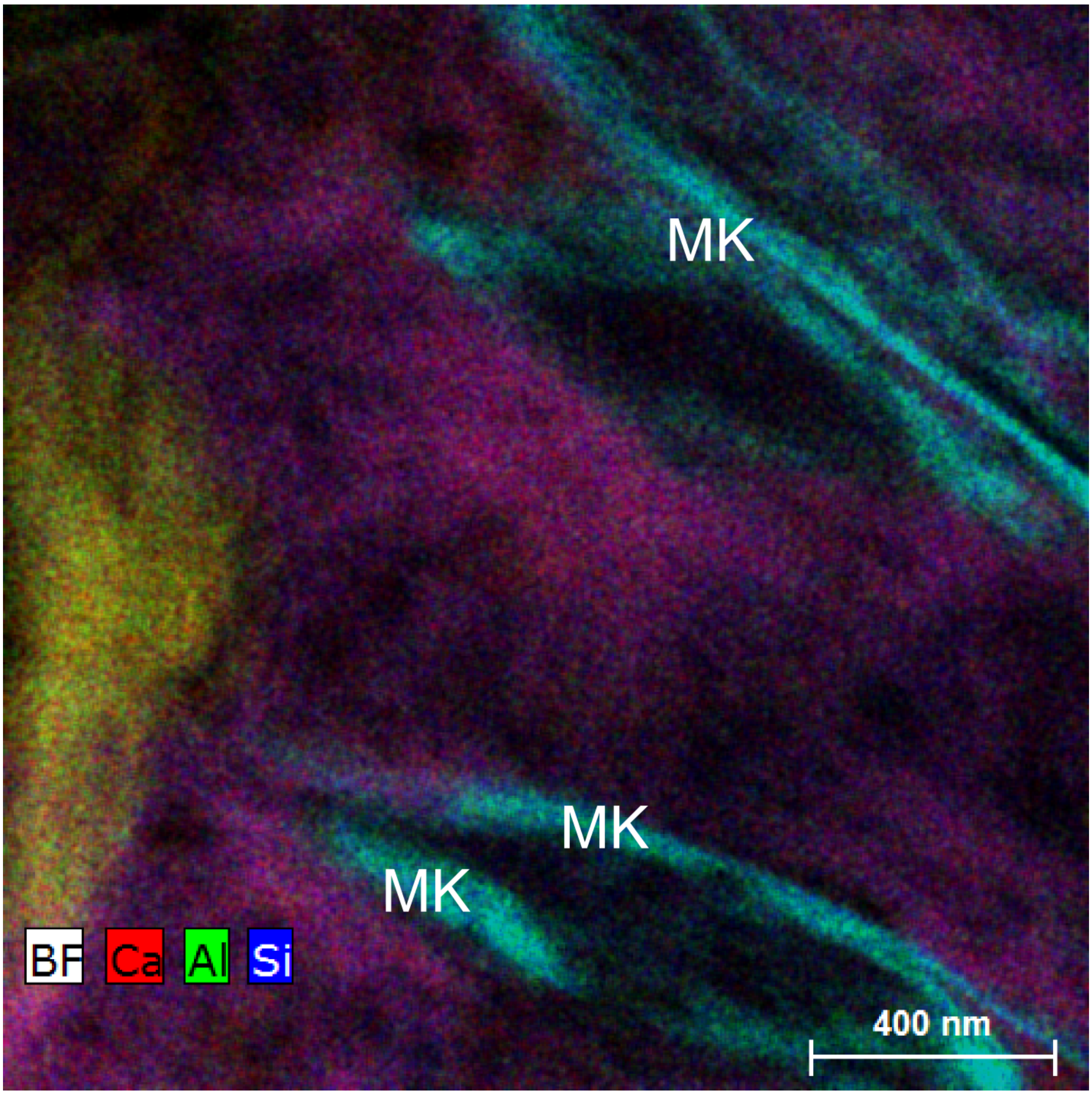

Figure A.4: Raw compositional map of the PC-20MK T20 blend. Pixels were averaged over the 3 neighbouring pixels.

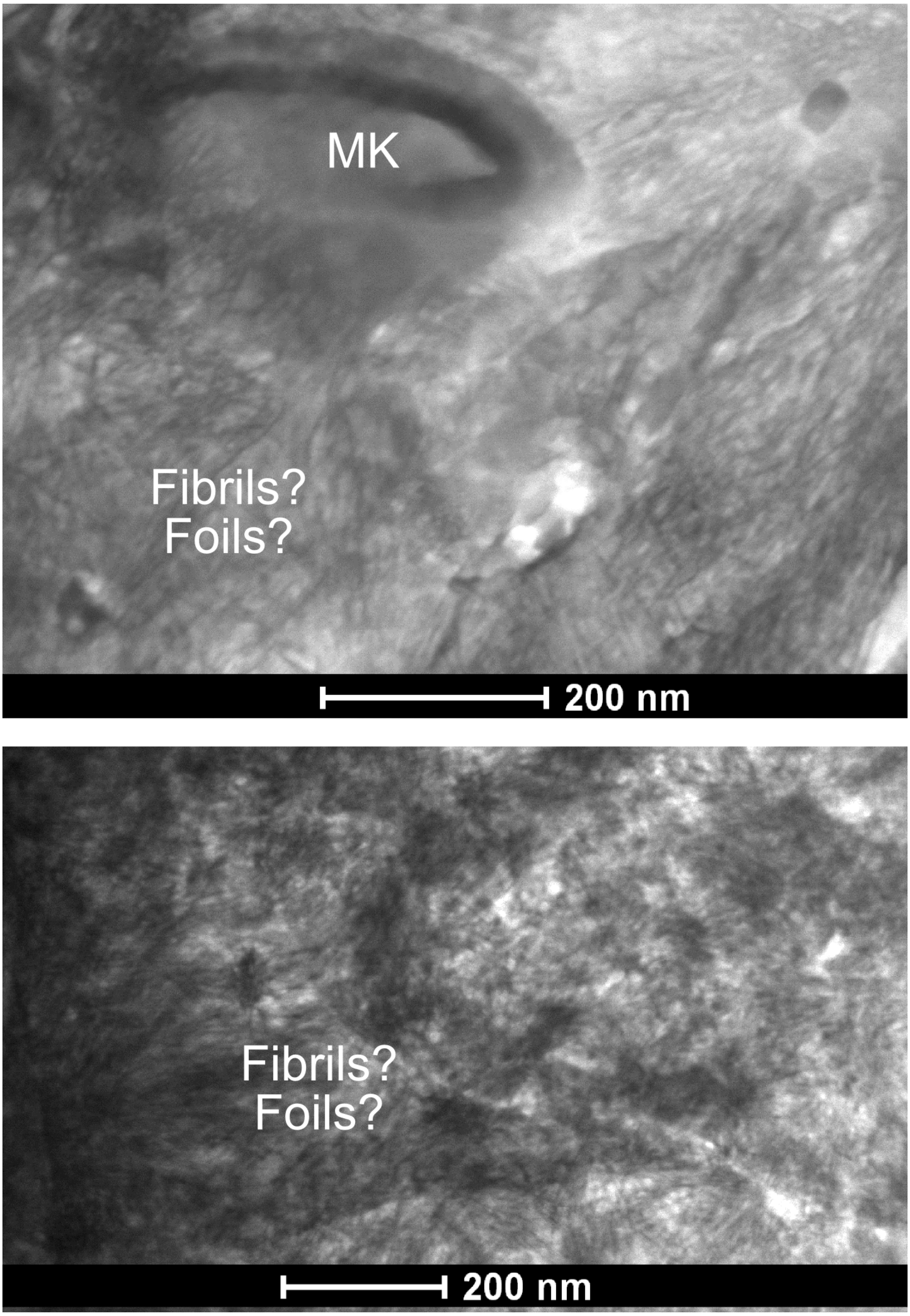

Figure A.5: BF STEM image of the MC*-MK T20 0.1 M KOH blend.

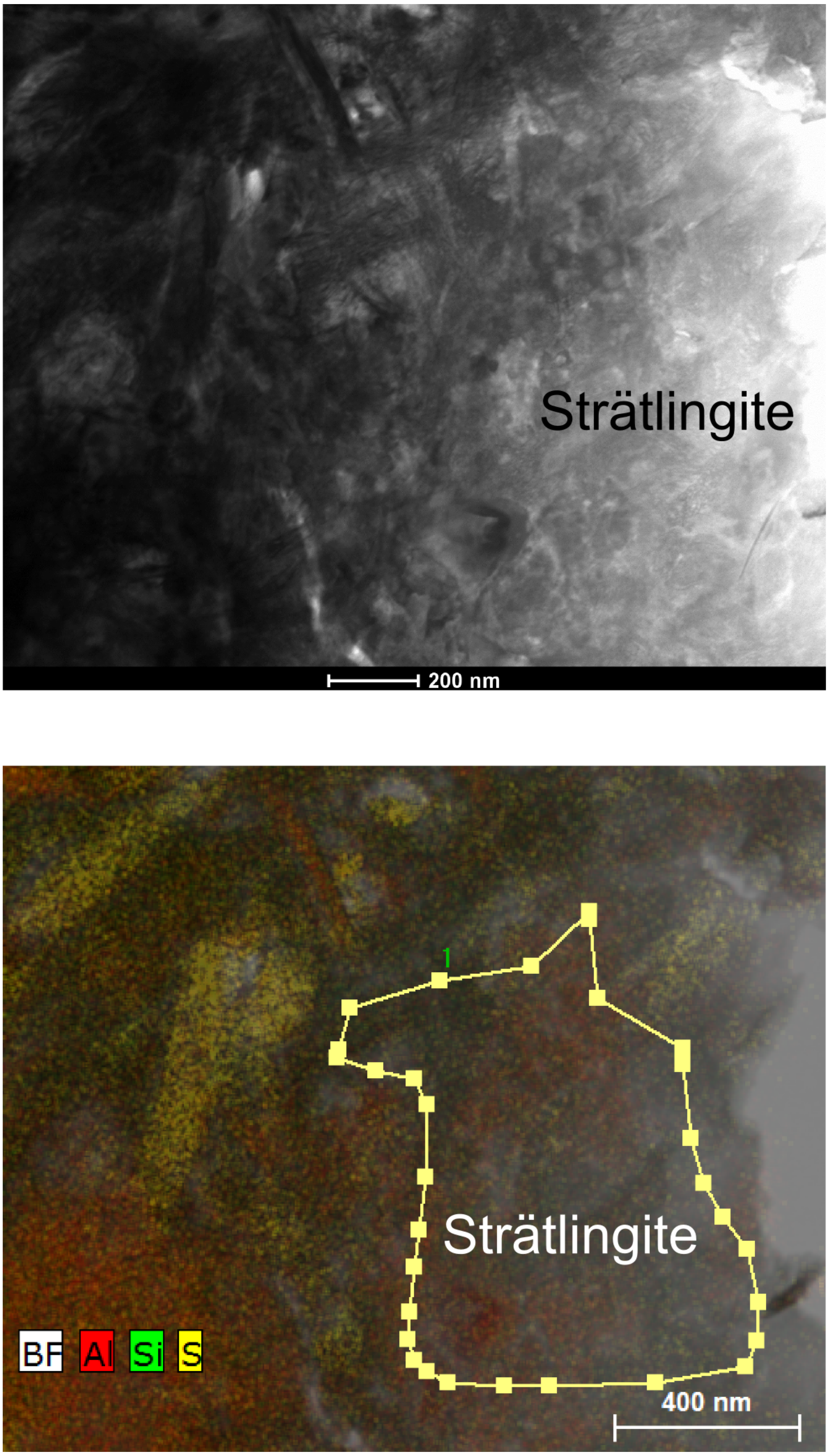

Figure A.6: (Top) BF image and (bottom) map of the MC*-MK T20 0.1 M KOH blend in a strätlingite region. Pixels were averaged over the 3 neighbouring pixels.

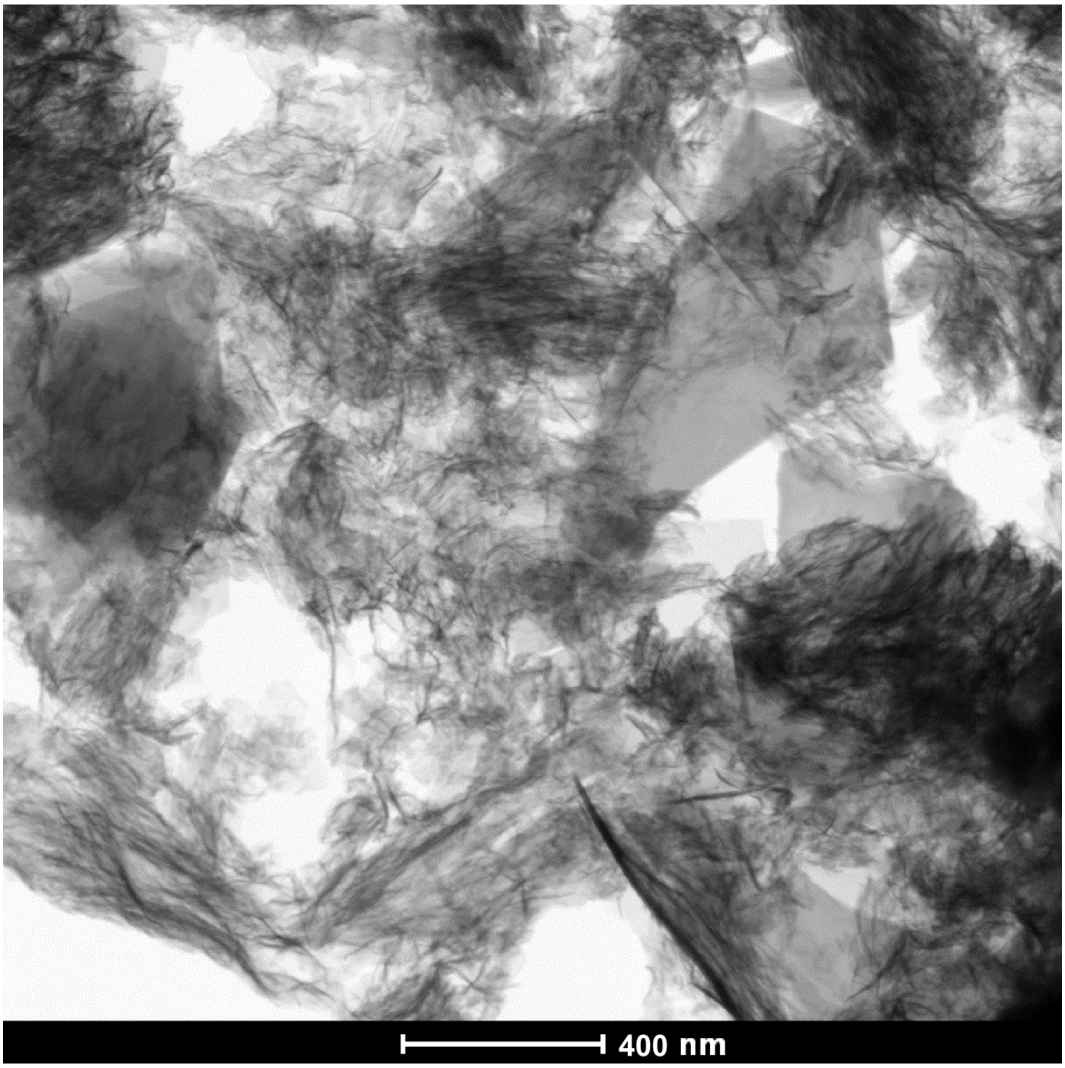

Figure A.7: Synthetic C–A–S–H containing strätlingite. The aimed ratios were Ca:Si = 1.00, Al:Si = 0.20. Strätlingite formed in distinctive platelets which were very sensitive to the electron beam.

A.3 Estimated composition

Even when analyses of inner and outer product regions where possible, the degree of intermixing was very high in all systems. Two examples where STEM-EDS was carried out in complement to SEM-EDS show that an estimation of the “least-intermixed” C–A–S–H can be obtained for alite blends by taking the average of the inner product points by SEM (Figures A.8 (a)- (b)) or the higher Si:Ca* values (Figures A.8 (c)- (d)) depending on the system studied.

Examples from Figure A.9 show that strätlingite is highly intermixed in SEM-EDS analyses and that points for C–A–S–H are too few to estimate the composition with any confidence.

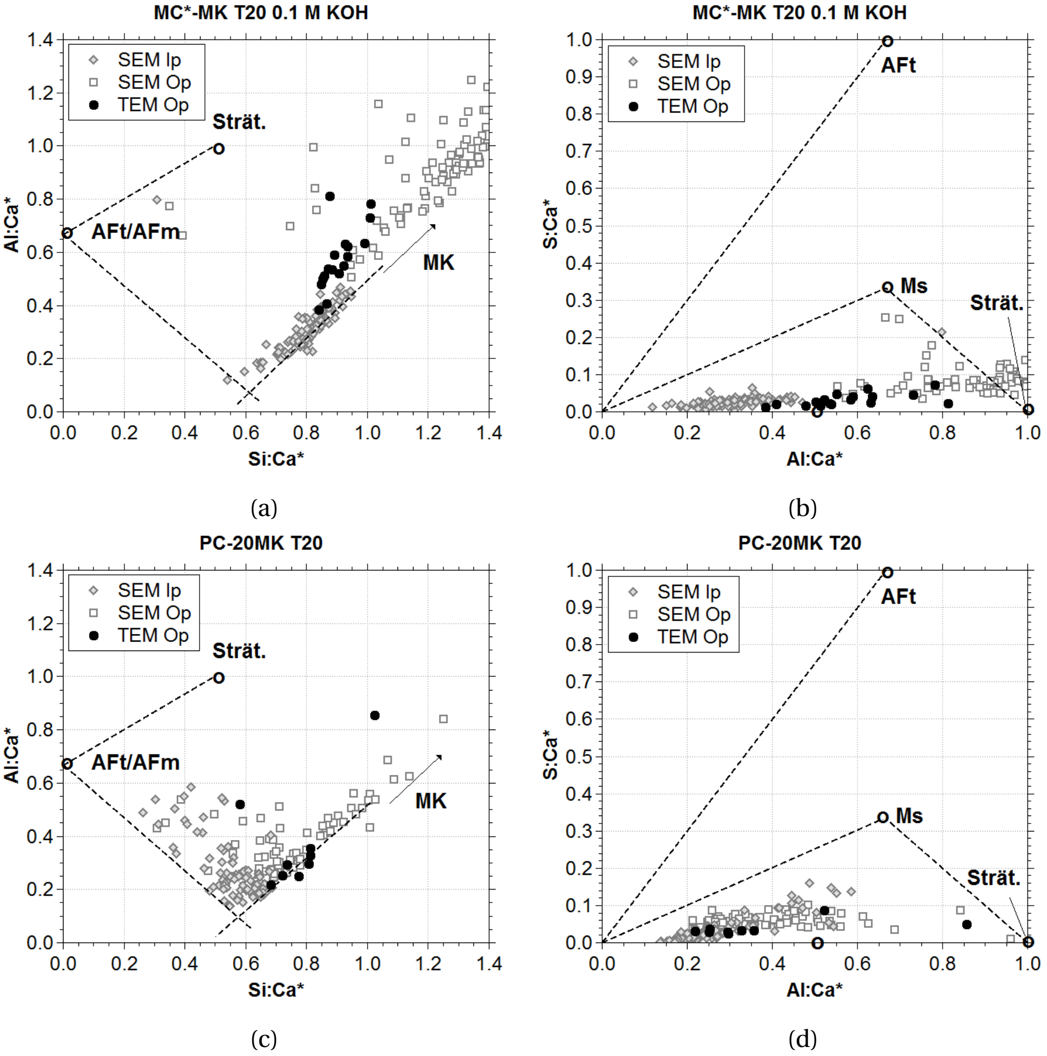

(a)

(b)

(c)

(d)

Figure A.8: (a)- (b) MC*-MK T20 0.1 M KOH. (c)- (d) PC-20MK T20.

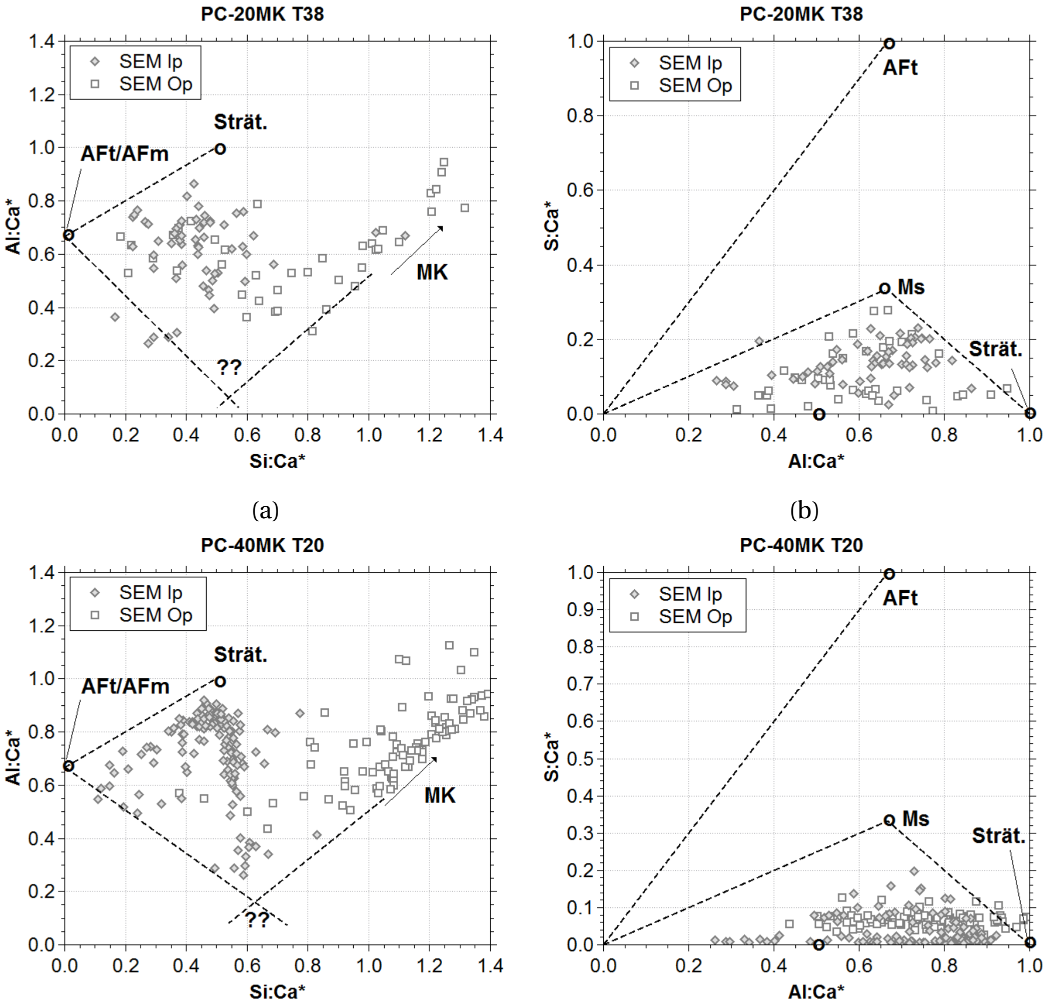

(a) (b)

(c) (d)

Figure A.9: (a)- (b) PC-20MK T38. (c)- (d) PC-40MK T20.

A.4 Comments

It is unclear to what extent we are dealing with extremely fine-scale formation of both C–A–S–H and strätlingite or whether there could exist a solid-solution between both phases because of the highly constrained nature of pastes with low water:binder ratio.

As mentioned at the end of the general discussion (p. 124), the values for Al:Si are very high considering the structure for C–A–S–H and the experimental results by NMR. The high values are not necessarily an overestimation from the STEM-EDS. Also, the morphology is somewhat fibrillar or somewhat foil-like and is not as well defined as in the synthetic sample observed in Figure A.7.

The overall decrease in Ca*:Si is less than the silica fume blends (see Figure 7.2, p. 120) and could partly explain why the fibrillar or foil-like morphology is not as well defined. Also, the thinner inner product regions seen in SEM could suggest that the high amount of aluminate in the system can somehow strongly hinder the dissolution of the silicate phases.

Bibliography

[1] J. Damtoft, J. Lukasik, D. Herfort, D. Sorrentino, E. Gartner, Sustainable development and climate change initiatives, Cement and Concrete Research 38 (2) (2008) 115–127.
URL http://www.sciencedirect.com/science/article/pii/S0008884607002153

[2] Where is the sector now? (2013).
URL http://lowcarboneconomy.cembureau.eu/index.php?page=where-is-the-sector-now

[3] B. Lothenbach, T. Matschei, G. Möschner, F. P. Glasser, Thermodynamic modelling of the effect of temperature on the hydration and porosity of portland cement, Cement and concrete research 38 (1) (2008) 1–18.

[4] B. Lothenbach, F. Winnefeld, Thermodynamic modelling of the hydration of portland cement, Cement and Concrete Research 36 (2) (2006) 209–226.

[5] B. Lothenbach, K. Scrivener, R. D. Hooton, Supplementary cementitious materials, Cement and Concrete Research 41 (12) (2011) 1244–1256.
URL http://www.sciencedirect.com/science/article/pii/S0008884610002632

[6] B. Lothenbach, D. Damidot, T. Matschei, J. Marchand, Thermodynamic modelling: state of knowledge and challenges, Advances in Cement Research 22 (4) (2010) 211–223, WOS:000282093100005.

[7] P. Hawkins, P. D. Tennis, R. J. Detwiler, The use of limestone in Portland cement: a state-of-the-art review, Portland Cement Association Skokie, IL, 2003.

[8] I. G. Richardson, The nature of c–s–h in hardened cements, Cement and Concrete Research 29 (8) (1999) 1131–1147.

[9] I. G. Richardson, G. W. Groves, Microstructure and microanalysis of hardened ordinary portland cement pastes, Journal of Materials Science 28 (1) (1993) 265–277.
URL http://apps.webofknowledge.com/full_record.do?product=UA&search_mode=GeneralSearch&qid=6&SID=R2@ciaHmaAHp72HE366&page=1&doc=3

[10] Taylor, H.F.W., Cement Chemistry, 2nd Edition, Thomas Telford, 1997.

[11] L. Dent Glasser, E. Lachowski, K. Mohan, H. Taylor, A multi-method study of c3s hydration, Cement and Concrete Research 8 (6) (1978) 733–739.
URL http://www.sciencedirect.com/science/article/pii/0008884678900820

[12] I. G. Richardson, G. W. Groves, Models for the composition and structure of calcium silicate hydrate (c–s–h) gel in hardened tricalcium silicate pastes, cement and concrete research 22 (6) (1992) 1001–1010.

[13] L. Dent Glasser, E. Lachowski, M. Qureshi, H. Calhoun, D. Embree, W. Jamieson, C. Masson, Identification of some of the polysilicate components of trimethylsilylated cement paste, Cement and Concrete Research 11 (5–6) (1981) 775–780.
URL http://www.sciencedirect.com/science/article/pii/0008884681900363

[14] I. G. Richardson, G. W. Groves, The incorporation of minor and trace elements into calcium silicate hydrate (c–s–h) gel in hardened cement pastes, Cement and Concrete Research 23 (1) (1993) 131–138.

[15] I. Richardson, G. Groves, The structure of the calcium silicate hydrate phases present in hardened pastes of white portland cement/blast-furnace slag blends, Journal of materials science 32 (18) (1997) 4793–4802.

[16] H. F. w. Taylor, Proposed structure for calcium silicate hydrate gel, Journal of the American Ceramic Society 69 (6) (1986) 464–467.
URL http://onlinelibrary.wiley.com/doi/10.1111/j.1151-2916.1986.tb07446.x/abstract

[17] T. H.F.W., Nanostructure of c–s–h: Current status, Advanced Cement Based Materials 1 (1) (1993) 38–46.
URL http://www.sciencedirect.com/science/article/pii/106573559390006A

[18] E. Bonaccorsi, S. Merlino, A. R. Kampf, The crystal structure of tobermorite 14 Å (plombierite), a c–s–h phase, Journal of the American Ceramic Society 88 (3) (2005) 505–512.
URL http://onlinelibrary.wiley.com/doi/10.1111/j.1551-2916.2005.00116.x/abstract

[19] E. Bonaccorsi, S. Merlino, H. F. W. Taylor, The crystal structure of jennite, ca9si6o18(OH)6·8h2o, Cement and Concrete Research 34 (9) (2004) 1481–1488.
URL http://www.sciencedirect.com/science/article/pii/S0008884604000134

[20] K. Garbev, M. Bornefeld, G. Beuchle, P. Stemmermann, Cell dimensions and composition of nanocrystalline calcium silicate hydrate solid solutions. part 2: X-ray and thermogravimetry study, Journal of the American Ceramic Society 91 (9) (2008) 3015–3023.
URL http://onlinelibrary.wiley.com/doi/10.1111/j.1551-2916.2008.02601.x/abstract

[21] I. G. Richardson, Tobermorite/jennite-and tobermorite/calcium hydroxide-based models for the structure of c–s–h: applicability to hardened pastes of tricalcium silicate,[beta]-dicalcium silicate, portland cement, and blends of portland cement with blast-furnace slag, metakaolin, or silica fume, Cement and Concrete Research 34 (9) (2004) 1733–1777.

[22] X. Cong, R. Kirkpatrick, Si MAS NMR study of the structure of calcium silicate hydrate, Advanced Cement Based Materials 3 (3-4) (1996) 144–156.
URL http://sciverse-shindig.elsevier.com/gadgets/ifr?container=default&mid=4&nocache=1&country=ALL&lang=ALL&view=profile&parent=http%3A%2F%2Fwww.sciencedirect.com%2Fscience%2Farticle%2Fpii%2FS1065735596900462%3A%2F%2Fwww.sciencedirect.com&up_startMeInvisible=y&up_shindigProxyBaseUrl=sciverse-shindig.elsevier.com&st=john.doe:john.doe:appid:cont:url:0:default&url=http%3A%2F%2Fae-content.elsevier.com%2Fsvapp%2F293358%2Fprod%2Fprivate%2Fspec.xml#rpctoken=1006317007

[23] A. Nonat, X. Lecoq, The structure, stoichiometry and properties of c–s–h prepared by c3s hydration under controlled conditions, in: Nuclear Magnetic Resonance Spectroscopy of Cement-Based Materials, Springer, Berlin, 1998, pp. 197–207.

[24] K. Mohan, H. Taylor, A trimethylsilylation study of tricalcium silicate pastes, Cement and Concrete Research 12 (1) (1982) 25–31.
URL http://www.sciencedirect.com/science/article/pii/0008884682900953

[25] P. Yu, R. J. Kirkpatrick, B. Poe, P. F. McMillan, X. Cong, Structure of calcium silicate hydrate c–s–h near-, mid-, and far-infrared spectroscopy, Journal of the American Ceramic Society 82 (3) (1999) 742–748.
URL http://onlinelibrary.wiley.com/doi/10.1111/j.1151-2916.1999.tb01826.x/abstract

[26] I. G. Richardson, The calcium silicate hydrates, Cement and Concrete Research 38 (2) (2008) 137–158.

[27] J. J. Chen, J. J. Thomas, H. F. Taylor, H. M. Jennings, Solubility and structure of calcium silicate hydrate, Cement and Concrete Research 34 (9) (2004) 1499–1519.
URL http://www.sciencedirect.com/science/article/pii/S000888460400211X

[28] A. Nonat, The structure and stoichiometry of c–s–h, Cement and Concrete Research 34 (9) (2004) 1521–1528.
URL http://apps.webofknowledge.com/full_record.do?product=UA&search_mode=GeneralSearch&qid=11&SID=1DBg3idEMg@f91lgPmK&page=1&doc=2

[29] H. Stade, W. Wieker, Zum aufbau schlecht geordneter calciumhydrogensilicate. i. bildung und eigenschaften einer schlecht geordneten calciumhydrogendisilicatphase, Zeitschrift für anorganische und allgemeine Chemie 466 (1) (1980) 55–70.
URL http://onlinelibrary.wiley.com/doi/10.1002/zaac.19804660107/abstract

[30] G. W. Groves, I. G. Richardson, D. I. Rodway, The carbonation of hardened cement pastes, Advances in Cement Research 3 (11) (1990) 117–125.
URL http://www.icevirtuallibrary.com/content/article/10.1680/adcr.1990.3.11.117

[31] G. W. Groves, A. Brough, I. G. Richardson, C. M. Dobson, Progressive changes in the structure of hardened c3s cement pastes due to carbonation, Journal of the American

Ceramic Society 74 (11) (1991) 2891–2896.
URL http://onlinelibrary.wiley.com/doi/10.1111/j.1151-2916.1991.tb06859.x/abstract

[32] I. G. Richardson, C. M. Dobson, G. W. Groves, A. R. Brough, The carbonation of OPC and OPC/silica fume hardened cement pastes in air under conditions of fixed humidity, Advances in Cement Research 5 (18) (1993) 81–86.
URL http://www.icevirtuallibrary.com/content/article/10.1680/adcr.1993.5.18.81

[33] S. Grangeon, F. Claret, C. Lerouge, F. Warmont, T. Sato, S. Anraku, C. Numako, Y. Linard, B. Lanson, On the nature of structural disorder in calcium silicate hydrates with a calcium/silicon ratio similar to tobermorite, Cement and Concrete Research 52 (2013) 31–37.
URL http://www.sciencedirect.com/science/article/pii/S0008884613001208

[34] S. Grangeon, F. Claret, Y. Linard, C. Chiaberge, X-ray diffraction: a powerful tool to probe and understand the structure of nanocrystalline calcium silicate hydrates, Acta Crystallographica Section B Structural Science Crystal Engineering and Materials 69 (5) (2013) 465–473.
URL http://scripts.iucr.org/cgi-bin/paper?S2052519213021155

[35] J. Taplin, A method for following the hydration reaction in portland cement paste, Australian Journal of Applied Science 10 (3) (1959) 329–345.

[36] V. Kocaba, Development and evaluation of methods to follow microstructural development of cementitious systems including slags, Ph.D. thesis, École Polytechnique Fédérale de Lausanne (2009).

[37] E. Gallucci, P. Mathur, K. Scrivener, Microstructural development of early age hydration shells around cement grains, Cement and Concrete Research 40 (1) (2010) 4–13.
URL http://www.sciencedirect.com/science/article/pii/S0008884609002579

[38] K. L. Scrivener, P. Pratt, Microstructural studies of the hydration of c 3 a and c 4 AF independently and in cement paste, in: Proc. Br. Ceram. Soc., 1984, p. 207.

[39] A. Bazzoni, Study of early hydration mechanisms of cement by means of electron microscopy, Ph.D. thesis, EPFL, Lausanne (2014).

[40] I. G. Richardson, G. W. Groves, Microstructure and microanalysis of hardened cement pastes involving ground granulated blast-furnace slag, Journal of Materials Science 27 (1992) 6204–6212.
URL http://www.springerlink.com/content/x7051l012608w0h0/

[41] A. Girão, I. Richardson, R. Taylor, R. Brydson, Composition, morphology and nanostructure of c–s–h in 70% white portland cement-30% fly ash blends hydrated at 55 °c., Cement and Concrete Research 40 (9) (2010) 1350–1359.
URL http://www.sciencedirect.com/science/article/B6TWG-4YW37GX-1/2/67988944df24cad03ddca4ade6065ec4

[42] M. D. Andersen, H. J. Jakobsen, J. Skibsted, Characterization of white portland cement hydration and the c-s-h structure in the presence of sodium aluminate by 27al and 29si MAS NMR spectroscopy, Cement and Concrete Research 34 (5) (2004) 857–868.
URL http://www.sciencedirect.com/science/article/pii/S0008884603003661

[43] M. D. Andersen, H. J. Jakobsen, J. Skibsted, Incorporation of aluminum in the calcium silicate hydrate (c–s–h) of hydrated portland cements: A high-field 27al and 29si MAS NMR investigation, Inorganic Chemistry 42 (7) (2003) 2280–2287.
URL http://pubs.acs.org/doi/abs/10.1021/ic020607b

[44] I. G. Richardson, The nature of the hydration products in hardened cement pastes, Cement and Concrete Composites 22 (2) (2000) 97–113.
URL http://www.sciencedirect.com/science/article/B6TWF-4019BRW-2/2/ac59c6d9d6e68141f4dc4b84ab61b467

[45] R. Taylor, I. Richardson, R. Brydson, Composition and microstructure of 20-year-old ordinary portland cement-ground granulated blast-furnace slag blends containing 0 to 100% slag, Cement and Concrete Research 40 (7) (2010) 971–983.
URL http://www.sciencedirect.com/science/article/B6TWG-4YN4X7X-3/2/589add005472c7bf588aaed0dae7d322

[46] C. Love, I. Richardson, A. Brough, Composition and structure of c–s–h in white portland cement-20% metakaolin pastes hydrated at 25 °c, Cement and Concrete Research 37 (2) (2007) 109–117.
URL http://www.sciencedirect.com/science/article/B6TWG-4MK0HX8-2/2/84c6e6ff2883e862987764357497ce17

[47] H. Stade, D. Müller, G. Scheler, Zum aufbau schlecht geordneter calciumhydrogensilicate. v 27ai-NMR-spektroskopische untersuchungen zur koordination des al in c–s–h (di, poly), Zeitschrift für anorganische und allgemeine Chemie 510 (3) (1984) 16–24.
URL http://onlinelibrary.wiley.com/doi/10.1002/zaac.19845100304/abstract

[48] H. Stade, D. Müller, On the coordination of al in ill-crystallized c-s-h phases formed by hydration of tricalcium silicate and by precipitation reactions at ambient temperature, Cement and Concrete Research 17 (4) (1987) 553–561.
URL http://www.sciencedirect.com/science/article/pii/0008884687901281

[49] M. D. Andersen, H. J. Jakobsen, J. Skibsted, A new aluminium-hydrate species in hydrated portland cements characterized by 27al and 29si MAS NMR spectroscopy, Cement and Concrete Research 36 (1) (2006) 3–17.
URL http://www.sciencedirect.com/science/article/pii/S0008884605001146

[50] I. G. Richardson, A. R. Brough, R. Brydson, G. W. Groves, C. M. Dobson, Location of aluminum in substituted calcium silicate hydrate (c-s-h) gels as determined by 29si and 27al NMR and EELS, Journal of the American Ceramic Society 76 (9) (1993) 2285–2288.

[51] X. Pardal, F. Brunet, T. Charpentier, I. Pochard, A. Nonat, Al-27 and si-29 solid-state NMR characterization of calcium-aluminosilicate-hydrate, Inorganic Chemistry 51 (3) (2012) 1827–1836, WOS:000300474700076.

[52] P. Faucon, A. Delagrave, C. Richet, J. M. Marchand, H. Zanni, Aluminum incorporation in calcium silicate hydrates (c–s–h) depending on their ca/si ratio, The Journal of Physical Chemistry B 103 (37) (1999) 7796–7802.
URL http://pubs.acs.org/doi/abs/10.1021/jp990609q

[53] S. Komarneni, R. Roy, D. M. Roy, C. A. Fyfe, G. J. Kennedy, A. A. Bothner-By, J. Dadok, A. S. Chesnick, 27al and 29si magic angle spinning nuclear magnetic resonance spectroscopy of al-substituted tobermorites, Journal of Materials Science 20 (11) (1985) 4209–4214.
URL http://link.springer.com/article/10.1007/BF00552416

[54] I. Garcia Lodeiro, A. Fernández-Jimenez, A. Palomo, D.E Macphee, Effect on fresh c–s–h gels of the simultaneous addition of alkali and aluminium, Cement and Concrete Research 40 (1) (2010) 27–32.
URL http://www.sciencedirect.com/science/article/pii/S0008884609002051

[55] E. Tajuelo, Private communication.

[56] A. Kumar, Private communication.

[57] R. Taylor, I. G. Richardson, R. M. D. Brydson, Nature of c-s-h in 20 year old neat ordinary portland cement and 10% portland cement-90% ground granulated blast furnace slag pastes, Advances in Applied Ceramics 106 (6) (2007) 294–301, WOS:000251791400003.

[58] M. M. Fernández, Effect of particle size on the hydration kinetics and microstructural development of tricalcium silicate, Ph.D. thesis, École Polytechnique Fédérale de Lausanne (2008).

[59] A. Quennoz, Hydration of c3a with calcium sulfate alone and in the presence of calcium silicate, Ph.D. thesis, École Polytechnique Fédérale de Lausanne (2011).

[60] V. Kocaba, E. Gallucci, K. L. Scrivener, Methods for determination of degree of reaction of slag in blended cement pastes, Cement and Concrete Research 42 (3) (2012) 511–525.
URL http://www.sciencedirect.com/science/article/pii/S000888461100295X

[61] H. Taylor, D. Newbury, Calcium hydroxide distribution and calcium silicate hydrate composition in tricalcium silicate and beta-dicalcium silicate pastes, Cement and Concrete Research 14 (1) (1984) 93–98.
URL http://www.sciencedirect.com/science/article/pii/000888468490084X

[62] M. Stucke, A. Majumdar, The composition of the gel phase in portland cement paste, Cement and Concrete Association, Slough, 1976, pp. 31–51.

[63] K. O. Kjellsen, A. Monsøy, K. Isachsen, R. J. Detwiler, Preparation of flat-polished specimens for SEM-backscattered electron imaging and x-ray microanalysis—importance of epoxy impregnation, Cement and Concrete Research 33 (4) (2003) 611–616.
URL http://www.sciencedirect.com/science/article/pii/S0008884602010293

[64] S. Diamond, Identification of hydrated cement constituents using a scanning electron microscope energy dispersive x-ray spectrometer combination, Cement and Concrete Research 2 (5) (1972) 617–632.
URL http://www.sciencedirect.com/science/article/pii/0008884672901159

[65] S. Diamond, C/s mole ratio of c-s-h gel in a mature c3s paste as determined by edxa, Cement and Concrete Research 6 (3) (1976) 413–416.
URL http://www.sciencedirect.com/science/article/pii/0008884676901058

[66] D. L. Rayment, A. J. Majumdar, The composition of the CSH phases in portland cement pastes, Cement and Concrete Research 12 (6) (1982) 753–764.
URL http://www.sciencedirect.com/science/article/pii/0008884682900394

[67] J. Bensted, P. Barnes (Eds.), Structure and Performance of Cements, second edition Edition, Spon Press, London, 2002.

[68] E. Lifshin, N. Doganaksoy, J. Sirois, R. Gauvin, Statistical considerations in microanalysis by energy-dispersive spectrometry, Microscopy and Microanalysis 4 (06) (1998) 598–604.

[69] L. Sawyer, D. C. Joy, D. Newbury, P. Echlin, C. Lyman, J. R. Michael, J. Goldstein, E. Lifshin, Scanning Electron Microscopy and X-ray Microanalysis - Third Edition, Springer, Berlin, 2003.
URL http://www.springer.com/materials/characterization+%26+evaluation/book/978-0-306-47292-3

[70] I. Richardson, L. Black, J. Skibsted, R. Kirkpatrick, Characterisation of cement hydrate phases by TEM, NMR and raman spectroscopy, Advances in Cement Research 22 (4) (2010) 233–248.
URL http://apps.webofknowledge.com/full_record.do?product=UA&search_mode=GeneralSearch&qid=3&SID=X2CL7c9mP2gH3Hf9ePh&page=1&doc=2

[71] N. W. Ritchie, D. E. Newbury, J. M. Davis, EDS measurements of x-ray intensity at WDS precision and accuracy using a silicon drift detector, Microscopy and Microanalysis 18 (04) (2012) 892–904.

[72] G. Cliff, G. W. Lorimer, The quantitative analysis of thin specimens, Journal of Microscopy 103 (2) (1975) 203–207.
URL http://onlinelibrary.wiley.com/doi/10.1111/j.1365-2818.1975.tb03895.x/abstract

[73] R. Barbarulo, H. Peycelon, S. Leclercq, Chemical equilibria between c–s–h and ettringite, at 20 and 85 °c, Cement and Concrete Research 37 (8) (2007) 1176–1181.
URL c

[74] C. Labbez, A. Nonat, I. Pochard, B. Jönsson, Experimental and theoretical evidence of overcharging of calcium silicate hydrate, Journal of Colloid and Interface Science 309 (2) (2007) 303–307.
URL http://www.sciencedirect.com/science/article/pii/S0021979707002445

[75] C. Labbez, I. Pochard, B. Jönsson, A. Nonat, C-s-h/solution interface: Experimental and monte carlo studies, Cement and Concrete Research 41 (2) (2011) 161–168.
URL http://www.sciencedirect.com/science/article/pii/S0008884610002310

[76] B. J. Dalgleish, P. L. Pratt, R. I. Moss, Preparation techniques and the microscopical examination of portland cement paste and c3s, Cement and Concrete Research 10 (5) (1980) 665–676.
URL http://www.sciencedirect.com/science/article/pii/0008884680900307

[77] C. Rößler, J. Stark, F. Steiniger, W. Tichelaar, Limited-dose electron microscopy reveals the crystallinity of fibrous c–s–h phases, Journal of the American Ceramic Society 89 (2) (2006) 627–632.
URL http://onlinelibrary.wiley.com/doi/10.1111/j.1551-2916.2005.00714.x/abstract

[78] R. Egerton, P. Li, M. Malac, Radiation damage in the TEM and SEM, Micron 35 (6) (2004) 399–409.
URL http://www.sciencedirect.com/science/article/pii/S0968432804000381

[79] C. Famy, A. Brough, H. Taylor, The c-s-h gel of portland cement mortars: Part i. the interpretation of energy-dispersive x-ray microanalyses from scanning electron microscopy, with some observations on c-s-h, AFm and AFt phase compositions, Cement and Concrete Research 33 (9) (2003) 1389–1398.
URL http://www.sciencedirect.com/science/article/pii/S0008884603000644

[80] S. Chatterji, N. Thaulow, Estimation of the chemical composition of precipitated phase by the electron beam microanalytical technique, X-Ray Spectrometry 9 (1) (1980) 5–7.
URL http://onlinelibrary.wiley.com/doi/10.1002/xrs.1300090104/abstract

[81] CIME/FEI super-x meeting, 13-14.02.2014, EPFL, lausanne.

[82] P. Yu, J. R. Kirkpatrick, Thermal dehydration of tobermorite and jennite, Concrete Science and Engineering 1 (3) (1999) 185–191.

[83] G. W. Groves, P. J. Sueur, W. Sinclair, Transmission electron microscopy and microanalytical studies of ion-beam-thinned sections of tricalcium silicate paste, Journal of the American Ceramic Society 69 (4) (1986) 353–356.
URL http://onlinelibrary.wiley.com/doi/10.1111/j.1151-2916.1986.tb04746.x/abstract

[84] K. O. Kjellsen, H. Justnes, Revisiting the microstructure of hydrated tricalcium silicate—a comparison to portland cement, Cement and Concrete Composites 26 (8) (2004) 947–956.
URL http://www.sciencedirect.com/science/article/pii/S0958946504000460

[85] E. Gallucci, K. Scrivener, Crystallisation of calcium hydroxide in early age model and ordinary cementitious systems, Cement and Concrete Research 37 (4) (2007) 492–501.
URL http://www.sciencedirect.com/science/article/pii/S0008884607000026

[86] B. Mota Gassó, Private communication.

[87] S. Galmarini, A. Aimable, N. Ruffray, P. Bowen, Changes in portlandite morphology with solvent composition: Atomistic simulations and experiment, Cement and Concrete Research 41 (12) (2011) 1330–1338.
URL http://www.sciencedirect.com/science/article/pii/S0008884611001207

[88] A. Muller, Porosity characterisation across different cementitious binders by a multi-technique approach, Ph.D. thesis, EPFL, Lausanne (2014).

[89] E. Gallucci, X. Zhang, K. Scrivener, Effect of temperature on the microstructure of calcium silicate hydrate (c-s-h), Cement and Concrete Research 53 (2013) 185–195.

[90] E. Berodier, Private communication.

[91] M. Antoni, J. Rossen, F. Martirena, K. Scrivener, Cement substitution by a combination of metakaolin and limestone, Cement and Concrete Research 42 (12) (2012) 1579–1589.
URL http://www.sciencedirect.com/science/article/pii/S0008884612002074

[92] B. Lothenbach, D. Rentsch, E. Wieland, Hydration of a silica fume blended low-alkali shotcrete cement, Physics and Chemistry of the Earth, Parts A/B/C.
URL http://www.sciencedirect.com/science/article/pii/S1474706513001241

[93] T. C. Holland, United States, Federal Highway Administration, Silica fume user's manual, Federal Highway Administration, Washington, D.C., 2005.

[94] G. W. Groves, S. A. Rodger, The hydration of c3s and ordinary portland cement with relatively large additions of micro silica, Advances in Cement Research 2 (8) (1989) 135–140.
URL http://www.icevirtuallibrary.com/content/article/10.1680/adcr.1989.2.8.135

[95] C. M. Dobson, D. G. C. Goberdhan, J. D. F. Ramsay, S. A. Rodger, 29si MAS NMR study of the hydration of tricalcium silicate in the presence of finely divided silica, Journal of Materials Science 23 (11) (1988) 4108–4114.
URL http://link.springer.com/article/10.1007/BF01106844

[96] A. Quennoz, K. L. Scrivener, Interactions between alite and c3a-gypsum hydrations in model cements, Cement and Concrete Research 44 (2013) 46–54.
URL http://www.sciencedirect.com/science/article/pii/S0008884612002372

[97] R. Barbarulo, Comportement des materiaux cimentaires: Actions des sulfates et de la temperature, Ph.D. thesis, ProQuest Dissertations And Theses; Thesis (Ph.D.)–Universite Laval (Canada), 2003.; Publication Number: AAINQ86729; ISBN: 9780612867291; Source:

Dissertation Abstracts International, Volume: 65-01, Section: B, page: 0334.; 267 p. (2003).
URL http://adsabs.harvard.edu/abs/2003PhDT.......201B

[98] B. Lothenbach, Private communication.

[99] A. C. A. Muller, K. L. Scrivener, A. M. Gajewicz, P. J. McDonald, Densification of c–s–h measured by 1h NMR relaxometry, The Journal of Physical Chemistry C 117 (1) (2013) 403–412.
URL http://dx.doi.org/10.1021/jp3102964

[100] Z. Dai, J. Skibsted, Private communication.

[101] D. Viehland, L. J. Yuan, Z. Xu, X. Cong, R. J. Kirkpatrick, Structural studies of jennite and 1.4 nm tobermorite: Disordered layering along the [100] of jennite, Journal of the American Ceramic Society 80 (12) (1997) 3021–3028.
URL http://onlinelibrary.wiley.com/doi/10.1111/j.1151-2916.1997.tb03228.x/abstract

[102] F. Deschner, F. Winnefeld, B. Lothenbach, S. Seufert, P. Schwesig, S. Dittrich, F. Goetz-Neunhoeffer, J. Neubauer, Hydration of portland cement with high replacement by siliceous fly ash, Cement and Concrete Research 42 (10) (2012) 1389–1400.
URL http://www.sciencedirect.com/science/article/pii/S0008884612001585

[103] F. Deschner, B. Lothenbach, F. Winnefeld, J. Neubauer, Effect of temperature on the hydration of portland cement blended with siliceous fly ash, Cement and Concrete Research 52 (2013) 169–181.
URL http://www.sciencedirect.com/science/article/pii/S0008884613001671

- CURRICULUM VITAE -

John ROSSEN
Av. d'Ouchy 75
1006 Lausanne

28 years old
Swiss nationality

+41 78 794 08 61
john.espen.rossen@gmail.com

Professional experiences

2010-2014 **Laboratory of construction materials (LMC), EPFL, Lausanne**

Teaching activities
- Teaching practical work to bachelor students.
- Assistant for *Introduction à la science des matériaux* given by Prof. Rappaz and Prof. Sorin.

Management inside the laboratory.
- Person in charge of the SEM and training new users.
- IT manager.

2009-2010 **Poseidon Helpdesk, EPFL, Lausanne**
IT support to students.

Research projects

2010-2014 **Laboratory of construction materials (LMC), EPFL, Lausanne**
Ph.D. thesis in collaboration with Empa
- *Composition and morphology of C-A-S-H in blended pastes of alite and cement*

2009-2010 **Laboratory of construction materials (LMC), EPFL, Lausanne**
Master project in collaboration with UCLV, university of Santa Clara in Cuba
- *Ternary cement blends based on metakaolin and limestone*

Studies

2010-2014 **EPFL, Lausanne, Switzerland**
Ph.D. student at Laboratory of construction materials (LMC)

2008-2010 **EPFL, Lausanne, Switzerland**
Master in Materials science and engineering
- Orientation: *Structural materials for transport, energy and infrastructure*

2009-2010 **EPFL, Lausanne, Switzerland**
Minor in Management, Technology and Entrepreneurship

2005-2008 **EPFL, Lausanne, Switzerland**
Bachelor in Materials science and engineering

Technical skills

Characterisation methods	SEM-EDS, TEM-EDS, TGA, XRD, Isothermal calorimetry
Programming	C, php, LabVIEW
Software	MS Office, Mathematica, LaTeX, Inkscape, Origin, Catia.
OS	Windows, OS X, Linux

Languages

English	Native language
French	Native language
German	Basic (B1 level)

Other interests

Music	Bass player. Former active member of two bands.
Travel	Travelled with the group *Nouvelle Planète* to Burkina Faso in a humanitarian trip.
Sport	Tennis, ski and bicycle (to work)
Photography	Video editing and photo retouching

Publications, presentations and posters

M. Antoni, J. Rossen, F. Martirena, K. Scrivener, **Cement substitution by a combination of metakaolin and limestone.** Cement and Concrete Research 42 (2012) 1579–1589

J. Rossen, B. Lothenbach, K. Scrivener, **C-S-H composition by EDS: considerations on operating conditions and data treatment**. *Conference paper and presentation* at the 14th Euroseminar on Microscopy Applied to Building Materials (EMABM 2013), 11 June 2013, Helsingør, DK.

J. Rossen, B. Lothenbach, K. Scrivener, **Optimising the experimental conditions for analysing calcium silicate hydrates in a white Portland cement paste**. *Conference paper and presentation* at the 33rd Cement and Concrete Science Conference, 2-3 September 2013, University of Portsmouth, UK.

J. Rossen, B. Lothenbach, K. Scrivener, **Study of C-A-S-H by SEM-EDX and STEM in pastes of water:binder = 0.4**, *Presentation at the* C-A-S-H workshop, Empa, Dübendorf, Switzerland (07.05.2014).

J. Rossen, K. Scrivener. **Assessing the C-S-H composition in matured cement paste samples.** Paper in preparation.

J. Rossen, B. Lothenbach, K. Scrivener, **Composition of C-S-H in pastes with increasing levels of silica fume addition.** Paper in preparation.